TGFβ Controls the Apico-Basolateral Orientation of Tumor Spheres and Is Correlated With Patient Outcome in Colorectal Cancer

Charlotte Canet-Jourdan

Thèse de doctorat

NNT : 2021UPASL030

université PARIS-SACLAY

TGFβ controls the apico-basolateral polarity orientation of tumor spheres and is associated with patient outcome in colorectal cancer

Thèse de doctorat de l'université Paris-Saclay

École doctorale n°582 : cancérologie : biologie - médecine - santé (CBMS)
Spécialité de doctorat : Aspects moléculaires et cellulaires de la biologie
Unité de recherche : Université Paris-Saclay, Inserm, Institut Gustave Roussy, Dynamique des Cellules Tumorales, 94800, Villejuif, France.
Référent : Faculté de médecine

Thèse présentée et soutenue à Villejuif, le 26 mars 2021, par

Charlotte Canet-Jourdan

Composition du Jury

Ama GASSAMA-DIAGNE DR, INSERM U1193	Présidente
Johanna IVASKA DR, Université de Turku	Rapportrice et Examinatrice
Danijela VIGNJEVIC DR, UMR144	Rappportrice et Examinatrice
Marc POCARD PU-PH, UMR965	Examinateur
Fanny JAULIN DR, U1279	Directrice de thèse

université PARIS-SACLAY

1. **ECOLE DOCTORALE N°582**
2. **Cancérologie : biologie - médecine - santé (CBMS)**
3.

Titre : La signalisation TGFβ contrôle la polarity apico-basolatérale de sphères tumorales et corrèle avec la survie des patients atteints d'un cancer colorectal.

Mots clés : cancer colorectal, polarité apico-basolatérale, TGFβ, intégrines

Résumé : La dissémination métastatique des cancers reste à ce jour, un problème de santé publique majeur. Les approches de biologie cellulaire, telles que les organoïdes, peuvent permettre de faire le lien entre les analyses histologiques et moléculaires, afin d'identifier les programmes morpho-oncogéniques sous-jacents à la dissémination des cancers. L'analyse systématique prospective d'effusions péritonéales de patients atteints d'un cancer colorectal (CCR) a permis l'identification d'un nouvel intermédiaire tumoral appelé Tumor spheres with inverted polarity (TSIPs). Les TSIPs sont des clusters cellulaires impliqué dans la dissémination métastatique des CCR dits « festonnés », mais leurs caractéristiques biologiques sont encore inconnues.

Tandis que toutes les TSIPs présentent une polarité apico-basolatérale inversée dans les liquides, nous démontrons ici qu'elles en présentent deux au sein des tissus et des cultures organotypiques: soit elles conservent leur topologie inversée dite "apical-out", soit elles adoptent um phénotype plus conventionnel dit "apical-in". Nous avons pu identifier que la signalisation TGFβ ainsi que celle impliquée dans les adhésions focales contrôlaient l'orientation de polairté des spheres. De plus, nous avons pu associer la topologie apical-out avec une moins bonne survie chez les patients.

Title : TGFβ controls the apico-basolateral orientation of tumor spheres and is correlated with patient outcome in colorectal cancer.

Keywords : colorectal cancer, apico-basolateral polarity, TGFβ, integrins

Abstract : The metastatic dissemination of cancer remains a major issue in patients' treatment. Cell biology approaches, such as organoids, have the potential to bridge histological and molecular analyses to decipher the onco-morphogenetic programs that fuel cancer dissemination. The systematic prospective analysis of peritoneal effusions from patients with colorectal carcinoma (CRC) identified new tumoral intermediates called Tumour Spheres with Inverted polarity (TSIPs). TSIPs are cell clusters mediating the metastatic spread of CRC evolving from the serrated pathway, but their underlying biology is unknown.

While all TSIPs harbor an inverted apico-basolateral polarity in fluids, here, we report two distinct topologies in tissues and organotypic culture: TSIPs either conserve the inverted "apical-out" polarity or switch to a conventional "apical-in" polarity. We identified TGFβ and focal adhesion signaling as the main drivers of polarity orientation. Moreover, the automated assessment of these phenotypes and the calculation of a polarity score proved that the apical-out histology is associated with poor patient survival.

This study identifies new tumour cell behaviors and their associated oncogenic pathways that could be exploited to stratify mucinous CRC patients with high risk of metastatic spread.

AKNOWLEDGMENTS

I would like to thank Fanny for the opportunity of doing a PhD in her lab, especially on this topic that I found fascinating since day one. With the technical academic training that I have, I had to cross path with people who could see passed it and believe in the potential that I had to a PhD. Fanny was one of those people and I'm sincerely thankful for it.

I'm also thanking Olivier Zajac who started this project. I know how much he cared about it and I was lucky enough to take over. I cherish the few months we spent together at the beginning of my PhD. I'm also grateful for the continuous relevant insights he gave me during those four years.

I would also like to thank Nadia Elkhatib who took over Olivier for my mentorship. Out of scientific curiosity and friendship, she was there to encourage me and she helped me through the hardest times of my PhD.

I'm truly grateful for having so many amazing people around me during those 4 years, Jean-Baptiste Lopez in particular who was my first master student and who is now, one of my closest friends. I'm also thinking about everyone in my team (past and present members) but also in Guillaume Montagnac's team, and Constance Lamy and Amaury Bongers. They all made it very easy on a daily basis.

I would like to thank my friends and family, even though they did not fully understand what I was doing, they have always given me support and showed me how proud of me they were. Especially my boyfriend, who was only by my side for the last year but it was definitely not the easiest one.

Finally, I would like to thank everybody who participated in some way to this experience. I learned a lot, scientifically and humanely.

TABLE OF CONTENTS

ABBREVIATIONS

Numbers

2D: two-dimensional

3D: three-dimensional

A

A/B: apico-basolateral

AEE: Apical early endosome

AC: Adenocarcinoma

AJ: Adherent junction

AJC: Apical junctional complex

AMIS: Apical membrane initiation site

AMT: Amoeboid-to-mesenchymal transition

Anx2: Annexin 2

AP: Adaptor protein

APC: Adenomatous polyposis coli

aPKC: Atypical protein kinase C

Arp: Actin-related protein

ASC: Adenosquamous carcinoma

Atoh1: Atonal homolog 1

B

BAR (domain): Bin, Amphiphysin, Rvs

BEE: Basolateral early endosome

bHLH: basic helix-loop-helix

BL: Basolateral

BM: Basement membrane

BMP: Bone morphogenic protein

bHLH: Basic helix-loop-helix

BrdU: Bromodeoxyuridine

C-D

CAF: Cancer-associated fibroblast

CBC: Columnar base cell

CDC42: Cell division control protein 42

C-ERMAD: C-terminal ERM-association domain

CKI: Casein kinase I

CIMP: CpG island methylator phenotype

CIN: Chromosomal instability

CMS: Consensus molecular subtype

CRC: Colorectal cancer

CRE: Common recycling endosome

CRISPR: Clustered regularly interspaced short palindromic repeats

CSS: Cancer-specific survival

CTC: Circulating tumor cell

Dlg: Disc large

Ds: Dachsous

DSS: Dextran sodium sulfate

E

E-cadherin: Epithelial cadherin

ECM: Extracellular matrix

EEA1: Early endosome antigen 1

EEC: Enteroendocrine cell

EMT: Epithelial-to-mesenchymal transition

EPHB2: Ephrin type B receptor 2

ER: Endoplasmic reticulum

ERM: Ezrin/radixin/moesin

F

F-actin: Filamentous actin

FAK: Focal adhesion kinase

FAP: Familial adenomatous polyposis

FERM: Four point one ERM

Fmi: Flamingo

Fz: Frizzled

G

GA: Golgi apparatus

GAP: GTPase activating protein

GDI: Guanine nucleotide dissociation inhibitor

GDP: Guanosine diphosphate

GEF: Guanine nucleotide exchange factor

GEMM: Genetically engineered mouse model

GI: Gastrointestinal tract

GPI: Glycosyl phosphoinositol

GSK3: Glycogen synthase kinase 3 beta

GTP: Guanosine triphosphate

H-L

HES: Hairy/enhancer of split

HEK: Human embryonic kidney

HGD: High grade dysplasia

HGF: Hepatocyte growth factor

HIPEC: Hyperthermic intraperitoneal chemotherapy

HNPCC: Hereditary nonpolyposis colorectal cancer

HP: Hyperplastic polyp

ID1: Inhibitor of differentiation 1

ILK: Integrin-lined kinase

ISC: Intestinal stem cell

JAM: Junctional adhesion molecule

KO: Knock-out

LBK: Liberkuhnian

Lgl: Lethal giant larvae

LGR5: Leucine-rich repeat-containing G protein-coupled receptor 5

LOH: Loss of heterozygosity

LRP: Lipoprotein receptor-related protein

M-N

MAPK: Mitogen-activated protein kinase

MAT: Mesenchymal-to-amoeboid transition

MDCK: Madin-Darby canine kidney

MeC: Medullary carcinoma

MET: Mesenchymal-to-epithelial transition

MiC: Micropapillary carcinoma

MMP: Matrix metalloproteases

MMR: Mismatch repair

MSI: Microsatellite instability

MSS: Microsatellite stable

MVB: Multivesicular body

MUC: Mucinous carcinoma

N-cadherin: Neural cadherin

NEC: Neuroendocrine carcinoma

NHERF: Na^+/H^+ exchange regulatory cofactor

NICD: Notch intracellular domain

NM-II: Non-muscle myosin II

NOS: Non-otherwise specified

P

PALS1: Protein associated with Lin Seven 1

PAP: Pre-apical patch

PAR: Partition defective

PATJ: PAS1-associated tight junction protein

PC: Peritoneal carcinomatosis

PCP: Planar cell polarity

PDGF: Platelet derived growth factor

PDO: Patient-derived organoid

PDX: Patient-derived xenograft

PDZ: Postsynaptic density/discs large/zonula occludens

PHD: Pleckstrin homology domain

PI: Phosphoinositide

PI3K: Phosphatidylinositol-3 kinase

PIP_2: Phosphatidylinositol 4,5-biphosphate, $PtdIns(4,5)P_2$

PIP_3: Phosphatidylinositol 3,4,5-triphosphate, $PtdIns(3,4,5)P_3$

PtdIns: Phosphatidylinositol

PTEN: Phosphatase and tensin homolog deleted on chromosome ten

PTM: Post-translational modification

R-S

RNA: Ribonucleic acid

RNAi: RNA interference

ROCK: Rho-associated coiled coil kinase

R-spondin: Roof plate-specific spondin

SCRIB: Scribble planar cell polarity protein

SeC: Serrated carcinoma

Shh: Sonic hedgehog

SMURF: SMAD-specific E3 ubiquitin protein ligase

SNARE: Soluble N-ethylmaleimide-sensitive factor attachment receptor

SNX: Sortin nexin

SRCC: Signet ring cell carcinoma

SSP: Sessile serrated pathway

SSA/P: Sessile serrated adenoma/polyp

T

TA cells: Transient-amplifying cells

TCF: T cell factor

TGFβ: Transforming growth factor-β

TGN: Trans-Golgi network

TIAM1: T lymphocyte invasion and metastasis-inducing protein 1

TJ: Tight junction

TME: Tumor microenvironment

TSA: Traditional serrated adenoma

TSG: Tumor suppressor gene

TSIP: Tumor sphere with inverted polarity

TSP: Traditional serrated pathway

V-Z

VAC: Vacuolar apical compartment

WASP: Wiskott-Aldrich syndrome protein

Wnt: Wingless interaction

WT: Wild type

ZO: Zonula occludens

INTRODUCTION

I. Colorectal cancer: from a digestive organ to a major worldwide health issue

A. The colon

The colon ensures intestinal homeostasis through many processes. It regulates the balance between secretion (via the crypt cells) and reabsorption (via the enterocytes) of water and electrolytes, through passive diffusion relying on sodium cytoplasmic gradients and active absorption using membrane aquaporines. Those mechanisms take place mainly in the ascending colon *(see Figure1)* because of its longer exposure time with the digestive bowl. The colon also displays a digestive function via its bacterial flora which generates energy through the fermentation of undigested carbohydrates and proteins.

Another important colonic function is the transport of undigested food and unabsorbed digestive metabolites towards the rectum for defecation. This is ensured by segmental and peristaltic contractions of the smooth muscle layers. The feces expulsion through the rectum is a complex process involving sphincters allowing continence[1].

4. Embryonic development

The gastrointestinal (GI) tract arises from the three embryonic sheets:

- The mesoderm gives rise to the digestive connective tissue such as the gut wall and the smooth muscle.
- The endoderm is the source of the digestive epithelium found in the gastrointestinal tract, liver, gallbladder and pancreas.
- The ectoderm will form the neural crests from which the enteric nervous system will arise[2].

The digestive tube starts forming around the 3rd week of embryogenesis, simultaneously, gastrulation occurs to form the embryonic layers listed above. The different digestive epithelial cell types are found starting week 12 and resemble adult intestinal cells by week 22[3]. Different signaling pathways intervene all along this process to ensure a healthy development, such as:

- Sonic hedgehog (SHH): promotes mesenchymal cells proliferation and villi formation[4]
- Bone morphogenic proteins (BMPs): ensures correct crypt formation[5] and stem cells localization[6]
- Wingless integration (WNT): promotes intestinal stem cells proliferation[7]
- Platelet derived growth factors (PDGFs): controls smooth muscle differentiation[8].

5. Architecture

a. Colon histology

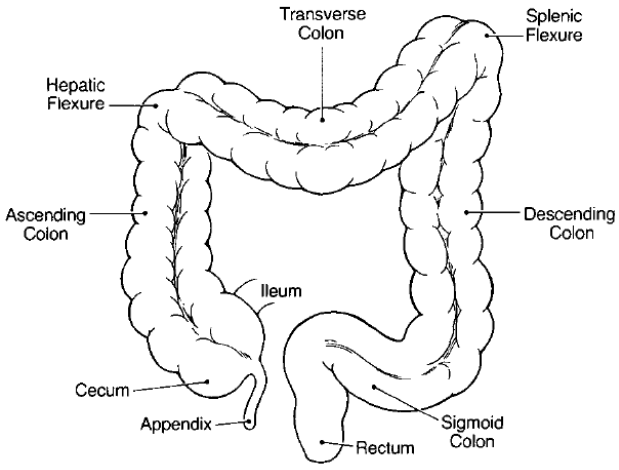

Figure 1: General anatomy of the colon. Adapted from Levine et al, 1989.

The colon represents the last 1-1.5m of the gastrointestinal tract. It starts at the end of the ileum, with the appendix and the cecum located in the right lower abdominal quadrant. Then, the ascending colon extends towards the hepatic flexure, connected to the splenic flexure via the transverse colon. The descending colon then proceeds to the left lower quadrant and gives rise to the sigmoid colon, ending with the rectum[2]. The colon also presents histological differences between its right and left part whose relevance will be discussed later in the pathology section.

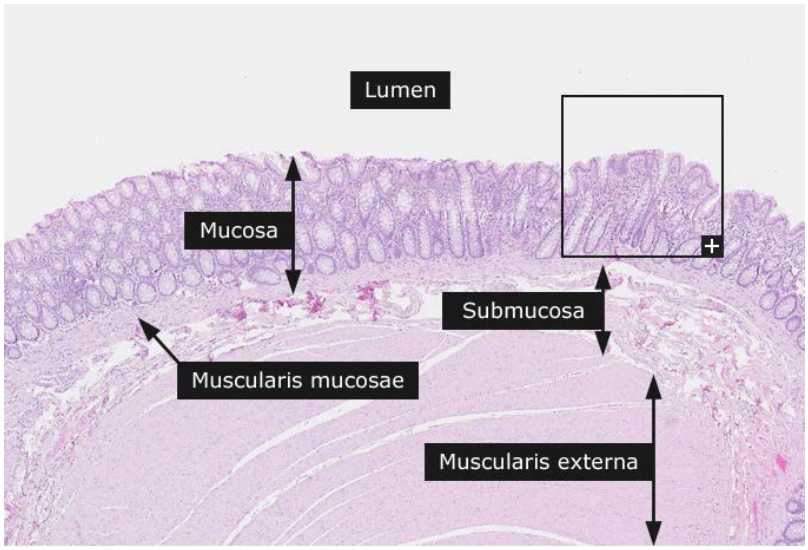

Figure 2: Normal colon histological slice, stained with hematoxylin and eosin, showing the different layers. From The human protein atlas.

The colon is composed of four layers[9] *(see Figure2)*:

- The mucosa, a thick sheet in contact with the lumen containing the tubular intestinal glands (crypts of Liberkuhn), and the lamina propria, the crypts' stroma, composed of connective tissue and inflammatory cells.
- The muscularis mucosae, a thin layer of smooth muscle delimiting the border between the mucosa and the submucosa.
- The submucosa, composed of loose connective tissue with blood, lymph vessels and nerves.
- The muscularis externa, consisting of an inner circular smooth muscle layer and a discontinuous longitudinal layer. This muscular sheet is divided into three muscular bands called the teniae coli.
- The serosa, representing the peritoneum visceral layer.

Our team focuses on colorectal carcinomas and their metastatic dissemination. Since they arise from the colon epithelium, the rest of the manuscript will aim at describing the cellular and molecular characteristics of this tissue, both in physiology and in pathology.

---

b. Colonic cells

The colon mucosal layer is composed of a columnar epithelium divided into numerous functional units: the crypts of Liberkuhn *(see Figure3)*. The crypts are epithelial invaginations into the underlying connective tissue which protect stem cells by putting them away from the digestive bowl and increase the colon surface[10]. To ensure organ integrity maintenance, the intestinal tract is daily self-renewing, thanks to intestinal stem cells (ISCs) located at the crypt base. They divide to produce transient-amplifying (TA) cells which are highly proliferative progenitors that will then, depending on environmental signals, commit to the absorptive or the secretory lineages. This differentiation process happens while cells migrate towards the top of the crypt[11].

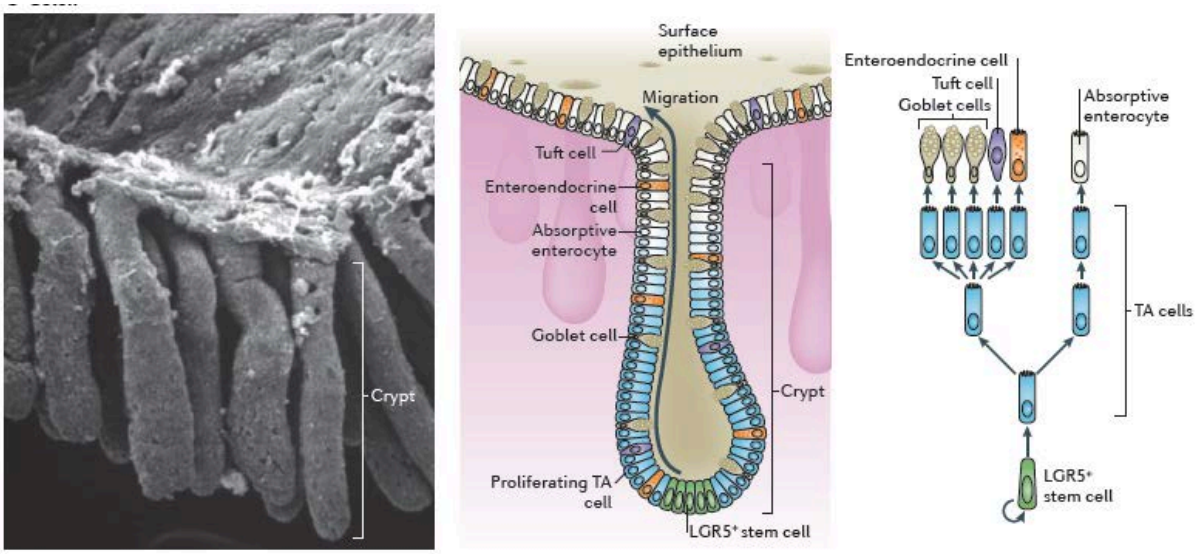

Figure 3: Colonic crypt architecture: (A) Electron microscopy of a crypt, (B) organization of cells throughout the crypt and (C) colonic cell lineages. From Bryant et al., 2008.

i. Stem cells

In homeostasis, stem cells are identified through the evaluation of their self-renewal and multipotency abilities[12], mainly using clonal lineage tracing[13]. This technique was used in the 1970s to first identify ISCs by radioisotope and 5+bromodeoxyuridine (BrdU) labelling of dividing intestinal cells. The results show a common origin of multipotent cells at the crypt base that were named crypt base columnar (CBC) stem cells. This was confirmed by the fact that ablation of those cell populations abolishes epithelial self-renewal[14]. Nowadays, to identify ISCs, most studies used the CBC stem cell marker Lgr5 *(see Figure4)*. Lgr5 (Leucine-rich repeat-containing G protein-coupled receptor 5) was the first identified CBC stem cell marker and was later found to be a WNT target gene selectively expressed in the cells within the base of adult intestinal crypts[15].

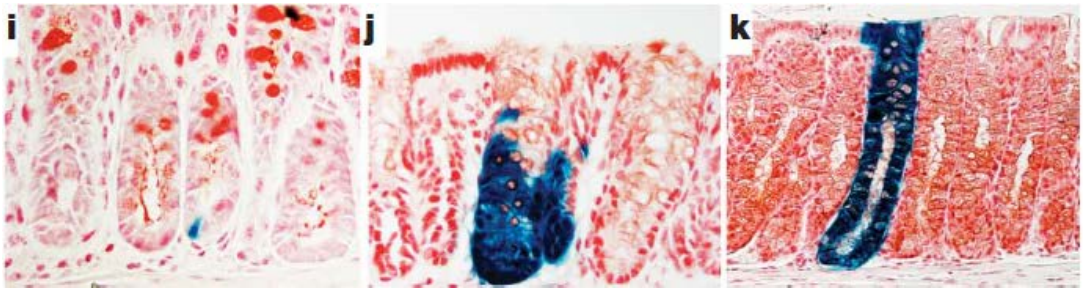

Figure 4: Lineage tracing in the colon using the Lgr5-EGFP-ires-Cre-ERT2/R26R-lacZ mouse model. Histological analysis of LacZ activity in the colon after (i) 24h, (j) 5 days and (k) 60 days induction. Barker et al., 2007.

This was later on confirmed by using $LGR5^+$ CBC stem cells to generate fully functional organoids[16], but the precise expression profile of $LGR5^+$ CBC stem cells cannot be determined because of the lack of LGR5 antibodies. Using FACS sorting methods, combinatorial microarray and proteomic approaches, a molecular signature for $LGR5^+$ CBC stem cells was established[17]. It revealed a list of approximately 500 genes preferentially expressed in those cells, with a strong WNT signature. Moreover, it was shown that LGR5 was capable of amplifying WNT signaling through the binding of one of its agonist, R-spondin (Roof plate-specific spondin)[18].

In fact, the Wnt signaling pathway *(see Figure5)* represents the primary driving force behind the proliferative ability of the intestinal epithelium, both in the healthy and carcinoma tissues. The main actor in Wnt canonical signaling pathway is β-catenin. In the absence of a Wnt signal, β-catenin is bound to the degradation complex composed of two tumor suppressors (axin and adenomatous polyposis coli (APC)) and two constitutively active kinases (glycogen synthase kinase 3β (GSK3) and casein kinase I (CKI)). GSK3 and CKI will phosphorylates β-catenin at its N-terminus, leading to its addressing and degradation at the proteasome. In this state, the transcriptional repressor Groucho is bound to the Wnt transcriptional factor T cell factor (TCF), preventing the transcription of Wnt targeted genes[19,20]. When Wnt ligands bind their receptors at the cell surface (Frizzled and low-density lipoprotein receptor-related protein (LRP), the consecutive signaling leads to the inactivation of the degradation complex. β-catenin then accumulates in the cytoplasm and translocates into the nucleus to bind TCF instead of Groucho. The TCF/β-catenin dimer forms an active transcriptional complex allowing the transcription of Wnt targeted genes, many of them playing a role in intestinal stem cell maintenance, such as Lgr5.

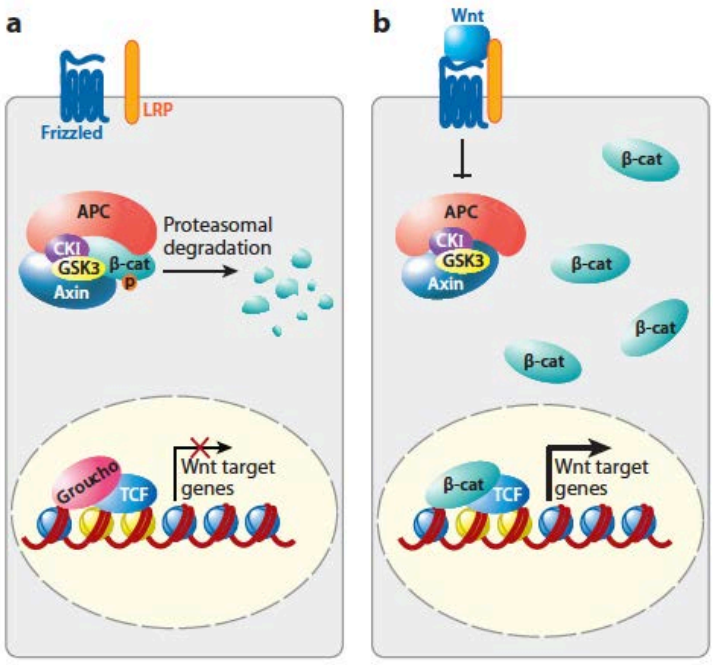

Figure 5: Schematic representation of the Wnt signaling pathway, in absence (a) or in presence (b) of a Wnt ligand. G. van der Flier et al, 2009.

ISCs can differentiate into two main lineages: the secretory (comprising of Goblet, tuft and enteroendocrine cells) and the absorptive (the enterocytes). Their engagement into one or the other lineage relies on the Notch signaling pathway. In particular, Notch is responsible for the lateral inhibition between identical adjacent cells, the first differentiating cell preventing its neighbor from engaging towards the same cell fate[21].

Notch encodes four single transmembrane receptors (NOTCH 1 to 4) and has five ligands (Delta-like 1, 3 and 4; Jagged 1 and 2). When a Notch receptor binds its ligand on an adjacent cell, it results in proteolytic cleavages of the receptor via the γ-secretase protease activity and the translocation of the Notch intracellular domain (NICD) into the nucleus. The NICD binds to a transcriptional repressor called CLS, allowing the transcription of Notch target genes such as the hairy/enhancer of split (HES) transcriptional repressors[22].

In intestinal cells, Notch signaling activates the expression of Hes1, which then represses the expression of atonal homolog 1 (Atoh1), a gatekeeper for the entry of cells into the secretory lineage. In fact, deletion of Hes1 increases the number of cells in the secretory lineage while decreasing the number of enterocytes[23] *(see Figure 6)*. On the opposite, deletion of Atoh1 results in a complete loss of all secretory lineages[24], and its overexpression is sufficient to induce TA cells differentiation into secretory cells[25].

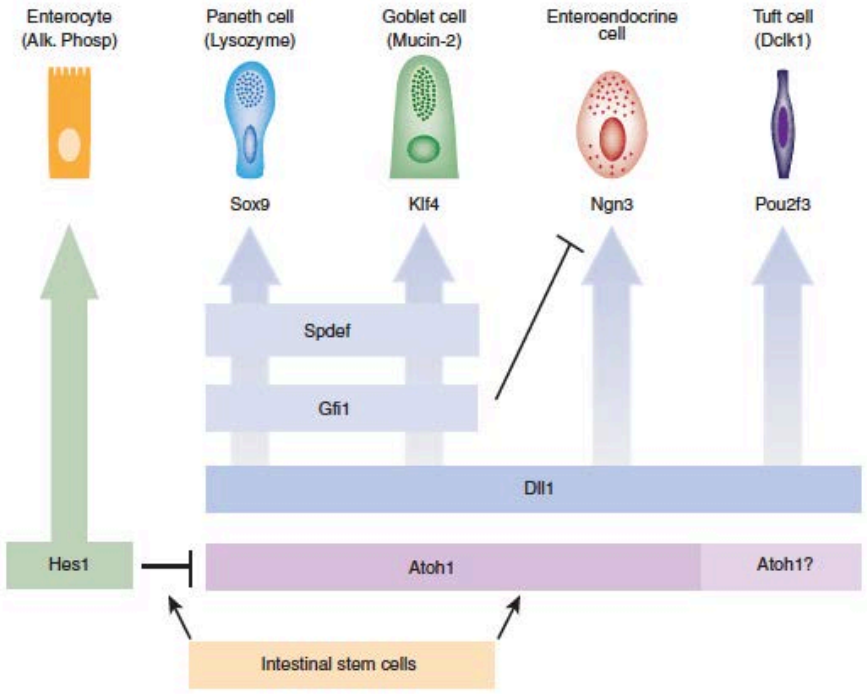

Figure 6: Notch signaling involvement in ISCs differentiation, Gerbe et al., 2016.

ii. Goblet cells

Goblet cells belong to the intestinal secretory lineage. They represent between 4-16% of epithelial cells from the duodenum to the descending colon[26]. They have a protective function through the production and secretion of mucins. The colon displays a two-layered mucus system where the inner layer, attached to the Goblet cells, function as a filter physically separating bacteria from epithelial cells. The outer layer arises from protease degradation of the inner layer and is a non-attached mucus[27] (mainly MUC2) allowing effective transport of gut contents and preventing shear and chemical damage[10].

The intestinal Goblet cells can be directly regulated by immune cells. For example, in case of inflammation, some excreted cytokines can bind to Goblet cells surface receptors and induce a hyperplasia and mucus hypersecretion to protect the epithelium[28].

iii. Enteroendocrine cells

The endocrine system is widely distributed throughout the body, participating in homeostasis by secreting hormones. In terms of cell number, the GI tract is the largest endocrine organ thanks to enteroendocrine cells (EECs) located in the intestinal mucosa and crypts[29].
Two types of EECs can be described: the “open-type” displaying an apical prolongation with microvilli in contact with the lumen thus allowing its chemosensing properties, and the “closed-type” located deeper into the crypt and lacking microvilli, responding indirectly to luminal content[30].

EECs produce and accumulates their secretory products (mainly hormones and peptides) into cytoplasmic granules which will be released upon stimulation at their basolateral membrane. They can act locally in a paracrine manner, directly stimulate nerve endings close to their release site and reach distant cells through the bloodstream, maintaining GI homeostasis. The EECs also participate in homeostasis through a gut-brain communication allowing the whole body to respond and adapt to the composition of its digestive bowl.

iv. Absorptive enterocytes

Enterocytes are the most abundant cell type in the GI tract (more than 80% of the intestinal epithelium) and are responsible for nutrient absorption. Fully differentiated enterocytes are characterized by plasmic membrane protrusions at their apical pole: the microvilli, forming the brush border. This structure is about 100nm in diameter and 1-3μm in length and considerably increases the exchange surface between the lumen of the digestive tract and the enterocytes[31]. It is important to note that the colon displays less enterocytes than the small intestine.

Apart from the mucus produced by Goblet cells, enterocytes display a mucinous coat at their surface. In fact, the microvilli are covered with a filamentous glycocalyx with large, negatively charged mucin-like glycoproteins. It forms a barrier from antigens and pathogens, but also provides a degradative environment promoting digestion and nutrients absorption[32].

Enterocytes are responsible for the transportation of macromolecules, either using:

- Transcellular transport: directly through the enterocytes. Nutrients uptake is done via pinocytosis and especially through clathrin- and caveolae-mediated endocytosis[33].
- Paracellular transport: between adjacent cells. Tight junctions are dynamic structures which can be involved in a transjunctionnal osmotic flow, allowing the diffusion of nutrients (if their size is inferior to 5500Da)[34].

They also have a role in the immune defense against pathogens. In fact, they can digest antigens and release the fragments into the blood and/or lymphatic vessels. They can also directly present antigens to T cells through class I and II MHC molecules at their surface[27].

v. Tuft cells

Tuft cells were initially observed in 1960s in the respiratory and the digestive systems by electron microscopy: they display a unique tubulovesicular system with an apical bundle of microfilaments connected to a microvilli tuft going into the lumen[35] *(see Figure8)*. They belong to the secretory lineage.

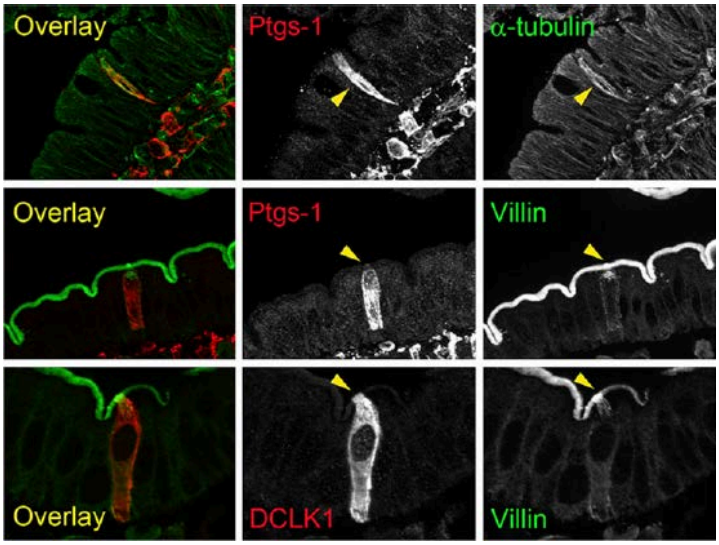

Figure 8: Immunostainings of intestinal tuft cells, Gerbe et al., 2012.

Based on structural similarities with the taste buds found within the tongue, tuft cells were said to have tasting properties. This was confirmed when many markers and members of the taste transduction pathway were found in those cells such as α-gutducin, β-endorphin, met-enkephalin and uroguanylin[36,37]. Tuft cells definitely have a chemosensory function since their secretion can be modulated depending on the saltiness or sugar concentration of a solution. They are known to be the only epithelial cells to have the whole enzymatic machinery for prostaglandin-2 biosynthesis. They secrete peptides and hormones involved in water and sodium transport[38] in the stomach where they are over-represented (over 30% of cells) and are thought to participate in neutralizing HCl to prevent gastric epithelial damage[39]. Despite all that, colon tuft cells are less studied and their function is still unknown.

B. Colorectal cancer

With nearly 2 million new cases and nine thousand deaths in 2020, colorectal cancer (CRC) is the second cause of cancer-related death worldwide[40]. There does not seem to be a gender prevalence and etiological factors and carcinogenesis mechanisms appear rather complex and heterogenous. Contributory agents include dietary habits (unsaturated fats, red meat, alcohol, low physical activity), inherited and somatic genetic alteration *(see Figure 9)*.

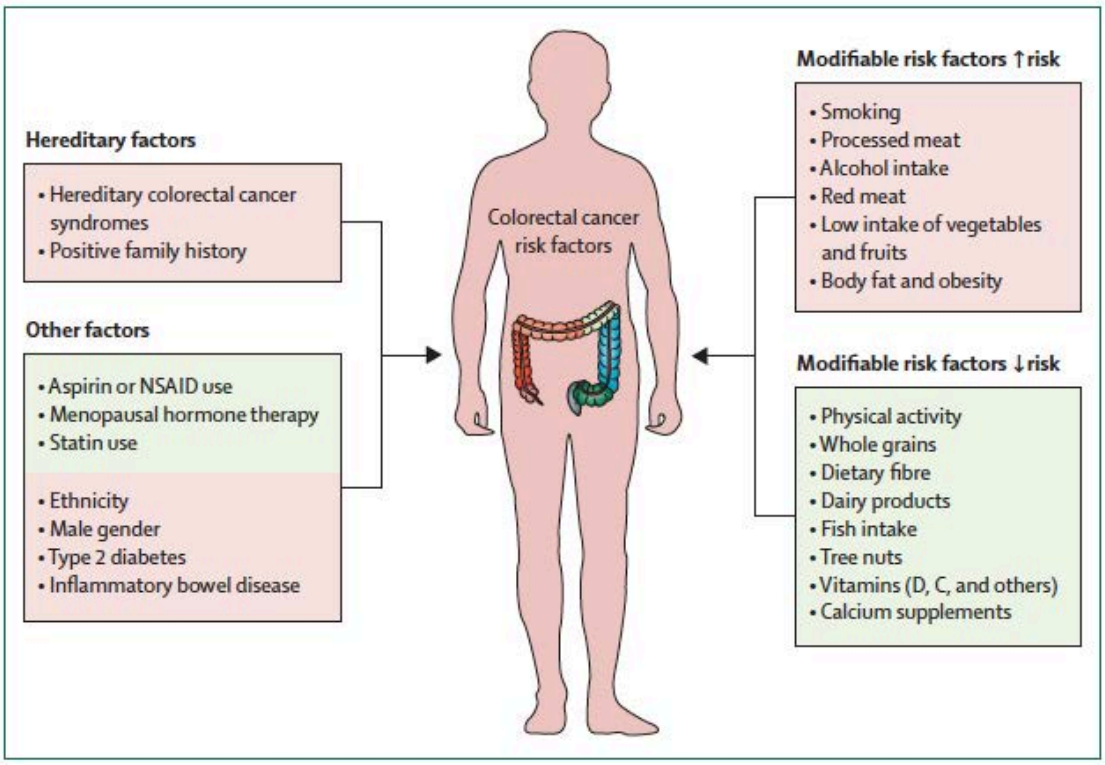

Figure 9: Risk factors in CRC, Dekker et al. 2019.

CRCs heterogeneity made their classification a challenge for the scientific community, both histologically and molecularly. Here, we will focus CRCs histology and Consensus molecular subtypes (CMS) which seem to be the most recent and relevant classifications obtained so far.

---

1. Histopathology (grade and prognosis)

a. Generalities

CRCs are diagnosed by anatomopathologists following an endoscopic biopsy or a polypectomy.

Then, CRCs are graded according to a TNM score[41]:

- T (for Tumor):
  - TX: the tumor cannot be measured
  - T0: no evidence of primary tumor or it cannot be found
  - Tis: the cancer cells are growing on the most superficial layer of the tissue, this is the *in situ* tumor
  - T1,2,3 or 4: characterizing the size and/or the invasion of nearby tissues, the higher the number, the deeper it has invaded.
- N (for Node):
  - Nx: the nearby lymph nodes cannot be evaluated
  - N0: they do not contain cancer cells
  - N1, 2 and 3: size, location and/or number of lymph nodes invaded by cancer cells, the higher the number, the greater the cancer spread in the lymph nodes.
- M (for Metastases):
  - M0: no metastases were found
  - M1: the cancer has spread to distant location(s).

Another criterion for tumors classification is the presence of immune cells within the tumor microenvironment (TME). It possess a prognostic value, even superior to TNM staging[42,43]and have been defined as the "immune contexture"[43,44] (type, orientation, density and location of immune cells in distinct tumor areas). This led to the establishment of a CRC prognostic marker called "immunoscore"[43,45,46] based on the presence of lymphocytes populations at the tumor center and at the invasive margin.

b. Histological CRC subtypes

i. Adenocarcinomas

More than 90% of patients display adenocarcinomas (ACs) meaning that cancer cells arise from the epithelial cells in the colon mucosa. They are characterized by a glandular structure depending on the epithelial characteristics maintained in the cancer cells:

- Well differentiated: more than 90% of the tumor is forming glands (10% of patients)
- Moderately differentiated: 50-95% of gland formation (70% of patients)
- Poorly differentiated: less than 50% of the tumor is forming gland (20% of patients)[47].

It is important to note that histological grading is only relevant for conventional adenocarcinoma. Indeed, some histological variants may display a high-grade morphology but behave like low grade lesions depending on their genetic alterations and expression profiles.

ii. Mucinous carcinomas

Apart from adenocarcinoma, other histological CRC variants can be observed, the second most common being mucinous carcinoma (MUC). A tumor is characterized as MUC when more than 50% of the surface analyzed is composed of mucus. Within this extracellular secretion, cancer cells can be found as individuals or as groups[48]. For a long time, MUC have been correlated with a poor prognosis but recent studies demonstrated that there was no difference in overall survival (OS) of MUC compared to AC after correction for stage[49,50]. Nevertheless, MUC present more metastases, especially in the peritoneum which lead to peritoneal carcinomatosis (PC) and is responsible for the poor outcome after palliative chemotherapy[51,52].

iii. Others

Micropapillary carcinoma (MiP):

MiP were first described in breast cancer and is now seen as a phenotypic component characterized by the presence of small tumor cells clusters within stromal areas[48]. A tumor is then defined as MiC when at least 5% of cells display this topology. They are more invasive than ACs and are associated with a poor prognosis. Those features combined with the high-grade cytologic features suggest that MiC should be considered as poorly differentiated at the histological scale, although the individual cells may have maintained their differentiated polarized features such as A/B polarity[53].

Serrated carcinoma (SeC):

This subtype presents glandular serration and can be accompanied by mucinous areas. Indeed, nearly 45% of SeC are found in MUC and suggests that MUC could arise from SeC. By performing an unsupervised clustering of expression data between SeC and AC, more than 200 genes were differentially expressed[54].

Medullary carcinoma (MeC):

MeC are characterized by the presence of poorly differentiated large cells displaying vesicular nuclei, eosinophilic cytoplasm and an important lymphocytes' infiltration. They are difficult to discriminate with poorly differentiated ACs and present a general better outcome[55].

Signet ring cell carcinoma (SRCC):

SRCC are identified via their typical phenotype with single cells displaying a large mucus vacuole putting their nucleus at its edge. Their poor prognosis is linked to their rapid progression and invasion towards the lymph nodes and the perineural system. Nevertheless, a high rate of recurrence has been observed leading to the recommendation to decrease aggressive treatments in SRCC patients[56]. Despite their poor outcome, the low frequency of this CRC prevents clinical trials from being developed.

Neuroendocrine carcinoma (NEC):

The development of specific antibodies towards neuroendocrine differentiation lead to the distinction of NEC which are characterized by the presence of at least 30% of differentiated neuroendocrine cells within the tumor[48]. Those CRCs are part of a spectrum going from ACs presenting neuroendocrine differentiation to NEC. There seems to be a clonal relationship between the adenocarcinoma cells and the neuroendocrine ones which can be traced back to the adenoma lesions[57].

Adenosquamous carcinoma (ASC):

ASCs resemble to ACs but are more advanced and present and poorer prognosis. However, since subtype is rare, really few clinical data are available[58].

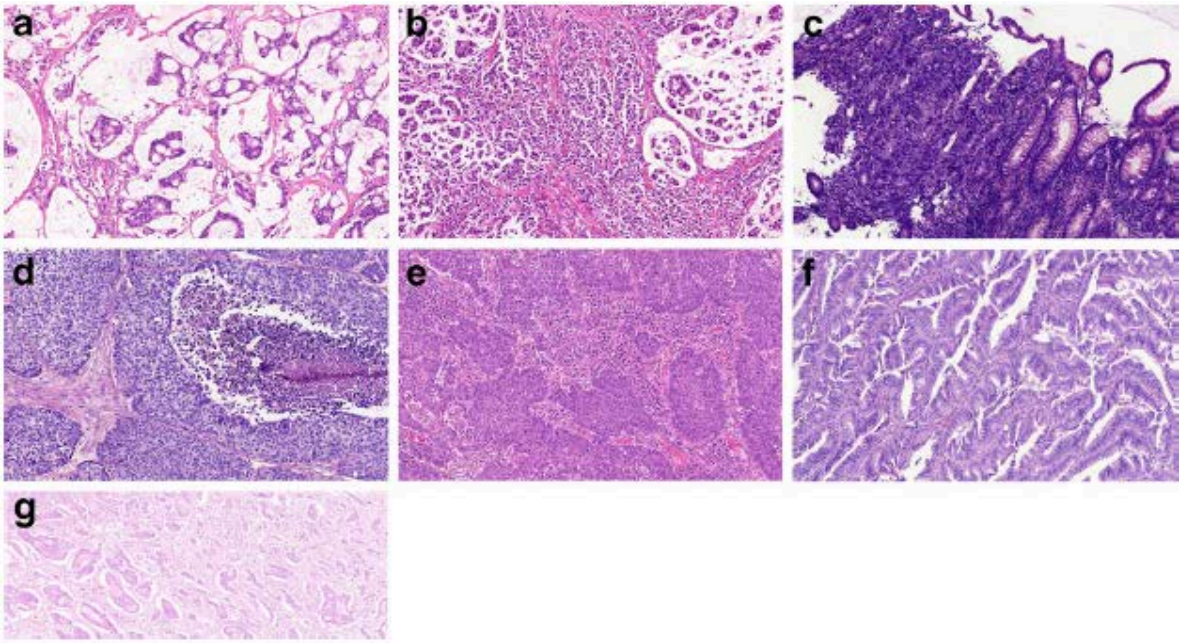

Figure 10: Different histological subtypes of CRC: (a) MUC, (b) SRCC, (c) NEC, (d) ASC, (e) MeC, (f) SeC, (g) MiC. From Nagtegaal & Hugen 2016.

2. Consensus molecular subtypes

a. Approach

Histological classification of CRCs has proven its efficiency in patient care's improvement, but molecular profiling should be able to identify clinically relevant groups for patient stratification and disease management. Recently, based on the individual work of 6 independent labs[59–64], a multicenter consortium presented a CRC consensus molecular classification which should allow a more refined stratification of patients and improve prognostication[65]. This gene-expression based classification gathers multiple criteria:

- **Chromosomal instability (CIN):** more than two-thirds of CRCs display this characteristic where some chromosomes are aneuploid and carry multiple structural aberrations.
- **Microsatellite instability (MSI):** consists in a hypermutable phenotype due to the loss of function in the mismatch repair (MMR) machinery. Microsatellites are short repetitive sequences enriched in polyadenine associated with *Alu* elements[66,67]which are particularly sensitive to replicative errors. MSI status was found in patients with Lynch syndrome, a hereditary condition leading to CRC usually starting at a young age. Thus, the MSI status represent a unique pathway for tumor development. Patients can present different levels of MSI (high or low) or be microsatellite stable (MSS). Moreover, the immunoscore mentioned above is related to the tumor's immunogenicity and thus, applied on MSI^{high} or MMR deficient patients.
- **CpG island methylator phenotype (CIMP):** many gene promoters are enriched in cytosine and guanine clusters which can be methylated by a DNA methyltransferase. This leads to the silencing of genes, and in cancer, of tumor suppressor genes (TSG). Like MSI, the methylation level can vary from a patient to another which is referred to as $CIMP^{high}$ or $CIMP^{low}$. Non-hereditary MSI CRCs usually develop in $CIMP^{high}$ tumours after silencing of MLH1, an MMR gene, due to the methylation on its promoter[68].

b. CMS 1-4

By combining gene expression-based approaches on the 6 independent datasets mentioned above and applying non-supervised clustering approaches, the Consortium identified four main Consensus Molecular Subtypes (CMS1-4) displaying specific patterns of genetic alterations which correlated with the clinical data of the associated patients *(see Figure12)*:

- CMS1 tumors are hypermethylated (CIMP), present a hypermutated profile and contains most of MSI samples. This is in line with the enriched BRAF mutated tumors in this group. Moreover, the CMS1 group is characterized by a diffuse immune infiltrate, associated to the MSI status[69].
- In CMS2 tumors, there is a strong epithelial signature combined with an upregulation of WNT and MYC downstream targets, known to be widely implied in CRC tumorigenesis.
- CMS3 tumors are enriched in multiple metabolic signatures which correlates with the occurrence of KRAS mutations, known to initiate an adaptation in cells' metabolism[70,71].
- Finally, CMS4 tumors harbor a mesenchymal expression profile with upregulations in genes involved in EMT, TGFβ signaling or matrix remodeling. display a large number of stromal cells, especially cancer-associated fibroblasts (CAFs) which have been described to influence and be influenced by tumor cells[72]. In fact, it is still a matter of debate as to decipher if the mesenchymal component observed in this subtype is due to an EMT-induced phenotype of cancer cells or to an important stromal cells contamination[73,74]. Nevertheless, the presence of a mesenchymal component is linked to worse outcomes in many cancers[75–77]

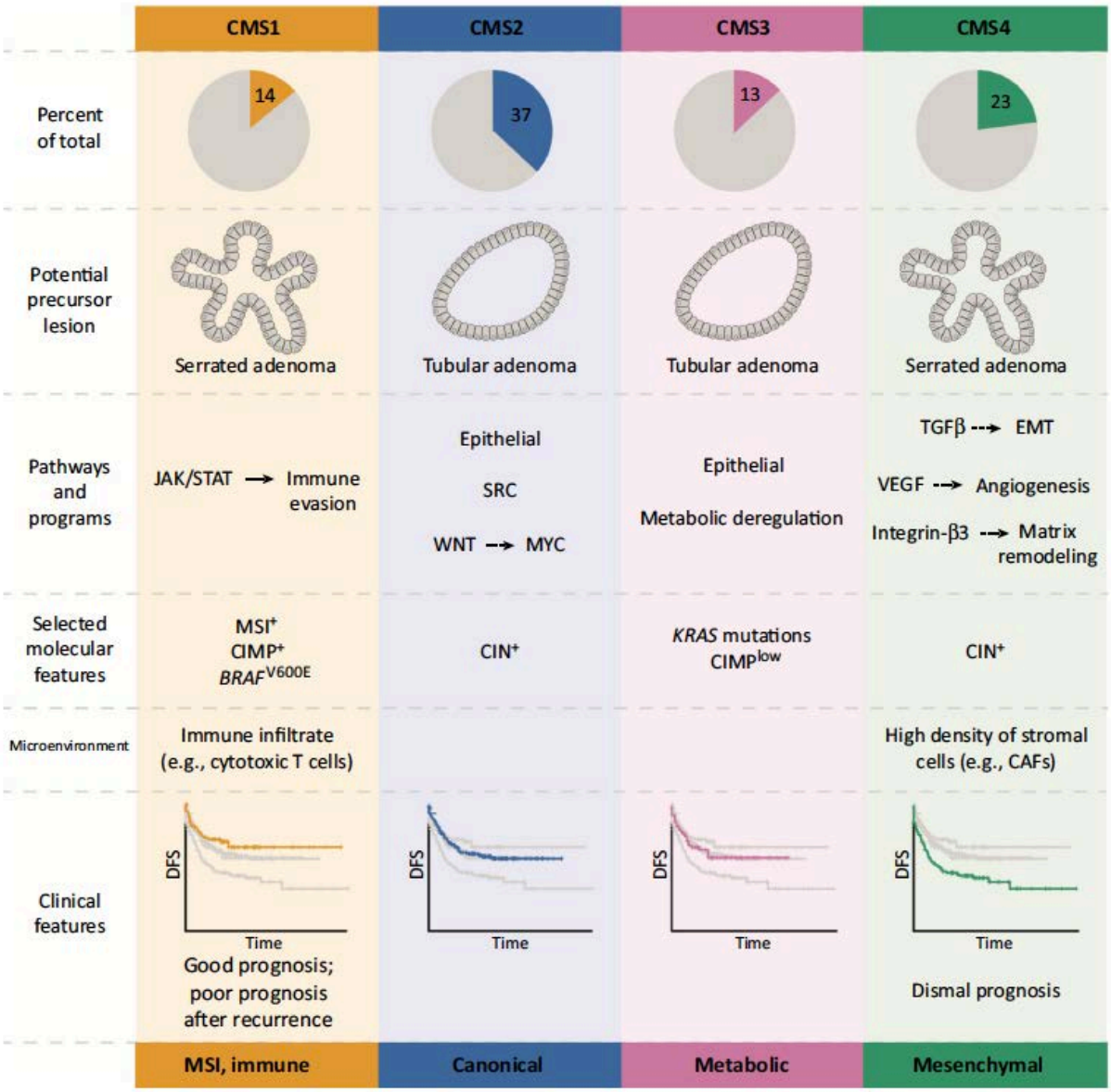

Figure 12: CMS groups and their characteristics Fessler et al., 2016.

It is important to note that 13% of CRCs do not fit into this classification with either a mixed or a partial molecular phenotype. This can be due to the sampling procedures which can differ between patients but more importantly, to tumor heterogeneity. Three parameters can influence the tumor cell populations found in patients: the cell-of-origin, the oncogenic pathway and the tumor microenvironment[78].

3. CRC developmental pathways

a. Cell of-origin

In order to explain that in a tumor, multiple cell populations can bear different oncogenic alterations, the cell-of-origin model was proposed. It relies on the fact that the first genetic lesions inducing tumorigenesis are found on a distinct cell type which will proliferate to form the tumor bulk. Several candidates were found in CRC: stem cells in which WNT activation leads to the development of adenomatous lesions[79] or differentiated cells acquiring tumor-initiating properties after being exposed to an external cue[80]. Thus, tumor heterogeneity can be explained by the presence of multiple cells-of-origin, each responsible for the expansion of a tumor subtype *(see Figure 13)*.

Indeed, the same mutation on different cell types will lead to the formation of different tumor phenotypes. For instance, the loss of APC gene expression on an ISC will lead to the formation of a tubular adenoma, whereas if it appears on a higher cell within the crypt, APC loss is not sufficient by itself and additional factors such as inflammation are required to induce carcinogenesis.

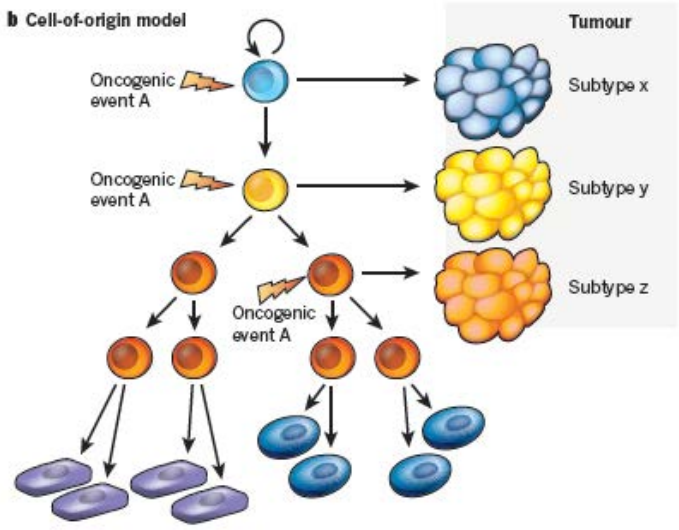

Figure 13: Cell-of-origin model for intratumoral heterogeneity, Visvader et al., 2011.

However, since the identity of cells along intestinal crypts does not rely on epigenetic marks but more on environmental cues, it is unlikely that CRC heterogeneity can only be explained through the cell-of-origin model. Nonetheless, based on the fact that the colon is divided into the proximal-right side and the distal-left side, originating from distinct embryonal precursors, an anatomical cell-of-origin model could contribute to CRC heterogeneity. Indeed, tumors arising from each side display specific molecular characteristics and physiopathological features[81]. It is still to decipher if this could lead to a proper clinical segmentation such as the separation between colon and rectal cancer *(see Figure14)*.

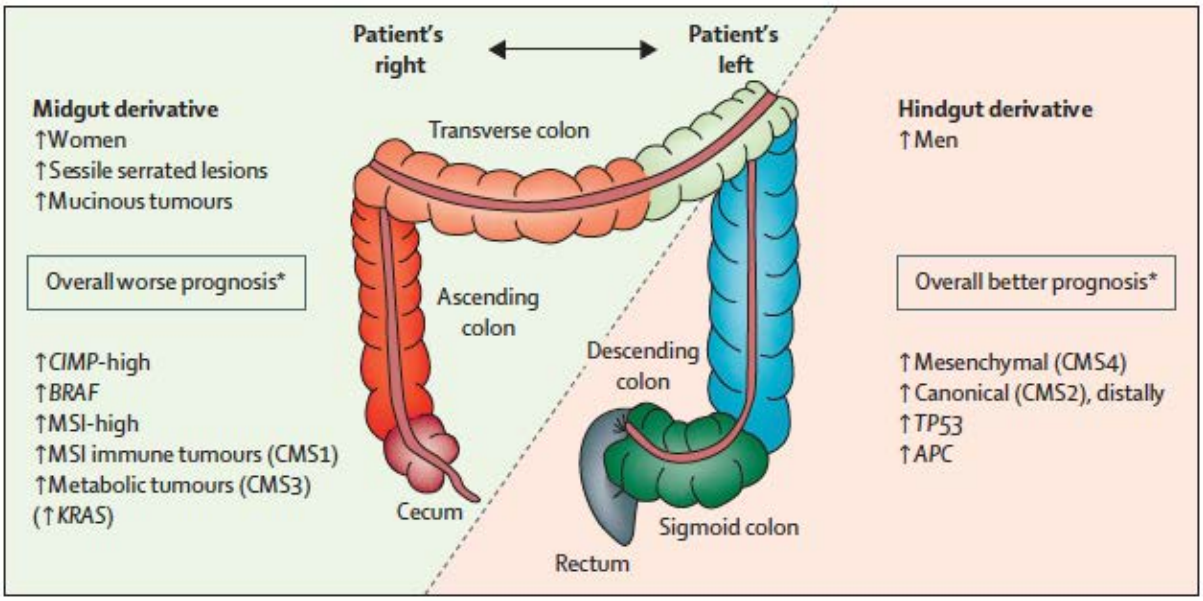

Figure 14: Comparison of proximal and distal CRCs, Dekker et al. 2019.

b. Oncogenic pathways

Another model used to explain tumor heterogeneity relies on cancer cells' oncogenic pathways. Indeed, different oncogenic alterations on the same cell type give rise to distinct tumors: APC loss on an ISC leads to a tubular adenoma, whereas the activating mutation $BRAF^{V600E}$ or $KRAS^{G12V}$ induces serrated lesions[78].

Only 3-5% of CRCs present a hereditary component with mutations associated with strong predisposing syndromes such as the familial adenomatous polyposis (FAP) or the hereditary nonpolyposis CRC (HNPCC, also called Lynch syndrome)[82]. The vast majority of CRCs are therefore sporadic with 20% displaying a family history which biological basis is unresolved.

By studying the hereditary forms of CRCs, two models of genetic alterations progressively leading from early neoplastic lesions to cancer were discovered and further confirmed in sporadic forms: the conventional adenoma-carcinoma sequence and the serrated pathway.

i. Adenoma-carcinoma sequence

The adenoma-carcinoma sequence is a well-defined model for tumorigenesis that arose from Vogelstein et al. in the 1990s and is based on the progressive accumulation of genetic modifications leading to the transformation of normal cells into tumor cells[83]. Those genetic modifications will mainly target two types of genes: oncogenes and tumor suppressor genes (TSGs). During carcinogenesis, the expression of oncogenes will be upregulated, whilst TSGs will be downregulated.

In the adenoma-carcinoma sequence, the first genetic alteration is carried by the APC gene with more than 95% of mutations leading to a frameshift or nonsense ones, mainly on both alleles, causing the protein to be truncated[84,85]. Since its inactivation is a starting point in many CRCs, APC is considered as a TSG. This gene is best described in the canonical WNT signaling as mentioned before, where it represents a binding partner for β-catenin, controlling its levels[86,87].

During CRC carcinogenesis, APC silencing leads to the accumulation of β-catenin, mimicking a constitutive WNT activation which allows them to be independent from the stem-cell niche. APC loss of function is followed by activation of the proto-oncogene KRAS. Ras proteins are a family of small-G proteins activated downstream of growth factor receptors, composed by three members (KRAS, HRAS and NRAS), commonly mutated in various cancer types[88]. In CRCs, KRAS somatic gain-of-function mutations are found in nearly 40% of patients, subsequently of APC alterations. The Ras proteins display many downstream effectors involved in cell proliferation such as the MAPK and PI3K pathways. KRAS mutations provides tumor cells with the ability to activate signaling pathways involved in cellular growth without the upstream activation of growth factors receptors.

This is followed by a loss of heterozygosity (LOH) on chromosome 18q and especially on SMAD2 and SMAD4. In normal colon epithelial cells, TGFβ has anti-proliferative and pro-apoptotic properties. Those alterations maintain the increased tumor cell growth induced by KRAS mutations[89]. This is maintained by further inactivation of the TSG p53. Indeed, subsequent LOH is found on chromosome 17p in around 70% of CRCs with more than 85% displaying a mutation on the p53 gene. This leads to an increase in cell proliferation by inactivation of cell cycle checkpoints and a decrease of apoptosis and autophagy[90].

ii. Serrated pathway

In the last 10 years, an alternative pathway leading to CRC was discovered after the observation of serrated polyps as early neoplastic lesions[91,92]. Between 15 and 30% of CRCs present those lesions and are associated with advanced diseases[93]. These tumors share an early activation of the MAPK pathway (BRAF or KRAS mutations), CIMP and MSI status[94].

The first TSP lesion (called TSA, for traditional serrated adenoma) can arise either from BRAF or KRAS mutation. Usually, TSAs associated with KRAS mutations evolve towards conventional adenomatous dysplasia and CRC, whereas BRAF mutations progress towards serrated adenocarcinoma (SAC). Both of them can lead to TSA high grade dysplasia through the hypermethylation and loss of expression of certain genes. TSA are predominantly localized in the distal colon or rectum[95].

The SSP starts with a BRAF mutation leading to the formation of a hyperplastic polyp (HP). Subsequently, the expression of two TSGs is modulated: p16 and IGFB7, involved in cell-cycle arrest[96,97]. First, they are overactivated following the MAPK pathway activation downstream of BRAF mutation. This leads to dormant HP lesions due to p16- and IGBF7-induced senescence. Then, the $CIMP^{high}$ background of those tumors induces the loss of expression of those two TSGs and the following evolution towards sessile serrated adenomas/polyp (SSA/P). Finally, the accumulation of genetic alterations on MLH1 associated with MSI, or MGTM with MSS, leads to the formation of SAC, preferably located in the proximal colon.

Altogether, these data demonstrate the heterogeneity of the serrated pathway which is still controversial among the scientific community. Much more needs to be done to truly elucidate this carcinoma developmental route. Moreover, since the presence of serrated adenoma lesions has been observed in many other cancers of the digestive tract, deciphering the SP mechanisms would benefit greatly to clinicians[95].

4. Tumor microenvironment

As mentioned before, TME has a major influence on tumor and is a useful tool for CRC classification. Indeed, in the last years it became clear that there is a crosstalk between cancer cells and diverse extrinsic components such as stromal cells or soluble factors, which can shape tumor development, heterogeneity and progression[98].

a. Cancer-associated fibroblasts

Cancer-associated fibroblasts (CAFs) are frequently recruited to tumor sites where they contribute to tumor growth and invasion in various ways. In the TME, different populations of CAFs can be observed whose origins are still unclear but mainly seems to come from the activation of normal fibroblasts by cancer cells.

They present dual skills by targeting cancer cells through their secretions which promote proliferation and invasion (such as TGFβ), and by remodeling their surrounding ECM, facilitating tumor cells' way throughout a complex environment[99,100].

b. Immune cells

The implication of the immune system in CRC carcinogenesis has been widely studied in the past 20 years with data showing that immunodeficient mice develop spontaneous tumors[101]and that tumors express neoantigens induce an anti-tumoral immune response[42] . The latter could lead to immunoediting, a process where tumor cells escape the immune surveillance by activating immunosuppressive pathways[102].

As mentioned before, immune cells are widely found in the TME of CMS1 tumors where many tumor-infiltrating lymphocytes[103] and cytotoxic T cells[104] are observed and may contribute to the better prognosis of this group. It is important to note that inflammation can also favor malignant transformation as it is the case concerning inflammatory bowel disease which has been described as an increased risk for CRC development[105]. In fact, it seems that CRC arising in this condition present a specific oncogenic route leading to a distinct type of CRC[106].

5. Metastatic routes

Metastases are the main cause of cancer-related deaths[107]. Around 20% of CRC patients are diagnosed with a stage IV disease with synchronal metastases, associated with a 13% five-year survival[108]. Mainly, CRC metastases are found at the liver, lungs and in the peritoneal cavity. Nevertheless, the underlying mechanisms driving CRC metastatic patterns are not well described. Numerous determinants can influence CRC invasive properties and metastatic sites.

a. Circulatory systems

The most common site for CRC metastases is the liver. Because of its important blood and lymph irrigation, cancer cells are thought to invade the liver through the portal system. The risk of developing such metastases increases with the tumor penetration depth into its surrounding tissue containing most vessels (submucosa, muscularis propria and pericolonic fat)[109].

The metastatic dissemination is a multistep process starting by the invasion into the surrounding matrix to reach blood and/or lymph vessels. Then starts the intravasation where cancer cells go through the endothelial wall to reach the systemic circulation. Tumour cell clusters are defined as emboles in the lymphatic vessels and called Circulating tumor cells in the blood stream (CTCs)[110]. Within the blood vessels, CTCs are protected from the shear stress or the immune system by platelets and neutrophils surrounding them and thus, forming a shield. CTCs will then exit the circulation by extravasation[111] but only a few will then survive and proliferate to form liver metastases.

b. Transcoelomic route

Another route of CRC dissemination is the transcoelomic spread where tumor cells detach from the primary tumor and invade through the entire digestive wall to reach the peritoneal cavity. The peritoneum is the largest serous membrane of the body, which facilitate the transport of fluids and cells across the abdominal cavity[112] . It is composed of two layers: the visceral one, covering all the abdominal organs, and the parietal one, lining the abdomen. Because of its non-adhesive surface, the peritoneum allows transcoelomic dissemination[113]. As mentioned above, CRC cancer cells will detach from the primary tumor and use the peritoneal transports to migrate through the abdominal cavity. Once they found a suitable secondary site, they will adhere, invade and proliferate to form metastases called peritoneal carcinomatosis (PC). Patients with PC have a poor prognosis and are generally in the disease terminal stage[114].

c. Iatrogenic dissemination

The concept of cancer cell dissemination during surgery through direct seeding during surgical procedure was first described in the late 1800s where metastases formed at a donor graft site, far from the primary site and which did not present any afferent drainage[115]. It is then possible that during the removal of a colorectal tumor, the resection causes a release of cancer cells in the abdominal cavity, contaminating it but also the surgeon's gloves and instruments. It is therefore sometimes recommended to change gloves and instruments before exploring the rest of the abdomen[116].

Even though the possibility of CRC cells disseminating through the iatrogenic route seems low, a clinical study with 22 patients operated for CRC showed the apparition of metachronous metastases displaying the same molecular signature as the primary tumor for five of them. Metastatic cells were sampled and shown to be able to adhere to the colonoscope and proliferate as organoids[117].

6. Perineural invasion

Perineural invasion (PNI) consist in the formation of metastases along the nerves. It represents a key CRC pathological feature since it occurs in around one third of patients[118] PNI is thought to be the route of least resistance for cancer cells since the sheath, the connective tissue covering the nerves is rather loose[119]. Disseminating cancer cells induce nerve damage leading to the secretion of neural regeneration factors which also promote cancer cell survival, proliferation and motility. PNI is associated with a reduced overall survival and disease-free survival since it renders complete tumor removal with safe margins rather challenging[120,121]. Moreover, since the precise mechanism of PNI remains unclear, there are no effective pharmacological strategies available yet.

Unfortunately, there is a lack of models recapitulating CRC's heterogeneity. Indeed, conventional cell culturing in 2D do not reflect tumor's metastatic abilities or response to treatments. In the next part of this manuscript, we will discuss the advantages and disadvantages of organoids and mouse models currently available to study CRC features.

---

7. Models

a. 3D models

In the late 1980s, the first 3D cultures of breast epithelia forming ducts in an ECM extract emerged and with it, the notion of organoids. They are defined by a 3D culture of various cell types coming from the same organ and recapitulating its expression profile and functions[122]. Nowadays, organoids are used in many fields (basic research, drug development, personalized medicine…) and specially in cancer research where tumor-derived organoids (tumoroids) represent the trending ex vivo model. The generation of CRC tumoroids is based on normal small intestinal ones or "mini-gut" where isolated intestinal stem cells are embedded in Matrigel (laminin- and collagen IV-rich matrix), a basement membrane substitute, and covered in a medium supplemented in niche factors to recapitulate the crypt microenvironment.

CRC tumoroids can be established experimentally after genome editing of normal tissue organoids using the CRISP-Cas9 technique to reproduce the two oncogenic pathways described before. Indeed, the introduction of mutations on *APC, TP53, SMAD4* and *KRAS*^{G12D} recapitulates the conventional adenoma-to-carcinoma sequence while mutations on *Braf*^{V600E}, *Cdkn2a*, *Tgfbr2*, *Znrf2* and *Rnf43* closely mimic the serrated pathway[123]. It is important to note that because of the heterogeneity of the genetic alterations involved in the serrated pathway, it is rather difficult to obtain a relevant experimental model.

Another way of developing CRC tumoroids is to directly cultivate tumor cells coming from biopsies. They are called Patient-derived organoids (PDOs). The PDOs have a robust predictive potential, conferring them the possibility to be used for personalized treatment[124].

Tumoroids are also a great model to study the TME by coculturing them with stromal or immune cells. For example, co-culturing mouse gastric organoids with mesenchymal cells induced various cell lineages[125]. Moreover, adding adipocytes into the culture of CRC tumoroids increases proliferation and aggressiveness of cancer cells[126].
In the past decade, an effort has been made in deciphering the role of the intestinal microbiota in health and disease. It was shown that various species of microorganisms have an influence on CRC carcinogenesis and certain bacteria are known to favorize cancer progression by dysregulating the immune system[127]. The exact mechanisms implied in this interaction are still unclear. To investigate this point, CRC tumoroids can be co-cultivated with microorganism (using microinjection into the tumoroids)[128].

Nevertheless, organoids present various limitations. First, human-derived organoids generated upon biopsies may vary from a laboratory to another based on the site of biospie and the different culture conditions (media composition, Matrigel batch, dissociation conditions). Second, except co-culturing methods, tumoroids culture do not recapitulate the complexity of cancer cells interaction with non-cancerous components[129]. Third, it has been shown that culturing pure tumoroids could be difficult and normal cells coming from adjacent healthy tissues might overgrow cancer cells[130]. Finally, the intratumoral heterogeneity might be lost after long-term expansion via the selection of certain clones favored by culture conditions.

Taking this into account, organoids and tumoroids represent a great tool for basic research as well as clinical investigations but more needs to be done to overcome their limitations.

b. Mouse models

Despite the usefulness of organoids to study CRC, animal models still represent the best preclinical tool to investigate cancer progression, metastases formation, interaction with other cell types and response to treatment.

The first mouse models appeared in 1915 with the development of carcinogen-induced models. They were obtained by injecting or feeding potential carcinogen components to mice and observe the apparition of tumors[131]. For example, Dextran sodium sulfate (DSS) was broadly used to induce colitis and thus, favorize the apparition of neoplastic lesions[132]. It is important to note that those models present an important amount of variability between strains and carcinogen exposure protocols and that they rarely induce CRC with invasive properties. Nowadays, they are used to study the influence of diet and the gut microbiome on CRC carcinogenesis.

i. Genetically engineered mice models (GEMMS)

In the 1990s, with the identification of the adenoma-carcinoma sequence by Vogelstein and Fearon[133] , the need for genetically engineered mice models (GEMM) to properly study CRC increased. The Cre-loxP tool was found very useful to develop tissue-specific conditional knock-out (KO) of TSGs or activation of oncogenes and to overcome the embryonic lethality of germline KO mice[134]. The genes involved in the adenoma-carcinoma sequence have different effects on CRC tumorigenesis in mice:

- *Apc*: *Apc* loss by itself is not sufficient to induce a malignant disease, in line with the fact that CRC development is the result of the sequential accumulation of multiple genetic alterations. However, *Apc* loss seems to be a key parameter in establishing CRC GEMM since and that restauration of *Apc* in *Apc* KO, *Kras* mutated and *TP53*-deficient mice leads to tumor regression[135]. Even though, *Apc* KO mice have limitations: the homozygous loss of *Apc* is lethal during embryonic development and Apc^{Min} mice only develop tumors in the small intestine.

- *TP53: In* patients, *TP53* is correlated with advanced cancer stages. In mice with a constitutively active Notch background, its combination with *Apc* loss increases invasiveness[136].
- *Smad4*: combined with *Apc*, *Smad4* loss accelerates tumor development and metastases formation[137].

Concerning the serrated pathway, the sole $BRAF^{V600E}$ mutation leads to the formation of hyperplastic crypts and to invasive carcinomas only when combined with mutations in *Apc* or *TP53*[138]. Some reasonable effort has been made to develop MSI mouse models but mutations on MMR genes led to hematopoietic diseases, except in *Apc* deficient mouse but this model does not represent the genetic alterations found in CRC patients[139].

While a tremendous amount of data about CRC carcinogenesis was obtain using GEMM, they do not represent what is found in patients because of the tumor location (mainly in the small intestine), the lack of genetic heterogeneity and the metastatic pattern. Moreover, they are expensive and time-consuming.

ii. Transplant models

Another way to study CRC development in vivo is to directly transplant cell lines, tumoroids or even patient tumor fragments into immunocompromised mice, either in the colon (orthotopic graft) or in another tissue (heterotopic graft). In patient-derived xenografts (PDXs), the subcutaneous engraftment of tumor fragments allows to develop large collection of tumors, allowing to mimic inter and intratumoral heterogeneity. Heterotopic models do not recapitulate CRC progression but can also be useful to assess a precise step of carcinogenesis. Such models include hematogenous dissemination after intravenous injection, specific metastatic colonization to the liver after splenic injection or peritoneal seeding after intraperitoneal injection[140].

Orthotopic models allow us to study tumor development in the adequate TME but it also involves complicated surgical procedures, except for the intrarectal injection. Two major drawbacks of transplant models rely on the use of immunocompromised mice, preventing interactions between cancer and immune cells and the murine stroma. In PDX, the patient stroma is replaced by the murine one, but it has been shown that the murine stroma architecture resembles the patients' and that murine stromal cells adopt a human-like phenotype[141]. The main limitation with PDXs is the low tumor take rate and the time required to establish a model.

Considering the tremendous amount of studies focusing on the interactions between the immune system and cancer cells for the development of immunotherapies, researchers are trying to implement the immune system of immunocompromised mice by injecting cells deriving from human bone marrow or hematopoietic stem cells[142].

In the recent years, two models combining organoids and mice models were developed to recapitulate the disease from the first polyps to metastases. First, O'Rourke and colleagues[143] used GEMMs harboring *KRAS*^{G12D} mutation and *TP53* conditional KO to form organoids in which they induced an *APC* loss-of-function using CRISPR/Cas9-mediated genome editing. After four to nine weeks post-implantation, more than half of the mice display stage I tumors, at 16 weeks two thirds of mice had a stage II disease with a tumor mass infiltrating into the adipose tissue and liver metastasis. They furthered demonstrated the WNT dependency of this model by restoring *APC* expression which led to tumor regression and cell differentiation. Thus, the orthotopic engraftment of *Apc*^{mut}*/Kras*^{G12D}*/p53*^{mut} organoids in syngeneic mice recapitulates the adenoma-carcinoma-metastasis program.

In the same issue, Roper and colleagues[144] published another model that relies on direct editing of mouse colon epithelial cells. To do so, they injected viruses that specifically infect epithelial cells using a Cre recombinase driven by a *Villin* promoter[79,145]and CRISPR/Cas9 to knock down *APC*. The infected cells were mainly locating at the crypt base, suggesting that stem cells were targeted. By sequencing the adenomatous lesions developed upon this technique, distinct *APC* inactivating mutations were observed suggesting that these tumors developed from two different cells. Thus, this model could be of great use to study cells-of-origin and subsequent alterations that would spontaneously appear during tumorigenesis.

As mentioned above, cancer cells' invasive abilities determine patients' prognosis. It relies on phenotypical changes allowing cells to detach themselves from the primary tumor, migrate towards distant sites and to colonize them. Considering the clinical challenge that metastatic cancers represent, they have been extensively studied in experimental models but the complexity of this process still prevents us from truly understanding the ins and outs of it. In the next part of this manuscript, I will start by introducing single cell migration and then, talk about how they can move as collectives.

II. **Invasion**

Single cells have been shown to migrate using two modes: a mesenchymal one, usually activated in epithelial-derived tumors by a transcriptional program called epithelial-to-mesenchymal transition (EMT) and an amoeboid one, hijacked from immune cells.

C. Single cell migration

1. EMT, a vast transcriptional program

a. In physiology

EMT has been described to play a crucial role in many cellular processes (such as stemness and cell-fate reprogramming) and controls the morphogenic events required for epithelial cells to migrate towards distant sites[146]. This is observed during embryogenesis where neural crests cells detach themselves from the dorsal neural epithelium and migrate as single mesenchymal cells before giving rise to mature structures such as the peripheral nervous system[146]. EMT relies on the expression of specific transcription factors (FTs) or drivers which will downregulate epithelial genes and upregulate mesenchymal ones.

In the next paragraph, I will briefly introduce epithelium organization and the proteins involved since they are the main EMT-targets. Their proper function will be discussed in a dedicated part (III. Epithelial cells: a polarized entity).

Epithelia are functional interfaces between the organs and their environment. They are composed of cohesive epithelial cells, adhering and communicating with each other through specialized intercellular junctions and displaying an apicobasolateral polarity (A/B polarity):

- The apical surface provides a luminal interface where exchanges between the digestive bowl and the cell can happen.
- The basolateral surface in contact with adjacent cells, ensures the barrier function through specialized junctions and relying on a layer of extracellular matrix called the basement membrane.

Those compartments differ in composition and organization, giving them specialized functions[147,148,149].

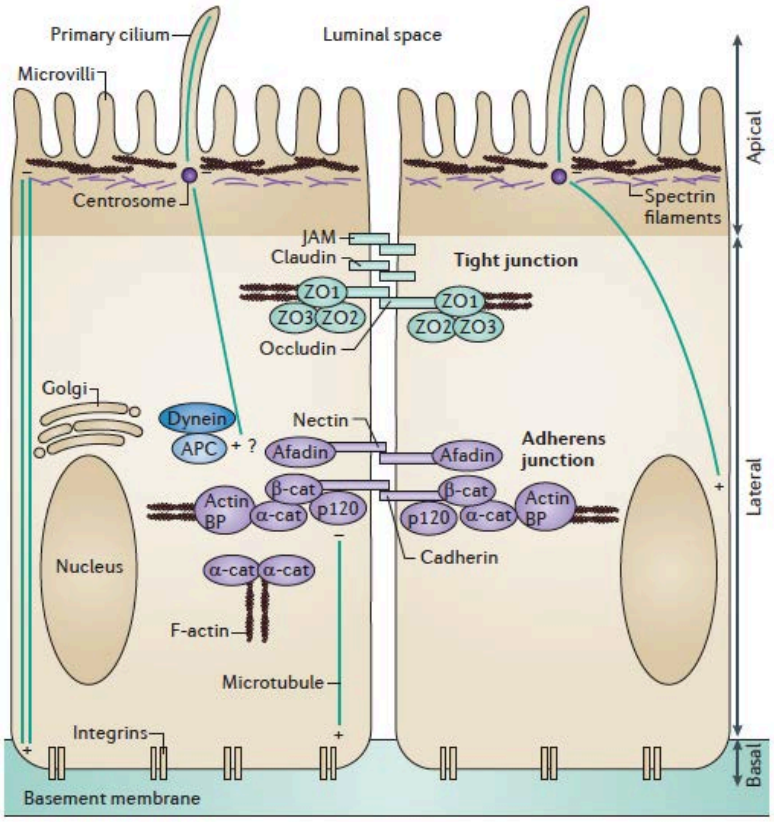

Figure16: Epithelial cell junctions and A/B polarity, Martin-Belmonte et al., 2012.

Neighboring cells display different types of junctions *(see Figure16)*: tight junctions (TJs), adherent junctions (AJs), desmosomes and gap junctions. TJs are located at the frontier between the apical and the basolateral pole and composed of occludin, claudin and junctional adhesion molecule (JAM). They possess a “fence” function, preventing specific membrane components from going from a pole to another, and a “gate” function, selectively allowing the diffusion of certain molecules. AJs composed of E-cadherin and nectin, provide strong intercellular connections. Proteins involve in cell-cell junctions such as E-cadherin are critical EMT-targets since their disruption lead the cells to detach from their neighbors, loose their differentiated features and potentially migrate.

Transcriptional program

Changes in gene expression patterns is under the control of microRNAs (miRNAs, inducing mRNA degradation), alternative splicing and FTs which activation is observed in early EMT and is described to be cell-type or tissue-dependent. Three master regulators have been extensively studied: SNAIL1, basic helix-loop-helix (bHLH, such as TWIST) and ZEB transcription factors *(see Figure17)*.

Their expression is induced by many signaling pathways such as WNT, Notch or growth factors, especially transforming growth factor-β (TGFβ)[150]. The fact that different signaling pathways are able to activate the same transcription factors shows that there is a cooperation between them, needed for both inducing and maintaining the EMT program in cells. For example, TGFβ signaling disrupt adherens junction which enables β-catenin to relocalize to the nucleus and be used by the WNT pathway[151].

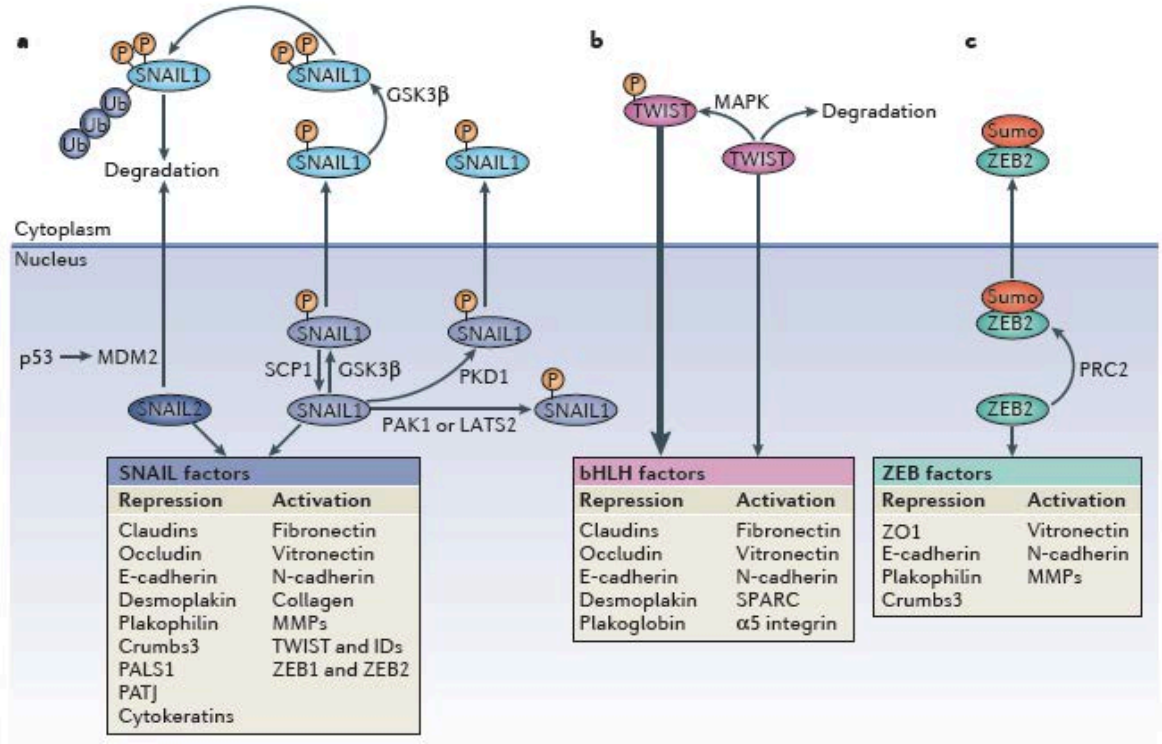

Figure17: Overview of EMT main drivers and their effectors, Lamouille et al. 2014.

Dissolution of cell-cell junctions and ECM remodeling

EMT relies on the downregulation of epithelial genes (such as *CDH1* coding for E-cadherin) combined with the upregulation of mesenchymal ones (such as *N-cadherin* to facilitate cells' detachment or fibronectin to promote migration). It can be accompanied by the cytoplasmic cleavage and thus degradation of E-cadherin, and the downregulation of junctional proteins expression (such as claudin and occludin, or diffusion of ZO-1[152]). Loss of cell-cell junctions induces the loss of A/B polarity since polarity proteins such as SCRIB are localized thanks to E-cadherin. Cells also remodel the ECM and change their interaction with it to enhance their motility. Mainly, EMT will induce an overexpression MMPs to degrade the ECM[153], and of integrins to facilitate the traction-based movement generated at the front via protrusions[154].

Reorganization of the cytoskeleton

To increase motility, cells need to reorganize their cortical actin to adopt a front-rear polarity *(see Figure18)*. New actin-rich membrane extensions are formed (lamellipodia, filopodia and invadopodia, the latter exerting an ECM degradation function[155,156]) along with actin stress fibers at the front, and a contractile rear at the back. The conversion from A/B to front-rear polarity and its maintenance is under the control of RhoGTPases and polarity proteins crosstalk. Those proteins are usually localized thanks to cell-cell junctions and maintained via mutual exclusions. This process will be further discussed in a dedicated part. The dissolution of cell-cell junctions allows RhoGTPases and polarity proteins relocalization. Indeed, PAR and Scribble complexes with PATJ relocalize to the leading edge where RAC1 and CDC42 promote actin-rich membrane protrusions[157] and integrin clustering, while RHOA is enhancing contractility through ROCK at the back[158], as described in the figure below.

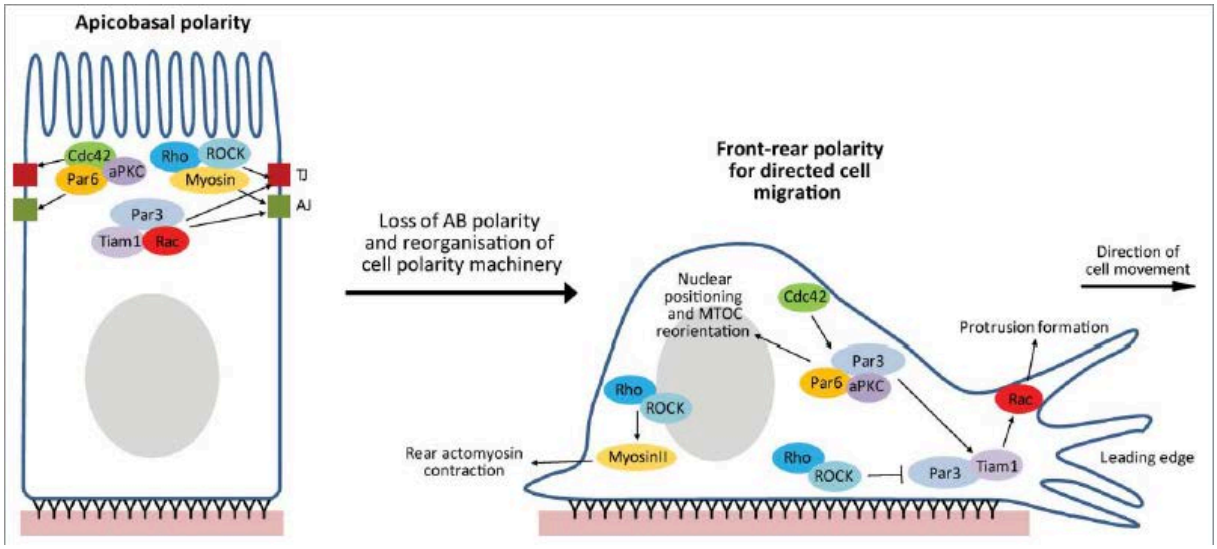

Figure18: Mack et al. 2014, Localization and interactions between RhoGTPases and polarity proteins in A/B and front-rear polarity.

To ensure epithelial integrity, cells can also regain their normal properties through the inverse process called mesenchymal-to-epithelial transition (MET), highlighting their plasticity. This process antagonizes the expression of EMT drivers through microRNAs (miRNAs) which binds mRNA and induce their degradation, allowing the re-expression of epithelial genes. It is to note that the expression of miRNAs is blocked by EMT transcription factors, highlighting the mutual antagonism governing this plasticity.

We previously demonstrated that TGFβ signaling, and especially its downregulation, is involved in the biogenesis of a tumoral intermediate correlated with a poor prognosis in MUC CRC patients. Since my PhD work aims at deciphering the effects of this downregulation on this tumoral intermediate, the next part will focus on TGFβ signaling among other EMT inducers.

---

b. TGFβ signaling

The human TGFβ family is composed of over 30 members with two ligand subfamilies (the TGFβ-activin-Nodal and the BMP subfamilies). They signal through the assembly of a hetero-tetrameric receptor complex composed of two type I (e.g. TGFBR1), considered as signal propagators and two type II receptors (e.g. BMPR2), known as activators. A ligand binding on its receptor induces the dimerization of type I and II receptors with the type II phosphorylating the type I receptor, which will then propagate the signal through an intracellular Ser/Thr kinase activity[159]. TGFβ signaling can be divided into canonical and non-canonical pathways depending on the cytoplasmic intermediates activated upon ligand binding.

Canonical signaling

SMAD signaling is considered as the canonical TGFβ pathway. SMADs are intracellular proteins which are phosphorylated by TGFBR1 upon ligand binding (BMPs activate SMAD1/5/8, TGFβ and activins activate SMAD2/3). We will refer to these SMADs as R-SMADs (receptor-phosphorylated SMADs). After phosphorylation, a R-SMAD dimer forms a hetero-trimer with SMAD4, translocate to the nucleus and bind to the DNA along with transcription factors, thus enabling TGFβ effects on gene expression[160]. Their turnover is under the control of GSK3 which phosphorylation will lead R-SMADs to be recognized by SMURF1 (SMAD-specific E3 ubiquitin protein ligase 1) and then addressed to the proteasome for degradation and recycling. WNT has been found to stabilize SMAD1, highlighting the cooperation between BMP and WNT pathway[161] as required during embryonic development. In fact, WNT act as an environmental factor needed for TGFβ-induced EMT, otherwise TGFβ would have a quiescent effect on epithelial cells[146].

Another way to end R-SMADs activity is via a negative feedback provided by SMAD-induced expression of SMAD7 which recruits SMURF at TGFβ and BMPs receptors[162,163]. The canonical pathway is the one responsible for TGFβ transcriptional effects involved in EMT. For example, in epithelial cells, TGFβ-activated SMAD proteins induce the expression of SNAIL with whom they cooperate to repress CDH1, the gene encoding for E-cadherin[164].

Non-canonical signaling

Different signals emanate directly from TGFBR2 which phosphorylates PARD6 leading to the recruitment of SMURF1 to target RHOA for degradation. cell-cell junctions are destabilized favoring the migratory phenotype[165,166]. TGFBR2 and BMPR2 can also directly phosphorylate LIMK1, an inhibitor of cofilin, an actin-depolymerization factor, thereby stabilizing actin filaments[167].

The TGFβ pathway has been studied for over 40 years but a lot remains to be decipher. The challenge relies on the fact that its effects on transcription can vary depending on the cell type and the cellular context. For example, TGFβ downregulates the expression of ID1 (Inhibitor of differentiation 1) in mammary epithelial cells, but upregulates it in metastatic breast cancer cells[168,169]. Three types of contextual determinants fashion the cellular response to this cytokine: the signaling transduction machinery (abundance and activity of ligands, receptors, intracellular signaling partners and regulators), its transcription partners (transcription factors, methylation agents or DNA-binding cofactors) and the epigenetic status of the cell (methylation marks or histone modifications)[170].

TGFβ signaling is involved in many processes such as cell proliferation, differentiation and tissue homeostasis to name a few. Its implication in EMT is undeniable and relies on both the canonical pathway via TGFBR1-SMAD proteins which induces the expression of mesenchymal genes while repressing epithelial ones and upregulates SNAIL and TWIST, and the non-canonical pathway resulting in TGFBR2-PAR6-induced RHOA degradation at TJs, with WNT providing the required transcriptional environment.

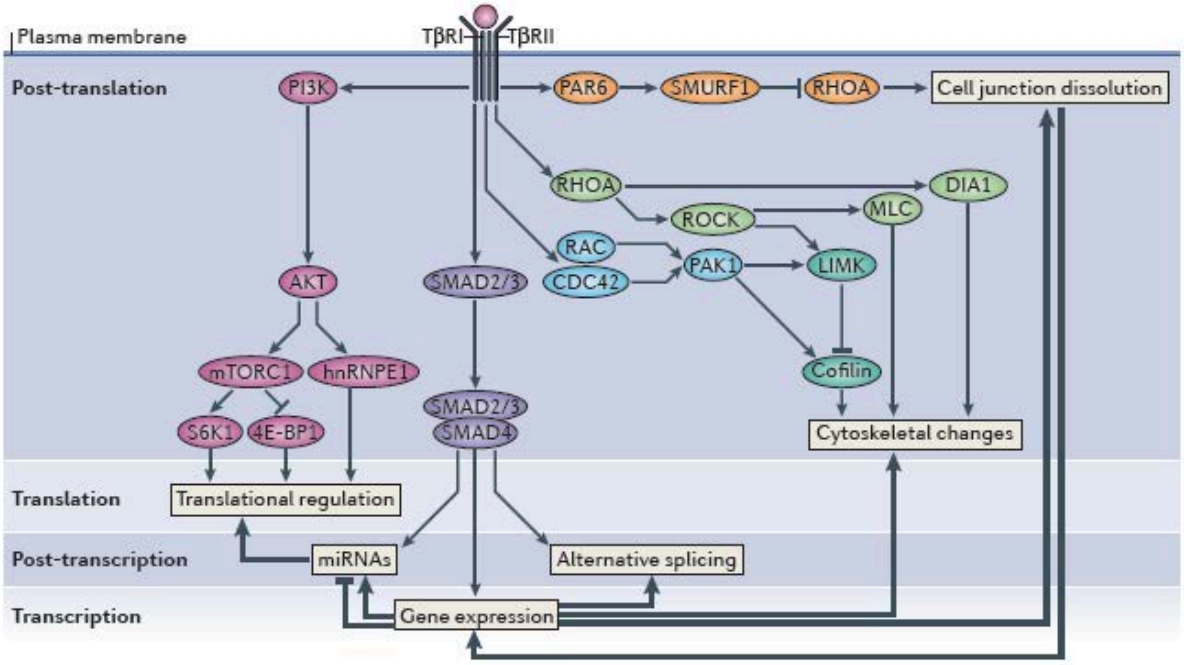

Figure19: TGFβ-induced EMT transcriptionnal effects, Lamouille et al., 2014.

c. EMT in cancer

The participation of EMT in cancer has been extensively studied as a normal cells' program highjacked by cancer cells where they gain stem cells properties by dedifferentiation and thus, resistance to apoptosis and invasive properties. The expression of EMT TFs has indeed been correlated with undifferentiated highly metastatic and therapy-resistant high-grade tumors[171].

Nevertheless, in the past decade EMT has been described has a transitional state (called "metastable", *(see Figure20)* since it seems not to be required for every step of the metastatic cascade. This has been shown in a study where they followed tumor cells expressing GFP-vimentin in a breast cancer mouse model, displaying an enrichment of GFP-positive cells in circulating tumor cells (CTCs) but not in metastases[76]. The fact that in breast cancer, EMT-like cancer cells represent less than 15% of the tumor bulk also highlight the fact that EMT is a limited focal event depending on tumor cells microenvironment[172]. Furthermore, EMT can be dispensable for the metastatic process.

It is the case in a mouse model of pancreatic ductal adenocarcinoma where the loss of SNAIL or TWIST does not impact metastasis formation[77]. Altogether, those data suggest that EMT is a very dynamic process where cells will more likely adopt partial EMT-phenotype depending on what suits best their survival in the environmental conditions they are in.

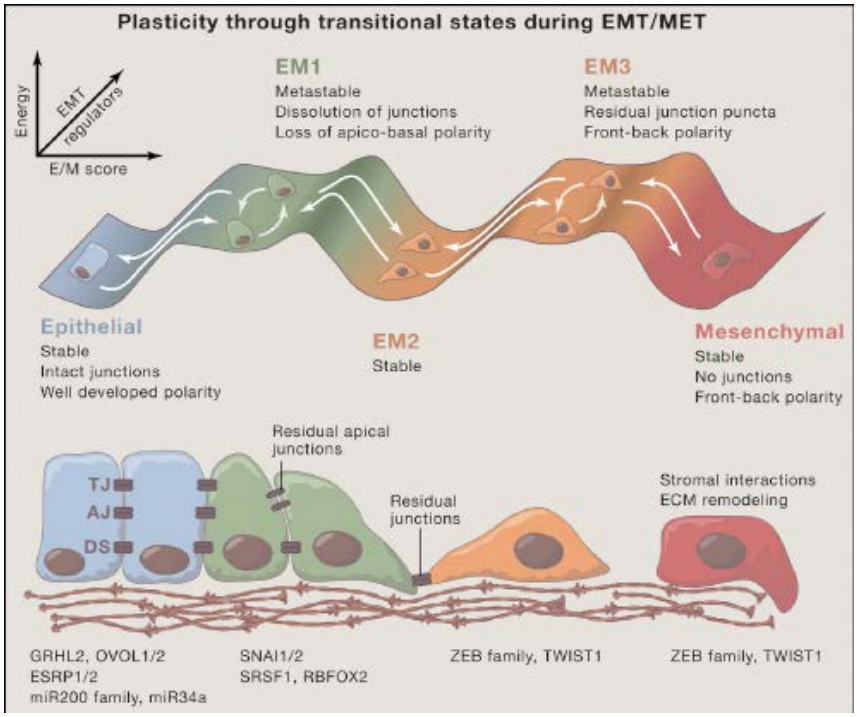

Figure20: Plasticity during EMT and MET, Nieto et al., 2016.

EMT also participates in many other cancer-related events favoring tumor progression:

- Cell survival: TGFβ-induced EMT effects on cells are contextual and it has been shown that in cells displaying an activated RAS pathway, it confers resistance to apoptosis via the expression of SNAIL[173] and oncogene-induced senescence via the expression of TWIST and ZEB1[174,175].
- Chemoresistance: as described before, cancer cells displaying a mesenchymal phenotype seems more resistant to chemotherapy. It has been demonstrated that upregulating the expression of miR-200c restores cancer cells sensitivity to chemotherapeutic agents[176]. Nevertheless, because of the lack of specific assessment of EMT in patients' tumor due to the adaptivity of this process, clinical targeting of EMT has not been successful so far[177].

- Immunosuppression: SNAIL1-expressing tumors are capable of immunoediting through the activation of immunosuppressive cytokines or regulatory T cells for example[178].
- Inflammation: the presence of a pro-inflammatory microenvironment is correlated with tumor progression. EMT is known to promote inflammation and can act on both cancer cells and stromal cells[179].
- Stemness: compared to colorectal cancer cells mainly displaying an epithelial phenotype, only EMT-like tumor cells are able to generate 3D organoids[180]. As described before, embryogenesis, ISCs and mesenchymal stem cells share many transcriptional factors and patterns of expression.

2. Single cell migration modes

Once cancer cells have detached from each other through the activation of EMT or other signals, they can migrate as individuals into the stroma. Single cell migration occurs through two different modes: either a traction-based (or mesenchymal) one where cells display protrusions at the front to grab ECM components, and a contractile cortex at the back to release adhesions and allow the cell body to move forward; opposed to a propulsive one (or amoeboid) which is adhesion-independent and relies on contractile forces. In the next part, I will describe the main changes cells have to undergo to power motility regardless of the migration mode, followed by a description of the mesenchymal and then the ameboid movement.

a. Migration determinants

Cell migration relies on different determinants:

- The cytoskeletal organization: this comprises cytoskeletal dynamics with actin filaments, intermediate filaments and microtubules. The actin cortex is composed of branched actin filaments aligned parallelly to the plasma membrane which assemble and disassemble locally, providing different types of cell protrusions[181]. This is under the control of RhoGTPases, cross-linking proteins (e.g. fascin, filamin and spectrins), actin-membrane-binding proteins (e.g. ERMs) and proteins allowing membrane curvature (e.g. amphiphysin)[182].

- Cell-ECM interactions: cells usually start to migrate after integrating an environmental cue. It can be molecules bind to fibers (the main membrane proteins regulating cell adhesion to the surrounding ECM are integrins[183]) or diffusing within the stroma produced by other cells at distance, migrating cells leading the way (paracrine signals) or the migrating cells itself (autocrine signals). Moreover, migrating cells evolve throughout ECM by degrading its components, mostly via the secretion of MMPs.
- Cell deformability: 3D confined environments display a complex meshwork of fibers which topology and viscoelasticity define movement direction but also require cells to adapt their shape. Most cellular components are highly deformable except the nucleus which is the largest and stiffest organelle[184].

b. Mesenchymal

Mesenchymal cells (such as fibroblasts or cancer cells) display protrusions at the front (thanks to CDC42 and RAC1 high activity) with long-lived cortical actin networks integrating stress fibers and focal adhesions (FAs), thus allowing a strong connection between the ECM and the cellular contractile apparatus *(see Figure21)*. FAs formation relies on integrins covalently binding to ECM components (e.g. collagen, fibronectin) to form adhesion complexes at the leading edge of moving cells which can mature with the recruitment of cytoplasmic adaptors (talin then kindlin and paxillin) and mechanical modulators (vinculin and p130Cas)[185]. Further engagement of NMII leads to the formation of focal adhesions (FAs) through integrin $\beta 1$ binding to collagen fibers within the ECM, which provide a stable anchorage and transmit force to the whole cell body. FAs turn over defines mesenchymal cells' velocity[186]. Those structures transmit force locally so cells can pull themselves forward. This is coupled with the secretion of matrix-degrading proteases at the front to decrease ECM confinement. Adhering cells need to disassemble ECM-binding adhesions at the contractile back (thanks to RHOA activation) to be pulled at the front[187].

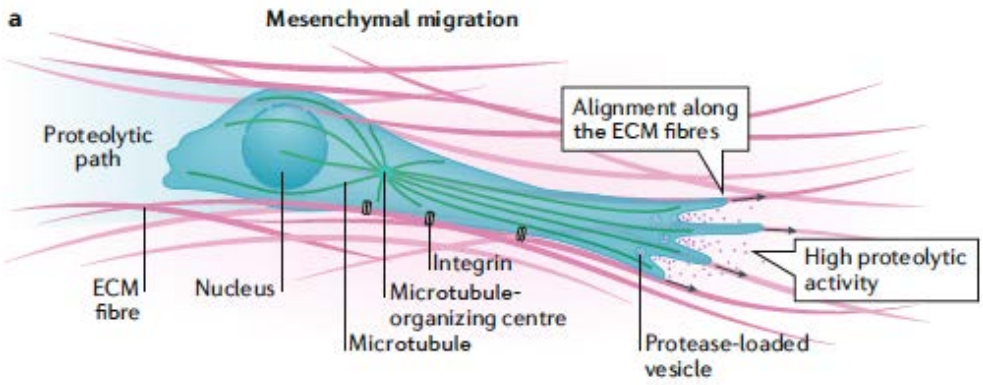

Figure21: Scheme representing mesenchymal migration, Yamada & Sixt 2019.

c. Ameboid

In homeostasis, amoeboid migration is used by immune cells to rapidly migrate towards an infection site. Amoeboid cells use a propulsive mode based on a retrograde actin flow and frictions forces in confined environment. It is important to note that the interactions between the cell membrane and the substrate are still poorly understood[188]. It is important to note that ameboid migration is only described in 3D since it relies mainly on confinement (to generate friction forces for example)[188].

Contrary to mesenchymal migration, amoeboid cells do not adhere to the ECM, either because (i) they do not express integrins or other proteins involved in FAs maturation, (ii) they migrate through a non-adhesive environment (e.g. vessels, in hypoxic conditions)[189] or (iii) they present a high cortical contractility downregulating the adhesive machinery *(see Figure22)*.

Amoeboid cells present short-lived actin foci with rapidly turned-over adhesion proteins providing weak forces[190]. Thus, amoeboid cells do not migrate using focalized actin stress fibers and traction. Instead, they use their contractile actomyosin cortical network to form low-adhesive membrane protrusions at the leading edge resulting from a local contractility weakening[187]. This is followed by the contraction of the rear, under the control of RHOA[191]. Thus, high actomyosin contractility provides the propelling forces required for movement generation but also favors a round shape which acts as an anti-adhesive factor[192].

Depending on the engagement of adhesion receptors, amoeboid cells can migrate using filopodia (like monocytes) which provides moderate force due to intermediate adhesions, or blebs (like primordial germ cells) which are non-adhesive but stiff structures allowing cells to use friction to their surrounding ECM to move[193]. Amoeboid cells display less ECM-degradation properties but are highly deformable.

Because they do not rely on the assembly/disassembly of multiproteic structures, amoeboid cells have a higher velocity than mesenchymal cells. Their migration speed will more depend on the ECM topology and its viscoelasticity to both provide confinement-induced frictions and deformability.

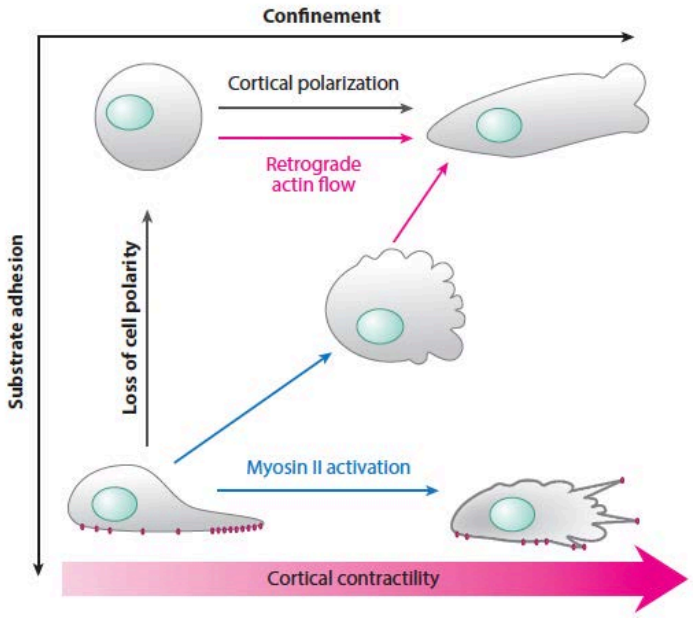

Figure22: Parameters favoring non-adhesive migration, Paluch et al. 2016.

Nevertheless, some ameboid cells display integrins like leukocytes which need to adhere to the endothelial wall during extravasation, but this engagement reflects an immobilization event rather than actual migration[188]. Indeed, studies in 3D and *in vivo* interfering with integrins demonstrated a reduced but not abolished migration of leukocytes and other amoeboid cells[194].

Thanks to Pan et al., we recently gained insight into the signaling pathways underlying amoeboid migration through the assessment of B-cell lymphomas dissemination. Indeed, amoeboid migration is also observed in blood cancers. They showed that amoeboid movement is triggered by STAT3 which induces RHOA activation and thus, a contractile phenotype[195].

D. Collective cell migration

1. Traction-based collective migration

In development, homeostasis and cancer, cells have demonstrated the ability to move collectively. This relies on the maintenance of cell-cell junctions during migration, allowing directionality for the group and the movement of cells that would be immobile otherwise. As in single cells, cell cohorts harbor a front-rear polarity axis and cytoskeletal rearrangements involving RhoGTPases. Collectives present leaders at the front displaying actin-rich protrusions applying traction forces on the surrounding ECM, and followers guided forward thanks to cell-cell junctions[196].

Cell-cell adhesion

Collective migration is enabled by the maintenance of cell-cell junctions, especially AJs. In mammal epithelial cells, E-cadherin establish a link between neighboring cells via homophilic interactions, and the actin cytoskeleton via catenins (p120-, α- or β-catenin)[197]. Destabilizing cadherins considerably alters collective movement[198]. Indeed, the association between cadherins and actin cables of neighboring cells allows the formation of a supracellular lateral actin organization. Throughout migration, cell-cell junctions are submitted to the cortical actin retrograde flow of the collective leading to their movement towards the rear until they are recycled back to the front and then re-engaged into AJs. Besides providing a physical link between cells, E-cadherin defines followers' polarity, preventing integrins from engaging with the ECM at cell-cell contacts[199,200]. Moreover, E-cadherin has been recently described as a survival factor in invasive ductal carcinomas by preventing oxygen-mediated apoptosis[201].

Leader/follower polarization

Leader cells are defined by their morphology, their position at the cohort's front and their interactions with the ECM. As in mesenchymal single cell migration, epithelial leaders interact with collagen-I through β1-integrins which leads to the formation of FAs and the recruitment of CDC42 and RAC1 at the front to promote actin polymerization and thus, protrusion formation. Cells become leaders through the expression of a transcriptional program such as in breast cancer[202] after or by sensing external cues such as growth factors (e.g. EGF) which receptors will activate integrins via an inside-out signaling. Recently, it has been shown that collectives can perform chemotaxis: leaders at the front displaying high RAC1 activity are attracted towards a gradient of a soluble cue, with the back of the cohort showing a collective contractile ring with activated RHOA[203].

Moreover, leader cells are responsible for the collective movement directionality through the secretion of proteases but also of ECM components, facilitating followers migration[204,205]. Leader cells tract follower cells displaying mechanosensing abilities. This is mediated by conformational changes of mechanotransducers upon stretching (such as talin in FAs or catenins in AJs) which will lead to the unmasking of other proteins modulating adhesions' strength. In collective cell migration, traction forces produced by leader cells will induce to the translocation of the protein Merlin, an ERM-like protein, thus promoting RAC1 activity and defining the front side of followers[206]. Moreover, tension increases junctional stability by unmasking cytoplasmic domains and allowing interactions between α-catenin with vinculin or actin for example[207].

Collective dissemination in cancer has been described a few times after strands or clusters of carcinoma cells presenting a partial EMT phenotype were observed at the tumor front and in metastases[208].

2. TSIPs

Recently, our team demonstrated that in MUC CRC patients, the main tumoral intermediate were tumor spheres displaying strong epithelial features and presenting an outward apical pole, in contact with their surrounding ECM *(see Figure 23)*. We called them TSIPs for Tumor spheres with inverted Polarity. They were first observed within peritoneal effusions of patients presenting peritoneal carcinomatosis (PC) and correlated with a poor prognosis.

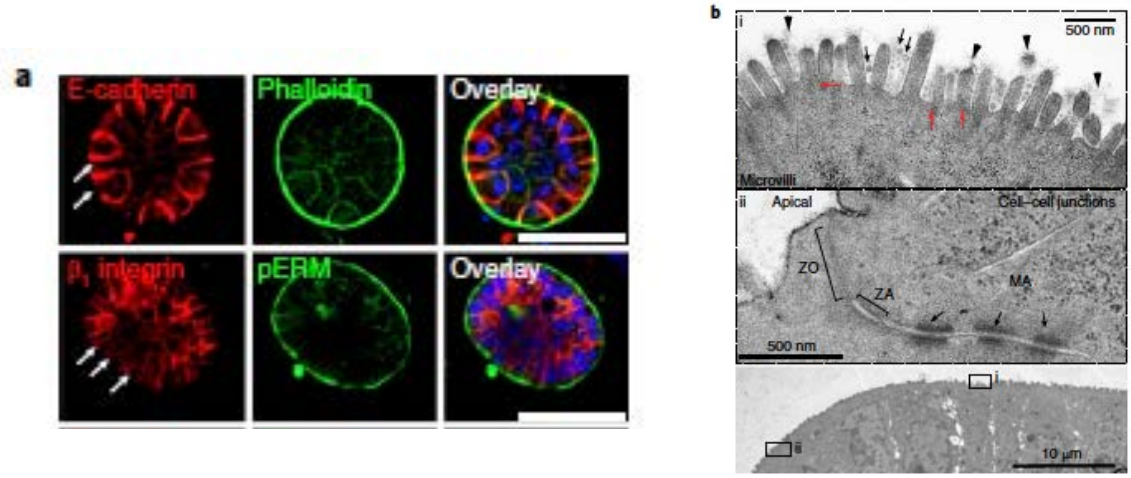

Figure23: TSIPs from peritoneal effusions (left panel: after embedding in collagen- gels, scale bar=50µm; right panel: electron microscopy showing the presence of microvilli at spheres surface), Zajac et al., 2018.

By comparing the expression profiles of TSIPs-producing (MUC) and non-producing (LBK) CRCs, we found that MUC CRCs were all associated with CIMP cancers and expressed the serrated gene signature. Serrated precursor lesions present apical invaginations into the lumen that can also be seen in MUC CRC patients' histological sections. Our data showed that TSIPs arise from apical budding into the lumen of serrated precursors evolving towards MUC CRC. During cancer progression, the luminal accumulation of TSIPs and mucus breaks the neoplastic epithelium, releasing TSIPs into the peritumoral stroma where they invade towards the peritoneal cavity. Moreover, using a GSEA, we were able to show that MUC CRC patients display a downregulation in the TGFβ pathway (canonical and non-canonical) and that this was sufficient to prevent TSIPs' formation in a mucinous CRC cell line. This correlates with the absence of EMT activation in these cancers.

Despite their unusual morphology and inverted A/B polarity, TSIPs possess a true metastatic ability. Indeed, using Patient-derived xenografts (PDXs), we were able to reform TSIPs that maintain patients' characteristics. By injecting them as TSIPs or after dissociation into single cells, we were able to demonstrate that TSIPs are much greater initiators of metastases' than their single cell counterparts. Their invasion capability occurs while keeping an outward apical pole and relies on a propulsive collective mode of invasion[209] *(see Figure24)*.

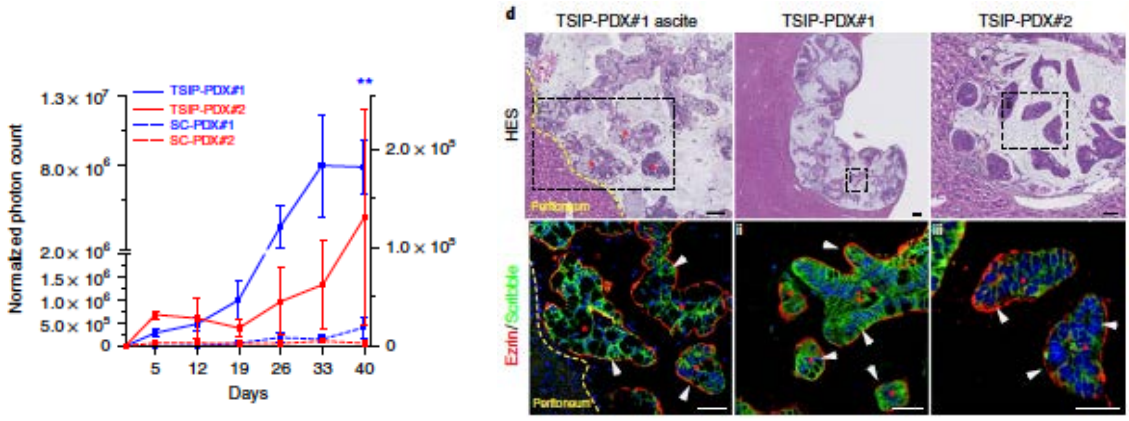

Figure24: TSIPs collective invasion relies on actomyosin contractility, Zajac et al., 2018.

Altogether, these data highlight the existence of a non-protrusive collective mode of invasion that is EMT-independent in serrated CRC subtypes, that we have named "collective amoeboid"[210].

3. Plasticity

Depending on intrinsic fitness or external cues, single cells can switch from a mesenchymal to an amoeboid phenotype and back. This is required *in vivo*, where cells can transition between tissues like leukocytes during immune surveillance, passing from the blood to interstitial tissue or like tumor cells during metastasis. Still, those processes are complex and difficult to study. *In vitro*, mesenchymal-to-amoeboid transition can be induced by putting mesenchymal cells in a non-adhesive environment[211], by increasing RHOA or decreasing RAC1 activity[212] or by increasing cell deformation via decreasing cells' proteolytic activity[213]. The reverse process can be observed by activating RAC1 or decreasing RHOA activity, increasing integrins-mediated adhesions or stimulate ECM degradation[214]. Migrating cells can also detach themselves from the collective to adopt a single-cell mode of invasion, mesenchymal or amoeboid.

This process can be induced by changes in ECM topology (e.g. confinement, complexity) or soluble factors. It leads to the downregulation of cell-cell junctions, especially E-cadherin, allowing them to detach themselves from the cohort[187].

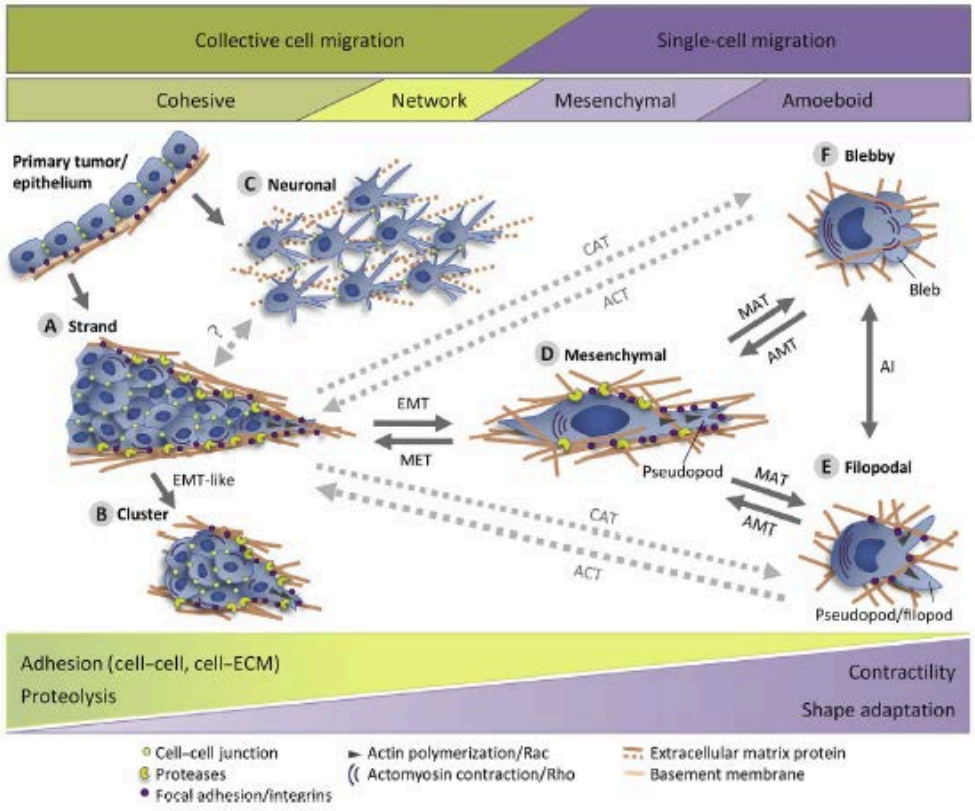

Figure25: Plasticity between invasion modes, te Boekhorst et al. 2016.

III. **Epithelial cells: a polarized entity**

A. At the tissue level: planar polarity

Throughout the evolution, epithelia are the most polarized tissue ever observed in metazoa. The intestinal epithelium is no exception and is highly polarized as well. To ensure its function, the intestine needs to be organized and its orientation coordinated within the plane of the epithelium, this is called Planar cell polarity (PCP). This allows epithelial cells to localize themselves among others and to establish specialized cell-cell junctions. It has been shown that the intestinal epithelium invaginations (called crypts) are under the control of PCP genes, in cooperation with small GTPases and some polarity proteins[215].

PCP was first studied in arthropods in the late 1970s[216] and especially in the fly, *Drosophila melanogaster*, whose eyes and wings are particularly polarized at the tissue level. This polarization in under the control of two sets of PCP factors: the Frizzled (Fz)/Flamingo (Fmi) core group and the Fat/Dachsous (Ds) system. They are asymmetrically distributed within the cell, giving it a proximal/distal polarity, due to intracellular feedbacks between them. At the tissue level, the coordination of this polarity relies on asymmetric intercellular contacts *(see Figure25)*. Despite a tremendous amount of work by the scientific community, the interactions between Fz/Fmi and Fat/Ds are still unclear, though it may seem, according to recent work that they are independent and work in parallel in *Drosophila*[217]*.*

Concerning the first cue leading to PCP proteins localization, a gradient of noncanonical Wnt signaling is thought to be implied since PCP involves Frizzled, a Wnt receptor, and is independent of its main intracellular component, β-catenin. Nevertheless, the absence of a planar polarity phenotype upon loss of WNT activity leaves the debate open. Concerning downstream effectors, PCP organization relies on directed targeting of intracellular vesicles for the delivery of polarity proteins and cytoskeletal reorganization, thus implying Rho-GTPases. Indeed, RHOA, RAC1, ROCK, CDC42 and myosin II have all been described as planar polarity effectors during gastrulation for example[215].

B. At the cell level: A/B polarity establishment

As mentioned before, epithelial cells display an apicobasolateral polarity, essential to their function. A/B polarity is defined by the asymmetric segregation of proteins and lipids to distinct membrane domains. The establishment of the apical and basolateral domain identities has been extensively studied during development. In the past two decades, tremendous progress has been made using 3D models of epithelial cells, mostly Madin-Darby canine kidney (MDCK) cells. Nevertheless, the sequence of events leading to a fully polarized epithelium is still unclear[218].

1. Cell-cell contacts: the first cue to polarization

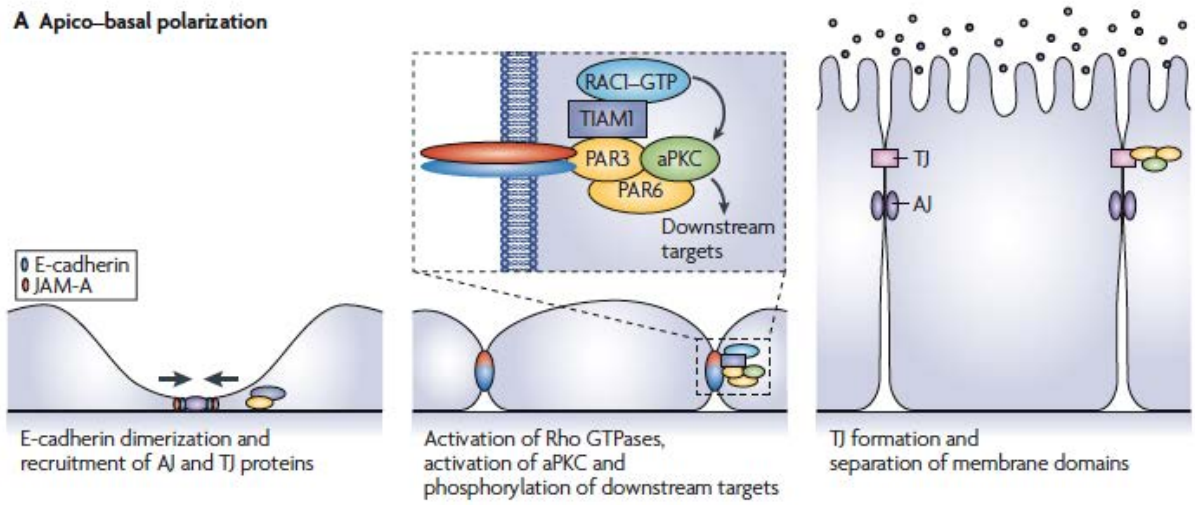

Figure26: Schematic representation of A/B polarization, Iden et al., 2008.

The study of cell lines revealed that the first cue for A/B polarization establishment is the dimerization of E-cadherin at cell-cell nascent adhesions (see Figure x). This leads to the recruitment of AJs and TJs proteins which will serve as a scaffold for the anchoring and localization of polarity proteins *(see Figure26)*.

Three complexes are involved in A/B polarity establishment:

- Phosphoinositides (PIs);
- Rho-GTPases;
- Polarity complexes:
    - PAR/aPKC, composed of Partition defective 3 and 6 (PAR3 and PAR6), and atypical protein kinase C (aPKC);
    - Crumbs, containing Crumbs (CRB), Protein associated with Lin Seven 1 (PALS1) and PAS1-associated tight junction protein (PATJ);
    - Scribble, consisting of Scrib, Disc Large (DLG) and Lethal giant larvae (LGL).

They interact through a mutual exclusion mechanism where the one prevents the expression of another one at this membrane compartment.

The identification of A/B polarity establishment components was mainly achieved on Drosophila and C. elegans. Most of the proteins have a homologue in vertebrates and the sequence of events is thought to be very similar between species.

My PhD works focused on the mechanisms required for A/B polarity orientation and maintenance. Therefore, I chose to give you an overview on the actors of A/B polarity establishment, and then focus more on the ones involved in orientation and maintenance.

---

2. Phosphoinositides and sphingolipids

Phosphoinositides (PIs) represent less than 15% of phospholipids in eukaryotes. Phosphatidylinositol (PtdIns), the precursor of PIs, is synthesized at the endoplasmic reticulum (ER) and delivered towards cellular membranes by vesicular transport or by cytosolic PtdIns transfer proteins. Its inositol ring phosphorylation leads to the formation of seven PIs species, with PtdIns(4)P and PtdIns(4,5)P_2 being the most represented. Each of them has a specific subcellular distribution with a preference for membranes subsets[219].

PIs are signaling and structural platforms thanks to the binding of cytosolic or membrane proteins to their head. As for their localization and levels, they are determined by their phosphorylated state, under the control of phosphoinositides kinases and phosphatases whose cellular localization is tightly regulated. Typically, phosphorylation of the inositol ring charges PtdIns negatively thus enabling electrostatic interactions, either with a cluster of basic residues (such as those found in actin regulatory proteins like profilin[220]) or folded structures (such as the pleckstrin homology domain, PHD[221] found in polarity proteins like Ezrin). Even though there is a large number of PI effectors, they all share a common motif known as the "PI code"[222]. There are 11-PI binding molecules known to specifically interact with PIs, thus establishing a spatiotemporal control of membrane-cytosol interactions, intracellular signaling and, as we focus here, membrane identity.

PIP3 at the basolateral membrane

PIs are key markers of A/B polarity with phosphatidylinositol 4,5-biphosphate (PIP_2) being segregated at the apical surface, and phosphatidylinositol 3,4,5-triphosphate (PIP_3) at the basal pole. The conversion from one-another is ensured by phosphatase and tensin homolog deleted on chromosome ten (PTEN) (for PIP_3 dephosphorylation into PIP_2) and phosphatidylinositol-3 kinase (PI3K) (for PIP_2 phosphorylation into PIP_3)[223]. Nevertheless, according to recent work, it is possible that PTEN is not the only PIP_2 spatial regulator. Indeed, phosphatidylinositol 5-kinase, known to promote PIP_2 production, is also found at the apical pole[224].

It has been shown that in unpolarized MDCK cells, both PIP_2 and PIP_3 are localized at cell-cell and cell-ECM contacts. Within the first stages of polarization, PIP_2 and PTEN become enriched at the apical membrane while PIP_3 stays at the basolateral pole. The role of PIs in cell A/B polarity establishment was confirmed by ectopic insertion of exogenous PIP_3 into the apical domain of well-polarized MDCK cysts. This was sufficient to relocalize basolateral components and PI3K as well as excluding apical proteins, totally inverting their polarity[225]. This result was recently reinforced by a study showing that decreasing PIP_2 levels by perturbing its cytosolic transportation is enough to impair A/B polarity in 3D MDCK cysts[226]. We do not know what localizes PTEN in MDCK cells, but it seems that it is the first molecular event leading to the formation of an apical membrane and lumen[227].

PIP2 define the apical membrane

Following apical membrane establishment, PIP_2 recruits and binds Annexin2 (Anx2) which is thought to be a mediator in the PIP_2-dependent actin cytoskeleton remodeling[227]. In turn, Anx2 binds the Rho-family small GTPase CDC42, a known actin modulator. Downregulation of CDC42 using RNA interference (RNAi) experiments disrupted the apical cytoskeleton and impaired lumen formation. Such defects have also been observed after downregulation of Axn2 and PTEN. Altogether, these results indicate the presence of a PTEN/PIP_2/Anx2/CDC42 axis linking PIP_2 and the actin cytoskeleton remodeling during A/B polarity establishment.

PIP_2 can also bind to the FERM domain of the ezrin/radixin/moesin (ERM) polarity proteins, known as adaptors between the plasma membrane and the actin cytoskeleton, and induce a conformational change releasing them from an autoinhibited state. PIP_2 and its synthesizing enzyme (PtdIns kinase type Iγ) can also bind the FERM domain of talin, increasing its affinity for integrins and helps generate PIP_2 at the apical membrane[228].

3. Rho-GTPases

By studying polarity establishment in *Drosophila melanogaster* and *Caenorhabditis elegans*, researchers found the first evidences for a crosstalk between polarity proteins and small GTPases[229]. Rho GTPases are enzymes of the family of small GTPases. They are hydrolases that act as major regulator of cytoskeletal organization *(see Figure 28)*. They control actin polymerization and contractility but also microtubule dynamics. Consequently, they regulate numerous cell processes such as migration, cell cycle progression, differentiation and as we focus here, A/B polarity[230]. Three Rho GTPases have been extensively investigated and they all have a key role in polarity establishment: CDC42, RHOA and Rac1. More precisely, CDC42 is involved in polarity proteins localization while RHOA and Rac1 transmit polarity orientation signals. They were first described in the early 1990s for their roles in several signaling pathways but share the same ability to link membrane receptors to the actin and microtubule cytoskeleton[231–233].

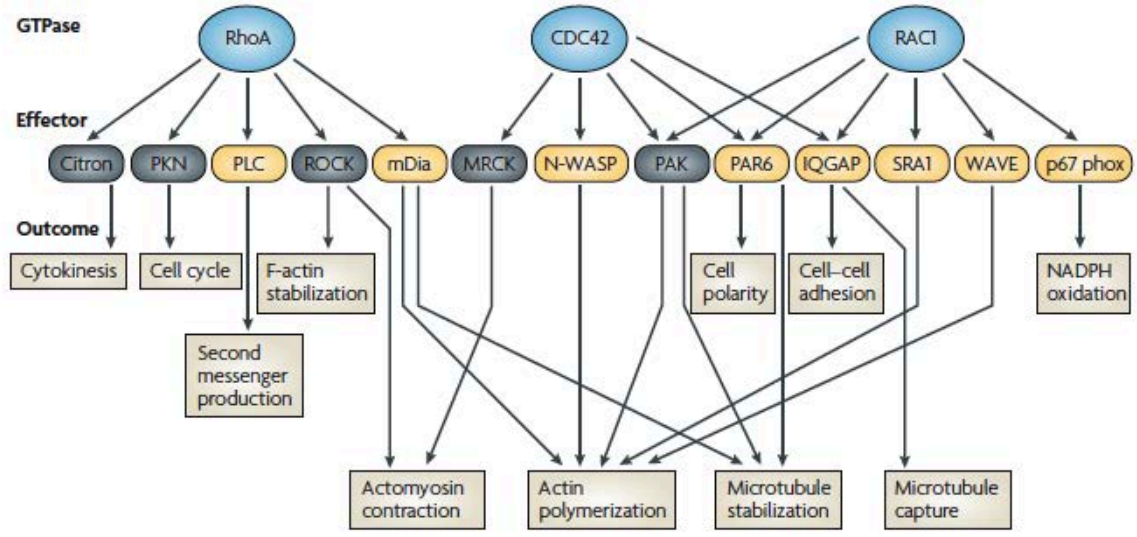

Figure28: RhoA, CDC42 and RAC1 and their effectors, Iden et al., 2008.

Rho GTPases are activated by numerous membrane receptors such as integrins, cadherins, Tyrosine kinases and G-coupled protein receptors[155]. Most RhoGTPases cycle between an active GTP-bound state and an inactive GDP-bound state. This is under the control of Guanine nucleotide exchange factors (GEFs) which catalyze the exchange between GDP and GTP for their activation, GTPase activating proteins (GAPs) which increase GTP hydrolysis and Guanine nucleotide dissociation inhibitors (GDIs) which sequestrate the GDP-bound form away from GEFs for their inactivation. Some "atypical" GTPases do not function as described here but are constitutively GTP-bound and their activity in under the control of post-translational modifications (PTMs)[234].

As seen in Figure 28, RhoGTPases are involved in cytoskeletal changes through actin polymerization and contractility:

- *Actin network regulation*

Two pools of cellular actin can be observed: a dynamic junctional one stabilizing cell-cell contacts, and a peripheral one composed of thin bundles required for epithelial cell shape[235]. It has been shown that actin polymerization and organization at cell-cell contacts involves two actin nucleators modulated by Rho GTPases which are the Arp2/3 complex, activated by Rac1 and CDC42 and needed for branched actin networks, and formin-1, under the control of RHOA and required for the polymerization of actin cables[236,237]. It also has been shown that there could be a Rac-GTP gradient under the control of A/B polarity, where apical polarity proteins (such as CDC42 and the PAR complex) bind the Rac-GEF T lymphocyte adhesion and metastasis-inducing protein 1 (TIAM1) and spatially control membrane protrusions[238]. By directly binding small GTPases, PIs spatially modulate their intracellular activity.

- *Contractility*

The other key component of cytoskeletal remodeling is non-muscle myosin II (NM-II), an actin-binding protein which is regulated by phosphorylation on its heavy and light chains[239]. A large number of kinases can modulate NM-II activity but one of major interest is the Rho-associated coiled coil kinase (ROCK) which presents two isoforms ROCKI and ROCKII. It has been shown that ROCKII can specifically bind PIP_3 through its PHD thus leading to a basolateral regulation of NM-II activity[240].

Despite the fact that ROCKI and II are highly homologous, studies in knockout mice showed that ROCKI could not compensate for ROCKII, implying that the two isoforms regulate distinct pools of NM-II[241]. Moreover, ROCK activity is linked to the enhancement of PTEN activity in Human embryonic kidney (HEK) cells[242], thus promoting apical identity.

CDC42

As mentioned earlier, CDC42 is involved in the apical domain identity establishment through the PTEN/PIP_2/Anx2/CDC42 axis. Indeed, after binding to Anx2, CDC42 in involved in the apical pole identity via binding and localizing apical proteins such as the PAR6/aPKC dimer through PAR6[243] and the Crumbs-Pals1-Patj complex in a Rab11a-dependent manner[244]. Moreover, CDC42 remodels the actin cytoskeleton via Arp2/3 to promotes nascent cell-cell adhesions: it promotes the formation of cytoplasmic protrusions in the form of filopodia in a N-WASP-dependent manner[245] and stabilize AJs by contributing to E-cadherin endocytosis and turnover through its effector IQGAP[246].

It seems that CDC42 activity is important in the early stages of cell-cell junctions' establishment and lumenogenesis. Indeed, the presence of CDC42-GAPs (such as SH3PB1 or ARHGAP17) at the apical pole during TJs maturation indicates a time and spatial inactivation of CDC42 which is required for the assembly of the sub-apical actin belt[247].

Rac1

Rac1 is known to be involved in two main processes during epithelial A/B polarity establishment: first, upon β1-integrins activation through ECM binding, Rac1 is involved in basement membrane assembly. This will be discussed in a dedicated section on A/B polarity orientation bellow. Second, Rac1 is involved in the establishment of early cell-cell adhesions[248]. Indeed, the first cell-cell contacts are initiated by actin-based E-cadherin-containing membrane protrusions which requires local Rac1 activation[249]. Expression of a constitutively active Rac1 mutant causes E-cadherin and actin filaments accumulation at cell-cell junctions[250] while expression of a dominant-negative form impedes cadherin-dependent cell-cell adhesions[251]. Those results highlight a key role for Rac1-dependent actin nucleation in nascent cell-cell junctions establishment, which have been shown to involve WAVE, a Rac1 direct effector responsible for its actin-polymerization effects[235].

Rac1 is recruited at cadherin-dependent nascent cell-cell junctions where it is locally activated by its GEFs Vav2[252] and Tiam1[253,254] which are previously recruited by E-cadherin to modulate Rac1 activity at those sites. In contrast to GEFs, GAPs at cell-cell junctions are less investigated but studies using a Rac1-FRET sensor showed that Rac1-GTP is present during a short period of time at primordial junctions, suggesting that Rac1 inactivators (GAPs or GDIs) are there to finely regulate its activity[255], as described above for CDC42.

Rac1 and RHOA antagonize each other with Rac1 decreasing RHOA activity through the activation of p190-RhoGAP at cell-cell junctions. This leads to the segregation of Rac1 at TJs and RHOA at the basal pole. This effect is also enhanced by E-cadherin-activation of Src at nascent cell-cell adhesions, which recruits p190-RhoGAP. However, RHOA-dependent actomyosin contractility is needed for the maturation of cell-cell junctions by promoting the formation of a contractile belt which is required for correct A/B polarization[256].
This highlights the spatiotemporally regulated balance between CDC42 and Rac1 at the apical pole and RHOA at the basolateral pole required during A/B polarity establishment[257].

RHOA

RHOA roles in A/B polarity are still controversial but it has been shown to be required for cell-cell adhesion. Indeed, RHOA is recruited at primordial cell-cell contacts by the Crumbs complex where it locally increases contractility through its effector ROCK to help cells in transforming nascent lamellipodia contacts into a local actomyosin belt as observed in mature AJs. RHOA also recruits Rac1 GAPs to prevent its activity at the apical domain[258,259]. This observation, in contradiction with previous ones about Rac1 enrichment at the apical pole, converge with a RHOA/Rac1 mutual exclusion during A/B polarity establishment, suggesting sequential participations and the presence of gradients of GTPases activities along the A/B axis[245].

RHOA is then inactivated at the apical pole via p190RhoGAP as described before but is thought to be later recruited at mature AJs to enhance E-cadherin endocytosis and turn over through Rac1-IQGAP inhibition[260,261]and to promote junctional contractility required for this process through its ROCK activation of NMII[262].

Overall, RhoGTPases and especially CDC42, Rac1 and RHOA are key determinants of A/B polarity establishment through their effects on the cytoskeleton coordinated by polarity complexes. They have opposite effects with RHOA enhancing cell contractility by regulating actin-myosin filaments assembly while Rac1 reorganize the cytoskeleton to form adhesive structures such as filopodia and lamellipodia. Their spatiotemporally regulation is not fully understood, probably due to the fact that there are at least 80 GEFs[263,264]and 50 GAPs[265] finely tuning their activity and only a few were deeply investigated for now.

4. Polarity complexes

a. Par3/Par6/aPKC

PAR proteins were the first identified in a cell polarization process in *C. elegans* asymmetric divisions in 1988. Using genetic screens to detect mutations impairing the asymmetry of those divisions, researchers were able to identify 6 genes: PAR1 and PAR4 were described as protein kinases, PAR3 and PAR6 display PDZ domains, PAR5 is a peptide-binding protein and PAR2 contains a zinc-binding domain and does not have any homologue in other species than in the worm. PAR1, PAR3, PAR5, PAR6 and aPKC interact to asymmetrically localize one another and define the concept of polarity protein complex[266]. In A/B polarity, the PAR6/PAR3/aPKC tripartite has been extensively studied and are strongly conserved between species, from worms to vertebrate.

There are three PAR6 proteins: PAR6A/C, PAR6B and PAR6D/G which can be found alone or together in different cell types. In epithelial cells, they are mainly found at TJs (PAR6A and G) and in the cytosol (PAR6A and B). PAR6 doesn't display any enzymatic activity, its role resides in binding and correctly localizing other proteins. Its downregulation impairs TJs[267,268]but its overexpression does not affect them[269]. PAR6 key role is to allow interaction between aPKC and its effectors such as PAR3 and LGL.

In mammals, two Par3 genes have been identified coding for PAR3A and B but only PAR3A can bind aPKC through its PDZ binding domain[270]. PAR3A localization is defined by its self-association with JAMs at nascent cell-cell junctions which can serve as a scaffold for the recruitment of proteins involved in TJs maturation such as PAR6 or aPKC[271,272]. Indeed, depletion or overexpression of PAR3 disrupts TJs and correct localization of PAR6 and aPKC[267,271,273].

aPKC displays two isoforms, aPKCλ/ι and aPKCζ which differ from conventional PKCs in displaying a N-terminal PB1 domain known to bind PAR6. In epithelial cells, aPKC is found at TJs, colocalizing with PAR proteins. Its kinase activity is essential for the correct localization of PAR3 and 6[274].

b. Crb/PALS1/PATJ

In 1990, Tepass and colleagues discovered a link between epithelial cell polarity and crumbs (crb) gene in *D. melanogaster*. *Crb* mutations disrupt the epithelial organization of the fly's epidermis[275]. Later on, two proteins were shown to interact with Crumbs: Stardust (PALS1 in mammals) and PATJ. Their downregulation results in the same defects observed after Crumbs perturbation, thus they emerged as a second polarity complex.

There are three CRB proteins (CRB1,2 and 3) which have different tissue localization, with CRB3 mainly found in epithelial cells. All of them display a FERM-binding domain on their cytoplasmic tails thus linking them to the cytoskeleton with CRB3 being found at TJs and at the apical pole[276,277].

PALS1 is a scaffold protein binding PATJ and found at the apical border. Its downregulation mislocalizes E-cadherin at the cell membrane and induces a loss of PATJ expression, showing that their mutual interaction is needed for their stability[278,279].

In mammals, two homologues of *Drosophila* Dpatj are found: PATJ and MUPP1. PATJ is known to interact with many TJs proteins such as ZO-3 and Claudin-1 at TJs. Indeed, downregulation or overexpression of PATJ prevents ZO-1, ZO-3 and Claudin-1 from correctly being localized at TJs highlights a PATJ function in stabilizing TJs[280–282]. Moreover, PATJ can bind PALS1 and CRB3, thus providing a link between lateral and apical domains components. MUPP1 displays a high level of homology with PATJ but its function is less described. It may serve a scaffold for TJs proteins in early cell-cell contacts such as Claudins and JAMs.

c. Scrib/Lgl/Dlg

The *SCRIB* (Scribble planar cell polarity protein) gene was identified as a polarity regulator in *Drosophila* where it is found at the basolateral membrane. Mutations in this gene prevents the correct localization of apical proteins without perturbing the basolateral domain, indicating a role for Scribble in excluding apical proteins from the basolateral (BL) domain[283]. It was then shown that it interacts with two other proteins: LGL and DLG, first identified as tumor suppressors. They were then found to overlap with Scribble without physical interactions being described between them[283,284].

There are five mammalian DLG (Disc large) proteins with DLG1 being the most studied one, especially in epithelial cells. DLG1 has been shown to bind with APC which is associated with β-catenin, and PI3K thus addressing it to the BL domain[285,286].

LGL1 and LGL2 are the two described LGL (Lethal giant larvae) proteins which are highly homologous and intensively studied in epithelial cells, they will be cited as LGL1/2 from now. They have been described to be bound to PAR6/aPKC in the early phases of A/B polarity establishment where aPKC will then phosphorylate LGL to detach it from the apical dimer thus excluding it from this pole[287,288].

d. Interactions and roles in A/B pol. Establishment

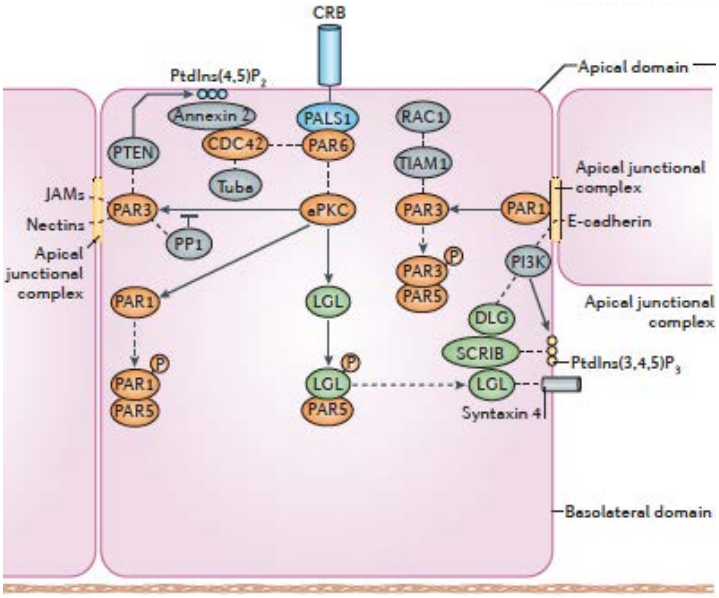

Figure29: A/B polarity establishment, cooperation between cell-cell adhesions, polarity complexes and RhoGTPases. Rodriguez-Boulan et al., 2014.

Following its activation, CDC42 recruits and binds aPKC, triggering its activation thus exerting its kinase activity on LGL. This leads to its dissociation from the PAR6/aPKC dimer, addressing it to the BL compartment where it can interact with DLG and Scribble[289]. Then, aPKC can phosphorylates PAR3 to form the activated apical PAR complex. Phosphorylated PAR3 accumulates at TJs and dissociate itself form PAR6/aPKC[290]. PAR1 is found at AJs where it phosphorylates PAR3, excluding it from the BL membrane and preventing its binding to aPKC. Moreover, PAR1 can be phosphorylated by aPKC to prevent its apical localization. Phosphorylated PAR1, PAR6 and LGL bind to PAR5 at the basal pole which stabilizes their presence at this site[291].

CRB3 can bind PAR6 directly or via PALS1 to promote TJs maturation. Indeed, cooperation between Crumbs and Par complexes is emphasized by the fact that the correct localization of ζaPKC at TJs is impaired by downregulation of PALS1[278]. Interestingly, in those cells, PAR3A was not mislocalized suggesting that it is not apically recruited by PAR6 but is more likely to be present at this pole through anchoring to JAM proteins[292].

The establishment of A/B polarity in epithelial cells requires a spatiotemporal regulation of polarity complexes. Their distinct localizations participate in the apical domain identity (for Par and Crumbs complexes) and basolateral domain identity (for Scribble) and gives functional insights into their mutual exclusion. Moreover, it seems that the Par complex, through its enzymatic activity via aPKC, has a dynamic role in membrane identity, while Scribble and Crumbs maintain it by mutually antagonizing each other.

For a long time, biological processes have been studied using 2D techniques, growing cells as monolayers, mainly on plastic and therefore, were really far from the epithelial organization found in vivo. The development of three-dimensional (3D) systems allows scientists to investigate the processes involved in epithelial morphogenesis in a more relevant manner. Today, the 3D Madin-Darby canine kidney (MDCK) seems to be one of the best models to investigate cell polarity[293–296]*. Indeed, once put in a gel of extracellular matrix (ECM), they are able to form a cyst, a spherical monolayer displaying a central lumen*[296]*. The results mentioned in the following paragraphs were obtained on 3D MDCK (unless otherwise mentioned).*

C. A/B polarity orientation and maintenance

1. Cyst morphogenesis

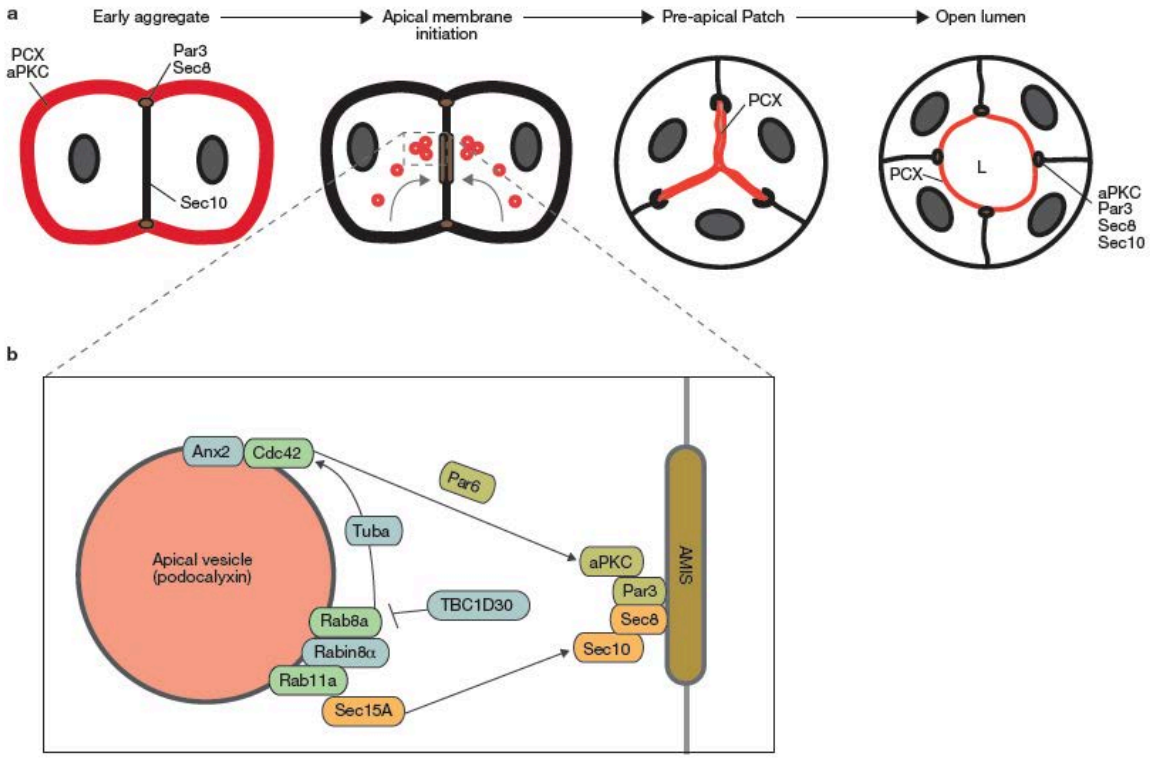

Figure30: Schematic representation of the molecular network for de novo lumen formation, Bryant et al., 2010.

The sequence of events leading to the establishment of a MDCK polarized cyst has been elucidated in 2010. At the two-cells level (or early aggregate), the apical protein podocalyxin (PCX) is found at the cell surface, in contact with the ECM. Following the polarization cue, PCX is internalized via Rab8a- and Rab11a-positive vesicles towards the common cell membrane to form Apical membrane initiation site (AMIS), in cooperation with the polarity dimer Par3/aPKC. The Anx2/CDC42 complex recognizes the Rab8a/Rab11a vesicles, regulating its apical transport.

This is thought to be mediated via a Tuba-dependent CDC42 activation, leading to Par6 binding thus correctly targeting the apical vesicle towards the AMIS, bearing the Par3/aPKC dimer. This leads to the formation of the Pre-apical patch (PAP), expanding into a lumen by pumps and channel[297].

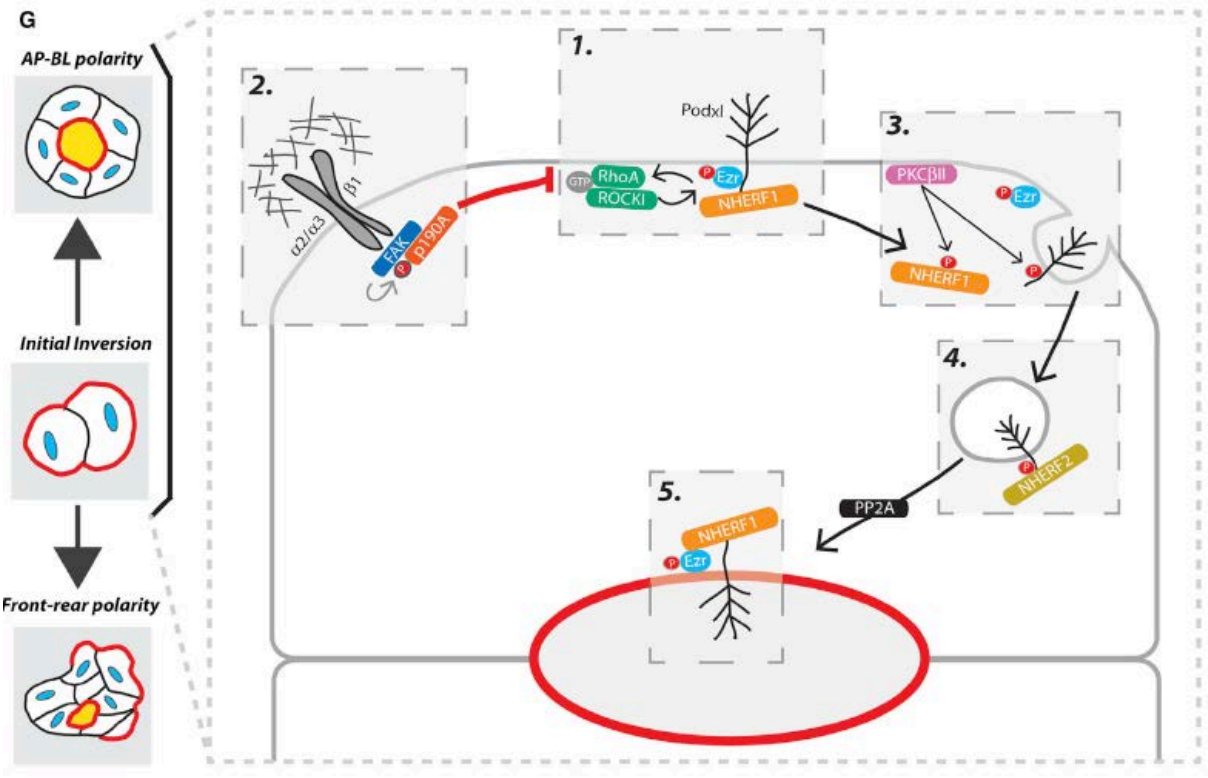

Figure31: A/B polarity orientation in MDCK cyst, Bryant et al., 2014.

In 2014 the mechanism was completed by demonstrating that A/B polarity orientation is regulated by ECM sensing and downstream RhoGTPases signaling. PCX is actually part of a complex with Na^+/H^+ exchange regulatory cofactor (NHERF1) and Ezrin. In suspension (or in an apical-out conformation obtained by blocking ECM sensing), the PCX/NHERF1/Ezrin complex is as the abutting membrane and is phosphorylated by high ROCK activity. After ECM detection by integrins (see following part for integrins description), the recruitment of FAK leads to the activation of p190-RhoGAP and thus, inactivation of RHOA and the subsequent dephosphorylation of Ezrin. Then, PKCβII dephosphorylates PCX which induces NHERF1 dissociation from Ezrin and endocytosis of PCX (via NHERF2) to the AMIS as described above. The phosphatase PP2A then dephosphorylates PCX and NHERF1 allowing the PCX/NHERF1/Ezrin complex to reassociate a the newformed lumen, permitting correct A/B polarization[298].

2. ECM sensing

In vitro experiments showed that when not surrounded by ECM (like in suspension), epithelial 3D structures display an inverted polarity with an outward apical pole. Once in matrix, they detect their surrounding environment through membrane receptors, mainly integrins and dystroglycan. Integrins are a family of transmembrane glycoproteins that form heterodimers composed of α-subunits and β-subunits. They can form 24 pairings with specific binding properties and tissue distributions[299].

Integrins are synthesized in the ER where they dimerize and bind to calcium in a bent inactive state. Then, they traffic through the Golgi to the plasma membrane where they are found in different states, depending on extracellular ligands' availability and the presence of intracellular (in)activators.

Integrins can be activated following an extracellular cue (outside-in activation) like the presence of Mg^{2+} or the binding of an ECM component. In this case, FAK is recruited, followed by talin, inducing the unfolding of the integrins extracellular domain, and the opening between the two subunits in the cytoplasm. Many cytoplasmic proteins are recruited upon integrins activation and establish the link with downstream signaling molecules and the actin cytoskeleton, allowing the formation of a nascent FA. Kindlins, which enhance talin-induced integrins activation, and the IPP complex (Integrin-linked kinase (ILK), PINCH and parvin) bind intracellularly and recruit focal adhesion proteins such as paxillin and α-actinin[300]. Moreover, through vinculin, talin binding to the actin cytoskeleton is strengthened and upon myosin-induced contraction, is stretched which is thought to be required for integrins activation[301]. This leads to integrin clustering and the maturation of the FA. Integrins then serve a biomechanical sensor, transmitting force to the ECM via the binding of their head and an extracellular component, and to the cytoskeleton via their actin-adaptor proteins (e.g talin or tensin)[302].

Another way to activate integrins is via cytoplasmic signals (inside-out activation). This requires the binding of talin to the cytoplasmic tail of the β-subunit. The mechanisms underlying this process are still unclear, some studies thought that in platelets, the activation of the small GTPase RAP1 was necessary for the targeting of talin from the cytoplasm to the membrane but the matter is still under debate[303].

Integrins can be endocytosed whether they are bound or not to their ligand and recycled through early endosomes where they can be addressed to lysosomes or recycled back to the membrane. It is to note that addressing integrins to lysosomes does not always result in their degradation, some can be retrogradely recycled back to the membrane[304]. Furthermore, integrins can still signal from the endosomes.

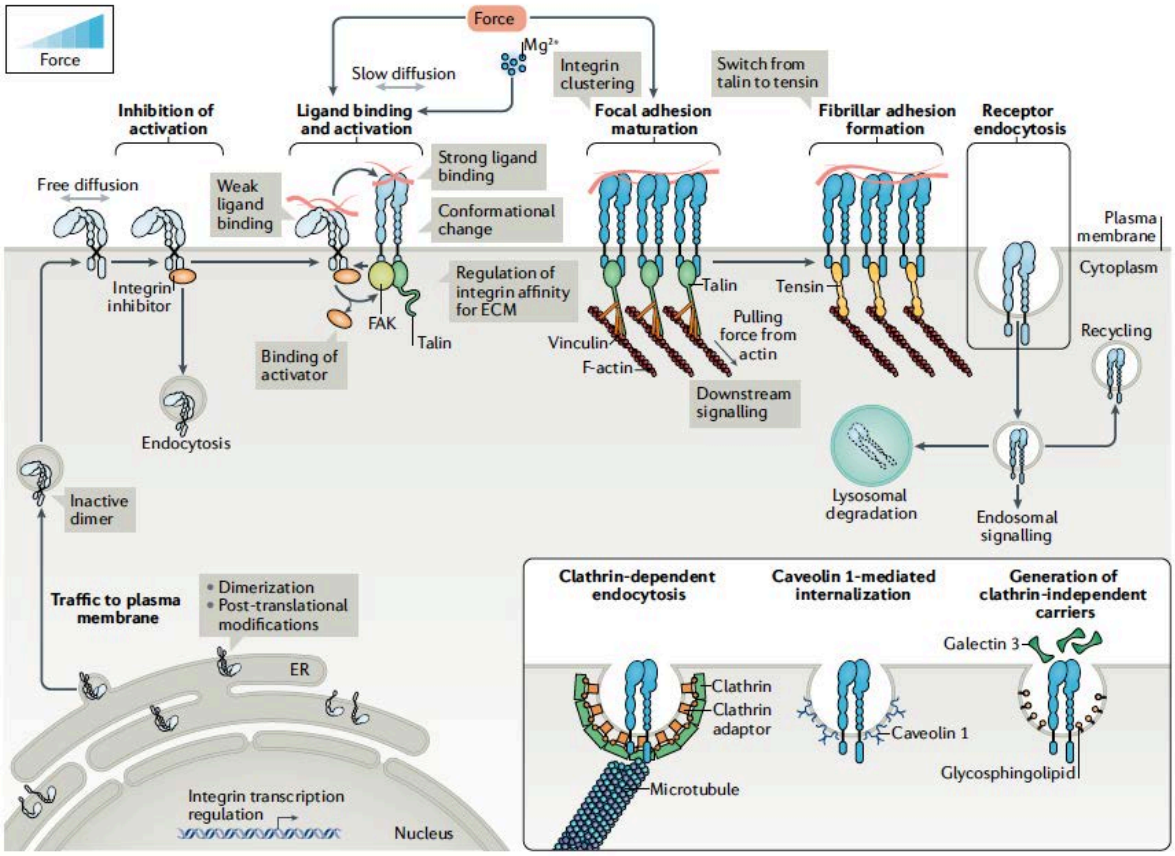

Figure32: Life of an integrin, Kechagia et al., 2019.

In collagen-rich stroma, $\alpha 2\beta 1$ and $\alpha 3\beta 1$ integrins are able to bind collagen fibers which triggers the signal for A/B polarization. This leads to the activation of Rac1 and the deposition of laminin at the basal pole, involving IRSp53. Indeed, impairing this adaptor decreases cell-ECM interactions and laminin deposition[305,306]. Moreover, FAK recruitment upon integrins activation leads to the p190-RhoGAP-mediated inactivation of RHOA at the basal pole. This reinforces Rac1 activity and thus cytoskeletal reorganization to form actin-rich protrusions, mediating adherence forces. Indeed, blocking $\beta 1$ integrins or inhibiting Rac1 leads to the inversion of cysts polarity displaying their apical pole in contact with the ECM[305,307]. In the same way, enhancing contractility through RHOA/ROCK/myosin II leads to an inverted polarity topology[308]. A similar phenotype has been observed in ductal breast carcinomas[309] and in mucinous colorectal cancer[209]. Whether polarity inversion was induced or occurring *in vivo* during tumorigenesis, cell-cell junctions and an asymmetrical distribution of polarity components were maintained, suggesting that A/B polarity establishment and orientation can use distinct and independent molecular mechanisms and that the latter mainly relies on ECM sensing.

The activation of Rac1 also leads to the assembly of a basement membrane away from protrusions formation via IRSp53, thus determining a protrusive apical pole and laminin-rich basal pole. Interestingly, O'Brien et al. demonstrated that Rac1 is required for laminin assembly but not for its secretion[305]. Moreover, IRSp53 locally activates actin polymerization factors (e.g WAVE) leading to a basally-organized actin network[306].

3. Sorting and polarized trafficking of transmembrane polarity proteins

As mentioned earlier, epithelial cells display a pronounced asymmetry through the A/B axis, giving rise to specific membrane domains both morphologically and functionally distinct. To ensure membrane identity, proteins need to be correctly sorted and addressed to the correct membrane compartment which relies on complex intracellular polarized trafficking routes, described by the following figure:

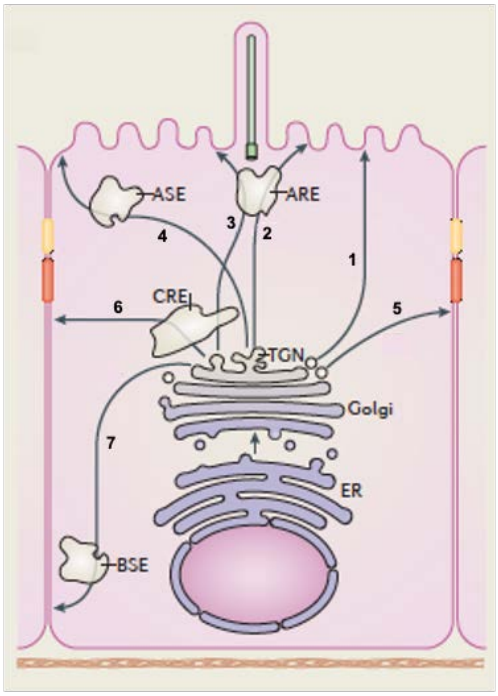

Figure33: Biosynthesis routes of polarity proteins, Rodriguez-Boulan et al., 2014.

After biosynthesis at the endoplasmic reticulum (ER, not shown), apical proteins traffic from the Trans-Golgi network (TGN) directly towards the apical pole (1) or shuttle through the Apical recycling endosome (ARE, 2), the Apical sorting endosome (ASE, 3) or the Common recycling endosome (CRE, 4) to be modified before being delivered to the correct membrane domain. In the same fashion, basolateral proteins traffick either directly to the basal pole (5) or through the CRE (6) or the Basolateral sorting endosome (7)[310].

Polarity protein endocytosis mainly involves clathrin-mediated endocytosis, especially for BL proteins. Clathrin-mediated endocytosis is a multistep process allowing the sorting and recycling of many membrane components through the transport of cargoes (composed of a transmembrane protein and its extracellular ligand) into the cytoplasmic compartment[311]. To date, four AP-complexes have been identified (AP-1 to 4) and localize to different cellular sites. The most studied variant of clathrin-associated AP-1 complex is AP-1B. Nevertheless, some studies have shown that BL protein sorting can be AP-independent and correct localization of proteins recognized through their dileucine motif are not impacted by AP-1B downregulation[312]. Moreover, not all A/B polarized cells express AP-1B, indicating the existence of other protein-sorting machineries. It is the case for E-cadherin and Na^+/K^+/ATPase which are recognized by ankyrins to traffic from the Golgi to the BL plasma membrane[313].

Opposed to basolateral components which are recognized via a cytoplasmic signal, apical sorting determinants can be localized at the transmembrane or the extracellular domains. The latter being the most studied, it seems to rely on N- and O-linked glycosylation of extracellular proteins[314,315]. This involves a family of sugar-binding proteins called galectins which cross-link proteins with carbohydrates to form glycans[316]. Indeed, depletion of galectin-3 mislocalized apical lipid-rafts to the basolateral pole[317]. Some apical proteins traffic through lipid rafts which are dynamic complexes of cholesterol, glycosphingolipids and proteins. They are recognized by clustering agents and are involved in the TGN[318]. The exact mechanisms leading to apical proteins sorting are not well described. It is thought that the BL sorting signals are "dominant", meaning that if a protein presents both apical and BL targeting signals, it will traffic to the BL domain. Some BL proteins can traffic to the apical pole via transcytosis if the BL signal is inactivated.

In epithelial cells, microtubules are bundled along A/B axis with the dynamic plus ends at the basal pole. They display motor proteins called kinesins which are small ATPases that bind vesicles and transport them along microtubules[319,320].

After their correct targeting, polarity proteins-containing vesicles need to be tethered and then fused with the appropriate membrane domain. This is mainly under the control of the Rab family of small GTPases (as shown on Figure). In the case of A/B polarity, annexins can modulate vesicle docking, especially Annexin2, find in the PTEN/PIP_2/Anx2/CDC42 axis, which is able to bind vesicles containing apical proteins and thus, be used as a scaffold for the correct localization of polarity proteins[321]. The fusion relies on the SNARE complex composed of vesicular-SNAREs (v-SNAREs) and target-SNAREs (t-SNAREs), which composition differs between the apical and the BL pole. Downregulation or mislocalization of SNAREs disrupt the correct delivery of A/B polarity proteins vesicles to the targeted membrane domain[322].

All the mechanisms listed above allow epithelial cells to generate specialized membrane and cytoplasmic domains, allowing them to ensure their functions within a tissue. This primary polarization of cells requires further maturation and stabilization of established structures, often referred to as A/B polarity maintenance. This process requires that the antagonism between all A/B polarity establishment actors (PIs, Rho GTPases and polarity complexes) remains unchanged so that they can be used as a scaffold for the recruitment of other components, reinforcing each membrane domain identity.

---

4. A/B polarity maintenance

Maturation of cell-cell junctions

As mentioned before, cell-cell junctions play a key role in A/B polarity. The assembly of AJs and TJs two complexes are highly interconnected since immature AJs are needed for TJs formation. Indeed, the initial contact between two neighboring cells relies on RAC1-mediated actin-based protrusions carrying E-cadherin, which will induce lamellipodia and filopodia formation through remodeling of the actin cytoskeleton. This demonstrates the close relationship between AJs and Rho GTPases that is needed for both establishment and maintenance of cell-cell contacts and thus A/B polarity *(see Figure34)*. Moreover, proteins composing AJs and TJs (respectively nectin, E-cadherin and occludin, claudin, JAM) recruit and bind cytoplasmic proteins which form the cytoplasmic plaque and represent a link between junctional proteins and the actomyosin cytoskeleton, through actin-binding proteins or RhoGTPases family members and effectors[237,249,251,323].

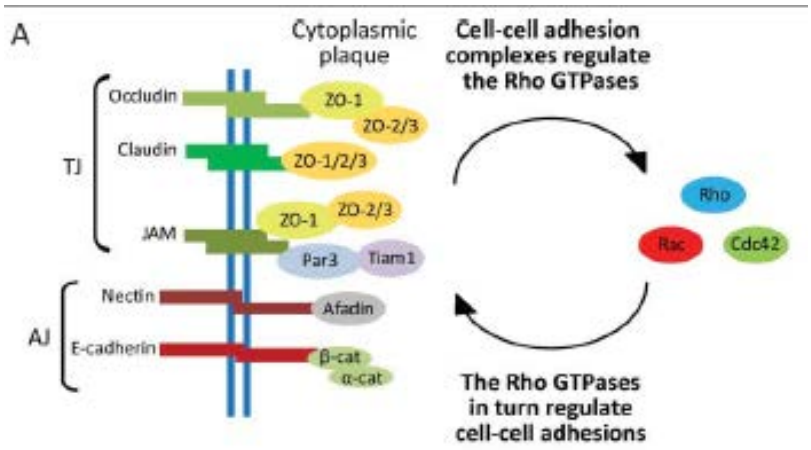

Figure34: Actors of cell-cell junction maturation, Mack et al. 2014.

ERM proteins

Maintaining a link between the plasma membrane and the actin cytoskeleton is of major importance in preserving A/B polarity in epithelial cells. This is ensured by the ERM (Ezrin, radixin, moesin) protein family belonging to the band 4.1 superfamily. They all display a plasma membrane-binding domain at their amino-terminus called FERM (Four point one ERM) and a carboxy-terminal domain known as C-ERMAD (C-terminal ERM-association domain) which is known to bind the FERM domain or filamentous actin (F-actin).

Despite their very similar structures, ERM proteins have different distributions (ezrin is exclusively found in epithelial cells while moesin is expressed in endothelial cells) suggesting that they are needed for distinct cell mechanisms. ERM are present in the cytoplasm in an inactivated conformation where the FERM domain and the C-ERMAD are bound. They are then recruited to the apical plasma membrane where they bind to PIP_2 and are phosphorylated, thus decreasing the affinity between their two domains, enabling F-actin to bind to the C-ERMAD[324].

In intestinal epithelial cells, ezrin is the only ERM expressed and is concentrated along cell-cell contacts in the crypt and is apically relocalized during cell differentiation and migration towards the surface. Deletion of ezrin in the mouse intestinal epithelium leads to abnormal microvilli appearance, indicating its role in shaping this structure through its interaction with the actomyosin cytoskeleton. Furthermore, ezrin has also been described to bind other membrane receptors thus apically stabilizing them[325].

Overall, A/B polarity maintenance involves the continuous segregation of multiple cellular components, ensuring membrane integrity required for cells to function during their entire lifespan. However, since A/B polarity establishment was first studied in simple organisms (Drosophila and C. elegans) which seem to only require on the cooperation between PIs, RhoGTPases and polarity complexes, since downregulation of other polarity components does not impact membrane identity.

Thus, one can wonder if the identification of a distinct step such as polarity maintenance is relevant, especially in mammals, based on the fact that it relies on maturation of already established structures and feedback loops to preserve the interaction of primary actors. What is described as polarity maintenance could be part of the polarity establishment process which would present a common set of early determinants between species. Moreover, it is possible that those processes were separated in order to simplify their understanding, but it is more likely that many steps are happening concomitantly. It is also important to note that first, much more is needed to totally apprehend the complexity of such events and second, that such further studies will require more physiological cellular models.

PhD AIMS

Cancer cell dissemination has been extensively studied and whether it is based on single cells or collective strands, it always seems to rely on the activation of at least, a partial EMT. This leads to the loss of epithelial characteristics due to an increase in TGFβ signaling. Mainly, epithelial cells lose their A/B polarity which is replaced by a front-rear one. Yet this conception is mostly gleaned from experimental model systems.

Four years ago, I applied for a PhD in Fanny Jaulin's lab because she was proposing a subject that was in line with my training and with what I was looking for in a PhD subject: it was a translational project combining a real fundamental investigation based on clinical observations, that implied modern technical approaches using 3D matrices, PDXs, mice models and patients' samples. In line with the lab standpoint, I believe that the cooperation between researchers and clinicians is mandatory and both parties benefit greatly from one another.

At the time I joined the team, we just discovered a new mode of CRC metastasis identified from explants retrieved from a cohort of 50 patients with metastatic colorectal cancer. This process relies on EMT-independent collective clusters of cancer cells called Tumor spheres with inverted polarity (TSIPs). Those spheres still express many epithelial markers (such as E-cadherin or CD133) and conserve their A/B polarity throughout the metastatic cascade. We made the intriguing observation that, once embedded in 3D collagen-I gels, two thirds of patients' spheres present an inverted polarity with an outward apical pole in contact with the ECM (called apical-out), while one third conserve a more conventional architecture with the relocalization of the apical pole away from the matrix by formation of a lumen (called apical-in).

Identifying the ins and outs of this remarkable tumor intermediate would allow us to gain a better understanding of EMT-independent dissemination pathways and A/B polarity in cancer cells. My PhD project aimed at:

(i) Deciphering the oncogenic molecular alterations allowing apical-out TSIPs to maintain their inverted polarity, even when surrounded by ECM, as such a topology was never described before.

(ii) Determining how these alterations relate to the molecular and cellular mechanisms of apico-basolateral polarization in normal epithelial cells.

(iii) Comparing the metastatic potential of TSIPs with the two polarity orientations. While in Zajac et al. we showed that apical-out TSIPs were able to initiate peritoneal metastatic in mice models, I wished to assess whether apical-in TSIPs were more or less invasive and whether this was a consequence of A/B polarity orientation.

(iv) Finally, I wanted to go back to patients' specimen to evaluate if TSIPs and their topology could be used as a clinical biomarker to improve patients' care. Indeed, since they are involved in advanced stages, we could benefit from a better understanding of their clinical relevance.

PUBLICATIONS

Organoids as preclinical models to improve intraperitoneal chemotherapy effectiveness for colorectal cancer patients with peritoneal metastases: Preclinical models to improve HIPEC.

Treating CRC patients with peritoneal carcinomatosis (PC) is still challenging because of the widespread metastases in the abdomen, across the peritoneum. Systemic chemotherapies have proven limited efficacy due to the low concentration of the cytotoxic compound that reach the peritoneal cavity. There is a need for a relevant preclinical model, allowing us to study this poorly investigated condition and to translate preclinical data to patient. In Roy et al., we used organoids to develop a representative model of response to chemotherapy and to identify new therapeutic approaches for patients.

In this paper, we first compare the chemotherapies used to treat PC across the world as there was no treatment consensus. We treated CRC organoids in vitro, in 3D collagen-I gels to determine their response to different molecules, used alone or in combination, and/or concentrations coinciding with patients' data. HIPEC is a particular treatment in the way that the chemotherapeutic agent is heated up to 43°C during the 30-90 min incubation into the peritoneal cavity. Then, the chemotherapeutic bath is removed. My contribution to this paper relied on the demonstration that treating organoids with Oxaliplatin at 43°C was not more efficient on two out of three of our organoid models (Figure 4: only significative in one model ($p<0.05$)). These results indicate that heating chemotherapy might not be effective. Overall, we demonstrate that even for the most efficient treatment, 1 hour incubation is insufficient to kill all the cells of the organoids.

Interestingly, I showed that by repeating treatment cycles (90min of Oxaliplatin every three days), I could demonstrate that this was sufficient to increase Oxaliplatin effects on two models with a high significance (Figure 6). Therefore, we proposed that PC patient could benefit from being treated by repetitive cycles of intraperitoneal chemotherapy.

Title: Organoids as preclinical models to improve intraperitoneal chemotherapy effectiveness for colorectal cancer patients with peritoneal metastases: Preclinical models to improve HIPEC

Authors: P. Roy, C. Canet-Jourdan, M. Annereau, O. Zajac, M. Gelli, S. Broutin, L. Mercier, A. Paci, F. Lemare, M. Ducreux, D. Elias, D. Malka, V. Boige, D. Goéré, F. Jaulin

PII: S0378-5173(17)30693-2
DOI: http://dx.doi.org/doi:10.1016/j.ijpharm.2017.07.084
Reference: IJP 16899

To appear in: *International Journal of Pharmaceutics*

Received date: 11-7-2017
Accepted date: 31-7-2017

Please cite this article as: Roy, P., Canet-Jourdan, C., Annereau, M., Zajac, O., Gelli, M., Broutin, S., Mercier, L., Paci, A., Lemare, F., Ducreux, M., Elias, D., Malka, D., Boige, V., Goéré, D., Jaulin, F., Organoids as preclinical models to improve intraperitoneal chemotherapy effectiveness for colorectal cancer patients with peritoneal metastases: Preclinical models to improve HIPEC.International Journal of Pharmaceutics http://dx.doi.org/10.1016/j.ijpharm.2017.07.084

Organoids as preclinical models to improve intraperitoneal chemotherapy effectiveness for colorectal cancer patients with peritoneal metastases

Preclinical models to improve HIPEC

Roy P[1] (PharmaD Stu), Canet-Jourdan C[1] (PhD stu), Annereau M[3] (PharmaD), Zajac O[1] (Ir), Gelli M[2] (MD), Broutin S[4] (PharmaD), Mercier L[4] (Tech), Paci A[4,5] (PharmaD; PhD), Lemare F[3] (PharmaD-PhD), Ducreux M[6] (MD-PhD), Elias D[2] (MD-PhD), Malka D[6] (MD), Boige V[6] (MD), Goéré D[2] (MD-PhD) and Jaulin F[1] (PhD)

[1] U-981, Gustave Roussy, Villejuif, F-94805, France

[2] Department of Surgical Oncology, Gustave Roussy, Villejuif, F-94805, France

[3] Pharmacy department, Gustave Roussy, Villejuif, F-94805, France

[4] Pharmacology and drug analysis department, Gustave Roussy, Villejuif, F-94805, France

[5] Pharmacokinetic and clinical pharmacy department, Paris-Saclay University, Châtenay-Malabry, F-92296

[6] Department of Medical Oncology, Gustave Roussy, Villejuif, F-94805, France

Graphical abstract

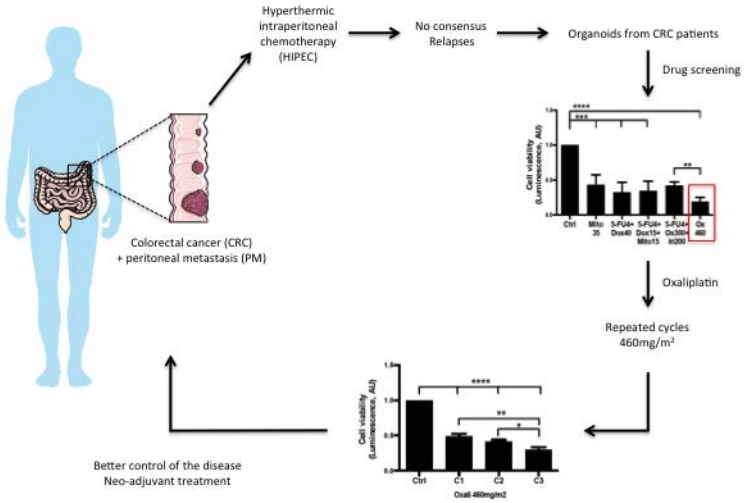

Synopsis

Organoids represent a relevant preclinical tool widely use to assess intravenous systemic chemotherapy efficiency in the context of personalized medicine. In this study, we use these "mini-organs" from colorectal carcinomas to identify the optimal cytotoxic-based protocols for the contact chemotherapy administered intraperitoneally to patients with peritoneal metastases.

Abstract

Background: Peritoneal metastases (PM), corresponding to tumor implants into the peritoneal cavity, are associated with impaired prognosis and low responsiveness to systemic chemotherapy. A new therapeutic approach has dramatically changed the prognosis of patients with PM from colorectal cancer (CRC), consisting in the association of a complete cytoreductive surgery followed by intraperitoneal chemotherapy associated to hyperthermia (HIPEC). Many drugs have been administered intraperitoneally, but no clear consensus has been approved. Therefore, relevant preclinical models are essentials for the efficient translation of treatments option into affected patients. **Method**: Organoids, the last generation of preclinical models, were used to rationalize and improve intraperitoneal chemotherapy. We tested several cytotoxics, combination, effect of hyperthermia, exposure duration and frequency. **Results**: Organoids were a representative model of response to chemotherapies used for the treatment of PM from CRC; 460mg/m^2 of oxaliplatin being the most efficient cytotoxic treatment. Repeated incubations with oxaliplatin; mimicking cycles of intraperitoneal treatment, resulted in an increased efficacy. **Conclusion & Discussion**: Organoids are relevant models to study the chemosensitivity of peritoneal metastases from CRCs. These models could be used for large scale drug screening strategies or personalized medicine, for colorectal carcinoma but also for PM from other origins.

Keywords

Peritoneal carcinomatosis
Colorectal carcinoma
Organoids
Preclinical
HIPEC

Introduction

Relevant preclinical models are essentials for the efficient translation of treatments option into affected patients. Cancer cells lines and mice xenograft have proven to be valuable in anti-cancer drug discovery, but they both comprise caveats. A third generation of preclinical models, named organoids, holds great appeal. Organoids grow *ex vivo* from normal or cancer stem cells in tridimensional matrices based-gels to develop into fully differentiated "mini-organs" recapitulating the architecture and function of mature normal or pathological organs[1-3]. This technology is already applied to the personalized treatment of patients with cystic fibrosis and proof-of-concept have been made for gene therapy and regenerative medicine[4-6]. As organoids generated from primary cancer explants represent inter and intra-tumour heterogeneity, they show great promises for translational research and clinical applications [7,8]. To date, all studies use organoids to investigate the effect of systemic chemotherapy delivered intravenously. In this study, we used organoids generated from colorectal carcinomas to identify optimal cytotoxic-based protocols for the contact chemotherapy administered intraperitoneally to patients with peritoneal metastases.

Peritoneal metastases (PM) correspond to the tumour implants into the peritoneal cavity from different solid organs, mostly from colorectal, gastric and ovarian carcinomas. The diagnosis of PM represent in most of cases a fatal issue and treatment based on systemic chemotherapy still offers poor survival[9]. Since nearly three decades, a new therapeutic approach has dramatically changed the prognosis of patients with PM from colorectal cancers and from primary peritoneal malignancies (i.e. pseudomyxoma and mesothelioma)[10-12]. This treatment consists in the association of a complete cytoreductive surgery (CRS) of all the visible peritoneal implants (maximum residual tumour size of 1 mm), followed by intraperitoneal chemotherapy associated to hyperthermia (HIPEC) to treat the remaining non visible tumour implants. Direct intraperitoneal chemotherapy allows to higher local concentration, increases local biodisponibility, with the aim of improving the effect of the cytotoxic drugs. Beside CRS and HIPEC, local administration of chemotherapy has also been used either in patients with unresectable PM to enhance the response to chemotherapy by the local effect[13-16], or after surgical resection of PM, in the adjuvant setting[17, 48]

Pharmacokinetics studies have been performed to determine the peritoneal and plasmatic concentrations of the cytotoxic administered directly into the peritoneum aiming to define the optimal cytotoxic and its optimal dosing. Indeed, the behavior of a drug administered into the peritoneal cavity is conveniently described by a two-compartment model: the first compartment represents the peritoneal cavity and the second is characterized by the central and peripheral compartments including the other tissues of the body that are in direct contact with the bloodstream. The intraperitoneal concentration of the cytotoxic can be defined as:

$$\frac{C_{peritoneum}}{C_{plasma}} = \frac{(plasma\ clearance) + (cavity\ clearance)}{(cavity\ clearance)}$$

Pharmacokinetic studies have shown that intravenous injections of 5-Fluorouracyl (5-FU) lead to a peritoneal concentration 100 fold lower than that obtained after direct intraperitoneal (IP) administration of 5-FU[18,19]. These results have been confirmed with Irinotecan and Mitomycin-C. However, since the introduction of this new approach, many drugs, at different concentrations and in diverse combination have been described worldwide; but actually, no clear consensus has been approved[20-24]. Therefore, the definition of the optimal cytotoxic drug, dosing, and administration route are still required.

Material and Methods

Organoids retrieval and preparation from Patient-Derived Xenograft: Four human colorectal tumour (IC-OO10P (CRC 1), IGR-0012P (CRC 2), LRB-0008M (CRC 3), IRG-0014P (CRC 4)) from the CReMEC tumour collection were maintained in immunocompromised mice as previously described by Julien et al.[21]. Briefly, small tumour fragments were subcutaneously engrafted on the flank of anesthetized mice (2.5% isoflurane). Tumour growth was measured at least once a week. When the volume reach 1500 mm3, mice were sacrificed and tumour were used for ex vivo experiments and 50mm3 fragments engrafted on the flank of new mice (up to 10 passages).

Organoids were prepared according to Sato et al[2] and adapted for muco-secreting tumours as follows: tumours between 1000-1500 mm3 were retrieved from the mice, minced into small fragments using a sterile scalpel and were incubated for 1h30 (45min

for 10P) at 37°C in a final volume of 5 ml of culture medium (DMEM) without fœtal bovin serum (FBS) and with 2 mg/ml collagenase IV (Sigma, C2139). The samples were then mixed with 20 ml of DMEM and filtered on 100 µm mesh size cell strainers (EASYstrainer, 542000). Digested tumour clusters were pelleted in by 4 pulse-centrifugations at 1500 rpm. The tumour fragments, free of single cells, were maintained 3 days in ultra-low attachment plates (Corning, CLS3471) in culture medium for PDX CRC2 and 3 or in Matrigel 3mg/mL (BD, 354230) 15% for PDX CRC1 and CRC4.

Organoids invasion in Collagen-I :

Rat-tail Collagen-I (Corning, 354236) was neutralized with 1.0 M NaOH–and 10x MEM (Life Technologies, 21430-02) according to the ratio: 1.0:0.032:0.1 (vol/vol). The concentration was then adjusted at 1,3-2 mg/ml with DMEM 1X and the collagen is incubated on ice for 1-1h15. Organoids embedded in neutralized Collagen-I were added on the pre-coated well at an average concentration of 10 organoids per microliter (NUNC 24-well chamber or Ibidi 8-well chamber). The gel was allowed to polymerize for 45 min at 37°C. Organoids were then cultured in culture medium supplemented with FBS 10 % and with or without cytotoxic drugs for different time point.

Cytotoxic drugs:

Cytotoxics were selected for their common use in PC treatment: Mitomycin-C KIOWA 10mg (Prostrakan, United Kingdom), 5-Fluorouracil (5-FU) 50mg/mL (Accord Healthcare, France), Oxaliplatin 5mg/mL (Accord Healthcare), Irinotecan 20mg/mL (Hospira, France) and Doxorubicin 200mg/100mL (TEVA), Paclitaxel 6mg/mL(KABI). Five cytotoxic mixtures were studied with a 2L/m^2 ceiling. Solvant was NaCl 0,9% (Fresenius):

- Triplet: 5-FU 400mg/m^2 (200mg/L) + Oxaliplatin 300mg/m^2 (150mg/L) + Mitomycin-C 15mg/m^2 (7,5mg/L)
- HIPEC: 5-FU 400mg/m^2 (2mg/L)[18]+ Oxaliplatin 300mg/m^2 (150mg/L) + Irinotecan 200mg/m^2 (100mg/L)
- Doxorubicin: 5-FU 400mg/m^2 (2mg/L)[18]+ Doxorubicin 40mg/m^2 (20mg/L)
- Mitomycin: Mitomycin-C 35mg/m^2 (17,5mg/L)
- Doxorubicin + Mitomycin: 5-FU 400mg/m^2 (2mg/L)[18] + Doxorubicin 15mg/m^2 (7,5mg/L) + Mitomycin-C 15mg/m^2 (7,5mg/L)

Cytotoxics were incubated during 30/60/90min at 37°C or 43°C and after a briefly wash out with DMEM continuing incubation for 48h with DMEM culture medium+FBS+PS.

Chemosensitivity assay:

Immunofluorescence: Samples were washed twice in PBS supplemented with calcium (0.1mM) and magnesium (1mM) and fixed in PFA 4% for 45min (organoids, peritoneum). Permeabilization was performed in PBS supplemented with 0.5% Triton(x100) during 45min. Primary antibodies were incubated overnight at 4°C at the dilutions listed below in antibody dilutent, PBS with 10% serum supplemented by 0.1% Triton(x100). Secondary antibodies (CyTM3-conjugated or Fluorescein (FITC) conjugated anti-Mouse or anti-Rabbit, Alexa Fluor 488 anti-rabbit 1:100, Jackson ImmunoResearch) and DAPI (1 µg/ml) were incubated 2h at room temperature. *Antibodies:* The following primary antibodies were used at the indicated dilutions: cleaved caspase 3 (1:100, Cell signalling, 9661), alexafluor 647 phalloidin (1:200, Life Technologies, A22287).

Luminescence: The reagent used to analysed cell viability was CelltitlerGlow (Promega). Samples were prepared by pipetting with a 1000mL cone to dissociate Collagen-I and release organoids in culture medium. CelltitlerGlow was added v/v to the culture medium. After manual marked plate shaking, mixture was leaved at room temperature during 30 minutes. Quantification was carried out with a Fluostar Optima luminometer. Survival was proportional to the luminescence signal.

Microscopy, images traitement and analyses:

Images were acquired using a SpinningDisk CSU-W1 (Yokogawa) with a ZylasCMOC camera piloted with an Olympus X83. Organoids survival was quantified with a < alive cells/total cells> ratio. Images for display were processed using ImageJ, Imaris or Metamorph softwares.

Platinum Determination

Platinum levels in organoids lysates were measured by a fully validated atomic absorption spectrophotometric method, on a PinAAcle 900Z spectrophotometer (Perkin Elmer, MA, USA). Briefly, 48h after Oxaliplatin treatment (460 mg/m^2) at 37°C or 43°, organoids were lysed using the CellTiter-Glo® kit (Promega, WI, USA). Untreated

organoids were used as controls. Lysats were centrifuged and stored at -20°C prior analysis.

Statistical Analyses:

All errors indicated in the text are SEM for quantitative values or error margin for percentages. Non-parametric, unpaired t-test and Mann-Whitney tests were performed to determine whether the difference between two groups was significantly different in their mean value using Prism 6.

Results

Assessing CRC cell viability using ATP-bioluminescence

We prepared organoids from patient-derived-xenografts (PDX) established from CRC tumours[25] as previously described[3]. In order to assess the chemosensitivity of CRC organoids to cytotoxic drugs, we opted for an ATP-bioluminescence assay[7]. Organoids were treated with 35mg/m^2 of Mitomycin-C (Mito-C), 4 or 400mg/m^2 of 5-Fluorouracil (5-FU) for 72 hours. The number of viable cells was measured by quantifying the level of ATP for each treatment and normalized to control conditions. Exposure to intraperitoneal concentration of Mito-C (35mg/m^2) and 5-FU (400mg/m^2), decreased ATP-bioluminescence by 80% and 60%, respectively (Fig.1A). In order to confirm that decreased ATP-bioluminescence was reflecting increased cell death, we stained control and treated organoids using immunofluorescence. Confocal microscopy revealed that, in control conditions, organoids were almost exclusively formed by live cells (Fig. 1B, left panel). In contrast, exposure to 35mg/m^2 Mito-C and 400mg/m^2 5-FU significantly decreased the number of viable cells detected by DAPI staining (Fig. 1B for immunostaining and 1C for quantification). The appearance of cleaved-caspase 3 (CC3) staining demonstrated that cell death induced by Mito-C and 5-FU was mainly attributed to apoptosis (Fig. 1B).

Therefore, the microscopy approach confirmed that CRC organoids are sensitive to cytotoxics and that ATP-bioluminescence is a robust and efficient assay to measure their chemosensitivity.

CRC organoids viability according to 5-FU concentrations

CRC patients with PM can either be treated by systemic chemotherapy or direct incubation of cytotoxics into the peritoneal cavity, such as during HIPEC[12,26]. Pharmacokinetic studies have shown that the intraperitoneal (IP) concentration of 5-FU was about 100 times lower after intravenous injection when compared with direct IP administration[18,19]. While 400 mg/m^2 of 5-FU significantly diminished cell viability, reducing its concentration to 4 mg/m^2 had no significant effect on organoids viability (Fig. 1A). These results were confirmed by immunofluorescence since we could not detect any significant cleaved caspase-3 staining in organoids treated with 4 mg/m^2 of 5-FU (Fig. 1B). These results show that our assay sensitivity is optimal to detect different tumour cell response to cytotoxic drugs. Second, this confirm that the lower access of the peritoneal cavity by the cytotoxic drug injected intravenously seriously compromises drugs cytotoxic effect, highlighting the pharmacological benefit of the IP route of administration.

Organoids viability according to the duration of exposure

We next compared the effect of the cytotoxic drugs after different times of exposure according to the protocols commonly used during HIPEC[21,27-29]. We used 35 mg/m^2 of Mito-C for 30, 60 and 90 min and assessed cell viability after 2 days (Fig. 2A). In order to assess the robustness of incubation time variation on different genetic background, we performed these tests on organoids generated from four independent CRC Patient-derived xenografts (PDXs) (CRC-1 to 4, Fig. 2B). After incubating Mito-C during 30 min, organoids viability was not significantly different than controls for CRC1 and CRC3 while it was decreased to 71% and 59% in CRC2 and CRC4, respectively (Fig. 2C, 2D, 2E and 2F). In these latest models, increasing Mito-C incubation to 60 and 90 min only mildly decreased cell viability (Fig. 2D and 2F) while these durations yielded significant death when compared to 30 min in CRC1 and CRC3 organoids, killing 50% to 63% of tumour cells at 90 min. (Fig.2C and 2E). In all models, we did not detect any significant differences between 60 and 90 min incubation time (Fig. 2C, 2D, 2E and 2F).

Together these experiments demonstrate that, 60 or 90 min treatment with 35 mg/m^2 of Mito-C are consistently efficient, independently of CRC genetic background while reducing incubation time to 30 min only trigger cell death in certain CRCs, but not others. Yet, in all models, 36% to 60% of CRC cells remained viable after 90 min of 35 mg/m2 of Mito-C (Fig. 2C, 2D, 2E and 2F).

Organoids viability according to the use of common cytotoxic agents

We then thought to use our assay to compare the efficiency of the drugs commonly administered to CRC patients with peritoneal metastases during HIPEC (see table for references, Fig. 3A). Organoids were incubated with different cytotoxics for 90 min and viability was assessed after 48 hours. CRC1 and CRC4 were globally more sensitive to the mentioned drugs than CRC2 and CRC3. In CRC1 and CRC4, the cell viability was reduced by more than 50% and up to 19% with limited variability among the different treatments (Fig. 3A for drugs and concentration and Fig.3B and 3E for the response). In contrast, the treatment by 5-FU4/Dox15/Mito15 had no significant effect on CRC2 and CRC3. In addition, Mito35 and 5-FU4/Dox40 had only limited cytotoxicity on these organoids, killing less than half of the CRC cells (Fig.3C and 3D). However, Oxaliplatin (Oxali) treatment (alone or in combination with 5-FU and Irinotecan) was at least as efficient in CRC2 and CRC3 than for CRC1 and CRC4, reducing cell viability by at least 2-fold and up to 8% (Fig.3C and 3D). Except for CRC4, we did not detect any significant difference between exposure to Oxali at the dose of 460mg/m^2 and the combination of Oxali at 300mg/m^2 with 5-FU and Irinotecan (5FU4/Ox300/Iri200, see Fig. 3B, 3C, 3D and 3E). Together, these results demonstrate that organoids sensitivity to cytotoxic agents varies among tumours and that Oxaliplatin, alone or in combination, has a broader cytotoxic action than other drugs, independently of the molecular background of the tumour.

Organoids viability according to the degree of hyperthermia

During HIPEC, the cytotoxics are incubated in a bath warmed-up to 41-43°C, a procedure supposed to increase cytotoxicity on classical 2D cell-lines cultures and in patients[30-32]. We therefore examined whether rising temperature during drug incubation could be more efficient and eradicate CRC organoids. We compared the viability of organoids exposed, or not, with Oxali 460mg/m^2 at 37°C and 43 °C. Increasing the temperature to 43°C did not significantly increased the cytotoxicity of Oxaliplatin CRC3 and CRC4 (Fig. 4B and 4C). However, CRC1 showed decreased chemoresistance when Oxali was heated to 43°C, yet, it did not completely kill the organoids either (Fig. 4A). Then we investigated if this difference of chemoresistance could be explained by platinum accumulation in organoids, measuring platinum in CRC1

and CRC3 after 48h at 37°C and 43°C. Platinum concentrations were significantly higher in CRC3 at 43°C compared to 37°C but no difference was observed for CRC1 (Fig. 4B).

Testing new combinations of cytotoxic agents

As none of the current cytotoxic treatments used during HIPEC completely killed organoids, we decided to investigate their response to alternative drug combinations. We thought to combine Oxali, the most powerful cytotoxic in our assay (Fig.3) and in CRC patients (recommended by the NCCN guidelines) with other drugs to identify synergistic associations. As recently proposed[19], we tested the combination of Oxali, Mito-C and 5-FU but we enhanced the doses at 300mg/m^2 of Oxali, 15mg/m^2 of Mito-C and 400mg/m^2 of 5-FU (that we named "triplet"). As a control, we also exposed organoids to each drug separately. The triplet strongly reduced all organoids viability and down to only 7% in CRC3. However, the triplet was not significantly more efficient than the treatment by Oxali alone at the dose of 460mg/m^2 (Fig. 5A, 5B, 5C and 5D). Then, we thought to combine the maximum concentration of Oxali with Mito-C at either 15 or 35mg/m^2. We could only detect mild variations and no significant added value of these combinations in all models (Fig. 5A, 5B, 5C and 5D).

In sum, these data show that the most powerful cytotoxic drug to decrease the rate of viable cells in CRC organoids is the Oxaliplatin at a dose of 460 mg/m^2 after 60 min exposure. Combinations to others cytotoxics doesn't seem to improve these results.

Repeated cycles of oxaliplatin exposure achieve the best cytotoxic effect

Finally, we used organoids to evaluate the efficiency of repeated IP administration of chemotherapy, as described in patients with unresectable peritoneal disease, or in an adjuvant setting after optimal surgical debulking. We choose to test repeated contact chemotherapy with Oxali as it was the most efficient cytotoxic in our preliminary results. Treating organoids made from CRC3 with repeated cycles of 90 min of Oxali 460 mg/m^2 every 3 days for 9 days maintained a selective pressure constraining tumour cell number to less than 5% of the initial tumour cell mass over extended period of time (Fig. 6A and 6C). In addition, treating organoids made from CRC4 and CRC2, less sensitive to Oxali, not only restrained regrowth from viable cells, but also improved the tumour cell reduction rates at each exposure. After only three cures, the protocol increased cell death induced by Oxali treatment by 1,6 and 3-fold in CRC2 and CRC4,

respectively (Fig. 6B and 6D). Using this approach we could obtain a much better control of the disease and attractively, in neo-adjuvant settings, induce a sufficient response, which could allow performing complete cytoreductive surgery.

Discussion

The use of cancer cell lines and murine models to improve the chemotherapeutic treatment of peritoneal carcinomatosis has so far been limited for several reasons. First, mice models of peritoneal carcinomatosis have been described in the literature[33]. However, in these small animals the low abdominal volume and the high peritoneal absorption, combined with the rapid tumour growth, weight loss, ascites formation and death are not representative of the human pathology. Larger animals, such as rabbits, seem to be more adequate models and present the advantage of being compatible with complete cytoreductive surgery like the one performed in humans before HIPEC; but animal care facilities handling such animals are rare[34]. Second, cancer cell lines cultured in conventional 2D conditions do not recapitulate the tridimensional (3D) architecture of the metastatic nodules, favouring drug penetration but probably failing to predict effective doses and chemoresistance *in vivo*. Indeed, in our study, the tridimensional organization of organoids has proven to be crucial to reveal that conventional drug posology rarely kills the entire tumour structure; an inner cancer cell core often remains viable, potentially initiating recurrent growth after treatment. As an example, exposing organoids to 400mg/m^2 of 5-FU (corresponding to 200mg/L) for 90 min only kills between 15% and 37% of CRC cells (Fig. 5). In contrast, using conventional CRC cell lines, Shimizu et al. showed up to 90% of CRC reduction rate, a stronger effect that is very likely favored by the monolayer organization of the cancer cells, but not representative of the tumour architecture and response[19].

Organoids have been used to identify new agents for the systemic chemotherapy of primary cancers[7,8]. However, for the first time, we investigated their relevance in the study of contact chemotherapies, when the cytotoxics are directly delivered to the metastases and their microenvironment, such as in the case of peritoneal malignancies. Likely because there is an immediate correlation between the administration and effective concentration, we validated the use of organoids as a relevant preclinical model to rationalize the treatment of CRC patients with PM. Moreover, using ATP-bioluminescence as a read-out for cancer cell viability we could extend our approach to

medium and large-scale screening strategies. These could be used to identify new compounds in the treatment of peritoneal metastases but also to tailor chemotherapy in the context of personalized medicine.

Currently, two chemotherapy protocols are mainly used intraperitoneally during HIPEC: Oxaliplatin or Mitomycin-C. However, many variations exist between the teams and there is no real consensus as to the dose to be used, the duration of HIPEC, the temperature or the modalities (closed- *versus* open-abdomen). It seems impossible to be able to compare the different modalities integrating all possible variables in randomized phase 3 trials. Therefore, the use of pre-clinical models to determine the most effective protocol is of great help. Oxaliplatin appears to be the most effective drug, irrespective of the duration of exposure, which must exceed 30 min, and regardless of temperature. Combination with other cytotoxics does not appear to improve cytotoxicity. These results should be confirmed on a larger number of organoid models; however, the use of Oxaliplatin at a dose of 460 mg / m^2 could be the "standard" protocol of HIPEC open-abdomen done in patients with colorectal PM[35]. Organoids could also be used to test individual chemosensitivity to different cytotoxic. It could also be proposed to perform a laparoscopy in patients who are candidates for a complete cytoreductive surgery followed by HIPEC[36,37], in order to ensure the resectability of the disease, and to perform biopsies of peritoneal tumour nodules, and then test their chemosensitivity to different drugs, and determine within less than two weeks, the cytotoxic to use, as proposed for gastric cancers by Hultman et al.[38].

This technique for assessing organoids chemosensitivity could also be used in patients with peritoneal recurrence after a first HIPEC. Indeed, an iterative HIPEC is more and more proposed in case of isolated peritoneal recurrence, accessible to a new complete cytoreductive surgery, in selected patients[39-43]. However, should the peritoneal relapse be considered as a failure of HIPEC, of the technique, or as a chemoresistance to the cytotoxic used during the first HIPEC. It would therefore be extremely interesting to test the chemosensitivity to different cytotoxics before programming a new HIPEC under these circumstances.

Conclusions

We demonstrated that repeated contact chemotherapy allowed to maintain a low rate of viable cells. These results are in accordance with the use of repeated intraperitoneal chemotherapy cycles in patients with unresectable peritoneal disease We opted for repeated cycles of platinum derived drug exposure, not heated, as done in patients mostly from ovarian and gastric carcinomas[44-46]. Using this approach we could obtain a much better control of the disease and attractively, in neo-adjuvant settings, induce a sufficient response, which could allow performing complete cytoreductive surgery. This approach is also in accordance with the survival benefit reported with the administration of intraperitoneal chemotherapy after optimal debulking for patients with ovarian carcinoma[47].

Acknowledgments

We thank the members of the Jaulin lab and Departments of Surgical and medical Oncology for discussion; Joel Raingeaud and Fotine Libanje for critical reading of the manuscript. This work was supported by the Gustave Roussy fund raising on colorectal cancer (Roulons pour le colon/mars bleu) and the ATIP-AVENIR program.

Bibliography

1. Clevers H. Modeling Development and Disease with Organoids. *Cell* 2016;165:1586–97.
2. Sato T, van Es JH, Snippert HJ, Stange DE, Vries RG, van den Born M, Barker N, Shroyer NF, van de Wetering M, Clevers H. Paneth cells constitute the niche for Lgr5 stem cells in intestinal crypts. *Nature* 2011;469:415–8.
3. Sato T, Stange DE, Ferrante M, Vries RGJ, van Es JH, Van den Brink S, Van Houdt WJ, Pronk A, Van Gorp J, Siersema PD, Clevers H. Long-term expansion of epithelial organoids from human colon, adenoma, adenocarcinoma, and Barrett's epithelium. *Gastroenterology* 2011;141:1762–72.
4. Dekkers JF, Wiegerinck CL, de Jonge HR, Bronsveld I, Janssens HM, de Winter-de Groot KM, Brandsma AM, de Jong NWM, Bijvelds MJC, Scholte BJ, Nieuwenhuis EES, Van den Brink S, et al. A functional CFTR assay using primary cystic fibrosis intestinal organoids. *Nat Med* 2013;19:939–45.
5. Dekkers JF, Berkers G, Kruisselbrink E, Vonk A, de Jonge HR, Janssens HM, Bronsveld I, van de Graaf EA, Nieuwenhuis EES, Houwen RHJ, Vleggaar FP, Escher JC, et al. Characterizing responses to CFTR-modulating drugs using rectal organoids derived from subjects with cystic fibrosis. *Sci Transl Med* 2016;8:344ra84.
6. Schwank G, Koo B-K, Sasselli V, Dekkers JF, Heo I, Demircan T, Sasaki N, Boymans S, Cuppen E, van der Ent CK, Nieuwenhuis EES, Beekman JM, et al. Functional repair of CFTR by CRISPR/Cas9 in intestinal stem cell organoids of cystic fibrosis patients. *Cell Stem Cell* 2013;13:653–8.
7. van de Wetering M, Francies HE, Francis JM, Bounova G, Iorio F, Pronk A, van Houdt W, Van Gorp J, Taylor-Weiner A, Kester L, McLaren-Douglas A, Blokker J, et al. Prospective derivation of a living organoid biobank of colorectal cancer patients. *Cell* 2015;161:933–45.

ACCEPTED MANUSCRIPT

8. Sachs N, Clevers H. Organoid cultures for the analysis of cancer phenotypes. *Curr Opin Genet Dev* 2014;24:68–73.
9. Franko J, Shi Q, Meyers JP, Maughan TS, Adams RA, Seymour MT, Saltz L, Punt CJA, Koopman M, Tournigand C, Tebbutt NC, Diaz-Rubio E, et al. Prognosis of patients with peritoneal metastatic colorectal cancer given systemic therapy: an analysis of individual patient data from prospective randomised trials from the Analysis and Research in Cancers of the Digestive System (ARCAD) database. *Lancet Oncol* 2016;17:1709–19.
10. Sugarbaker PH. Peritoneal carcinomatosis: natural history and rational therapeutic interventions using intraperitoneal chemotherapy. *Cancer Treat Res* 1996;81:149–68.
11. Elias D, Lefevre JH, Chevalier J, Brouquet A, Marchal F, Classe J-M, Ferron G, Guilloit J-M, Meeus P, Goéré D, Bonastre J. Complete cytoreductive surgery plus intraperitoneal chemohyperthermia with oxaliplatin for peritoneal carcinomatosis of colorectal origin. *J Clin Oncol* 2009;27:681–5.
12. Verwaal VJ, van Ruth S, de Bree E, van Sloothen GW, van Tinteren H, Boot H, Zoetmulder FAN. Randomized trial of cytoreduction and hyperthermic intraperitoneal chemotherapy versus systemic chemotherapy and palliative surgery in patients with peritoneal carcinomatosis of colorectal cancer. *J Clin Oncol* 2003;21:3737–43.
13. Chan DYS, Syn NL-X, Yap R, Phua JNS, Soh TIP, Chee CE, Nga ME, Shabbir A, So JBY, Yong WP. Conversion Surgery Post-Intraperitoneal Paclitaxel and Systemic Chemotherapy for Gastric Cancer Carcinomatosis Peritonei. Are We Ready? *J Gastrointest Surg* 2017;21:425–33.
14. Ishigami H, Kitayama J, Kaisaki S, Hidemura A, Kato M, Otani K, Kamei T, Soma D, Miyato H, Yamashita H, Nagawa H. Phase II study of weekly intravenous and intraperitoneal paclitaxel combined with S-1 for advanced gastric cancer with peritoneal metastasis. *Ann Oncol* 2010;21:67–70.
15. Canbay E, Mizumoto A, Ichinose M, Ishibashi H, Sako S, Hirano M, Takao N,

ACCEPTED MANUSCRIPT

Yonemura Y. Outcome data of patients with peritoneal carcinomatosis from gastric origin treated by a strategy of bidirectional chemotherapy prior to cytoreductive surgery and hyperthermic intraperitoneal chemotherapy in a single specialized center in Japan. *Ann Surg Oncol* 2014;21:1147–52.
16. Yonemura Y, Canbay E, Li Y, Coccolini F, Glehen O, Sugarbaker PH, Morris D, Moran B, Gonzaletz-Moreno S, Deraco M, Piso P, Elias D, et al. A comprehensive treatment for peritoneal metastases from gastric cancer with curative intent. *Eur J Surg Oncol* 2016;42:1123–31.
17. Le Brun J-F, Campion L, Berton-Rigaud D, Lorimier G, Marchal F, Ferron G, Oger AS, Dravet F, Jaffre I, Classe J-M. Survival benefit of hyperthermic intraperitoneal chemotherapy for recurrent ovarian cancer: a multi-institutional case control study. *Ann Surg Oncol* 2014;21:3621–7.
18. Van der Speeten K, Stuart OA, Mahteme H, Sugarbaker PH. Pharmacology of perioperative 5-fluorouracil. *J Surg Oncol* 2010;102:730–5.
19. Shimizu T, Sonoda H, Murata S, Takebayashi K, Ohta H, Miyake T, Mekata E, Shiomi H, Naka S, Tani T. Hyperthermic intraperitoneal chemotherapy using a combination of mitomycin C,5-fluorouracil, and oxaliplatin in patients at high risk of colorectal peritoneal metastasis: A Phase I clinical study. *Eur J Surg Oncol* 2014;40:521–8.
20. Ceelen WP, Flessner MF. Intraperitoneal therapy for peritoneal tumors: biophysics and clinical evidence. *Nat Rev Clin Oncol* 2010;7:108–15.
21. Elias D, Antoun S, Goharin A, Otmany AE, Puizillout JM, Lasser P. Research on the best chemohyperthermia technique of treatment of peritoneal carcinomatosis after complete resection. *Int J Surg Investig* 2000;1:431–9.
22. Kusamura S, Dominique E, Baratti D, Younan R, Deraco M. Drugs, carrier solutions and temperature in hyperthermic intraperitoneal chemotherapy. *J Surg Oncol* 2008;98:247–52.
23. Emoto S, Sunami E, Yamaguchi H, Ishihara S, Kitayama J, Watanabe T. Drug

ACCEPTED MANUSCRIPT

development for intraperitoneal chemotherapy against peritoneal carcinomatosis from gastrointestinal cancer. *Surg Today* 2014;44:2209–20.
24. Braam HJ, Schellens JH, Boot H, van Sandick JW, Knibbe CA, Boerma D, van Ramshorst B. Selection of chemotherapy for hyperthermic intraperitoneal use in gastric cancer. *Crit Rev Oncol Hematol* 2015;95:282–96.
25. Julien S, Merino-Trigo A, Lacroix L, Pocard M, Goéré D, Mariani P, Landron S, Bigot L, Nemati F, Dartigues P, Weiswald L-B, Lantuas D, et al. Characterization of a large panel of patient-derived tumor xenografts representing the clinical heterogeneity of human colorectal cancer. *Clin Cancer Res* 2012;18:5314–28.
26. Bloemendaal ALA, Verwaal VJ, van Ruth S, Boot H, Zoetmulder FAN. Conventional surgery and systemic chemotherapy for peritoneal carcinomatosis of colorectal origin: a prospective study. *Eur J Surg Oncol* 2005;31:1145–51.
27. Jacquet P, Averbach A, Stephens AD, Stuart OA, Chang D, Sugarbaker PH. Heated intraoperative intraperitoneal mitomycin C and early postoperative intraperitoneal 5-fluorouracil: pharmacokinetic studies. *Oncology* 1998;55:130–8.
28. Elias D, Matsuhisa T, Sideris L, Liberale G, Drouard-Troalen L, Raynard B, Pocard M, Puizillou JM, Billard V, Bourget P, Ducreux M. Heated intra-operative intraperitoneal oxaliplatin plus irinotecan after complete resection of peritoneal carcinomatosis: pharmacokinetics, tissue distribution and tolerance. *Ann Oncol* 2004;15:1558–65.
29. Elias D, Otmany El A, Bonnay M, Paci A, Ducreux M, Antoun S, Lasser P, Laurent S, Bourget P. Human pharmacokinetic study of heated intraperitoneal oxaliplatin in increasingly hypotonic solutions after complete resection of peritoneal carcinomatosis. *Oncology* 2002;63:346–52.
30. Shimizu A, Mammoto A, Italiano JE, Pravda E, Dudley AC, Ingber DE, Klagsbrun M. ABL2/ARG tyrosine kinase mediates SEMA3F-induced RhoA inactivation and cytoskeleton collapse in human glioma cells. *J Biol Chem* 2008;283:27230–8.
31. Pelz JOW, Vetterlein M, Grimmig T, Kerscher AG, Moll E, Lazariotou M, Matthes N,

Faber M, Germer C-T, Waaga-Gasser AM, Gasser M. Hyperthermic intraperitoneal chemotherapy in patients with peritoneal carcinomatosis: role of heat shock proteins and dissecting effects of hyperthermia. *Ann Surg Oncol* 2013;20:1105–13.

32. Atallah D, Marsaud V, Radanyi C, Kornprobst M, Rouzier R, Elias D, Renoir J-M. Thermal enhancement of oxaliplatin-induced inhibition of cell proliferation and cell cycle progression in human carcinoma cell lines. *Int J Hyperthermia* 2004;20:405–19.

33. Francescutti V, Rivera L, Seshadri M, Kim M, Haslinger M, Camoriano M, Attwood K, Kane JM, Skitzki JJ. The benefit of intraperitoneal chemotherapy for the treatment of colorectal carcinomatosis. *Oncol Rep* 2013;30:35–42.

34. Tang L, Mei L-J, Yang X-J, Huang C-Q, Zhou Y-F, Yonemura Y, Li Y. Cytoreductive surgery plus hyperthermic intraperitoneal chemotherapy improves survival of gastric cancer with peritoneal carcinomatosis: evidence from an experimental study. *J Transl Med* 2011;9:53.

35. Elias D, Bonnay M, Puizillou JM, Antoun S, Demirdjian S, Otmany El A, Pignon JP, Drouard-Troalen L, Ouellet JF, Ducreux M. Heated intra-operative intraperitoneal oxaliplatin after complete resection of peritoneal carcinomatosis: pharmacokinetics and tissue distribution. *Ann Oncol* 2002;13:267–72.

36. Pomel C, Appleyard T-L, Gouy S, Rouzier R, Elias D. The role of laparoscopy to evaluate candidates for complete cytoreduction of peritoneal carcinomatosis and hyperthermic intraperitoneal chemotherapy. *Eur J Surg Oncol* 2005;31:540–3.

37. Jayakrishnan TT, Zacharias AJ, Sharma A, Pappas SG, Gamblin TC, Turaga KK. Role of laparoscopy in patients with peritoneal metastases considered for cytoreductive surgery and hyperthermic intraperitoneal chemotherapy (HIPEC). *World J Surg Oncol* 2014;12:270.

38. Hultman B, Mahteme H, Sundbom M, Ljungman M, Larsson R, Nygren P. Benchmarking of gastric cancer sensitivity to anti-cancer drugs ex vivo as a basis for drug selection in systemic and intraperitoneal therapy. *J Exp Clin Cancer Res* 2014;33:110.

ACCEPTED MANUSCRIPT

39. Cashin PH, Graf W, Nygren P, Mahteme H. Cytoreductive surgery and intraperitoneal chemotherapy for colorectal peritoneal carcinomatosis: prognosis and treatment of recurrences in a cohort study. *Eur J Surg Oncol* 2012;38:509–15.

40. Golse N, Bakrin N, Passot G, Mohamed F, Vaudoyer D, Gilly F-N, Glehen O, Cotte E. Iterative procedures combining cytoreductive surgery with hyperthermic intraperitoneal chemotherapy for peritoneal recurrence: postoperative and long-term results. *J Surg Oncol* 2012;106:197–203.

41. Mogal H, Chouliaras K, Levine EA, Shen P, Votanopoulos KI. Repeat cytoreductive surgery with hyperthermic intraperitoneal chemotherapy: review of indications and outcomes. *J Gastrointest Oncol* 2016;7:129–42.

42. Williams BHM, Alzahrani NA, Chan DL, Chua TC, Morris DL. Repeat cytoreductive surgery (CRS) for recurrent colorectal peritoneal metastases: yes or no? *Eur J Surg Oncol* 2014;40:943–9.

43. Brouquet A, Goéré D, Lefevre JH, Bonnet S, Dumont F, Raynard B, Elias D. The second procedure combining complete cytoreductive surgery and intraperitoneal chemotherapy for isolated peritoneal recurrence: postoperative course and long-term outcome. *Ann Surg Oncol* 2009;16:2744–51.

44. Sugarbaker PH, Cunliffe WJ, Belliveau J, de Bruijn EA, Graves T, Mullins RE, Schlag P. Rationale for integrating early postoperative intraperitoneal chemotherapy into the surgical treatment of gastrointestinal cancer. *Semin Oncol* 1989;16:83–97.

45. Tsubamoto H, Takeuchi S, Ito K, Miyagi Y, Toyoda S, Inoue K, Kanazawa R, Hosoda Y, Shibahara H. Feasibility and efficacy of intraperitoneal docetaxel administration as salvage chemotherapy for malignant gynaecological ascites. *J Obstet Gynaecol* 2015;35:69–73.

46. Fushida S, Kinoshita J, Yagi Y, Funaki H, Kinami S, Ninomiya I, Fujimura T, Nishimura G, Kayahara M, Ohta T. Dual anti-cancer effects of weekly intraperitoneal docetaxel in treatment of advanced gastric cancer patients with peritoneal carcinomatosis: a feasibility and pharmacokinetic study. *Oncol Rep* 2008;19:1305–10.

ACCEPTED MANUSCRIPT

47. Jaaback K, Johnson N, Lawrie TA. Intraperitoneal chemotherapy for the initial management of primary epithelial ovarian cancer. *Cochrane Database Syst Rev* 2016; CD005340.

48. Morgan RJ Jr, Armstrong DK, Alvarez RD, et al. Ovarian Cancer, Version 1.2016, NCCN Clinical Practice Guidelines in Oncology. *J Natl Compr Canc Netw*. 2016;14: 1134-1163.

Figure Legends

Figure 1

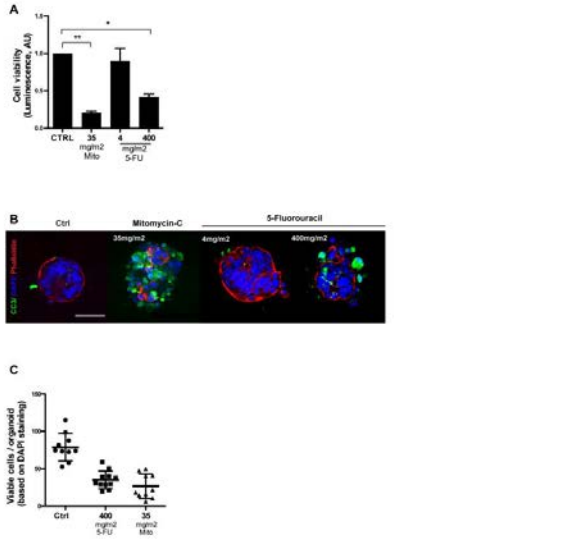

ATP-bioluminescence is a robust and efficient assay to measure the chemosensitivity of CRC organoids.
Drug response of patient-derived CRC organoids after a 72h exposure to 35mg/m2 of Mito (Mitomycin-C), 400 or 4 mg/m2 of 5-FU (5-Fluoruracil). The CRC cell viability in organoids was measured with ATP-LUM **(A)** or immunofluorencence **(B,C)** assays.
(A) The ATP-LUM assay consists in measuring the ATP rate which is proportional to the number of viable cells. The signal is normalized to control condition and organoid number in each well.
(B) For the immunofluorescence assay, we fixed organoids and stained using DAPI (blue), Cleaved-Caspase-3 (green) and Phalloidin (red). Using confocal microscopy, we acquired Z-stacks and displayed one representative median section. Scale bar = 50µm.
(C) The number of dead cells (labelled by cleaved caspase-3) and live cells (positive for DAPI only) per organoid was counted using software assisted annotation, then, the ratio viable cells / total cells was calculated.
For each conditions, data are displayed as the average from n=3 experiments, error bar represent SEM and P-values were calculated using unpaired T-test (**p<0.01, *p<0.05)

Figure 1

ATP-bioluminescence is a robust and efficient assay to measure the chemosensitivity of CRC organoids

Drug response of patient-derived CRC organoids after a 72h exposure to 35mg/m2 of Mito (Mitomycin-C), 400 or 4 mg/m2 of 5-FU (5-Fluoruracil). The CRC cell viability in organoids was measured with ATP-LUM (A) or immunofluorescence (B, C) assays.

(A) The ATP-LUM assay consists in measuring the ATP rate which is proportional to the number of viable cells. The signal is normalized to control condition and organoid number in each well.

(B) For the immunofluorescence assay, we fixed organoids and stained using DAPI (blue), Cleaved-Caspase-3 (green) and Phalloidin (red). Using confocal microscopy, we acquired Z-stacks and displayed one representative median section. Scale bar = 50 μ m.

(C) The number of dead cells (labelled by cleaved caspase-3) and live cells (positive for DAPI only) per organoid was counted using software assisted annotation, then, the ratio viable cells / total cells was calculated.

For each conditions, data are displayed as the average from at least n=3 experiments, error bar represent SEM and P-values were calculated using unpaired T-test (**p<0.01, *p<0.05)

-

Figure 2

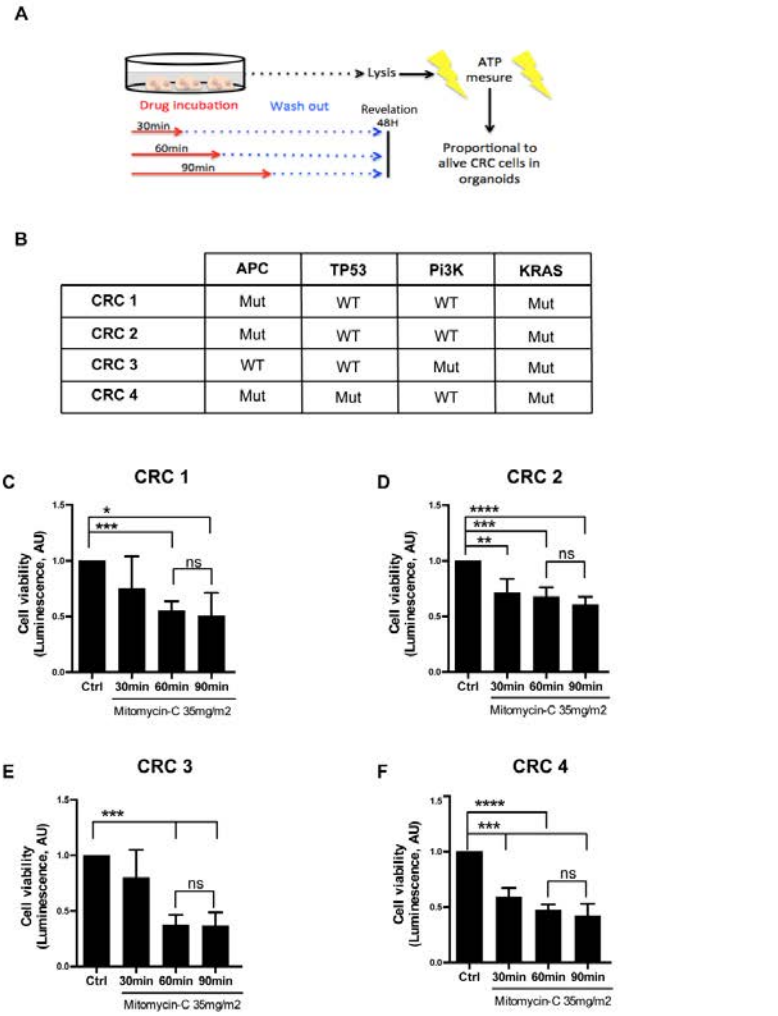

	APC	TP53	Pi3K	KRAS
CRC 1	Mut	WT	WT	Mut
CRC 2	Mut	WT	WT	Mut
CRC 3	WT	WT	Mut	Mut
CRC 4	Mut	Mut	WT	Mut

Kinetic study of contact chemotherapy using IP concentration of Mitomycin-C.
(A) Schematic representation of the experimental strategy: Organoids were incubated with Mitomycin-C at 35mg/m2 during 30, 60 and 90 min. Then, the drug was washed-out and the organoids viability was assessed after 48 hours.
(B) Molecular profiles of the four CRC patient-derived-xenografts used to produce organoids.
(C-F) Cell viability was measured using the ATP-LUM assay for organoids made from CRC1-4. Luminescence signal is normalized to control conditions and organoids number in each well. For each conditions, data are displayed as the average from n=3 experiments, error bar represent SEM and P-values were calculated using unpaired T-test (****p<0.0001, ***p<0.001, **p<0.01, *p<0,05)

Figure 2

Kinetic study of contact chemotherapy using IP concentration of Mitomycin-C

(A) Schematic representation of the experimental strategy: Organoids were incubated with Mitomycin-C at 35mg/m^2 during 30, 60 and 90 min. Then, the drug was washed-out and the organoids viability was assessed after 48 hours.
(B) Molecular profiles of the four CRC patient-derived-xenografts used to produce organoids.
(C-F) Cell viability was measured using the ATP-LUM assay for organoids made from CRC1-4. Luminescence signal is normalized to control conditions and organoids number in each well. For each conditions, data are displayed as the average from at least n=3 experiments, error bar represent SEM and P-values were calculated using unpaired T-test (****p<0.0001, ***p<0.001, **p<0.01, *p<0,05)

Figure 3

A

HIPEC MIXTURE	REFERENCES
Mito 35mg/m2	Prada-Villaverde et al. 2014
5-FU 4mg/m2 + Dox 40mg/m2	Harrison et al. 2008
5-FU 4mg/m2 + Dox 15mg/m2 + Mito 15mg/m2	Sugarbaker et al. 2011
5-FU 4mg/m2 + Ox 300mg/m2 + Iri 200mg/m2	Elias et al. 2004
Ox 460mg/m2	Hompes et al. 2014

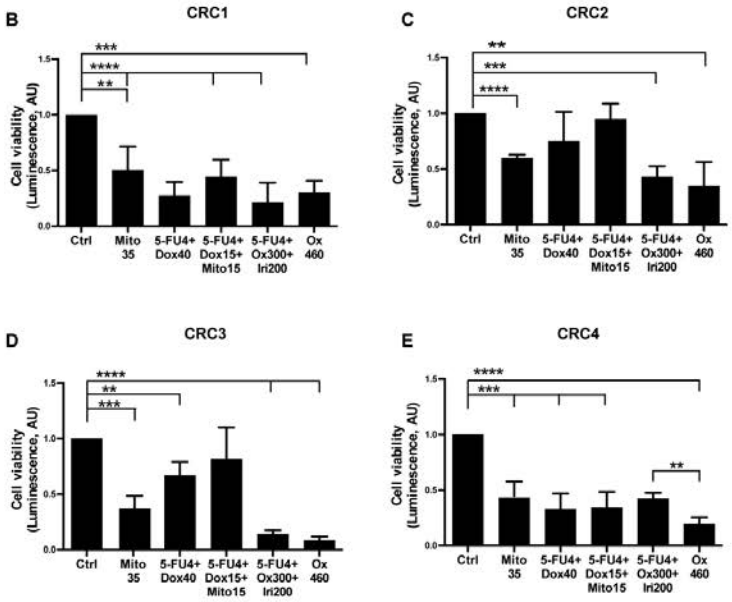

Efficiency of conventionnal cytotoxics used for HIPEC on CRC organoids.
(A) Summary table of cytotoxics concentrations and combinations commonly used during HIPEC with their references in the litterature.
(B-E) Organoids were generated from CRC1-4. CRC cell viability was assessed by ATP-LUM after 90min incubation with cytotoxics (mg/m2, fully described in table A) followed by 48 hours incubation in normal media. The luminescence signal was normalized to control condition and the number of organoids in each well. For each conditions, data are displayed as the average from n=3 experiments, error bar represent SEM and P-values were calculated using unpaired T-test (****p<0.0001, ***p<0.001, **p<0.01).

Figure 3

Efficiency of conventional cytotoxics used for HIPEC on CRC organoids

(A) Summary table of cytotoxics concentrations and combinations commonly used during HIPEC with their references in the literature.

(B-E) Organoids were generated from CRC1-4. CRC cell viability was assessed by ATP-LUM after 90min incubation with cytotoxics (mg/m2, fully described in table A) followed by 48 hours incubation in normal media. The luminescence signal was normalized to control condition and the number of organoids in each well. For each conditions, data are displayed as the average from at least n=3 experiments, error bar represent SEM and P-values were calculated using unpaired T-test (****$p<0.0001$, ***$p<0.001$, **$p<0.01$).

Figure 4

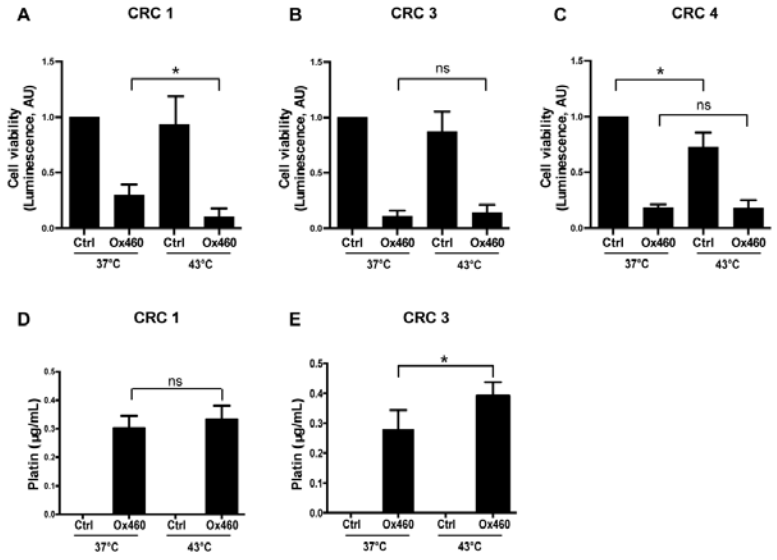

Mimicking HIPEC by increasing temperature during Oxaliplatin incubation does not significantly increase CRC organoids death.
(A-C) Cell viability analysis by ATP-LUM after 90 min incubation at 37°C or 43°C with Oxaliplatin 460mg/m2 on organoids made from CRC1 **(A)**, CRC2 **(B)** and CRC4 **(C)**. The luminescence signal was normalized to control condition and the number of organoids in each well. For each conditions, data are displayed as the average from n=3 experiments, error bar represent SEM and P-values were calculated using unpaired T-test (*p<0,05).
(D-E) Platinum determination in organoids incubated at 37°C and 43°C. Ox : Oxaliplatin (460 mg/m2), Control : untreated. For each conditions, data are displayed as the average from n=4 experiments, error bar represent SEM and P-values were calculated using Mann-Whitney test (*p<0.05).

Figure 4

Mimicking HIPEC by increasing temperature during oxaliplatin incubation does not significantly increase CRC organoids death.

(A-C) Cell viability analysis by ATP-LUM after 90 min incubation at 37°C or 43°C with oxaliplatin 460mg/m2 on organoids made from CRC1 (A), CRC2 (B) and CRC4 (C). The luminescence signal was normalized to control condition and the number of organoids in each well. For each conditions, data are displayed as the average from n=3 experiments, error bar represent SEM and P-values were calculated using unpaired T-test (*p<0,05).

(D-E) Platinum determination in organoids incubated at 37°C and 43°C. Ox : Oxaliplatin (460 mg/m2), Control : untreated. For each conditions, data are displayed as the average from at least n=3 experiments, error bar represent SEM and P-values were calculated using Mann-Whitney test (*p<0.05).

FIGURE 5

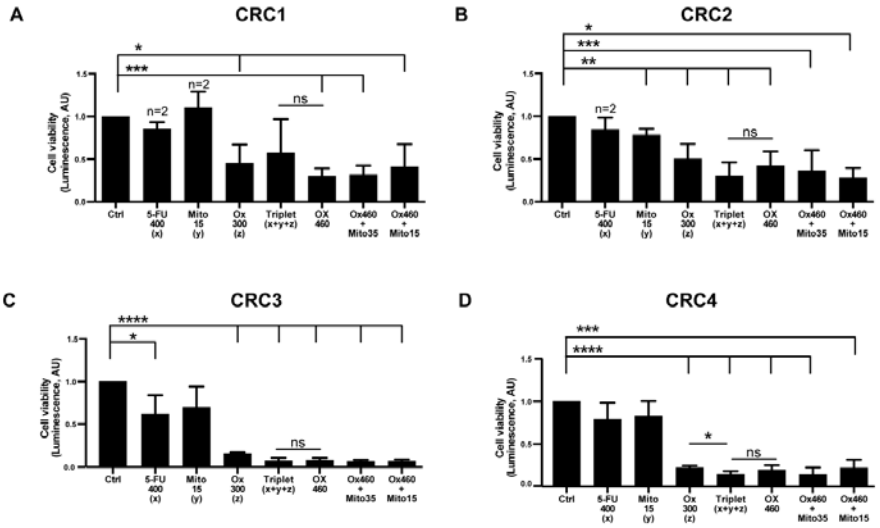

Combining cytotoxics is not more efficient at inducing CRC organoids death than Oxaliplatin 460mg/m2 alone. Organoids made from CRC1 **(A)**, CRC2 **(B)**, CRC3 **(C)** and CRC4 **(D)** were incubated for 90 min with the following drugs, alone or in combination: Ox 300 or 460mg/m2, Mito-C 35 and 15mg/m2, 5-FU 400mg/m2. Cell viability was assessed using ATP-LUM after 48 hours at 37°C. The luminescence signal was normalized to control condition and the number of organoids in each well. For each conditions, data are displayed as the average from n=3 experiments, error bar represent SEM and P-values were calculated using unpaired T-test (****p<0.0001, ***p<0.001, **p<0.01, * p<0.05).

Figure 5

Combining cytotoxics is not more efficient at inducing CRC organoids death than oxaliplatin 460mg/m2 alone

Organoids made from CRC1 (A), CRC2 (B), CRC3 (C) and CRC4 (D) were incubated for 90 min with the following drugs, alone or in combination: Oxali 300 or 460mg/m2, Mito-C 35 and 15mg/m2, 5-FU 400mg/m2. Cell viability was assessed using ATP-LUM after 48 hours at 37°C. The luminescence signal was normalized to control condition and the number of organoids in each well. For each conditions, data are displayed as the average from at least n=3 experiments, error bar represent SEM and P-values were calculated using unpaired T-test (****p<0.0001, ***p<0.001, **p<0.01, * p<0.05).

FIGURE 6

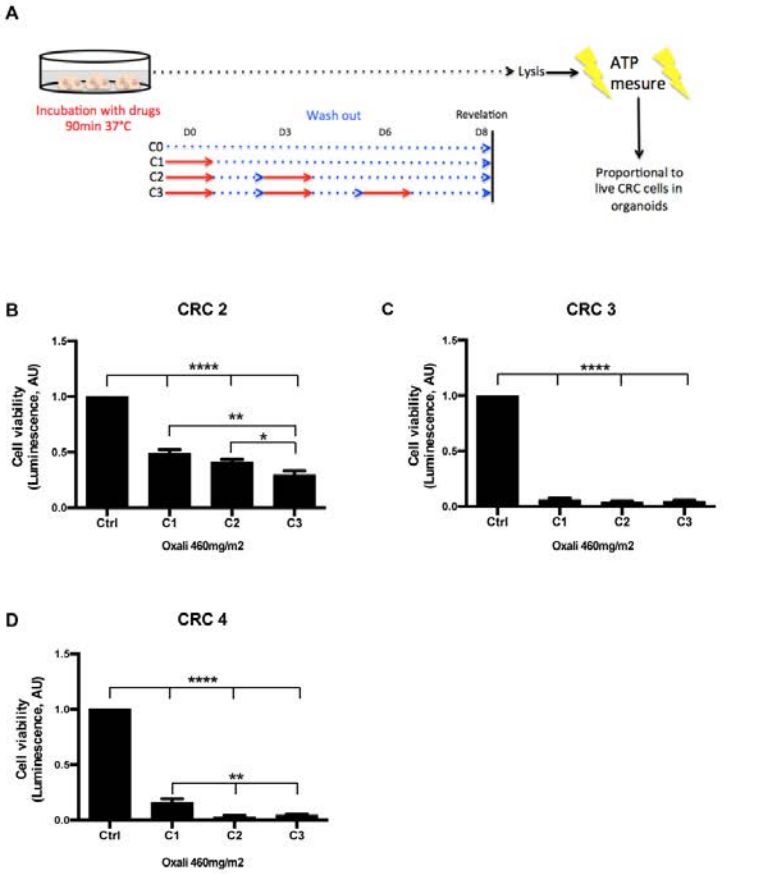

Repeated cycles of Oxaliplatin is the most efficient protocol to reduce CRC organoids viability.
(A) Schematic representation of the experimental strategy for organoids repeated exposure to 460mg/m2 of Oxaliplatin during 90 min at 37°C.
(B-D) the viability of organoids made from CRC2-4 was assessed by ATP-Lum after 8 days in culture (submitted to 1 (C1), 2 (C2) or 3 (C3) cures of Oxaliplatin 460mg/m2. The luminescence signal was normalized to control condition and the number of organoids in each well. For each conditions, data are displayed as the average from n=3 experiments, error bar represent SEM and P-values were calculated using unpaired T-test (****p<0.0001, ***p<0.001, **p<0.01, * p<0.05).

Figure 6

Repeated cycles of oxaliplatin is the most efficient protocol to reduce CRC organoid viability.

(A) Schematic representation of the experimental strategy for organoids repeated exposure to 460mg/m2 of Oxaliplatin during 90 min at 37°C.

(B-D) the viability of organoids made from CRC2-4 was assessed by ATP-Lum after 8 days in culture (submitted to 1 (C1), 2 (C2) or 3 (C3) cures of Oxaliplatin 460mg/m2. The luminescence signal was normalized to control condition and the number of organoids in each well. For each conditions, data are displayed as the average from at least n=3 experiments, error bar represent SEM and P-values were calculated using unpaired T-test (****p<0.0001, ***p<0.001, **p<0.01, * p<0.05).

Tumor spheres with inverted polarity drive the formation of peritoneal metastases in patients with hypermethylated colorectal carcinomas

In the article by Zajac et al. we published the first evidence of collective cancer dissemination maintaining epithelial features and presenting and inverted A/B polarity. Through the collection of primary explants, we showed that the tumor intermediates in poor prognosis CRCs display a robust epithelial organization with the expression of cell-cell junction proteins (such as E-cadherin and ß-catenin) and basolateral markers (such as Scribble, ß1-integrins and EpCam) on internal cell membranes. At the spheres' periphery, we were able to observe the expression of many apical proteins like ezrin, villin, NHERF1 or CD133. This was confirmed by electron microscopy allowing us to confirm this inverted polarity with the presence of microvilli on the outward pole of spheres.

TSIPs are found in CRC patients with histotypes of poor prognosis such as micropapillary, cribriform or mucinous (MUC). These cancers emerge from the serrated carcinogenic pathway. TSIPs arise from the saw-tooth pattern associated with these cancers by a dynamic process that has been named endophytic growth. Groups of tumor cells detach from the serrated lesions towards the lumen, thus generating spheres with an inverted A/B polarity. We also demonstrated that MUC CRC patients display a downregulation in TGFß signaling pathway, both in the canonical and non-canonical pathways, which promotes TSIPs formation in an in vitro model of endophytic growth. TGFß also has an effect on TSIPs polarity. Indeed, in this paper I was able to demonstrate that stimulating TSIPs with TGFβ is sufficient to disrupt their apical-out polarity in 3D collagen-I gels. Using shRNA, I established that this was relying on the TGFβ non-canonical pathway through ParD6 (Figure 6a), which has been described to play a role in contractility through the inhibition of ROCK.

Finally, we could demonstrate that the apical-out topology is maintained throughout the metastatic cascade. Indeed, apical-out TSIPs have been found in primary tumors, peritoneal effusions as well as in distant metastases. By putting TSIPs on top of peritoneum explants from the same patient, we could show that spheres invade the explant without changing their topology.

Furthermore, by injecting PDXs spheres into the peritoneal cavity of mice, we could observe that TSIPs are also able to form metastases and that their inverted topology is conserved.

Altogether, by studying patients' samples of metastatic CRCs, we have identified a new tumoral intermediate which relies on a collective organization with a strong epithelial signature and an inverted /AB polarity.

ARTICLES
https://doi.org/10.1038/s41556-017-0027-6

nature cell biology

Tumour spheres with inverted polarity drive the formation of peritoneal metastases in patients with hypermethylated colorectal carcinomas

Olivier Zajac[1,10], Joel Raingeaud[1], Fotine Libanje[1], Celine Lefebvre[1], Dora Sabino[1], Isabelle Martins[2,3], Pétronille Roy[1], Clara Benatar[1], Charlotte Canet-Jourdan[1], Paula Azorin[1], Mélanie Polrot[4], Patrick Gonin[4], Salima Benbarche[5], Sylvie Souquere[6], Gerard Pierron[6], Damien Nowak[1], Ludovic Bigot[1], Michel Ducreux[7], David Malka[7], Camille Lobry[5], Jean-Yves Scoazec[8], Clarisse Eveno[9], Marc Pocard[9], Jean-Luc Perfettini[2,3], Dominique Elias[7], Peggy Dartigues[8], Diane Goéré[7] and Fanny Jaulin[1*]

Metastases account for 90% of cancer-related deaths; thus, it is vital to understand the biology of tumour dissemination. Here, we collected and monitored >50 patient specimens ex vivo to investigate the cell biology of colorectal cancer (CRC) metastatic spread to the peritoneum. This reveals an unpredicted mode of dissemination. Large clusters of cancer epithelial cells displaying a robust outward apical pole, which we termed tumour spheres with inverted polarity (TSIPs), were observed throughout the process of dissemination. TSIPs form and propagate through the collective apical budding of hypermethylated CRCs downstream of canonical and non-canonical transforming growth factor-β signalling. TSIPs maintain their apical-out topology and use actomyosin contractility to collectively invade three-dimensional extracellular matrices. TSIPs invade paired patient peritoneum explants, initiate metastases in mice xenograft models and correlate with adverse patient prognosis. Thus, despite their epithelial architecture and inverted topology TSIPs seem to drive the metastatic spread of hypermethylated CRCs.

As a critical step in cancer progression, and a challenge to patient treatment, tumour cell dissemination has been the subject of intense investigations. It is commonly assumed that the progression and dissemination of carcinomas are associated with the loss of epithelial architecture and apico–basolateral polarity[1–3] as an epithelial-to-mesenchymal (EMT) programme is activated and undifferentiated single tumour cells escape from the primary tumour[4,5]. To reach secondary sites, these single cells use two distinct mechanisms: a traction-based mesenchymal migration that requires actin-rich protrusions and adhesion to the extracellular matrix (ECM), or a propulsive amoeboid locomotion that relies on the peripheral contractility of the actomyosin cortex to squeeze between ECM fibres[6–8]. Nevertheless, the metastatic dissemination of carcinomas can occur without activation of the EMT programme[9,10], and it has been proposed that collective migration could contribute to cancer spread[6,11,12]. Similar to the collective movements orchestrating embryonic development, leader cells sense and adhere to their environment to exert the dragging forces pulling the rest of the cohort[13,14]. However, the knowledge we have on cancer cell dissemination essentially comes from experimental model systems, in vitro and in animals, and the mechanisms underlying the metastatic spread in patients are under-investigated. The respective contribution of tumour cell collectives and individual cells remains unclear, and whether cancers can use specific strategies to disseminate in the body has never been addressed.

Here, we explored colorectal carcinoma (CRC) dissemination to the peritoneum (peritoneal carcinomatosis). CRCs, the second-leading cause of cancer related-death, evolve through distinct genetic and epigenetic pathways. The majority of CRCs arise through the chromosomal instability pathway, which is initiated by adenomatous polyposis coli (APC) loss of function[15,16]. However, cancers with poor prognosis mainly originate from the CpG island methylator phenotype (CIMP) group of CRCs[17–20]. About 10% of these hypermethylated tumours evolve toward microsatellite instability (MSI-high), whereas most of them remain microsatellite stable (MSS) or display an intermediate phenotype (MSI-low)[21–23]. CIMP cancers develop from serrated polyps and progress toward specific histological subtypes of CRCs with dismal outcome (mucinous (MUC), micropapillary and cribriform)[24,25]. CRCs metastasize to the liver, the lung and the peritoneum, which is a serous membrane lining the abdominal organs[26,27]. Tumour cells reach the peritoneal cavity by full-thickness invasion of the digestive wall or via systemic circulation. They then attach to the peritoneum and invade through the connective tissue, producing dozens of metastatic nodules, which substantially worsen patient outcome[28,29]. To date, the molecular and cellular mechanisms underlying CRC metastatic seeding of the peritoneum are unknown.

In this systematic prospective study, we applied cell biology methods to study live tumour specimens collected from 56 patients with CRC who were undergoing cytoreductive surgery. Our results revealed that collective behaviour predominates in the peritoneal microenvironment, and, unpredictably, cancer cell apico–basolateral polarity is maintained, but inverted, during the metastatic spread.

[1]U-981, Gustave Roussy, Villejuif, France. [2]Université Paris Saclay, Villejuif, France. [3]U-1030, Gustave Roussy, Villejuif, France. [4]Plateforme d'Evaluation Préclinique, AMMICA UMS 3655/ US 23, Gustave Roussy, Villejuif, France. [5]UMR-1170, Gustave Roussy, Villejuif, France. [6]UMR-9196, Gustave Roussy, Villejuif, France. [7]Digestive Cancer Unit, Gustave Roussy, Villejuif, France. [8]Pathology Department, Gustave Roussy, Villejuif, France. [9]UMR-965, Lariboisière Hospital, Paris, France. Present address: [10]Department of Translational Research, Institut Curie, Paris, France. *e-mail: fanny.jaulin@gustaveroussy.fr

Results

Tumour spheres with inverted polarity predominate in peritoneal effusions of patients with CRCs of poor prognosis. To characterize CRC dissemination to the peritoneum, we collected and examined ex vivo peritoneal effusions from 43 patients with CRC with peritoneal metastases who were undergoing cytoreductive surgery. We identified single tumour cells and clusters (defined as aggregates of four or more cells) co-expressing the CRC markers epithelial cell adhesion molecule (EpCam) and cytokeratin 20 (CK20). Both were negative for vimentin (Supplementary Table 1a and Supplementary Fig. 1a). When compared to single cells, tumour cell clusters were the most frequent (68%) and, comprising 257 ± 45 cells on average, the most abundant tumour intermediates (by 66-fold; Supplementary Table 1a). Conventional cytology analyses confirmed the presence of tumour cell clusters, and observation by phase microscopy enabled us to discriminate between irregular and spherical cluster morphologies, segregating in different patients. Tumour spheres, defined by their round shape and smooth edges, represent 88% of all clusters (Supplementary Fig. 1b,c and Supplementary Table 1a).

Strikingly, tumour spheres exhibit a robust epithelial organization. The adherens junction proteins E-cadherin and β-catenin are concentrated at contacts between tumour cells. The basolateral proteins Scribble, β_1 integrin and EpCam are found within the spheres on internal membranes. By contrast, the apical markers ezrin, villin, atypical protein kinase C, sodium–hydrogen exchanger regulatory factor 1 (NHERF1), CD133 (also known as prominin 1) and prominent actin bundles are enriched at the periphery of the spheres (Fig. 1a,c and Supplementary Fig. 1d). This polarized epithelial organization was confirmed using electron microscopy, which revealed the presence of densely packed microvilli covered with glycocalyx at the external surface, together with tight junctions, adherens junctions and desmosomes at zones of cell–cell contacts (Fig. 1b). These experiments, together with staining for zonula occludens 1 and the Golgi apparatus, show that, in contrast to normal epithelial tissues, the spheres display an inverted apico–basolateral polarity, with their apical pole oriented outwards (Fig. 1a and Supplementary Fig. 1e). We named these structures tumour spheres with inverted polarity (TSIPs). Despite their robust epithelial architecture, TSIPs almost exclusively associated with histological subtypes with an adverse prognosis and increased metastases occurrence, including MUC tumours, the second most common form of CRCs[30,31] (Fig. 1d). To evaluate whether TSIPs could act as malignant tumour intermediates, we analysed peritoneal effusions from 13 patients with advanced disease but without peritoneal metastases (Supplementary Table 1b). These samples were all free from TSIPs, demonstrating that TSIPs are specifically associated with peritoneal metastases as expected if they are key intermediates in the process of tumour dissemination (Fig. 1e). Moreover, TSIPs were found in 88% of poor prognosis but only in 45% of good prognosis patients with CRC with peritoneal metastases (ref. [32]) (Fig. 1f). In addition, the number of TSIPs found in effusions correlates with the peritoneal cancer index, an integrated measure of the extent, number and size of the metastatic nodules[33] (Fig. 1g).

Hence, TSIPs are tumour intermediates with a robust epithelial identity and an inverted apico–basolateral polarity that have disseminated to the peritoneal cavity of patients with CRC with poor prognosis.

TSIPs form through the collective apical budding of hypermethylated CRCs. We initially reasoned that TSIPs could originate from the adhesion and/or proliferation of disseminated single mesenchymal cells following a mesenchymal-to-epithelial transition[4]. However, when we analysed the gene expression profiles of MUC CRCs and normal samples from two different data sets (Carte d'identité des tumeurs (CIT) and The Cancer Genome Atlas (TCGA))[17,19] with gene set enrichment analysis (GSEA)[34], we did not detect any activation of an EMT programme in MUC CRCs[35] (Supplementary Fig. 2a,b). As a further test of this hypothesis, we collected and monitored single cells from peritoneal effusions. To avoid selecting for epithelial states ($EpCam^+$), we also used total single-cell fractions or only depleted for CD45-positive haematopoietic cells. The single tumour cells did not proliferate or aggregate to form multicellular structures over a period of 9 days, whether they were grown in suspension or in ECM (Matrigel and collagen-I; Fig. 2a,b). Instead, these cells tended to rapidly die in isolation, whereas tumour cells remained viable and proliferated within collectives, so that 67.5 ± 7.5% of TSIPs were alive after 9 days (Fig. 2c). When TSIPs were dissociated using trypsin, the resulting single cells died almost as rapidly as the single-cell fractions (Fig. 2c), suggesting that cell–cell interactions provide important survival signals. Using the mucus-secreting line LS174T[36] and patient-derived xenografts (PDX#1 and PDX#2)[37], we confirmed that MUC CRC single cells died, even in the presence of collagen-I or laminin-rich matrices (Fig. 2d–f). Supplementing Matrigel with Y27632 as previously described[38], allowed single cells from PDX#1 (11 ± 5%) and PDX#2 (6 ± 4%) to subsist, proliferate and generate small colonies, which did not display TSIP features (Fig. 2f). The survival of single cells in suspension could be prolonged by promoting the aggregation of LS174T single cells (Fig. 2g). This depended on E-cadherin engagement, as shown by the effect of function-blocking antibodies and a calcium-chelating agent (Fig. 2h). Together, these results show that MUC CRC single cells are both short-lived and unable to form TSIPs, neither in suspension nor in ECM matrices.

We then investigated whether TSIPs could form in primary tumours. Histological sections of TSIP-producing CRC specimens revealed densely organized tumour cell clusters outlined by villin or ezrin immunostaining, demonstrating that TSIPs exist in primary tumours of patients, as well as in lymph nodes and peritoneal metastases (Fig. 3a,b and Supplementary Fig. 3a–c). We investigated whether core polarity proteins could participate in TSIP formation by altering the apico–basolateral polarity of tumour cell groups. However, silencing the polarity proteins ParD3, Scribble or Llgl2 in small clusters of LS174T cells embedded in three-dimensional (3D) matrices did not promote polarity inversion and TSIP formation (Fig. 3c and Supplementary Fig. 4a,b).

How then do TSIPs form and propagate? To identify the cellular and molecular events associated with TSIP-based dissemination, we compared the transcriptomic profiles of TSIP-producing (MUC) and non-producing (Lieberkuhnian (LBK)) CRCs. Using two independent data sets, we noted that virtually 100% of MUC CRCs associate with CIMP cancers, rather than chromosome instable cancers (CIN), and express the serrated gene signature[17,18,39] (Fig. 3d,e). The serrated precursor lesions harbour serial bulges that protrude apically into the lumen of the neoplastic glands[25] (ii in Fig. 3f, red arrows). Ezrin immunostaining of serrated precursors and MUC primary tumours suggested that TSIPs could be generated by budding as the serrated lesions progress toward MUC CRCs (iii in Fig. 3f and iii in Supplementary Fig. 3b). To test this hypothesis, we grew several cell lines in culture. Only the mucus-secreting LS174T cell line was found to bud. Over 7–8 days, LS174T cultures liberated in suspension 267 ± 25 TSIPs that displayed an inverted apico–basolateral polarity (Fig. 3g,h). Strikingly, time-lapse imaging revealed that immobilized patient TSIPs themselves bud. These buds formed and grew over a period of ~3 days, leading to scission events that liberated new independent and viable TSIPs (Fig. 3i and Supplementary Video 1).

These experiments support the idea that CIMP MUC CRCs possess an intrinsic and specific mode of propagation through the generation of TSIPs by a morphogenetic event that we named collective apical budding (Supplementary Fig. 7c). Through this process,

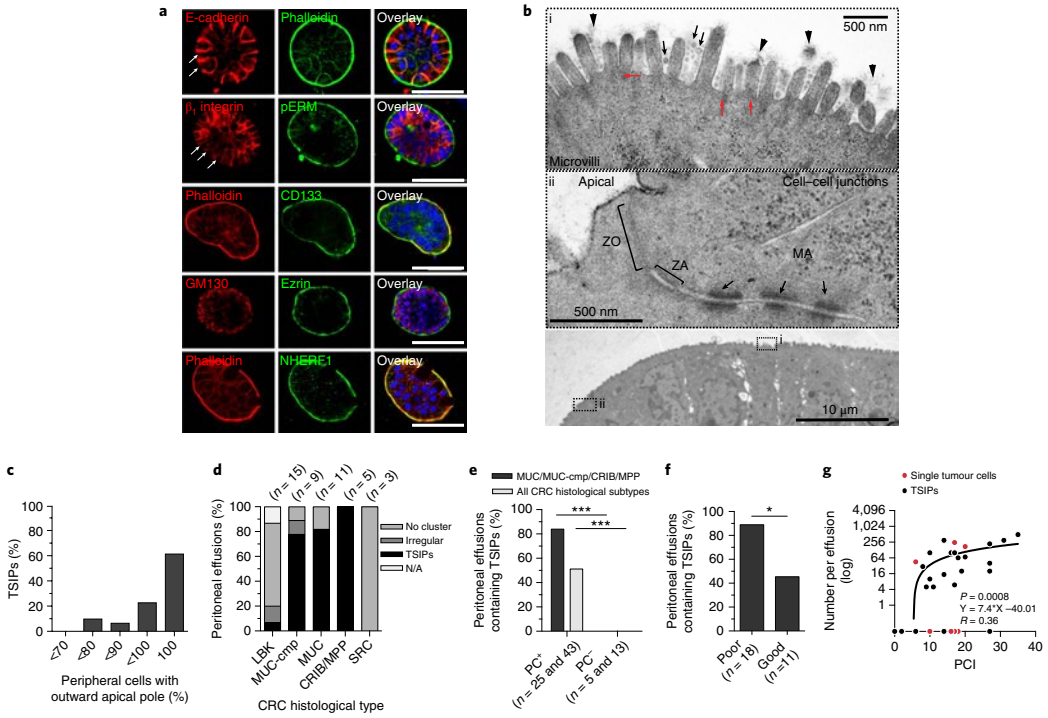

Fig. 1 | TSIPs predominate in peritoneal effusions of patients with CRCs of poor prognosis. a, TSIPs collected from patients' peritoneal effusions were immunostained for E-cadherin, β1 integrin, ezrin, pERM (phospho-ezrin-radixin-moesin), CD133, NHERF1, GM130, phalloidin and DAPI (one median section of a confocal Z-stack is displayed). Arrows point to the absence of basolateral markers at the apical membrane. Representative images are from three (pERM, CD133, NHERF1, GM130 and DAPI) or seven (ezrin and phalloidin) independent patient samples. Scale bars, 50 μm. **b**, Electron microscopic micrographs of TSIPs: region (i) shows the peripheral membrane of outer cells decorated with microvilli containing actin-containing core rootlets (red arrows), glycocalyceal bodies (black arrows) and glycocalyx coating (arrowheads), ultrastructural markers of intestinal cells. Region (ii) points to the tripartite junctional complex between adjacent peripheral cells of the TSIP. Similar structures were observed from 10 TSIPs from 2 independent patients. MA, macula adherens (desmosomes); ZA, zonula adherens; ZO, zonula occludens. **c**, Quantification of polarity inversion on TSIPs from peritoneal effusions. The graph shows the distribution of the TSIPs depending on the percentage of peripheral cells with outward apical ezrin relative to the total peripheral cell number in one confocal Z-section (30 TSIPs from 6 patients). **d**, Frequency of tumour cell clusters (TSIPs or irregular) stratified by CRC histological subtypes (LBK, MUC, MUC-component (cmp), cribriform/micropapillary (CRIB/MPP) and signet ring cell (SRC)). **e**, Correlation between TSIPs and patient metastatic status (PC^+, patient with peritoneal carcinomatosis; PC^-, patient without peritoneal carcinomatosis) considering all CRCs or only the indicated subtypes (two-sided Fisher's exact test, $^{***}P = 0.0009$ and 0.0007, respectively). **f**, Correlation between the frequency (%) of TSIP-positive peritoneal effusions and patient outcome after cytoreductive surgery and hyperthermic intraperitoneal chemotherapy treatment (MUC, CRIB and MPP CRC subtypes; two-sided Fisher's exact test, $^{*}P = 0.03$). **g**, Linear regression of the number of TSIPs ($n = 28$) or single tumour cells ($n = 11$) for each patient, in a log scale, plotted against the peritoneal cancer index (>1,000 TSIPs from patients 8 and 12 were excluded). $P = 0.0008$ indicates the correlation between the peritoneal cancer index (PCI) and the number of TSIPs in the 95% confidence interval. Y represents the equation of the curve. In all graphs, *n* represents the number of patients.

tumour cell collectives detach from the primary tumour, reverting the topology of their apico–basolateral polarity. TSIPs initially accumulate in the lumen of MUC CRC glands (i in Supplementary Fig. 3b). As the cancer progresses, active budding and increased mucus secretion breach the neoplastic epithelial monolayers, with the glandular architecture being progressively lost to the benefit of TSIPs (Fig. 3a,b and iii in Supplementary Fig. 3b).

Canonical and non-canonical transforming growth factor-β signalling regulate TSIP production by collective apical budding. To identify the molecular mechanisms underlying TSIP formation by collective apical budding, we analysed the pathways that were differentially regulated in TSIP-producing tumours using GSEA. The analysis revealed that transforming growth factor-β (TGF-β) signalling was downregulated in MUC CRCs (Fig. 4a). This correlates with the elevated frequency of somatic mutations in genes encoding TGF-β receptors in these tumours (Fig. 4b). To test the influence of TGF-β on TSIP production in LS174T cultures, we first verified that, as previously described[40], transcriptomic slippages correct part of the frameshift mutations in the genes encoding the TGF-β receptors, giving rise to low but functional signalling (detected by increased Smad2 phosphorylation upon TGF-β stimulation; Fig. 4c). TGF-β treatment reduced TSIP-LS174T production by 6.3 ± 0.05 fold (whereas Noggin had no effect; Fig. 4d). Conversely, inhibition

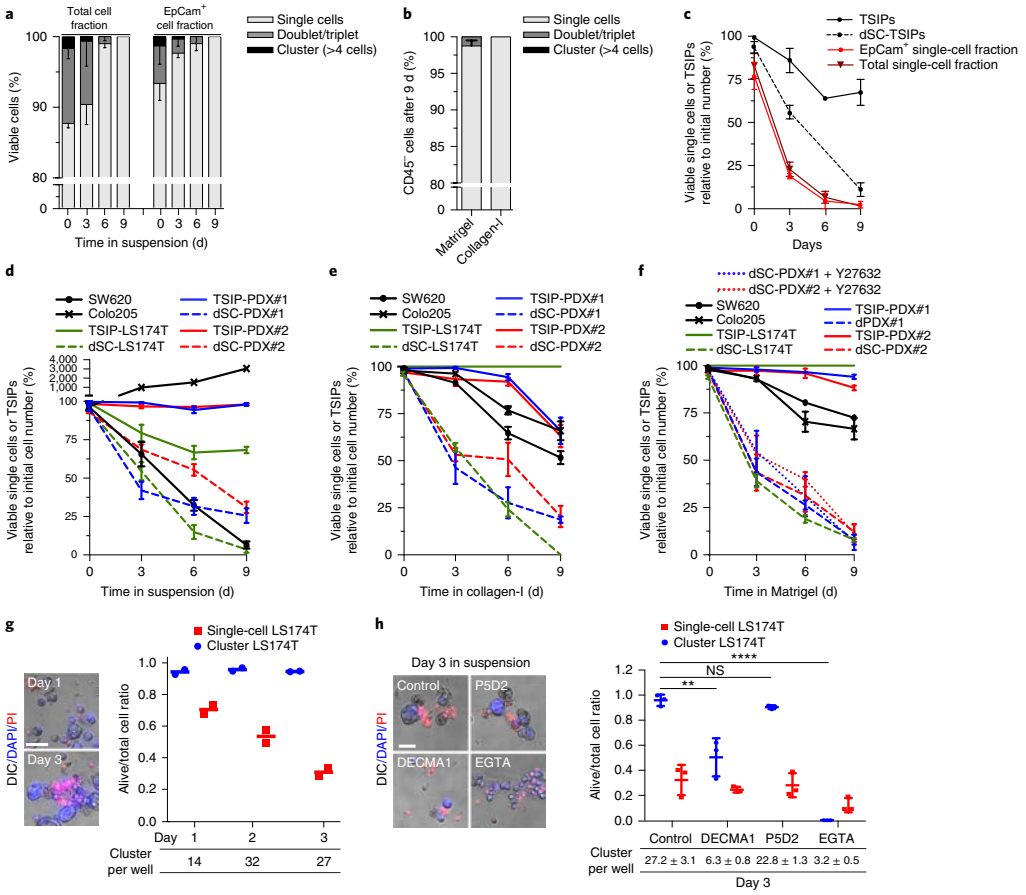

Fig. 2 | MUC CRC cell survival is sustained by cell–cell interactions. a, Total single-cell fractions and EpCam-positive (EpCam$^+$)-enriched single-cell fractions from peritoneal effusions were isolated from $n=3$ independent patients. Viable single cells, doublets plus triplets, and clusters found in suspension were quantified for up to 9 d. **b**, The CD45-negative (CD45$^-$) single-cell fractions from peritoneal effusions were isolated from $n=3$ independent patients and embedded in collagen-I or Matrigel. After 9 d, single cells, doublets plus triplets, and clusters were quantified after CK20 and vimentin staining. **c**, Line graph representing the percentage of viable TSIPs or single cells (total fraction, EpCam$^+$ or obtained by the trypsinization of TSIPs) over 9 d quantified by DIC and trypan blue. The results are from $n=3$ independent patients and expressed as a percentage relative to the initial cell or TSIP numbers. **d**–**f**, Line graphs showing the percentage of viable cells or TSIPs relative to the initial number. The adherent cell line SW620 and the non-adherent Colo205 were used as controls. Controls, dSCs and TSIPs were seeded (100–250 spheres/cells per ml) in suspension (**d**), in collagen-I (**e**) or in Matrigel (**f**), with or without Y27632 and cultivated for 9 d. Data from $n=3$ independent experiments. **g**, Graph showing the ratio between living and total cells in clusters and unclustered single cells after promoting the aggregation of LS174T dSCs from two independent experiments (the average number of clusters per well is indicated for each day). PI was used to highlight dead cells. Representative pictures of LS174T cluster formation and viability corresponding to the quantification are shown (DAPI in blue; PI in red). **h**, Graph representing the ratio between living and total LS174T cells in clusters and unclustered single cells in medium, DECMA1 (an E-cadherin function-blocking antibody, 12 μg ml^{-1}), P5D2 antibody (a β_1 integrin function-blocking antibody, 1 μg ml^{-1}) or EGTA (4 mM). Representative images of cluster formation and viability are shown. *P* values were calculated from $n=3$ independent experiments using unpaired two-sided *t*-test (****$P<0.0001$, **$P=0.0078$, not significant (NS) $P=0.128$). All graphs represent mean ± s.e.m. Scale bars in **g** and **h**, 50 μm.

of TGF-β receptor type 1 (TGF-βR1) by SB431542 or short interfering RNA (siRNA), increased TSIP-LS174T production by 3.9 ± 0.4 and 2 ± 0.13 fold, respectively (Fig. 4d and Supplementary Fig. 4c), without altering cell proliferation (Supplementary Fig. 4d). To investigate the contribution of downstream players, we depleted receptor-activated Smad (R-Smad) proteins. Silencing Smad2, but not Smad3 or Smad4, mimicked TGF-βR1 depletion, increasing TSIP-LS174T formation by 3 ± 0.4 fold (Fig. 4e and Supplementary Fig. 4e). This probably reflects specific features of Smad2 among R-Smads[41]. Furthermore, silencing the non-canonical effector

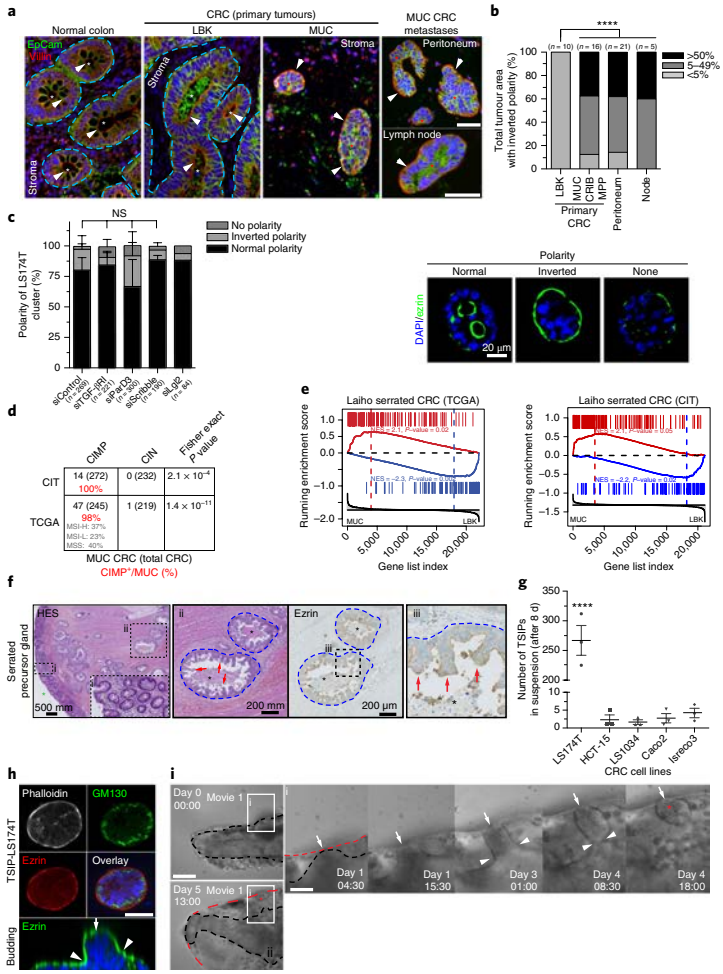

Fig. 3 | TSIPs form by collective apical budding from serrated/hypermethylated CRCs. a,**b**, Histological sections of a normal colon, primary tumours and metastases stained for EpCam and villin. The number of samples analysed is indicated in **b**. Arrowheads indicate the apical poles; white asterisks indicate the luminal cavities and red asterisks indicate TSIPs (**a**). The percentage of tumour area with inverted polarity (**b**). Two-sided Fisher's exact test in comparison with LBK (****$P<0.0001$). **c**, Apico–basolateral polarity of LS174T clusters grown in collagen-I, based on ezrin staining. Data shown as mean ± s.e.m. from $n=3$ independent experiments (except siLgl2, $n=2$). Two-sided unpaired *t*-test (NS, $P>0.05$). **d**, Distribution of MUC CRC samples from TCGA and CIT in the CIMP and CIN tumour groups according to gene expression classification as previously described[16]. The one-sided Fisher's exact test compares the distribution of MUC CRC in the CIMP and CIN phenotypes to the rest of the samples. The percentage represents the proportion of MUC CRC with a CIMP signature. MSI-H, microsatellite instable high; MSI-L, microsatellite instable low; MSS, microsatellite stable. **e**, GSEA of the Laiho gene sets[39] in the MUC versus LBK CRCs from TCGA and CIT data sets ($n_{MUC/CIT}=15$, $n_{LBK/CIT}=188$, $n_{MUC/TCGA}=61$, $n_{LBK/TCGA}=389$). Laiho_up (red) and Laiho_down (blue) gene sets are from the C2 collection of MSigDB. The reference list of genes was sorted using the significance of the test comparing gene expression in MUC and LBK samples. NES, normalized enrichment score. Red and blue dashed lines indicate the leading edge. **f**, Histological sections of serrated precursor lesions (representative of three independent patients) stained using haematoxylin–eosin–saffron and anti-ezrin. The boxed regions show (i) normal glands and (ii and iii) serrated glands. Asterisks indicate the lumen (green, intestine; black, glands); the blue dashed lines indicate the basal pole of the neoplasic gland; and red arrows indicate budding towards the lumen. **g**, Quantification of TSIPs released in suspension by 2D culture of CRC cell lines over $n=3$ independent experiments. Data are shown as mean ± s.e.m. ****$P<0.0001$ calculated by one-way ANOVA test. **h**, Images of LS174T representative of three independent experiments. Bottom panel, orthogonal view of an adherent cell; the arrow points to the budding region and the arrowheads to the neck region. Top panel, TSIP-LS174T in suspension. **i**, DIC sequences of patient's TSIP. Black dashed lines indicate the TSIP periphery; the red dashed lines indicate the mucus front. Time is shown in hours:minutes. The boxed region i is shown at high magnification on the right panel.Arrows points to the budding region, arrowheads to the fission region and the red asterisk indicates the newly formed TSIP (representative of two independent recordings). Scale bars in **a**, **h** and **i**, 50 µm.

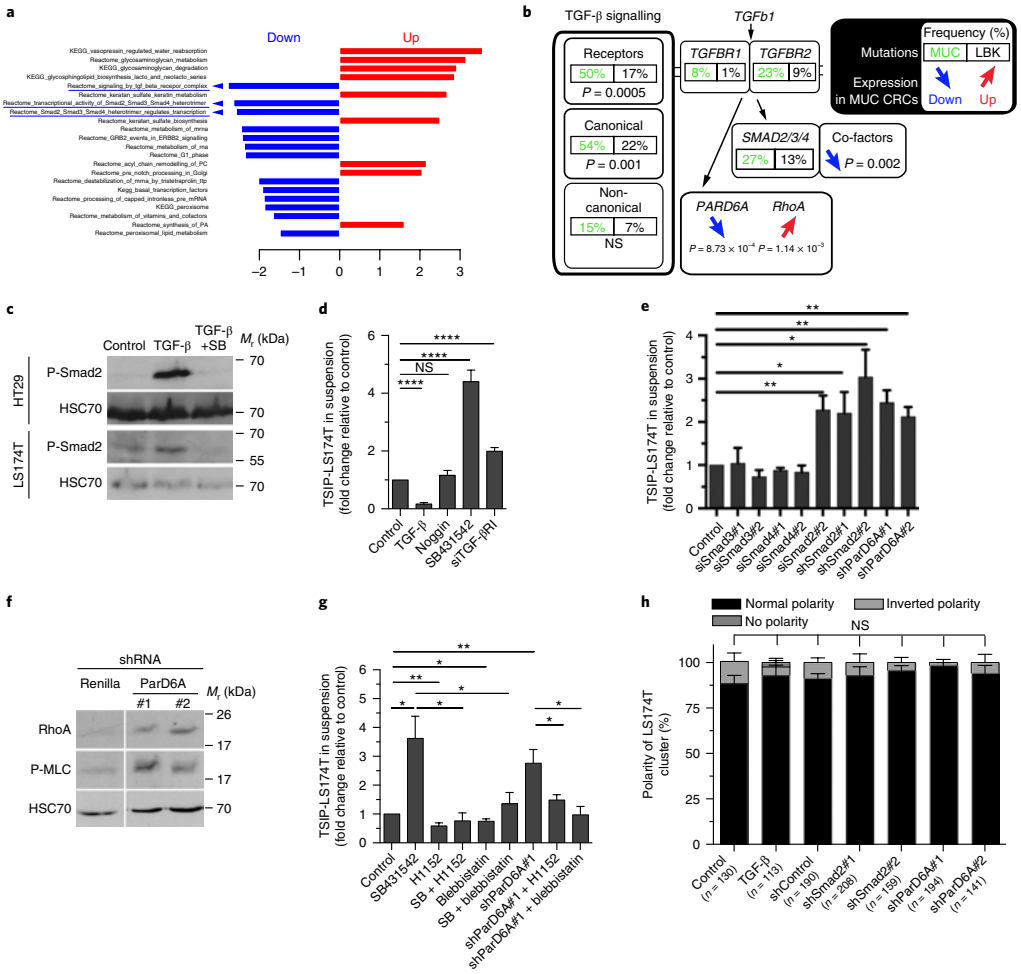

Fig. 4 | Decreased canonical and non-canonical TGF-β signalling promotes TSIP formation by collective apical budding. a, Significantly enriched pathways in MUC versus LBK samples in the CIT and TCGA data sets ($n_{MUC/CIT}=15$, $n_{LBK/CIT}=188$, $n_{MUC/TCGA}=61$, $n_{LBK/TCGA}=389$). Enrichment was computed with GSEA (FDR < 0.2). Blue and red horizontal bars show the normalized enrichment score (NES) of the pathway in the CIT data set. See also Supplementary Table 1. **b**, Data extracted from the TCGA data set[9] (Supplementary Table 2). The frequency of mutations in MUC (left box, $n_{MUC/TCGA}=26$ samples) and LBK (right box, $n_{LBK/TCGA}=174$ samples) for each gene or group of genes (left panel). The one-sided Fisher's exact test for the difference in the frequency in the two histologies is given if $P<0.05$ (NS, $P=0.136$). Individual genes significantly contributing to the differential expression or mutation in the group of genes (right panel). The blue and red arrows indicate a significant differential expression (GSEA for a set of genes and limma voom for individual genes). **c**, Immunoblot analysis of Smad2 phosphorylation (P-Smad2) in HT29 and LS174T cell lines, untreated or treated for 1 h with SB431542 (SB; 10 μM) and/or TGF-β (10 ng ml^{-1}), repeated in three biologically independent experiments. HSC70 was used as a loading control. **d**,**e**,**g**, TSIPs produced by LS174T cultures normalized to control conditions (untreated, control siRNA (non-targeting) or shRNA (Renilla)). The number of independent experiments (sample size, *n*) are as follows: for **d**, control ($n=7$), TGF-β ($n=6$, $P_{TT}<0.0001$), Noggin ($n=3$, $P_{TT}=0.25$) SB431542 ($n=7$, $P_{TT}<0.0001$) and siTGF-βR1 ($n=5$, $P_{TT}<0.0001$). For **e**: control ($n=6$), siSmad3#1 ($n=5$, $P_{TT}=0.001$), siSmad3#2 ($n=6$, $P_{TT}=0.02$),siSmad4#1 ($n=6$, $P_{TT}=0.44$),siSmad4#2 ($n=6$, $P_{TT}=0.08$), siSmad2#2 ($n=6$, $P_{TT}=0.007$), shSmad2#1 ($n=5$, $P_{TT}=0.0388$), shSmad2#2 ($n=6$, $P_{TT}=0.0174$), shParD6A#1 ($n=6$, $P_{TT}=0.0014$) and shParD6A#2 ($n=5$, $P_{TT}=0.001$). For **g**: control ($n=4$), SB431542 (SB; $n=4$, $P_{TT}=0.0137$), H1152 ($n=8$, $P_{TT}=0.002$), SB + H1152 ($n=4$, $P_{TT}=0.0124$), blebbistatin ($n=6$, $P_{TT}=0.01$), SB + blebbistatin ($n=4$, $P_{TT}=0.0382$), shParD6A#1 ($n=4$, $P_{TT}=0.003$), shParD6A#1 + H1152 ($n=4$, $P_{TT}=0.048$), shParD6A#1 + blebbistatin ($n=4$, $P_{TT}=0.0191$). **f**, Immunoblot analysis of the LS174T cell line infected with lentiviruses encoding shRNA against Renilla or ParD6A using RhoA and phospho-T18/S19-MLC antibodies, representative from three biologically independent experiments. HSC70 was used as a loading control. The white line indicates where bands from two parts of the gel were spliced together. **h**, Polarity of LS174T clusters, control or transfection by the mentioned shRNAs (see Fig. 3a for phenotypes). All graphs represent mean ± s.e.m. *P* values in **d**, **e**, **g** and **h** were calculated using two-sided unpaired *t*-test (****$P<0.0001$, ***$P<0.001$, **$P<0.01$, *$P<0.05$, NS $P>0.05$).

ParD6A augmented TSIP-LS174T production by up to 2.4 ± 0.3 fold and increased the levels of RhoA and the phosphorylation of myosin-II (Fig. 4e,f and Supplementary Fig. 4f). Furthermore, inhibition of Rho-associated protein kinase (ROCK) and myosin-II using pharmacological inhibitors, decreased TSIP-LS174T production in control and short hairpin ParD6A (shParD6A)-treated cells (Fig. 4g). By contrast, interfering with the TGF-β pathway did not promote the reversion of polarity in small clusters of LS174T embedded in the ECM (Fig. 4h), and silencing Scribble, Llgl2 or ParD3 did not contribute to TSIP production by LS174T budding (Supplementary Fig. 4g).

Thus, these results show that the progression from serrated/CIMP precursor lesions to MUC CRCs is associated with low canonical and non-canonical TGF-β signalling, both of which participate in TSIP formation by collective apical budding.

TSIPs collectively invade in their apical-out topology. As TSIPs are present all along the path of cancer dissemination and because single cells are unable to survive in isolation and generate TSIPs, we reasoned that TSIPs may spread via a collective mode of invasion[14]. To test this hypothesis, we collected fragments of peritoneum from a non-metastatic region during surgery and incubated them ex vivo with paired patient's TSIPs. After 3 days, we stained the tissues for CK20 and ezrin, revealing that, in 77 ± 19% of cases, TSIPs collectively invaded peritoneal explants. We could not detect any instance of single-cell invasion (Fig. 5a,b). To further validate these findings, we embedded patient TSIPs into collagen-I matrices and monitored their behaviours. In all cases, and in line with our previous results (Fig. 2), the single cells that were released through TSIP spontaneous dissociation (5% of cases), or from TSIP delamination, died and stained positive for cleaved caspase-3 (arrowheads in Fig. 5c and Fig. 5d,e). This absence of mesenchymal cell invasion contrasts with the bona fide EMT observed in irregular clusters that were isolated from peritoneal effusions (Supplementary Fig. 2c). Strikingly, most TSIPs maintain their outward apical pole in contact with the ECM, yet, collectively invade into the 3D gel (Fig. 5c,f,g). We confirmed these results using TSIPs generated from PDX#1 and PDX#2 (Supplementary Fig. 5a,b). Like patient TSIPs, TSIP-PDX#1 and TSIP-PDX#2 both maintain their outward apical pole and migrate through collagen-I gel with an average centroid displacement of 47.6 ± 3.7 µm and 15.5 ± 1.6 µm over 6 days, respectively (Fig. 5d,g–i, Supplementary Fig. 5c and Supplementary Video 2).

Thus, TSIPs undergo collective invasion in their apical-out topology. They seem to migrate slower than most cancer cell lines[42]. However, their speed is in the order of magnitude of collective invasion rates measured in vivo and the scale of cancer progression in patients[43,44].

TSIP collective invasion is driven by the peripheral apical actomyosin contractility. Then, we wanted to decipher the molecular mechanism underlying the collective invasion of TSIPs. We first examined whether the TGF-β pathway, which controls TSIP formation, could also contribute to the apico–basolateral polarity orientation of TSIPs in the ECM. Stimulating TSIPs with TGF-β strongly reduced the number of TSIPs with inverted polarity to 13.3 ± 3.7%. This could partially be rescued by the expression of shParD6A, but not shSmad2 (Fig. 6a,b). Treating TSIPs with the ROCK inhibitor Y27632 completely abolished TSIP polarity inversion, and blebbistatin reduced it to 32.7 ± 16.5%, confirming that non-canonical TGF-β signalling is essential to maintain the outward apical pole of TSIPs in the ECM (Fig. 6a,b). Next, to identify the molecular machinery driving TSIP invasion, we inhibited the proteins known to control collective migration, such as focal adhesion kinase (FAK), Rac1 or integrins, and analysed TSIP-PDX#1 displacement and invasion speed over 6 days. None of the treatments affected TSIP-PDX#1 movement, which is consistent with these basolateral proteins being segregated away from collagen-I and the absence of protrusion detected by video microscopy (Fig. 6c, Supplementary Fig. 5c,d and Supplementary Video 2). To address the contribution of apical proteins to TSIP invasion, we incubated TSIPs in Matrigel. This induced a long-lasting inhibition of apical membrane polarization, but preserved the peripheral actomyosin cortex[45] (Fig. 6a,b). In these conditions, TSIP-PDX#1 invaded even more efficiently, with an average displacement of 79 ± 7.2 µm (Fig. 6d and Supplementary Fig. 5e). We then hypothesized that the increased actomyosin contractility generated by low non-canonical TGF-β signalling could mediate the force-generation propelling TSIPs in 3D environments, similar to the mechanism reported for single cells undergoing amoeboid migration[8]. In line with this hypothesis, immunostaining revealed that myosin-II was phosphorylated at the peripheral apical cortex of TSIPs (Supplementary Fig. 5f). Moreover, inhibiting ROCK and myosin-II significantly reduced TSIP-PDX#1 average displacement from 49.9 ± 3.6 µm to 29.7 ± 2.5 µm and 22.4 ± 1.5 µm, respectively (Fig. 6d and Supplementary Fig. 5e). Inhibiting myosin-II activity had a greater effect than Y27632 on TSIP migration but not on apico–basolateral polarization (Fig. 6a,b). This confirmed that, at the apical pole of TSIPs, the contractility of the actomyosin cortex, and not the membranous proteins, has a prevalent role in migration.

Thus, TSIPs invade tissues using a unique mode of collective invasion that does not involve the formation of adhesion-based protrusions. Rather, it relies on the high contractility of the apical peripheral actomyosin cortex resulting from decreased non-canonical TGF-β signalling.

TSIPs are efficient initiators of metastases. To assess whether TSIPs possess tumour-initiating properties, we used mice xenograft models. We injected TSIPs (TSIP-PDX#1 and TSIP-PDX#2) expressing the luciferase reporter gene into the peritoneal cavity of immunodeficient mice. As a control measure, we injected the equivalent number of single cells. Bioluminescence monitoring demonstrated that TSIP-PDX#1 and TSIP-PDX#2 efficiently seed peritoneal metastases (TSIP-PDX#1 was 60-times more efficient than TSIP-PDX#2 at colonizing the peritoneum (Fig. 7a,b) and also gave rise to abundant ascites). By contrast, by 40 days, the tumour burden was 20-fold lower or absent in mice injected with their single-cell counterparts, respectively (Fig. 7a,b). The presence of metastases was confirmed when mice were killed and measured using a modified peritoneal cancer index assessment[33] (Supplementary Fig. 6a). In the ascites, TSIP-PDX#1 propagated surrounded by mostly apoptotic caspase-3-positive single tumour cells (Fig. 7d and Supplementary Fig. 6b,c). Staining using haematoxylin–eosin–saffron or an antibody against human major histocompatibility complex (MHC) class I demonstrated the presence of MUC secondary tumours that had deeply invaded the peritoneum, penetrating several organs (the liver, the bladder and the intestine; Fig. 7d, top panels). We investigated the architecture of metastases initiated by TSIPs. They were almost exclusively composed of cohesive epithelial EpCam-positive/vimentin-negative tumour cell masses (Fig. 7c–f and Supplementary Fig. 6d). In mice injected with TSIP-PDX#1 and TSIP-PDX#2, 1% and 3% of tumour cells, respectively, were visible as individuals, among which only cells from TSIP-PDX#2 expressed vimentin, alone or in combination with EpCam (Fig. 7e,f and Supplementary Fig. 6d). Finally, staining for ezrin and Scribble proved that tumour cell groups all displayed an inverted apico–basolateral polarity, as we observed in patients with MUC CRC (Fig. 7d, bottom panels, compared with Fig. 3a and Supplementary Fig. 3c).

Together, these data demonstrate that TSIPs are efficient initiators of peritoneal metastases and that EMT and MUC CRC single tumour cells do not make a significant contribution to this process.

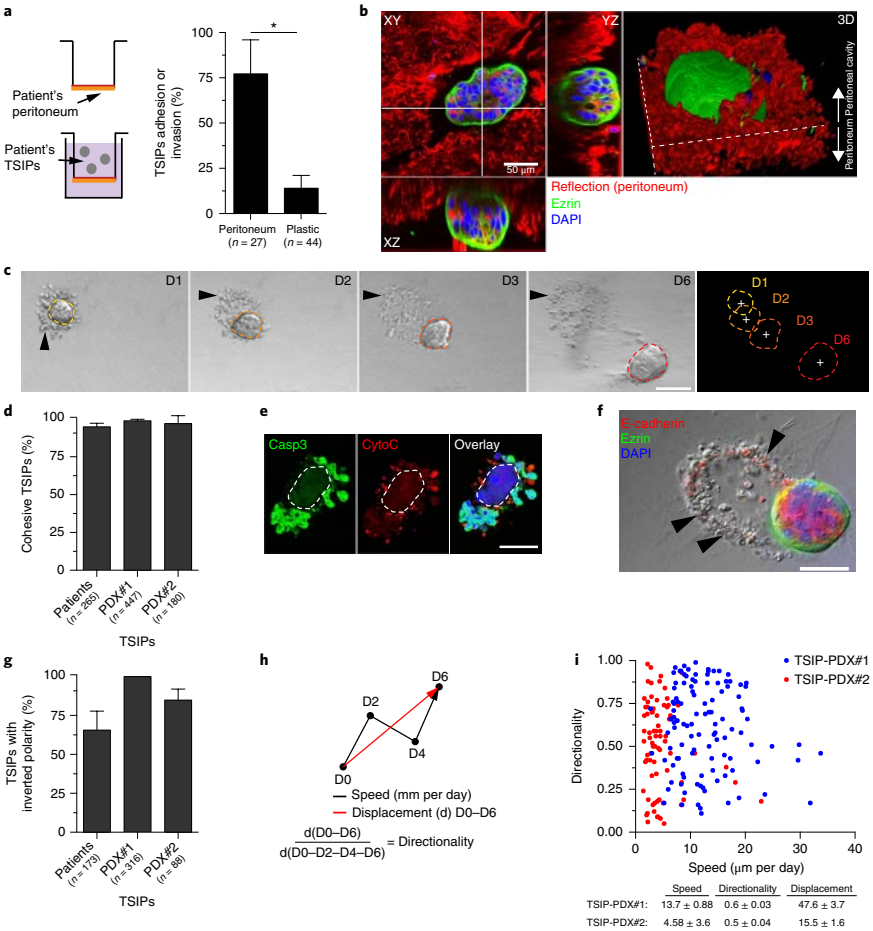

Fig. 5 | TSIPs collectively invade in their inverted topology. a, Left panel, schematic representation of the peritoneum invasion assay. Right panel, associated bar graph shows the quantification of TSIPs adhesion or invasion in paired peritoneum or a plastic dish after 3 d in culture represented as a percentage of the initial TSIPs incubated (*n* represents the number of TSIPs from three patients; two-sided unpaired *t*-test **P* = 0.0345). **b**, Representative images of TSIP-invading peritoneum explant from matching patients from two different patients samples, stained for ezrin and DAPI. The peritoneum is visualized by reflection microscopy. The XZ and YZ images represent orthogonal views of the Z-stack. The right panel displays a 3D reconstruction. **c**, Time-lapse sequences of patient TSIP displacement in collagen-I gel monitored by DIC microscopy over 6 d (D0–D6). Arrowheads point to cell debris. TSIP perimeters and centroids are highlighted by coloured dashed lines and white crosses, respectively. TSIP displacements were observed from three independent patients. **d**, Number of cohesive TSIPs from patients, PDX#1 and PDX#2 after 6 d in collagen-I, represented as the percentage of the total TSIPs. *n* represents the total number of TSIPs analysed from seven patients for primary samples or three independent experiments for TSIP-PDX. **e**, Patients' TSIPs were stained for Hoechst-33342, cytochrome *c* (CytoC), and cleaved caspase-3 (Casp3), repeated for five patients. Dashed lines represent the TSIP periphery. **f**, Representative image from three different patients' TSIPs collected and embedded into collagen-I. After 6 d, TSIPs were stained for ezrin, E-cadherin and DAPI. Arrowheads show cell corpses and debris. **g**, Bar graph representing the number of TSIPs with inverted polarity after 6 d in collagen-I (as a percentage of cohesive TSIPs). *n* represents the total number of TSIPs analysed from seven patients for primary samples or three independent experiments for TSIP-PDX. **h**, Schematic representation of the measurements of TSIP displacement. **i**, Speed (µm per day) plotted against the directionality for TSIP-PDX#1 ($n = 114$ TSIPs) and TSIP-PDX#2 ($n = 75$ TSIPs) from three independent experiments. The table shows the mean ± s.e.m. speed, displacement and directionality. Scale bars, 50 µm, unless otherwise specified. The graphs in **a**, **d** and **g** represent mean ± s.e.m.

Discussion

In summary, by investigating specimens from patients with metastatic CRC, we have identified a collective and epithelial mode of cancer dissemination, based on collective budding, growth and invasion processes. Remarkably, TSIPs, which constitute the malignant metastatic intermediates linking primary tumours to peritoneal

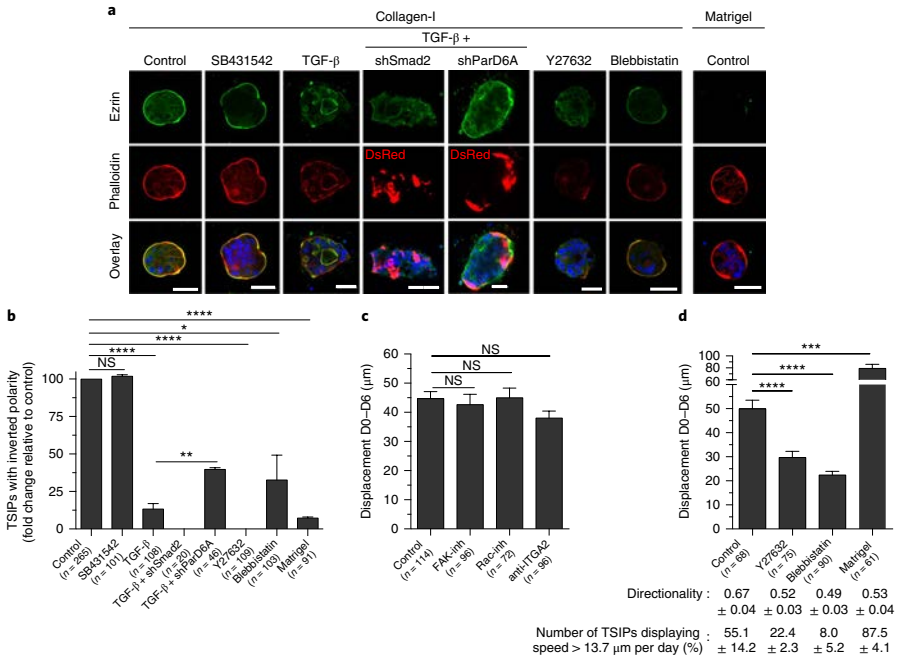

Fig. 6 | TSIPs collective invasion is driven by ROCK and myosin-II activity downstream of the non-canonical TGF-β signalling. a, Representative images from three biologically independent experiments of TSIP-PDX#1 in collagen-I (or Matrigel) in control conditions or treated with SB431542, TGF-β, Y27632, blebbistatin or a combination of TGF-β stimulation after transduction with shSmad2 and shParD6A (infected cells expressed DsRed). After 3 d, TSIPs were fixed and stained using anti-ezrin, phalloidin and DAPI to assess their apico-basolateral polarity (the quantification is in Fig. 6b). Scale bars, 50 μm. **b**, Percentage of TSIPs with inverted polarity after 3 d in collagen-I, normalized to the control condition. TSIPs were treated with SB431542, TGF-β, Y27632, blebbistatin or a combination of TGF-β stimulation after infection with lentiviruses encoding shSmad2 and shParD6A. Alternatively, TSIPs were incubated in Matrigel (3 mg ml^{-1}). *n* represents the number of TSIPs quantified per condition. TGF-β + shSmad2 experiments were performed twice. **c**, TSIP-PDX#1 displacement (D0–D6) in collagen-I in the control condition or supplemented with inhibitors of FAK (FAK-inh; PF-573228) and Rac (Rac-inh; NSC23766) or integrin α_2 function-blocking antibody (anti-ITGA2). The total number of TSIPs across the three independent experiments is indicated in the graph. **d**, TSIP-PDX#1 displacement (D0–D6) in collagen-I supplemented with the ROCK inhibitor Y27632, blebbistatin or in Matrigel. The total number of TSIPs across the three independent experiments is indicated in the graph. The associated table shows the directionality (mean ± s.e.m.) and the percentage of TSIPs with an invasion speed of >13.7 μm per day for the above-mentioned conditions. All graphs represent mean ± s.e.m. *P* values were calculated using two-sided unpaired *t*-test (****$P < 0.0001$, ***$P < 0.001$, *$P < 0.05$, NS $P > 0.05$).

metastases, retain a robust epithelial architecture and an inverted apico–basolateral polarity during their dissemination (see the graphical summary in Supplementary Fig. 7).

Although we cannot exclude the possibility that some of the vimentin-positive cells contribute to the disease, these cells do not generate multicellular structures ex vivo and rapidly die in isolation, as reported for circulating tumour cell clusters in the bloodstream[46]. Moreover, our results are in agreement with recent mouse models of breast and pancreatic carcinomas that demonstrated the formation of distant metastases independently of EMT activation[9,10]. TSIPs form and propagate in specific histological subtypes of CRCs with dismal outcome and increased occurrence of peritoneal metastases, which evolve from the CIMP/serrated pathway[30,31]. Although there is no mouse models of these cancers, our results are in line with the phenotypes of *TGFBR1*-knockout and *SMAD3*-knockout mice, which induce the differentiation of goblet cells and MUC intestinal malignancies, respectively[47,48]. In addition, the low TGF-β signalling could explain the lack of EMT activation in these tumours[49–51].

Our findings contradict the prevailing consensus that carcinoma progression is accompanied by the loss of epithelial architecture and polarity[52,53]. Yet, whereas the normal apico–basolateral polarity is maintained at the cellular level, the neoplastic tissue organization is profoundly altered, with the protective apical pole in contact with patient fluids and tissues. This may enable TSIPs to survive in multiple environments and help them to evade immune surveillance. Interestingly, TSIPs invade tissues using a unique mode of collective invasion that does not involve the formation of adhesion-based protrusions[54,55] but is reminiscent of propulsive amoeboid single-cell migration[56], a process that has never been reported for collectives. Moreover, collective apical budding does not occur from normal epithelia. Although we have seen cancer formation and progression as the result of improper reactivation of normal developmental processes, TSIP biology suggests that neoplastic epithelia may develop specific strategies to colonize the body. This clinical cell biology research provides an alternative conception of cancer dissemination and is vital if we are to use an understanding of the biology of tumour progression to the benefit of cancer patients.

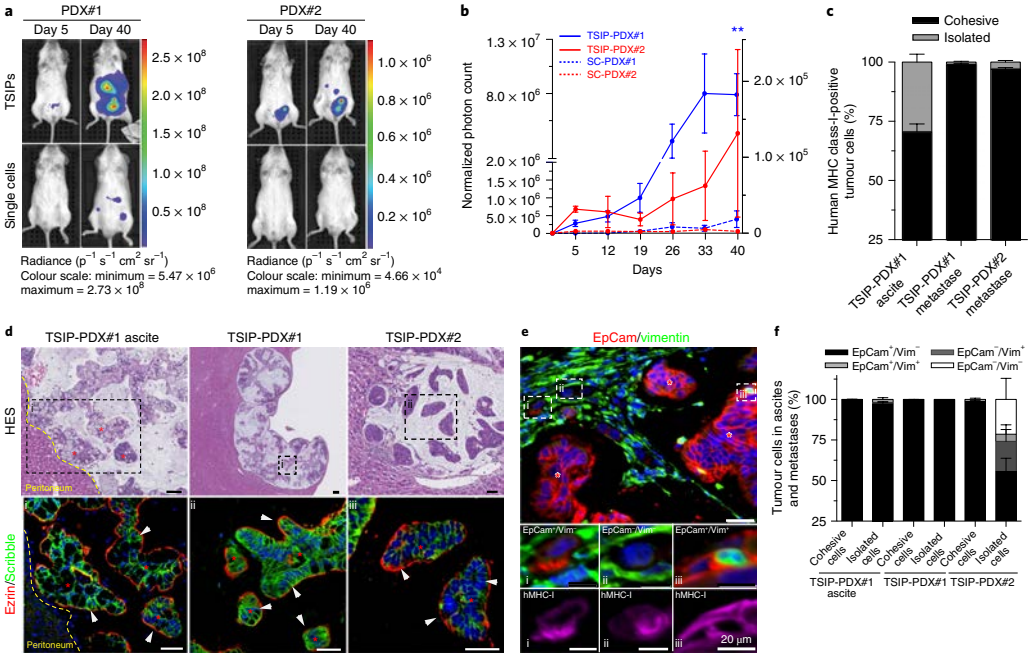

Fig. 7 | TSIPs are efficient initiators of metastases. a, Representative bioluminescence images collected from 5 mice per group, 5 or 40 d after intraperitoneal injection of TSIPs or single cells obtained from PDX#1 and PDX#2 expressing luciferase. **b**, Peritoneal metastases growth curves from mice injected intraperitoneally with TSIPs or single cells obtained from PDX#1 and PDX#2 expressing luciferase ($n = 5$ mice for each group). The bioluminescence signal was measured every week for each individual mouse. *P* values were calculated using unpaired two-sided *t*-test at 40 d (**$P = 0.005$). **c**, Quantification of cohesive and isolated tumour cells in metastases and ascites formed by the injection of TSIP-PDX#1 and TSIP-PDX#2 into the mice peritoneal cavity. Tumour cells were identified by antibodies against human MHC class I, and represent $n = 880$, $n = 1{,}795$ and $n = 2{,}985$ cells, respectively, from three different mice. **d**, Representative images of histological sections of metastases from 5 mice collected 40 d after intraperitoneal injection of TSIP-PDX#1 and TSIP-PDX#2 (3 different mice for TSIP-PDX#1 ascites). Top panels, tumour section were stained using haematoxylin–eosin–saffron (HES); bottom panels show high magnification of the boxed regions (i, ii and iii) immunostained for ezrin, Scribble and DAPI (blue). Red asterisks indicate TSIPs and arrowheads point to their outward apical pole. **e**, Representative images of histological sections of metastases from five mice injected with TSIP-PDX#1 or TSIP-PDX#2 stained using antibodies against human MHC class I (hMHC-1; purple), vimentin and EpCam. Boxed regions (i, ii and iii) are shown at high magnification to reveal markers expressed by single cells. Red asterisks indicate TSIPs. The quantification is displayed in panel **f**. **f**, Bar graph showing the proportions of EpCam-expressing and vimentin-expressing tumour cells (identified by human MHC class I staining) among the isolated or cohesive population of the ascites or metastases. From the left to the right of the graph, $n = 510$, 270, 1,771, 24, 2,964 and 61 cells, respectively, pooled from three different mice. Scale bars, 50 µm, unless otherwise specified. All graphs represent mean ± s.e.m.

Methods

Methods, including statements of data availability and any associated accession codes and references, are available at https://doi.org/10.1038/s41556-017-0027-6.

Received: 11 July 2017; Accepted: 12 December 2017;
Published online: 5 February 2018

References

1. Bilder, D. Epithelial polarity and proliferation control: links from the *Drosophila* neoplastic tumor suppressors. *Genes. Dev.* **18**, 1909–1925 (2004).
2. Huang, L. & Muthuswamy, S. K. Polarity protein alterations in carcinoma: a focus on emerging roles for polarity regulators. *Curr. Opin. Genet. Dev.* **20**, 41–50 (2010).
3. Muthuswamy, S. K. & Xue, B. Cell polarity as a regulator of cancer cell behavior plasticity. *Annu. Rev. Cell. Dev. Biol.* **28**, 599–625 (2012).
4. Nieto, M. A., Huang, R. Y.-J., Jackson, R. A. & Thiery, J. P. EMT: 2016. *Cell* **166**, 21–45 (2016).
5. Thiery, J. P., Acloque, H., Huang, R. Y.-J. & Nieto, M. A. Epithelial–mesenchymal transitions in development and disease. *Cell* **139**, 871–890 (2009).
6. Friedl, P. & Alexander, S. Cancer invasion and the microenvironment: plasticity and reciprocity. *Cell* **147**, 992–1009 (2011).
7. Liu, Y.-J. et al. Confinement and low adhesion induce fast amoeboid migration of slow mesenchymal cells. *Cell* **160**, 659–672 (2015).
8. Paluch, E. K., Aspalter, I. M. & Sixt, M. Focal adhesion-independent cell migration. *Annu. Rev. Cell. Dev. Biol.* **32**, 469–490 (2016).
9. Fischer, K. R. et al. Epithelial-to-mesenchymal transition is not required for lung metastasis but contributes to chemoresistance. *Nature* **527**, 472–476 (2015).
10. Zheng, X. et al. Epithelial-to-mesenchymal transition is dispensable for metastasis but induces chemoresistance in pancreatic cancer. *Nature* **527**, 525–530 (2015).
11. Friedl, P., Locker, J., Sahai, E. & Segall, J. E. Classifying collective cancer cell invasion. *Nat. Cell. Biol.* **14**, 777–783 (2012).
12. Cheung, K. J., Gabrielson, E., Werb, Z. & Ewald, A. J. Collective invasion in breast cancer requires a conserved basal epithelial program. *Cell* **155**, 1639–1651 (2013).

13. Montell, D. J., Yoon, W. H. & Starz-Gaiano, M. Group choreography: mechanisms orchestrating the collective movement of border cells. *Nat. Rev. Mol. Cell. Biol.* **13**, 631–645 (2012).
14. Friedl, P. & Gilmour, D. Collective cell migration in morphogenesis, regeneration and cancer. *Nat. Rev. Mol. Cell. Biol.* **10**, 445–457 (2009).
15. Pino, M. S. & Chung, D. C. The chromosomal instability pathway in colon cancer. *Gastroenterology* **138**, 2059–2072 (2010).
16. Vogelstein, B. et al. Genetic alterations during colorectal-tumor development. *N. Engl. J. Med.* **319**, 525–532 (1988).
17. Cancer Genome Atlas Network. Comprehensive molecular characterization of human colon and rectal cancer. *Nature* **487**, 330–337 (2012).
18. Guinney, J. et al. The consensus molecular subtypes of colorectal cancer. *Nat. Med.* **21**, 1350–1356 (2015).
19. Marisa, L. et al. Gene expression classification of colon cancer into molecular subtypes: characterization, validation, and prognostic value. *PLoS. Med.* **10**, e1001453 (2013).
20. Juo, Y. Y. et al. Prognostic value of CpG island methylator phenotype among colorectal cancer patients: a systematic review and meta-analysis. *Ann. Oncol.* **25**, 2314–2327 (2014).
21. Weisenberger, D. J. et al. CpG island methylator phenotype underlies sporadic microsatellite instability and is tightly associated with *BRAF* mutation in colorectal cancer. *Nat. Genet.* **38**, 787–793 (2006).
22. Phipps, A. I. et al. Association between molecular subtypes of colorectal cancer and patient survival. *Gastroenterology* **148**, 77–87 (2015).
23. Ward, R. L. et al. Adverse prognostic effect of methylation in colorectal cancer is reversed by microsatellite instability. *J. Clin. Oncol.* **21**, 3729–3736 (2003).
24. Bettington, M. et al. The serrated pathway to colorectal carcinoma: current concepts and challenges. *Histopathology* **62**, 367–386 (2013).
25. O'Brien, M. J., Zhao, Q. & Yang, S. Colorectal serrated pathway cancers and precursors. *Histopathology* **66**, 49–65 (2015).
26. van Gestel, Y. R. B. M. et al. Patterns of metachronous metastases after curative treatment of colorectal cancer. *Cancer Epidemiol.* **38**, 448–454 (2014).
27. Segelman, J. et al. Incidence, prevalence and risk factors for peritoneal carcinomatosis from colorectal cancer. *Br. J. Surg.* **99**, 699–705 (2012).
28. Sugarbaker, P. H. Peritoneal carcinomatosis: natural history and rational therapeutic interventions using intraperitoneal chemotherapy. *Cancer Treat. Res.* **81**, 149–168 (1996).
29. Franko, J. et al. Prognosis of patients with peritoneal metastatic colorectal cancer given systemic therapy: an analysis of individual patient data from prospective randomised trials from the Analysis and Research in Cancers of the Digestive System (ARCAD) database. *Lancet Oncol.* **17**, 1709–1719 (2016).
30. Hugen, N., van de Velde, C. J. H., de Wilt, J. H. W. & Nagtegaal, I. D. Metastatic pattern in colorectal cancer is strongly influenced by histological subtype. *Ann. Oncol.* **25**, 651–657 (2014).
31. Numata, M. et al. The clinicopathological features of colorectal mucinous adenocarcinoma and a therapeutic strategy for the disease. *World J. Surg. Oncol.* **10**, 109 (2012).
32. Goéré, D. et al. Is there a possibility of a cure in patients with colorectal peritoneal carcinomatosis amenable to complete cytoreductive surgery and intraperitoneal chemotherapy? *Ann. Surg.* **257**, 1065–1071 (2013).
33. Mohamed, F., Cecil, T., Moran, B. & Sugarbaker, P. A new standard of care for the management of peritoneal surface malignancy. *Curr. Oncol.* **18**, e84–e96 (2011).
34. Subramanian, A. et al. Gene set enrichment analysis: a knowledge-based approach for interpreting genome-wide expression profiles. *Proc. Natl. Acad. Sci. USA* **102**, 15545–15550 (2005).
35. Davidowitz, R. A. et al. Mesenchymal gene program-expressing ovarian cancer spheroids exhibit enhanced mesothelial clearance. *J. Clin. Invest.* **124**, 2611–2625 (2014).
36. Tom, B. H. et al. Human colonic adenocarcinoma cells. I. Establishment and description of a new line. *Vitro* **12**, 180–191 (1976).
37. Julien, S. et al. Characterization of a large panel of patient-derived tumor xenografts representing the clinical heterogeneity of human colorectal cancer. *Clin. Cancer Res.* **18**, 5314–5328 (2012).
38. Sato, T. et al. Long-term expansion of epithelial organoids from human colon, adenoma, adenocarcinoma, and Barrett's epithelium. *Gastroenterology* **141**, 1762–1772 (2011).
39. Laiho, P. et al. Serrated carcinomas form a subclass of colorectal cancer with distinct molecular basis. *Oncogene* **26**, 312–320 (2007).
40. de Miranda, N. F. C. C. et al. Transforming growth factor β signaling in colorectal cancer cells with microsatellite instability despite biallelic mutations in *TGFBR2*. *Gastroenterology* **148**, 1427–1437 (2015).
41. Brown, K. A., Pietenpol, J. A. & Moses, H. L. A tale of two proteins: differential roles and regulation of Smad2 and Smad3 in TGF-beta signaling. *J. Cell. Biochem.* **101**, 9–33 (2007).
42. Maiuri, P. et al. The first World Cell Race. *Curr. Biol.* **22**, R673–R675 (2012).
43. Alexander, S., Koehl, G. E., Hirschberg, M., Geissler, E. K. & Friedl, P. Dynamic imaging of cancer growth and invasion: a modified skin-fold chamber model. *Histochem. Cell. Biol.* **130**, 1147–1154 (2008).
44. Giampieri, S., Pinner, S. & Sahai, E. Intravital imaging illuminates transforming growth factor beta signaling switches during metastasis. *Cancer Res.* **70**, 3435–3439 (2010).
45. O'Brien, L. E. et al. Rac1 orientates epithelial apical polarity through effects on basolateral laminin assembly. *Nat. Cell. Biol.* **3**, 831–838 (2001).
46. Aceto, N. et al. Circulating tumor cell clusters are oligoclonal precursors of breast cancer metastasis. *Cell* **158**, 1110–1122 (2014).
47. McCauley, H. A. et al. TGFβ signaling inhibits goblet cell differentiation via SPDEF in conjunctival epithelium. *Development* **141**, 4628–4639 (2014).
48. Zhu, Y., Richardson, J. A., Parada, L. F. & Graff, J. M. *Smad3* mutant mice develop metastatic colorectal cancer. *Cell* **94**, 703–714 (1998).
49. Lamouille, S., Xu, J. & Derynck, R. Molecular mechanisms of epithelial–mesenchymal transition. *Nat. Rev. Mol. Cell. Biol.* **15**, 178–196 (2014).
50. Ozdamar, B. et al. Regulation of the polarity protein Par6 by TGFß receptors controls epithelial cell plasticity. *Science* **307**, 1603–1609 (2005).
51. Giampieri, S. et al. Localized and reversible TGFβ signalling switches breast cancer cells from cohesive to single cell motility. *Nat. Cell Biol.* **11**, 1287–1296 (2009).
52. Bilder, D., Li, M. & Perrimon, N. Cooperative regulation of cell polarity and growth by *Drosophila* tumor suppressors. *Science* **289**, 113–116 (2000).
53. Zhan, L. et al. Deregulation of Scribble promotes mammary tumorigenesis and reveals a role for cell polarity in carcinoma. *Cell* **135**, 865–878 (2008).
54. Wang, X., He, L., Wu, Y. I., Hahn, K. M. & Montell, D. J. Light-mediated activation reveals a key role for Rac in collective guidance of cell movement in vivo. *Nat. Cell. Biol.* **12**, 591–597 (2010).
55. Hegerfeldt, Y., Tusch, M., Bröcker, E.-B. & Friedl, P. Collective cell movement in primary melanoma explants: plasticity of cell–cell interaction, β1-integrin function, and migration strategies. *Cancer Res.* **62**, 2125–2130 (2002).
56. Callan-Jones, A. C. & Voituriez, R. Actin flows in cell migration: from locomotion and polarity to trajectories. *Curr. Opin. Cell. Biol.* **38**, 12–17 (2016).

Acknowledgements

We thank all the patients who participated in this study and the medical staff for their assistance with the acquisition of primary human specimens. We also thank the members of the Jaulin Lab and the Digestive Cancer Unit for discussion, B. Baum for mentoring and support, and S. Deborde, B. Goud and G. Kreitzer for critical reading of the manuscript. We thank D. Vignjevic, S Guilmeau, the Plateforme Anticorps Recombinant (Curie Institute), DSHB (University of Iowa) and J. Zuber for reagents and the technical services provided by PFIC core facility, module HCP (F. Drusch and V. Marty), O. Bawa, V. Roufiac, S. Piterboth and I. Villa. This work was supported by the CNRS and INSERM (the ATIP-AVENIR program), the Gustave Roussy Foundation (Roulons pour le colon, Natixis), Canceropole (Emergence) Taxe d'apprentissage Gustave Roussy (2016 to C.C.J.).

Author contributions

O.Z., J.R., F.L., D.S., S.S., G.P., I.M., P.R., C.B., P.A. and J.-L.P. designed the research, performed the experiments and analysed the data. L.B., M. Polrot and P.G. carried out the mice experiments. C.L. analysed the microarray and RNA-sequencing data. D.E., D.G., C.E., M. Pocard, M.D. and D.M. provided clinical samples. P.D. and J.-Y.S. performed the histological analyses. F.J. conceived the project, designed the research and wrote the manuscript. All authors provided intellectual input.

Competing interests

The authors declare no competing financial interests.

Additional information

Supplementary information is available for this paper at https://doi.org/10.1038/s41556-017-0027-6.

Reprints and permissions information is available at www.nature.com/reprints.

Correspondence and requests for materials should be addressed to F.J.

Publisher's note: Springer Nature remains neutral with regard to jurisdictional claims in published maps and institutional affiliations.

Methods

Recovery and characterization of peritoneal effusions from patients with CRC. The human study protocols followed all relevant ethical regulations in accordance with the declaration of Helsinki principles. The study was approved by the ethics committee (CPP IDF 10), under protocol NI-2015-06-03, at Gustave Roussy and Lariboisière Hospitals. Written informed consent was obtained from all patients. Peritoneal effusions from a total of 59 patients with CRC were collected. The patients received neoadjuvant chemotherapy 2–3 weeks before surgery. The peritoneal effusion samples were collected at the onset of hyperthermic intraperitoneal chemotherapy treatment. Immediately after laparotomy, and before cytoreductive surgery, serous fluid was collected by addition and reabsorption of 500 ml of saline solution. The fluids were processed in the laboratory within 2 h after collection for characterization and functional experiments. The freshly isolated samples were transferred to sterile tubes and centrifuged at 1,500 rpm for 10 min. The peritoneal cancer index[35] was evaluated during surgery. Counting and characterization of cells in the peritoneal effusion total fraction was done after Ficoll Paque Plus (17-1440-02, GE Healthcare) centrifugation following the manufacturer's protocol. A part of the interphase was removed and cells were cytospined at 1,500 rpm for 5 min on a Superfrost Plus glass slide (10149870, Thermo Scientific). Then, the cells were fixed in 4% paraformaldehyde (PFA) (15710, Electron Microscopy Sciences) for 5 min and washed with PBS. The cell count was performed on the cytospin slides.

Separation of tumour clusters and single cells. The rest of the interphase was carefully collected and transferred to a new sterile tube. DMEM medium containing 4.5 g per litre glucose, glutaMAX (31966021, Life Technologies) and 1% penicillin–streptomycin (P/S; 15140-122, Life Technologies) was added to a final volume of 10 ml. Differential centrifugations, spin down until 2,000 rpm, were performed at least 4 times. During these centrifugations, the supernatants were saved for the single tumour cells enrichment and analyses procedures. The clusters that were present in the pellet were counted: some of them were fixed in 4% PFA for 45 min and immobilized for immunofluorescence and characterization; the other part was directly used for functional studies. TSIPs were defined as tumour clusters with spherical shape and smooth surface, and irregular clusters were defined by their uneven shape and rim. In parallel, single cells were pulled down by centrifugation at 1,500 rpm for 5 min and resuspended in fresh medium. The total number of single cells was counted in a Neubauer chamber and trypan blue (Life Technologies) was used to assess cell viability; an aliquot was used for cytospin (total single-cell fraction, see description below). Prior to functional studies (proliferation, aggregation and survival), to exclude any small aggregates that would have formed during the manipulation, the single-cell suspension was filtered with a pre-separation filter (20 µm) (130-101-812, Miltenyi Biotec). Single cells were used as such or enriched for CRC cells using EpCam-coated microbeads and MS columns (130-061-101 and 130-041-301, Miltenyi Biotec) or after exclusion of the CD45-positive population using EasySepTM Human CD45 Depletion Kit (18259, STEMCELL,) following the manufacturer's protocol.

Animal studies. Animal experiments were compliant with French legislation and European Union Directive 2010/63. The project was validated by the Ethical Committe (CEEA) no. 26 and was then granted French government authorizations under numbers 517-2015042114005883 and 2734-2015111711418501. Mice were obtained from Charles River, and were housed and bred at the Gustave Roussy animal core facility (accreditation number E-94-076-11). Animals were humanely euthanized according to end points that were validated by the Ethical Commitee and the French government (Ministère de l'Enseignement Supérieur, de la Recherche et de l'Innovation).

Organoids retrieval and preparation from TSIP-PDX. Two human CRCs (PDX#1 corresponding to LRB-0009C and PDX#2 corresponding to IGR-0012P) from the CReMEC tumour collection were maintained in NSG mice (NOD-scid IL2Rγ^{null}, from Charles River) as previously described[37]. Briefly, small tumour fragments were subcutaneously engrafted on the flank of anaesthetized mice (2.5% isoflurane). Tumour growth was measured at least once a week. When the volume reached 1,500 mm^3, mice were killed and tumours were used for ex vivo experiments, and 50 mm^3 fragments were engrafted on the flank of new mice. Organoids were prepared as previously described[38], and were adapted for mucus-secreting tumours as follows: the PDX#1 or PDX#2 tumours between 1,000–1,500 mm^3 were retrieved from the mice, minced into small fragments using a sterile scalpel and were incubated for 90 min at 37 °C in a final volume of 5–10 ml of culture medium (DMEM) without FBS and with 2 mg ml^{-1} collagenase (C2139, Sigma). The samples were then mixed with 20 ml of DMEM and filtered on 100-µm mesh size cell strainers (542000, EASYstrainer). Digested tumour clusters were pelleted in by 4 pulse-centrifugations at 1,500 rpm. The tumour fragments, which were free of single cells, were maintained for 3 d in ultra-low attachment plates (CLS3471, Corning) in culture medium. Then, organoids were pelleted at 1,500 rpm and characterized (staining with apico–basolateral polarity markers (see results in Supplementary Fig. 6a,b) showed that the organoids displayed the characteristics of TSIPs retrieved from the patients). TSIPs-PDX were used for survival and invasion experiments, as well as for mice intraperitoneal injections.

Mice intraperitoneal injections. TSIPs and single cells obtained from PDX#1 and PDX#2 (above) were transduced using green fluorescent protein (GFP)-luciferase lentiviruses (see below for lentiviral particle production). Immediately after PDX tumour dissociation and mucin removal, tumour fragments were incubated with lentiviruses at a concentration of 600,000 viruses per ml in a 6-well ultra-low attachment plate. The medium was changed after 2 d, and single cells were obtained by trypsinization. Transduced TSIPs (1×10^4), or the equivalent number of single cells, were resuspended into 100 µl culture media and injected intraperitoneally using a 25 G needle. The mice were monitored by bioluminescence imaging every 7 d until 40 d post-injection.

Bioluminescence imaging. All bioluminescence imaging experiments were performed using an IVIS Spectrum CT pre-clinical in vivo imaging system (PerkinElmer Life Sciences). Mice were anaesthetized with 2.5% isoflurane, received caudal intravenous injection of 150 mg per kg of D-Luciferin (E1605, Promega) and were imaged after 2 min. The settings (acquisition time, f/stop and binning) were applied differently from one experiment to another, taking into account the metastasis development and the consecutive increasing levels of emitted photons.

Invasion assays. *Collagen-I assays.* Rat-tail collagen-I (354236, Corning) was neutralized with 1.0 M NaOH and 10× MEM (21430-02, Life Technologies) according to the ratio: 1.0/0.032/0.1 (vol/vol/vol). The concentration was then adjusted to 1.3–2 mg ml^{-1} with DMEM 1× and the collagen was incubated on ice for 60–75 min. The TSIPs embedded in neutralized collagen-I were added on top of the pre-coated well at a concentration of 1–2 TSIPs per ml (ibidi 8-well chamber). The gel was allowed to polymerize for 45 min at 37 °C. TSIPs were then maintained in culture medium supplemented with 10% FBS for up to 6 d (3 d for TGF-β (20 ng ml^{-1}, P01137, R&D System), SB431542 (10 µM, S1067, Sellekchem) alone or in combination with a lentivirus encoding shSmad2 and shParD6A) and fixed for staining. Media were supplemented with a FAK inhibitor (10 µM, 869288-64-2, Sigma), NSC-23766 (50 µM, 2161, Tocris), integrin α_2 function-blocking antibody (5 µg ml^{-1}, sc-13346, Santa Cruz), Y27632 (25 µM, 688000, Calbiochem) and blebbistatin (10 µM, 203391, Calbiochem).

Matrigel assays. TSIPs were embedded into 3 mg ml^{-1} Matrigel (354230, BD) and incubated in a pre-coated 8-well chamber (ibidi). After polymerization, culture medium supplemented with 10% FBS was added.

TSIP polarity assessment. After incubation into collagen-I or Matrigel, the apico–basolateral polarity of TSIPs was quantified after immunostaining using anti-ezrin. TSIPs are considered to have inverted polarity when at least 75% of the total peripheral cells displayed an outward apical pole in one confocal Z-section.

Ex vivo peritoneum invasion assay. During surgery, peritoneal fragments were excised in a non-tumoural region (which was confirmed by histology preparation). Patient peritoneum explants were immediately sealed at the bottom of a transwell insert (PIEP12R48, Millipore; the polyethylene terephthalate membrane (PET) membrane was removed) using collagen-I. After insertion into 24-well culture plates, the insert was filled with culture medium. The side that lines the peritoneum cavity faced the upper chamber. TSIPs collected in matching patients were seeded on top of the peritoneum in the upper chamber. The invasion assay lasted for 3 d, and then the peritoneal tissue was washed in PBS supplemented with Ca^{2+} and Mg^{2+} and fixed in 4% PFA.

LS174T budding assay. 24 h after plating the LS174T cell line (4×10^5 cells in a 22-cm^2 tissue culture dish or 1×10^5 cells in a 10-cm^2 dish for Fig. 3g), the medium was changed and the cells were incubated with normal medium or treated as follows: TGF-β (10 ng ml^{-1}), SB431542 (10 µM), H1152 (2 µM, 2414, Tocris), blebbistatin (10 µM) or Noggin (100 ng ml^{-1}, 120-10 C, Peprotech). At day 7, 8 and 9, the plates were hit 20 times on the bench, the medium collected and centrifuged for 8 s at 500 g to pellet the TSIPs and the supernatant transferred back to the plates. TSIPs-LS174T were then counted under light microscope and TSIP counts added for 3 consecutive days.

LS174T morphogenesis assay. LS174T 2D cell cultures were partially dissociated with trypsin (0.25%)-EDTA and filtered through 20-µm pre-seperation filters (Milteny Biotech). The harvested clusters (<5 cells) were embedded in a mix of collagen-I (rat-tail neutralized, as described in the invasion assay, and used at a final concentration of 1.3 mg ml^{-1}) and Matrigel (final concentration of 4.5 mg ml^{-1}) in an ibidi plate. Single cells died, but small clusters survived and were grown for 7 d at 37 °C. Their polarity was assessed after fixation and ezrin immunostaining. Most clusters developed as cysts, with the apical pole surrounding 1–3 lumens. The polarity was considered inverted (that is, the apical pole faced the ECM gel) when >50% of the cells displayed a peripheral ezrin staining (and no lumen). The non-polar structures showed a diffuse ezrin localization.

Single-cell assays from patients' primary samples and cell lines. *Single-cell obtention.* Single cells from patients' peritoneal effusions were isolated as described

above. Dissociated single-cell (dSC) suspensions were obtained from TSIPs, PDX#1 and PDX#2, LS174T and SW620 by dissociation using trypsin (0.25%)-EDTA for 7–10 min, and filtered through 20-µm pre-separation filters. As controls, TSIPs from patients, PDX#1, PDX#2 and LS174T were incubated in similar conditions. Survival and proliferation in suspension were addressed by plating single cells in ultra-low attachment 96-well plates at 10–100 cells per ml. Proliferation was followed by light microscopy, and survival was assessed with trypan blue and propidium iodide (PI) at day 0 and every 3 d. Hoechst was used to count nuclei. LS174T aggregation was promoted by increasing the cell concentration to 4,000 cells per ml.

ECM gel assays. Single cells were obtained by dissociation as described above, and embedded in either Matrigel (354238, Corning, diluted, with medium, to a final concentration of 3.5 µg ml^{-1}) with or without Y27632 at a concentration of 25 µM or collagen-I (rat-tail collagen-I neutralized and polymerized as described for the invasion assays). They were seeded in an ibidi plate at 37 °C and cultured with adequate supplemented medium. Survival was assessed throughout a period of 9 d.

TSIP mitotic index was calculated as the ratio between mitotic cells and the total cell number, expressed as a percentage. Mitotic and interphasic nuclei were stained with 4,6-diamidino-2-phenylindole (DAPI) and identified by their morphology.

Culture condition and transfection of cell lines. LS174T (Sigma) were grown in EMEM medium supplemented with 1% non-essential amino acids, 10% FBS and 50 µg ml^{-1} penicillin, 50 µg ml^{-1} streptomycin (P/S). Colo205 (American Type Culture Collection, ATCC) were cultured in RPMI-1640 medium supplemented with 1 mM sodium pyruvate, 10% FBS and P/S. SW620 and Caco-2 (ATCC) were grown in DMEM medium supplemented with 1 mM sodium pyruvate, 10% FBS and P/S. HCT-15 and LS1034 (ATCC) were grown in RPMI-1640 medium supplemented with 10% FBS and P/S. All cell lines were maintained in a humidified incubator at 37 °C under a 5% CO_2 atmosphere. siRNA transfection into LS174T was achieved using DharmaFECT 1 according to the manufacturer's instructions. siRNA were purchased from Dharmacon: siGENOME human Smad2 (D-003561-04 (#2)), Smad3 (D-020067-01 (#1) and D-020067-04 (#2)), Smad4 (D-003902-05 (#1) and D-003902-07 (#2)) and non-targetting #2 (D-001206-14-05), ON-TARGETplus human ParD3 (L-015602-00), Scribble ((L-010500-00), Llgl2 (L-019812-01) and TGF-βR1 (M-003929-02).

Virus production, shRNA sequences and infection. *Virus production.* GFP-luciferase, shParD6A and shSmad2 lentiviruses were obtained by co-transfecting the lentiviral vector pFUGW-Pol2-ffLuc2-eGFP (Addgene 71394), pRRL.TRE3GdsRed-ShParD6A and pRRL.TRE3GdsRed-Smad2 (ref.[37]) with the packaging vectors pMD2G (Addgene) and pCMVdR8,74 (Addgene) into HEK293T cells with the transfection reagent jetPRIME (114-15, Polyplus). Lentiviruses containing supernatants were collected on days 2 and 3 following transfection, concentrated by ultra-centrifugation (50,000 g for 2 h) and stored at −80 °C.

shRNA sequences. Complementary DNA (cDNA) sequences used to make shRNA lentiviruses are as follows: Smad2#1: 5′-GAACAAACCAGGTCTCTTG-3′ ; Smad2#2: 5′-GGTGTTCGATAGCATATTA-3′; ParD6A#1: 5′ -GCCAGGTTTCCTCAGTCATAGA-3′; and ParD6A#2: 5′ -AACAGCCATAACCTCATTGTCA-3′.

Hybridized complementary oligonucleotides were inserted in the XhoI/EcoRI sites of pRRL.TRE3GdsRed.

Infection. LS174T (5×10^4 cells) were transduced using lentiviruses, amplified and sorted by FACS on a double GFP (infection)-positive and DsRed (a red fluorescent protein; shRNA induction)-positive signal following induction of ParD6A and Smad2 shRNA expression (Tet-On regulated) by addition of 100 ng ml^{-1} doxycycline (D9891, Sigma-Aldrich). In parallel, a shRNA Renilla construct cell line was made as a control. For organoids infection, see the 'Mice intraperitoneal injections' section above.

Immunoblot. Cells were lysed with SDS sample buffer (62.5 mM Tris-HCl (pH 6.8), 10% glycerol, 0.002% bromophenol blue, 2% SDS and 5% β -mercaptoethanol), and lysates were boiled for 10 min. The samples were subjected to SDS–PAGE and proteins were transferred to nitrocellulose membranes (GE Healthcare). Membranes were incubated for 30 min in blocking solution (TBS containing 0.1% Tween-20 and 3% BSA) and further incubated with the appropriate primary antibody overnight at 4 °C. The membranes were then washed three times with 0.1% Tween-20/TBS and incubated for 45 min with secondary antibody conjugated to horseradish peroxidase; anti-mouse horseradish peroxidase (dilution of 1:10,000; NA931V, GE Healthcare) or anti-rabbit horseradish peroxidase (dilution of 1:3,000; 7074S, Cell Signalling Technology). Bound antibodies were detected with enhanced chemiluminescence. The exact reference, dilution and validation statement for each primary and secondary antibodies are included in Supplementary Table 4.

Quantitative RT–PCR. The total RNA fraction was isolated using RNeasy Mini Kit 50 (Qiagen) and applied to reverse transcription using High-Capacity RNA-to-cDNA Kit (Applied Biosystems). The cDNA was analysed by quantitative PCR (qPCR) using GoTaq qPCR Master Kit (Promega) with QuantiStudio 7Flex Real-Time PCR System (Applied Biosystems). Reaction parameters were 95 °C for 1 min, followed by 45 cycles of 95 °C for 10 s, 60 °C for 10 s and 72 °C for 20 s. The triplicate mean values were calculated using GAPDH gene transcription as reference for normalization. For RT–PCR the following primers were used:

Smad2Fwd: 5′-GCTTGAGAAAGCCATCACCACT-3′ ; Smad2Rev: 5′-AGGCCTGTTGTATCCCACTGA-3′ ; ParD6AFwd: 5′-CGCGCAGTCCCGATAGCATC-3′ ; ParD6ARev: 5′-AGAACTCCTGGAAGCCGCTC-3′ ; ParD3Fwd: 5′-TGTATGCCCAAGTCAAGAAGCC-3′ ; ParD3Rev: 5′-TGCCTCAGACGCTGTATCCG-3′ ; Llgl2Fwd: 5′-GCAACTGGCGTTCACATCGA-3′ ; Llgl2Rev: 5′-AGTAGTGTGTGCTCATCGCG-3′; GAPDHFwd: 5′-CTTTTGCGTCGCCAGCCGAG-3′; and GAPDHRev: 5′ -CCAGGCGCCCAATACGACCA-3′.

Immunofluorescence, immunohistochemistry, antibodies and histology. *Immunofluorescence.* Samples were washed twice in PBS supplemented with Ca^{2+} (0.1 mM) and Mg^{2+} (1 mM) and fixed in 4% PFA for 45 min (TSIPs and peritoneum) or 10 min (cytospins and single cells). Permeabilization was performed in PBS supplemented with 0.5% Triton X-100 for 45 min (5 min for cytospins, single cells and slides from mice metastasis). Primary antibodies were incubated overnight at 4 °C at the dilutions listed below in antibody diluent, PBS with 10% serum supplemented by 0.1% Triton X-100. Secondary antibodies (Cy3-conjugated or fluorescein isothiocyanate (FITC)-conjugated anti-mouse or anti-rabbit, Alexa Fluor 488 anti-rabbit 1:100, Jackson ImmunoResearch) and DAPI (1 µ g ml^{-1}) were incubated overnight at 4 °C for 2 h at room temperature. Slides were mounted using Fluoromont-G (Southern Biotech).

The exact reference, dilution and validation statement for each primary and secondary antibodies are included in Supplementary Table 4.

Histology. CRC and peritoneum specimens obtained after surgical resection were formalin fixed and paraffin embedded according to routine protocols. Peritoneal effusions were concentrated by centrifugation and fixed in formalin, then embedded for cytoblock. Sections (3 µm) of formalin-fixed and paraffin-embedded samples were deparaffinized, unmasked (pH 8) and rehydrated before haematoxylin–eosin–saffron or alcian blue staining, immunohistochemistry or immunofluorescence.

Immunohistochemistry. Sections were immunostained with ezrin (1:100; 610603, BD Biosciences) or anti-CK20 mouse monoclonal antibody (clone Ks20.8, Dako). Stainings were performed with Ventana BenchMark XT immunostainer (Ventana Medical Systems) using the UltraView DABv3 kit (Ventana). The chromogene was 3,3′-diaminobenzidine (DAB) in all the stainings. Histochemical staining with Alcian Blue (pH 2.5) was performed with Ventana BenchMark Special Stains (Ventana Medical Systems) utilizing the V1.00.0010 process. Peritoneal effusion smears were stained using May–Grünwald–Giemsa.

Live imaging, electron microscopy, image treatment and analyses. *Microscopy acquisition and live imaging.* Images were acquired using an Olympus Epifluorescence inverted ×73 microscope or a SpinningDisk CSU-W1 (Yokogawa) with a ZylasCMOC camera piloted with an Olympus ×83 microscope. TSIP behaviours in 3D culture were imaged by differential interference contrast (DIC) time-lapse microscopy, with motorized stage, temperature and CO_2 controllers. Images were recorded every 30 min for 6 d for patient samples and every 2 d for organoids. Sphericity, shape factor and perimeter were measured using the Cellsens Dimension software (Olympus) from DIC images. TSIP polarity was assessed by calculating the ratio between peripheral cells with or without ezrin staining from one median section.

Analyses of TSIP trajectories from DIC time-lapse sequences. The TSIP perimeter was delineated manually, and the TSIP centroid position was calculated using ImageJ. TSIP centroid displacement was automatically tracked using ImageJ and verified by visual inspection before further quantification. The speed (µm per day) was calculated as the total distance travelled over 6 d, the displacement (µm) as the length between the centroid positions at day 0 and day 6, and the directionality as the ratio between the distance and the displacement.

Images for display were processed using Metamorph or ImageJ software.

Electron microscopy. Isolated TSIPs were fixed in 2% glutaraldehyde in 0.1 M PBS (pH 7.3) and deposited in drops of neutralized collagen (2 mg ml^{-1}) that were allowed to polymerize for 10 min at room temperature laid on a glass coverslip. TSIPs were washed for 30 min in PBS, post-fixed with 2% osmic acid at room temperature and rinsed in water. Samples were dehydrated in ethanol and embedded in Epon. Polymerization was complete after 48 h at 60 °C. Ultra-thin sections were collected on 100 mesh grids coated with Formvar and carbon,

stained with uranyl acetate and lead citrate, and observed with a FEI Technai Spirit transmission electron microscope at 80 Kv. Digital images were taken with a SIS MegaviewIII CCD camera.

Expression profiles and sample phenotype definitions. *CIT.* The gene expression profiles from 15 MUC, 188 LBK and 19 normal samples were obtained from the CIT collection of patient samples as described previously[19] (GSE39582). Analyses of differential expression were done using the *t*-test from the ClassComparison package in R.

TCGA expression data. TCGA RNA-sequencing raw count data were obtained from GSE62944 (ref. [58]). We retrieved 41 normal colon, 61 MUC CRC and 389 LBK samples. Analyses of differential expression were performed using the limma voom procedure[59].

TGF-β pathway. The Reactome signalling TGF-β receptor complex and activin receptors have been classified according to the function of genes into three categories: receptors, canonical component and non-canonical components.

TCGA mutation data. Somatic mutations were retrieved using the data set of 276 samples as previously described[17] available from the cBioPortal: http://www.cbioportal.org/study?id=coadread_tcga_pub#summary. The significance of the differential prevalence of mutations per gene or per set of genes between MUC ($n=26$) and LBK ($n=174$) groups was calculated with Fisher's exact test.

Cell lines. We obtained gene expression profiles for ovarian cancer cell lines from GSE26805. We retrieved nine clearance-competent (invasive high) and six clearance-incompetent (invasive low) cell lines as defined in the original publication[35]. The EMT signature was broken into a mesenchymal gene set and an epithelial gene set according to the direction of expression changes in the cell lines.

Gene-set activity computation. The activity of a gene set in a sample was computed the following way: we first z-transformed the gene expression profiles to normalize the expression of each gene across samples. We then computed the enrichment score of a gene set using this z-transformed matrix of expression, as described in the GSEA original publication[34]. The enrichment score corresponds to the relative activity of a gene set in a sample as compared to all others. Hence, samples with high enrichment scores are the samples with the highest relative expression of the genes belonging to this set among the samples belonging to the gene expression matrix.

GSEA. GSEA was implemented in R and follows the method previously described[34]. Null distribution was obtained by 1,000 sample-shuffling. Gene signatures were obtained by ranking the genes according to the sign of the statistics (S) and the P value of the test with the following metric: $-1\times(S)\times\log(P, 10)$.

MUC versus LBK pathway enrichment analysis. Pathways were obtained from the KEGG and Reactome pathways from the C2 collection of the MSigDB database. To identify pathways enriched in CIT and TCGA data sets, we first analysed the two data sets independently. The GSEA P values were then integrated using the Stouffer method and corrected for multiple hypothesis testing with a false discovery rate (FDR) following the Benjamini–Hochberg procedure. Significant pathways were defined as those satisfying FDR < 0.2.

Statistics and reproducibility. Significance was tested with unpaired two-tailed Student's *t*-test, one-way analysis of variance (ANOVA), linear regression using GraphPad Prism or one-sided and two-sided Fisher's exact test (using R and http://www.socscistatistics.com/tests/fisher/Default2.aspx), with the level of significance set at $\alpha=0.05$ (95% confidence interval). The method used, P values and n numbers are indicated in the figure legends. P values of significance are represented as $^{****}P<0.0001$, $^{***}P<0.001$, $^{**}P<0.01$ and $^{*}P<0.05$. The exact value is indicated when possible.

No statistical method was used to predetermine sample size. No animals were excluded from the study. No method of randomization was used. The investigators were not blinded to allocation during experiments or outcome assessment.

Peritoneal effusions were collected from independent patients. The exact number of effusions analysed is indicated in each figure legend.

All experiments, including the experiment using patient specimens, were repeated at least three times independently under similar technical conditions, except for Figs. 2g,3c (Llgl2) and 6b (TGF-β + shSmad2) where the experiments were performed twice. For each figure panel, the exact number of biological replicates is indicated in the legend.

Quantitative data are represented as mean ± s.e.m., unless otherwise specified in the legend.

Representative experiments, including western blots and immunostainings, were repeatedly observed from at least three independent biological replicates, except the western blots in Supplementary Fig. 4c (siTGF-βR1) and the stainings in Supplementary Fig. 1d (atypical protein kinase C-ζ) and Supplementary Fig. 2c (EMT) that were done only two times.

Life Sciences Reporting Summary. Further information on experimental design is available in the Life Sciences Reporting Summary.

Data availability. Secondary accessions: the human colon cancer RNA-sequencing and mutation data sets used to support the findings of this study are both derived from the TCGA Research Network (http://cancergenome.nih.gov/) and are available from GSE62944 and the cBioPortal (http://www.cbioportal.org/study?id=coadread_tcga_pub#summary), respectively. The human colon cancer microarray data from the CIT cohort are available from GSE39582. The gene expression profiles for ovarian cancer cell lines are available from GSE26805.

Source data for Fig. 4a,b are provided in Supplementary Tables 2 and 3. Source data for Fig. 3h and Supplementary Fig. 5c are provided in Supplementary Videos 1 and 2. All other data supporting the findings of this study are available from the corresponding author upon reasonable request.

References

57. Fellmann, C. et al. An optimized microRNA backbone for effective single-copy RNAi. *Cell. Rep.* **5**, 1704–1713 (2013).
58. Rahman, M. et al. Alternative preprocessing of RNA-sequencing data in The Cancer Genome Atlas leads to improved analysis results. *Bioinformatics* **31**, 3666–3672 (2015).
59. Law, C. W., Chen, Y., Shi, W. & Smyth, G. K. voom: Precision weights unlock linear model analysis tools for RNA-seq read counts. *Genome Biol.* **15**, R29 (2014).

Apico-basolateral polarity orientation is controlled by TGFβ and integrin signaling and correlated with patient survival in mucinous colorectal cancer.

Authors: Charlotte Canet-Jourdan[1], Olivier Zajac[3], Jérôme Cartry[1], Christophe Desterke[2], Joel Raingeaud[1], Jean-Baptiste Lopez[1], Mélanie Polrot[4], Patrick Gonin[4], Sylvie Souquere[5], Gerard Pierron[5], Nicolas Signolle[6], Julien Adam[6], Peggy Dartigues[7], Maximiliano Gelli[8], Valeria Barresi[9], Michel Ducreux[8] and Fanny Jaulin[1*].

Affiliations:

[1] INSERM U-1279, Gustave Roussy, Villejuif, F-94805, France.

[2] Inserm, UMR-935, Villejuif, F-94800, France

[3] Institut Curie, PSL Research University, CNRS UMR 144, F-75005 Paris, France.

[4] Plateforme d'Evaluation Préclinique, AMMICA UMS 3655/ US 23, Gustave Roussy, Villejuif, F-94805, France

[5] UMR-9196, Gustave Roussy, Villejuif, F-94805, France

[6] INSERM Unit U981, Experimental Pathology, Gustave Roussy, 94805 Villejuif, France.

[7] Pathology Department, Gustave Roussy, Villejuif, F-94805, France

[8] Digestive Cancer Unit, Gustave Roussy, Villejuif, F-94805, France

[9] Department of Diagnostics and Public Health, University of Verona, Verona 37129, Italia

*Correspondence to: Fanny Jaulin: fanny.jaulin@gustaveroussy.fr

The authors declare no competing financial interests.

ABSTRACT

The metastatic dissemination of cancer remains a major cause of mortality. Cell biology approaches have the potential to bridge histological and molecular analyses to decipher the onco-morphogenetic programs that fuel cancer invasion and dissemination. The systematic prospective analysis of peritoneal effusions from over 50 patients with colorectal carcinoma (CRC) identified Tumour Sphere with Inverted polarity (TSIPs). TSIPs are malignant tumor cell clusters mediating the metastatic spread of CRC evolving from the serrated pathway, including the mucinous histotype[326]. While all TSIPs harbor an inverted apico-basolateral polarity in fluids, here, we report two distinct topologies in tissues and organotypic culture: TSIPs either conserve the inverted “apical-out” polarity or switch to a conventional “apical-in” polarity. We derived tumor explants from mucinous CRC patient-derived xenografts that recapitulate the features of primary specimens. Expression analysis and functional experiments carried ex vivo identified TGFb and focal adhesion signaling as the main drivers of polarity orientation in these cancers. An automated morphometric segmentation allowing the quantification of apical-in and apical-out components and the calculation of a polarity score proved that the apical-out histology is associated with poor patient survival. This study identifies new tumor cell behaviors and their associated oncogenic pathways that could be exploited to stratify CRC patients with high risk of metastatic spread.

INTRODUCTION

With one million new cases worldwide every year, colorectal carcinoma (CRC) is the second leading cause of cancer-related death. Large scale molecular analyses of CRCs’ genomes and expression profiles have documented CRC heterogeneity and identified consensus molecular subtypesd. Combined together these analyses indicated that sporadic CRCs develop through two main oncogenic pathways: the Chromosomal INstability pathway (CIN) that usually starts with the loss-of-function of the APC tumor suppressor gene and leads to numerous chromosomal losses and amplifications[327]. This neoplastic transformation, often localized in the left colon, is associated with the most common histological form of CRC (NOS/Lieberkuhnian). The other group of CRCs progresses in the right colon along the serrated pathway, named after the “saw-tooth” morphology of their common precursor lesions[328].

Serrated CRCs are initiated by either KRAS or BRAF gain-of-function mutations and harbor the CpG Islands Methylation Phenotype (CIMP)[95,329]. 15% of CIMPs CRC evolve toward the microsatellite instable phenotype but most of them retain a stable or low level of microsatellite instability and progress toward the most aggressive histotypes of CRCs, i.e. mucinous (MUC), micropapillary and cribriform[92].

Almost all CRC patients will succumb from metastases seeded by invasive cancer cells. Despite the heterogeneity of CRCs, invasion and dissemination has principally been studied in the sole context of the epithelial-to-mesenchymal transition (EMT). This model proposes that carcinoma progression and invasion are associated with the loss of epithelial architecture as the EMT transcriptional program is activated to promote the dissociation into single cells endowed with migratory and proteolytic activities[146,171,172]. Numerous correlative evidences between CRC progression and EMT activation have been found[330,331]. Yet, it is still unclear whether this transcriptional program is causative to invasion and metastases formation or enabling other cell properties such as stemness or resistance to chemotherapies[172]. 3D reconstruction of CRC histological specimens demonstrated the absence of individual single cells at the tumor margins[332] and point to tumour “buds” or “clusters” as the tumor intermediates conquering the invasive front[333]. In line with this morphological assessment, the fine molecular analysis of patient tumor specimens revealed that the mesenchymal signature associated with CRC is not activated in cancer cells, but rather amplified in the peritumoral stroma[74].

Genetically engineered mice models may shed some light on the participation of EMT to CRC metastatic spread, but such studies have already shown that EMT is dispensable for metastases formation in other carcinomas such as pancreatic and breast cancers[76,77]. In fact, in breast, lung, prostate cancers and sarcomas, functional studies have proven the predominant participation of collective cancer cell behaviors in the metastatic seeding of secondary lesions[202,208,334–336]. These tumor cell clusters harbor increased migratory fitness and survival capabilities, allowing them to navigate the peritumoral stroma but also circulate into the hematogenous system to reach secondary organs[337].

Yet, the mechanism that fuels the metastatic spread of digestive cancers are under-investigated and understanding the oncogenic pathways and cellular components underlying CRC dissemination remains a major unmet medical need.

Cell biology approaches have the potential to bridge the knowledge gained from histological and molecular studies in order to decrypt tumor cell invasive behaviors and open new avenues of prognostic or therapeutic investigations. To capture the malignant tumor intermediates contributing to CRC metastatic spread in patients our laboratory specialized in the retrieval and monitoring of live tumor explants from primary or metastatic sites at the time of cytoreductive surgery. We conducted two prospective systematic studies that revealed a predominant collective behavior and a strong epithelial addiction from these explants. However, depending on their molecular and histological types, CRCs adopt two distinct strategies based on the topology and migratory properties of their tumor intermediates[209,338]. The analyses of peritoneal effusions revealed that about 50% of the metastatic patients harbored large spherical clusters containing hundreds of cancer cells with a robust epithelial architecture and, strikingly, an inverted apico-basolateral polarity. Their apical surface is surrounding the tumor cell cluster and facing outwards, in contact with patients' fluids. We named them TSIPs for Tumor Spheres with Inverted Polarity[209]. Despite their differentiated features, TSIPs are associated with high peritoneal metastatic burden and poor patient prognosis. Using patients explants and experimental model systems, we identified a TSIP-based metastatic cascade that is fully collective and epithelial, without detectable contribution of EMT or single cells. Strikingly, TSIPs were only found in patients harboring CRC that evolved along the serrated pathway (88% harboring KRAS or BRAF mutation) and gave rise to the mucinous, micropapillary and cribriform histotypes[209].

Here, we combined the study of live primary cancer explants and MUC CRC histological and molecular data to investigate TSIPs invasion. This study uncovered a switch in apico-basolateral polarity orientation associated with two subtypes of MUC CRCs. Combining functional and histological approaches, we revealed the signaling pathways controlling these two topologies and identified they are associated with different patient outcome.

RESULTS

Primary tumor explants revealed an apico-basolateral polarity switch in the metastatic dissemination of mucinous CRCs to the peritoneum.

TSIPs retrieved from the peritoneal effusions of patients with metastatic colorectal carcinoma at the time of surgery were immediately embedded in collagen-I gels. As reported previously, 66% of the TSIPs retain the same inverted apico-basolateral polarity they displayed in suspension[209]. However, the remaining 34% of TSIPs lost their peripheral apical staining in collagen-I. Instead, basolateral proteins, such as EpCam and E-cadherin, localized at the extracellular matrix (ECM) abutting membrane (Fig.1A, 1B and 1C). Concomitantly, a large central cavity formed within the cell cluster (stars, Fig. 1A and 1C). The enrichment of the actin staining at the membrane outlining the cavity suggested that an apical pole has formed there, which was confirmed using the apical marker ezrin (Fig. 1C). Together, the staining revealed that, while all TSIPs have an inverted "apical-out" topology in suspension in patient peritoneal effusions, 34% of them reverted their polarity to a conventional "apical-in" polarity when embedded in ECM. To assess whether this could also happen during tissue invasion, we monitored TSIPs invading into peritoneum explants[209]. In this assay, we detected TSIPs forming a central lumen outlined with a robust actin staining, reminiscent of the observation made in collagen-I gels (Fig. 1D). To exclude any experimental artefact, we explored the histology of tumor specimens from our patient cohort. Hematoxilin Eosin Safran (HES) staining identified two distinct histological architectures, which was very homogenous in some patients and consistent with the TSIP phenotype ex vivo (Fig. 1E and 1F). As an example, Patient#6, who had all TSIPs retaining their apical-out topology in collagen-I, presented solid cell masses with an outward ezrin staining, proving the inverted topology in the metastatic tissue (Fig. 1E and 1F top panel). Patient#1, who had 78,7% of TSIPs reverting to an apical-in phenotype in collagen-I, had metastases with a glandular organization, where the apical pole of cancer cell faces large luminal cavities (Fig. 1E and 1F bottom panel). Together, these results show that all patients harbor TSIPs with an inverted apico-basolateral polarity in suspension in peritoneal effusion ("apical-out" phenotype). Yet, for a third of the patients, the TSIPs do not maintain this inverted polarity in ECM-rich tissues and switch to a normal polarity orientation with an inward apical pole surrounding a central lumen ("apical-in" phenotype Fig. 1G).

Apico-basolateral polarity orientation is a cell-autonomous features of mucinous CRCs

The robust correlation between tumor architecture and TSIP topology ex vivo, both in peritoneum and collagen-I invasion assays, suggested that the polarity orientation is a cell-autonomous feature. To validate this hypothesis, we selected three patient-derived xenograft (PDX) mice models from an independent collection of CRCs[339]. We selected 3 CRC histotypes producing TSIPs (mucinous (MUC) CRC) and analyzed the architecture of the human tumor into the mice subcutaneous stroma. As for patients, we identified two morphologies: PDX#1 and PDX#2 are composed of tumor cell masses delineated by an outward ezrin staining corresponding to the apical-out phenotype. In contrast, PDX#3 harbored a glandular organization with lumens surrounded by apical membranes, corresponding to the apical-in phenotype (Fig. 2A). Small tumors fragments were maintained in suspension for 3 days to mimic the TSIPs in the peritoneal effusion and then embedded in collagen-I gel to assess their polarity. While all TSIPs have an inverted apico-basolateral polarity in suspension (Supp Fig. 1A and 1B), they adopt different topologies in collagen-1 that are consistent with the tumor histological architecture in mice (Supp Fig. 2). Respectively 84,4% and 97,8% of TSIPs produced from PDX#1 and PDX#2 maintained their apical-out topology in collagen-I (Fig. 2B and 2C). To the contrary, TSIPs from PDX#3 reverted to an apical-in phenotype and formed lumens in collagen-I (Fig. 2B and 2C). This polarity switch is not an artefact from the markers used in immunofluorescence as we could detect opposite topologies by electron microscopy, showing microvilli at internal (apical-in) or external (apical-out) membranes (Fig. 2D). Thus, the PDXs recapitulate the observations made from the patients and attest there are two topologies in MUC CRC based on the orientation of their apico-basolateral polarity. The distinct topologies appear in the murine stroma and simple collagen-I gels, showing this feature is mostly cell autonomous.

Apical-out and apical-in explants harbor different expression profiles

The PDX explants providing truthful experimental models, we used them to compare the expression profiles of the two topologies and identify the mechanism of polarity orientation in MUC CRCs. PDX#1, PDX#2 and PDX#3 explants were maintained in suspension or embedded into collagen-I for 3 days, then their RNA was extracted and analyzed (Fig. 3A, in triplicates). Whole transcriptome experiments were investigated in each experimental condition for each PDXs. Human Clarium S chip were performed for each condition and after RMA normalization a supervised analysis was investigated by Analysis of Variance. The response of the PDXs to collagen-I was measured by Significance Analysis for Microarray algorithm in transcriptome. These analyses revealed that collagen-1 regulated more genes in PDX#3 (156 specific genes, supplementary table 1) as compared to PDX#1 and PDX#2 (34 specific genes, supplementary table 2), among which only 2 are in common (Fig. 3B). In line with these results, the global gene signature of collagen-I response allowed to drastically discriminate collagen-I embedded PDX#3 from all other transcriptomic profiles (Euclidean distances, Fig. 3C). This is confirmed to be significant by unsupervised principal component analysis (p-value = 2.84e-11, Fig. 3D and supplementary Fig 3). In order to identify the pathways differentially activated by collagen-I in PDX#3 *versus* PDX#1 and PDX#2, we performed Gene Set Enrichment Analysis (GSEA). This revealed a repression of cell cycle progression and an activation of the Sonic Hedgehog (SHH), Transforming Growth Factor beta (TGFβ), Hypoxia and Focal adhesion pathways with respective NES of +2.07, +2.33, +2.67 and +1,47 (Fig. 2E and 2F). Together, this analysis identified the pathways activated by collagen-I in PDX#3 (apical-in) and revealed that these pathways are not induced in apical-out CRCs after embedding in ECM.

Downregulated TGFβ signaling prevents normal apico-basolateral polarity orientation in TSIPs

To assess which one(s) of these signaling pathway(s) control(s) polarity orientation, we performed interference experiments using the PDX explants in collagen-1 gels. To mimic hypoxia ex vivo, we incubated organoids from PDX#1 and PDX#2 with desferrioxamine (DFO), an inhibitor of HIF1α degradation. This treatment did not impact the polarity orientation as compared with controls (Supplementary Fig. 4A and 4B). Thus, the hypoxic status of the cells is correlated to polarity, but not causative to its orientation.

No major component of the SHH pathway were differentially regulated between apical-in and apical-out tumors, neither this pathway was reported to regulate apico-basolateral polarity. Thus, we next investigated the participation of TGFβ signaling in polarity orientation. We first aimed at inhibiting the TGFβ pathway in TSIPs generated from PDX#3. Organoids were treated with two independent inhibitors of TGFβ receptor II (TGFBR2), SB431542 and A83-01. The drugs were added to the collagen-I gels (treatment) or in preceding their embedding in the matrix (pre-treatment). Both inhibitors prevented the polarity reversion that occurs when TSIPs from PDX#3 are embedded into collagen-I (Fig. 4A). While the proportion of apical-in spheres dropped, the apical-out phenotype increased significantly, from 0% to 25.56% and 87.78% after treatment with SB431542 and A83-01 respectively (Fig. 4B). Conversely, we stimulated organoids made from PDX#1 and PDX#2 with TGFβ and assessed for polarity orientation. We observed a clear response of PDX#1 to TGFβ associated with a significant drop in the number of TSIPs with inverted apical-out polarity, from 81.95% to 26.42% (Fig. 4C and 4D). In contrast, the TSIPs from PDX#2 treated with TGFβ were indistinguishable from the controls, all in their apical-out topology (Fig. 4C and 4D). Exome sequencing of TGFβ receptors and effectors identified that all harbored the TGFBR2 frame-shift mutation reported to decrease TGFβ signaling[340] while only PDX#2 display a loss-of-function mutation in Smad4 (Fig. 4E, supp Fig. 4C) and decreased levels of mRNA (Supp Fig. 4D). This likely explains why this tumor is insensitive to TGFβ stimulation. Thus, the experiments validated the participation of the TGFβ pathway to the control of apico-basolateral polarity orientation of TSIPs in MUC CRCs.

The balance between integrin-mediated adhesion and contractility controls polarity orientation in CRCs

The focal adhesion pathway is also activated in PDX#3 embedded in collagen-I, but not in the PDX#1 and PDX#2 which retain their apical-out topology. Interestingly, integrin β1 (ITGB1) controls the orientation of apico-basolateral polarity in normal renal cell lines through the downregulation of the actomyosin contractility[341]. Thus, we tested whether ITGB1 and contractility could regulate polarity orientation in CRCs. TSIPs from PDX#1 and PDX#2 were incubated with Y27632 to inhibit ROCK, an important activator of myosin activity.

This treatment reduced the number of spheres with inverted polarity by 27.6 and 5.9fold, respectively. Strikingly, this is associated with the appearance of internal apical membranes surrounding one or several luminal cavities, reminiscent of the apical-in topology (Fig. 5A and 5B). Conversely, inhibiting ITGB1 with AIIB2 function blocking antibodies and shRNA or increasing contractility with calyculin-A strongly repress the apical-in phenotype in PDX#3, with the vast majority of TSIPs retaining their apical-out topology in collagen-I (87.33%, 52.07% and 90.02% respectively, Fig. 5C and 5D). Thus, the core machinery controlling A/B polarity orientation in normal cell is at play in the topology of MUC CRCs.

We then investigated whether the balance between adhesion and contractility could relate to defective TGFβ signaling. We first hypothesize that decreased activation of non-canonical TGFβ could increase the level of RHOA, ROCK and therefore contractility. However, western blot experiments showed that the amount of phosphorylated myosin-II, a read-out for ROCK activity and contractility[342], is similar in the 3 MUC CRC PDXs (Data not shown). We then reasoned that integrin function could be impaired. We showed that ITGB1 controls the apical-in orientation of PDX#1 and PDX#2 treated with Y27632 (Fig. 6A and 6B) or TGFβ (Fig. 6C and 6D) proving the integrin is functional and do not harbor loss-of-function mutations. Yet, TGFβ is a known regulator of ITGB1 transcription and the microarray analysis revealed that PDX#1 and PDX#2 harbored lower levels of mRNA coding for ITGB1 (Fig. 6E). In line with this, we found that the levels of ITGB1 protein detected by immunofluorescence in PDX#1 and PDX#2 are lower than in PDX#3 (Fig. 6F and 6G). Together, these results show that the balance between ITGB1-mediated adhesion and actomyosin contractility is involved in the inverted apical-out topology of TSIPs in collagen-I.

Histological assessment of apical-out clusters and polarity score stratifies MUC CRC patient survival.

In order to determine if A/B polarity orientation could impact clinical outcome, we performed a histological analysis from a published annotated cohort of MUC CRC patients[333]. The apico-basolateral polarity of Cytokeratin 20 positive clusters was determined using an algorithm created in Definiens Developer XD (Definiens, Munich, Germany) software for 36 patient specimens.

Based on their shape and their localization relative to the stroma and the mucus (stained by the Alcian Blue), clusters were classified into apical-in or apical-out categories (Fig 7A). The results obtained through this morphometry analysis are consistent with the cohort of CRC patients with peritoneal carcinomatosis (Fig. 1B), showing that two third (27/36) of the patients harbored mostly apical-out organization while de remaining third (9/36) display a glandular apical-in architecture (Fig 7B). We also calculated a polarity score, based on the ratio between apical-in and apical-out components. For the prediction of death from mucinous CRC, we used Receiver Under Operating characteristics (ROC) analyses to calculate the most accurate cut-off values of the number of apical-out clusters and the polarity score.

Log rank test with Kaplan-Meier curves showed that patients harboring a CRC with a high number of apical-out clusters (> 92) had a significantly shorter cancer-specific survival (CSS) than patients having a CRC with a low count of apical-out clusters (≤ 92) (P = 0.04; H.R.: 2.5; C.I.: 1-6.3) (Fig. 7C). Similarly, the patients having a CRC with a low polarity score (ratio between apical-in and apical-out < 2.75) had significantly shorter CSS than those harboring a CRC with a high score (≥ 2.75) (P = 0.02; H.R.: 3.1; C.I.: 1.1-8.4) (Fig. 7D). Together, these data point to two subgroups of MUC CRC patients based on the topology of the TSIPs they produced and the architecture of their tumor. The biology of these cancers is different as is the clinical outcome of the patients, the apical-out cancers being associated with shorter survival.

TSIPs apico-basolateral polarity is neither an advantage nor a disadvantage in terms of metastatic abilities (not submitted).

Since apical-out TSIPs are found in majority in patients, we reasoned that the apical-out topology could confers TSIPs an advantage in terms of metastatic abilities. To test that, we injected TSIPs in the peritoneal cavity of mice treated with PBS or IgG for control groups. (Fig.NS control A). After 6 weeks, we evaluated invasion using the Peritoneal carcinomatosis index (PCI, Fig.NS control E) and assess polarity phenotype by quantifying the presence of a luminal cavity, reminiscent of the apical-in topology, on HES staining of samples displaying macroscopic nodules. The phenotype was rather mixed in PDX#1 and PDX#3 (Fig.NS control B. top right an Fig. NS control C). Since PDX#3 slides presenting many clusters embedded in mucin, they did not present any luminal cavities since no ECM is at their abutting surface to trigger apico-basolateral polarity reversion. To truly evaluate the proportions of clusters able to form a luminal cavity, we quantified only clusters in contact with stromal components.

By doing so, the percentage of clusters displaying an apical-in topology increased (1.2fold) and is consistent with PDX#3 ex vivo results. Then, PCI assessment (Fig. NS control E) demonstrated that PDX#1 is able to induce a peritoneal carcinomatosis, whereas PDX#2 an PDX#3 did not invade the abdominal compartment (Fig. NS control F).

In treated groups, polarity reversion was achieved in PDX#1 and PDX#3 but not in PDX#2 (Fig. NS treated B and C). Indeed, the presence of a luminal cavity reminiscent of the apical-in topology increased by 1.72fold the Y27632 group (control mean=35.68±8.93%; treated mean=61.62±9.58%), and decreased by 3.78fold in the AIIB2 group (control mean=54.48±25.51%; treated mean=14.66±17.13%) in PDX#1 and PDX#3 respectively. Nevertheless, inverting TSIPs polarity did not impact their metastatic abilities (Fig. NS treated D), suggesting that A/B polarity is neither an advantage or a disadvantage in metastatic seeding.

FIGURES

Figure 1: Primary tumor explants revealed an apico-basolateral polarity switch in the metastatic dissemination of mucinous CRCs to the peritoneum.

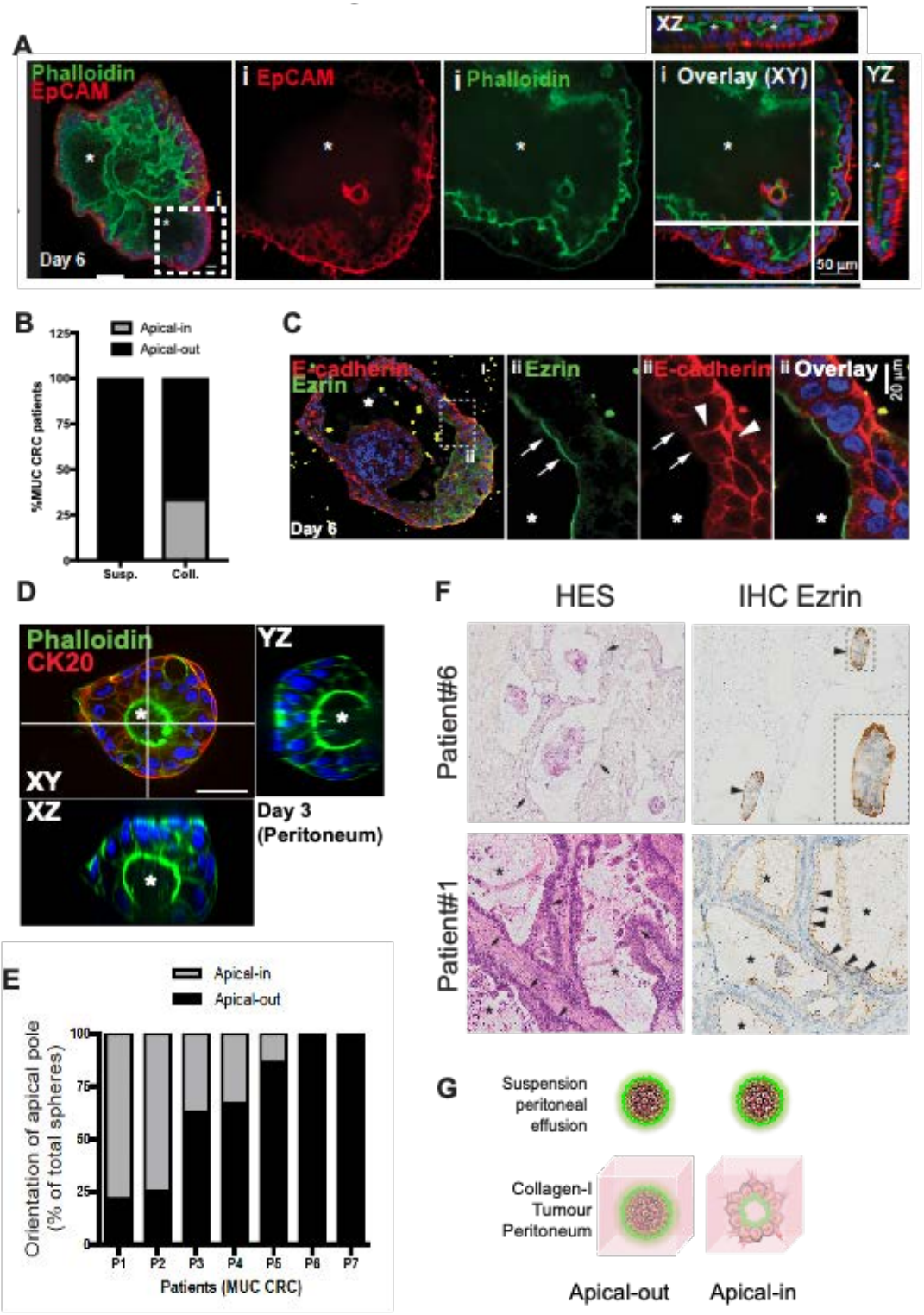

Figure 1: Primary tumor explants revealed an apico-basolateral polarity switch in the metastatic dissemination of mucinous CRCs to the peritoneum.

(A) Representative image of a patient MUC CRC sphere forming a luminal cavity after 3 days in collagen, immunostained for EpCam, phalloidin and DAPI.

(B) Quantification of TSIPs polarity in suspension (in peritoneal effusions) and in collagen. The graph shows the percentage of apical-out vs. apical-in spheres based on the outward or luminal localization of ezrin respectively, in one confocal-Z-section (30 TSIPs/patient for 7 patients).

(C) Representative image of an apical-in patient MUC CRC sphere after 3 days in collagen, immunostained for ezrin, E-cadherin and DAPI.

Figure 2: Apico-basolateral polarity orientation is a cell-autonomous features of mucinous CRCs.

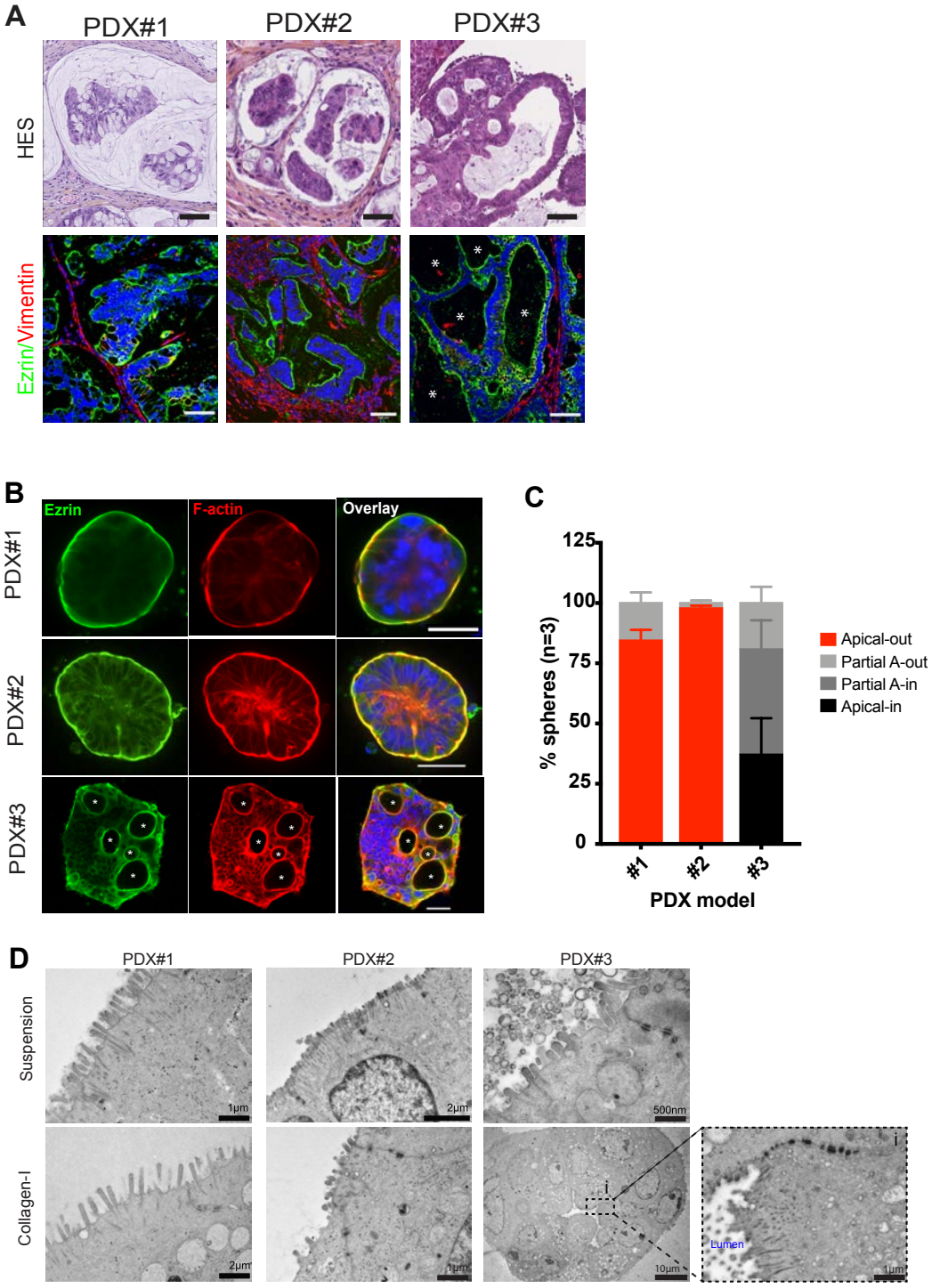

Figure 2: Apico-basolateral polarity orientation is a cell-autonomous features of mucinous CRCs.

(A) HES staining (top panel) and ezrin, vimentin and DAPI immunostaining (bottom panel) of subcutaneous MUC CRCs tumours: apical-out (PDX#1 and #2) and apical-in (PDX#3) PDX tumors. Scale bar=50μm (top panel) and 100μm (bottom panel). *=lumen.

(B) TSIPs from PDXs after 3 days in collagen-I gels, immunostained for ezrin, F-actin and DAPI. Scale bar=50μm. *=lumen.

(C) Quantification of PDXs' TSIPs A/B polarity orientation based on Supplementary figure1 criteria in one confocal-Z-section (n=3 independent experiments).

(D) Electron microscopy of PDXs spheres in suspension or after 3days in collagen-I gel showing microvilli at the periphery for PDX#1 and PDX#2 and internal membranes for PDX#3.

Figure 3: apical-out and apical-in explants harbor different expression profiles.

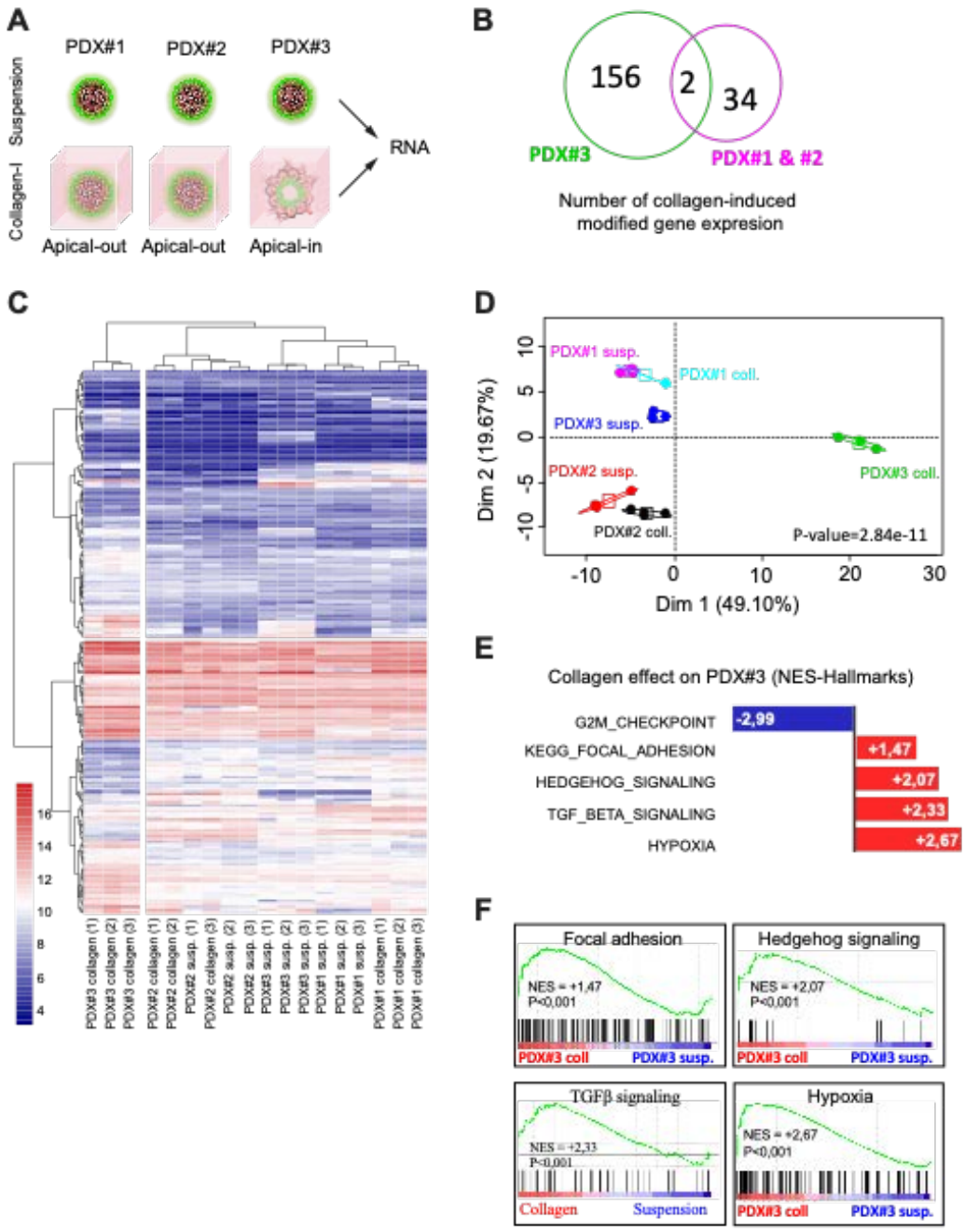

Figure 3: apical-out and apical-in explants harbor different expression profiles.

(A) Schematic representation of the protocol used to generate mRNA for the microarray. TSIPs' RNA were extracted either after 3 days in suspension or in collagen-I gels.

(B) Venn diagram representing the number of genes regulated by collagen-I embedding.

(C) Discrimination of PDX#3 in response to collagen-I stimulation. Corresponding to supplementary table #1.

(D) Results from (B) and (C) are confirmed by an unsupervised principal component analysis.

(E,F) The Gene set enrichment analysis revealed that PDX#3 spheres in collagen-I specifically repress the cell cycle progression (G2M checkpoint) and activate four pathways: Focal adhesion, Sonic Hedgehog, TGFβ and hypoxia signaling.

Figure 4: Downregulated TGFβ signaling prevents normal apico-basolateral polarity orientation in TSIPs.

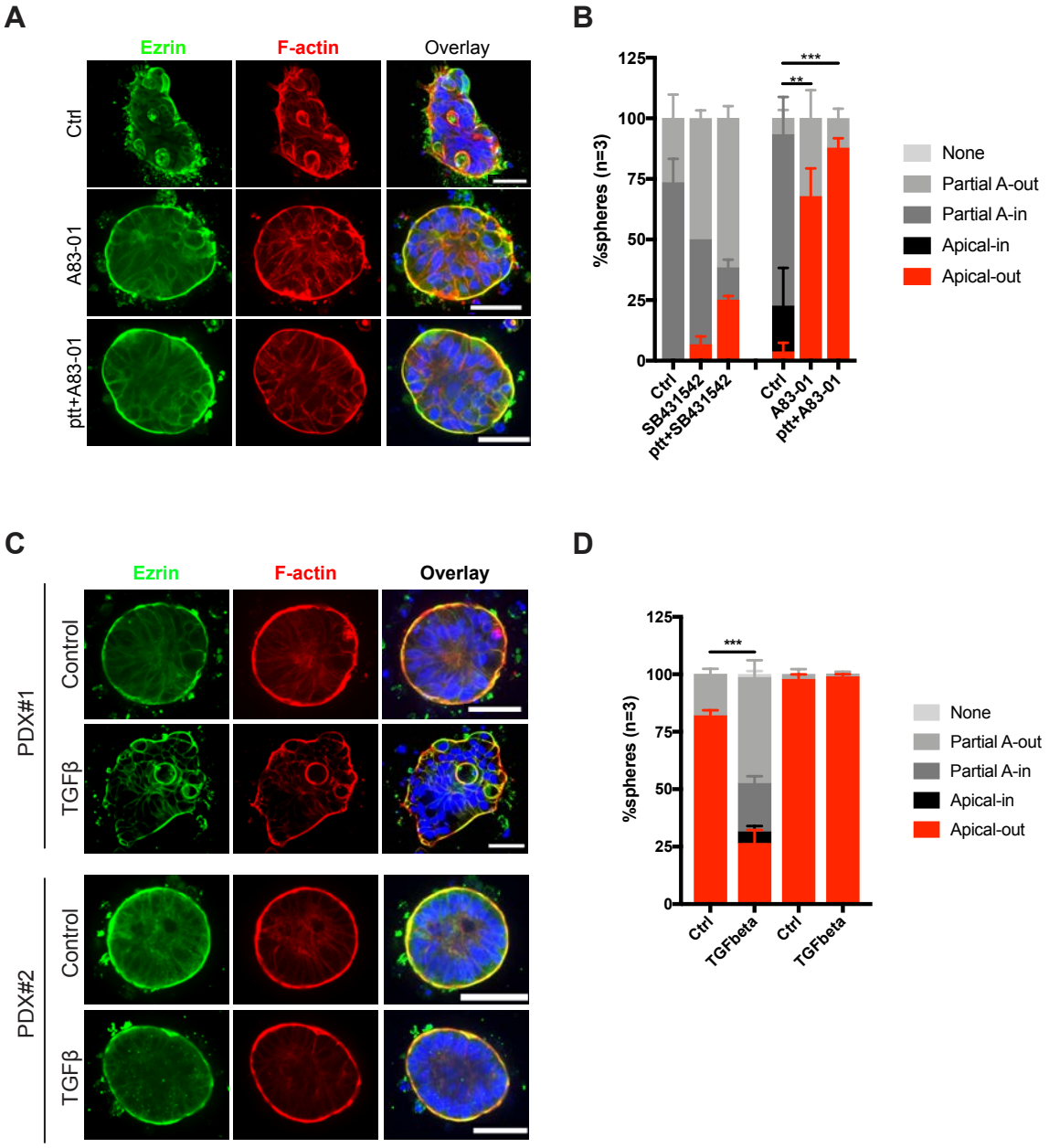

E

	TGFBR2 (c.458delA)	SMAD4 (c.804G>A)
PDX#1	MUT*	WT
PDX#2	MUT*	MUT
PDX#3	MUT*	WT

Figure 4: Downregulated TGFβ signaling prevents normal apico-basolateral polarity orientation in TSIPs.

(A) Immunostainings for ezrin, F-actin and DAPI in control condition, of PDX#3 treated with A83-01 (10mM) or pretreated in suspension for 3 days and then treated in collagen-I gels for 3 days (10mM).

(B) Quantification of PDX#3 sphere's phenotypes treated and pre-treated with SB431542 (10μM) or A83-01 (10mM).

(C) Immunostainings for ezrin, F-actin and DAPI after 3 days treatment of TGFβ (20ng/mL) for PDX#1 and #2 or SB431542 (10μM) for PDX#3.

(D) Quantifications of PDX#1 and PDX#2 spheres' phenotypes after TGFβ treatment.

(E) Summary table recapitulating TGFβ signaling pathways mutations in PDXs, obtained by whole exome sequencing (corresponding to Supp Fig. 4A). *frameshift mutation corrected by transcriptomic slippage and responsible for low TGFβ signaling[340].

Figure 5: The balance between integrin-mediated adhesion and contractility controls polarity orientation in CRCs.

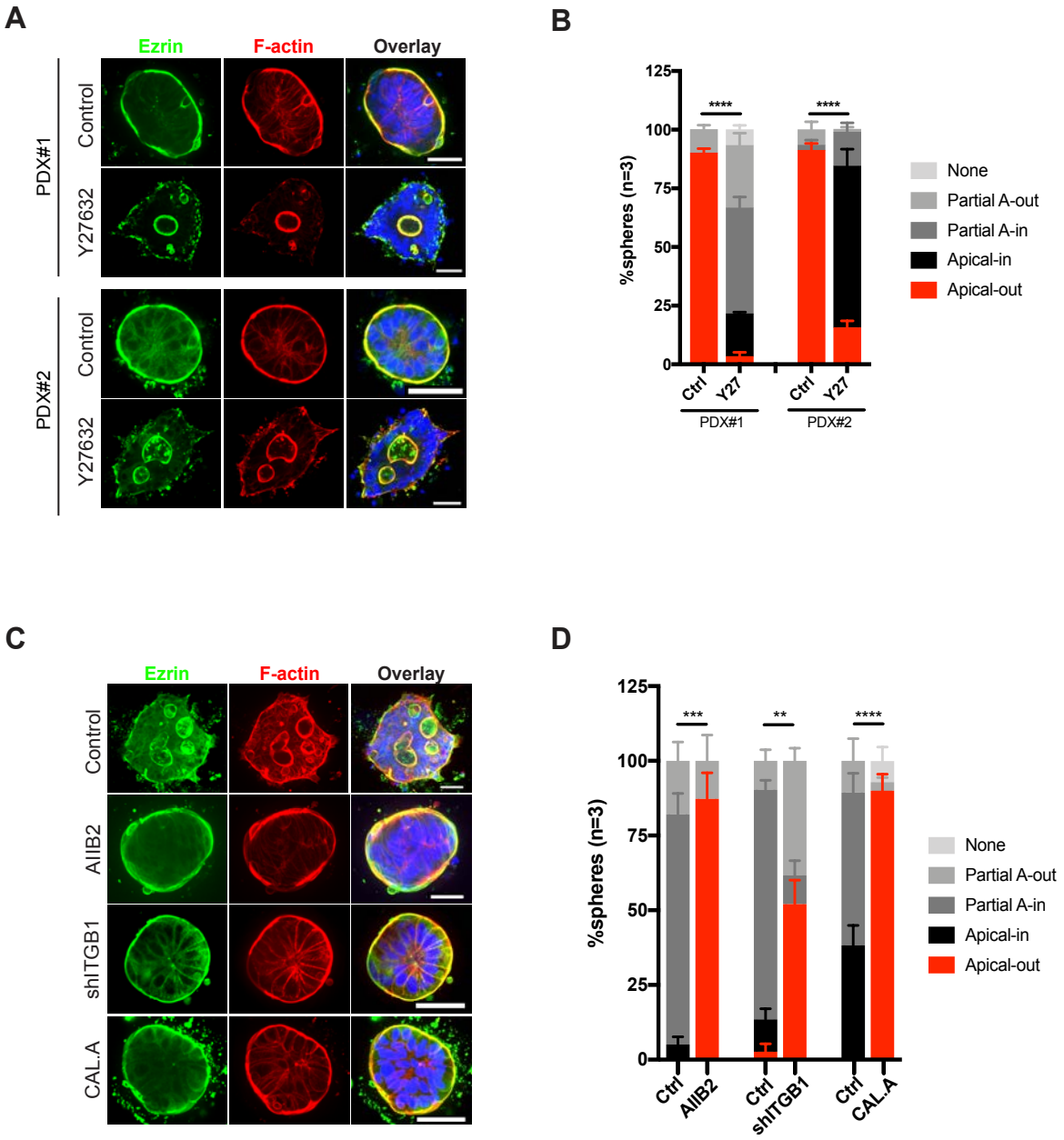

Figure 5: The balance between integrin-mediated adhesion and contractility controls polarity orientation in CRCs.

(A) Spheres from PDX#1 (top panel) and PDX#2 (bottom panel) immunostained for ezrin, F-actin and DAPI after treatment with Y27632 (25μM).

(B) Quantifications of PDX#1 and PDX#2 spheres' phenotypes after Y27632 treatment.

(C) Spheres from PDX#3 after treatment with AIIB2 (1μg/mL), shITGB1 or Calyculin-A (1nM) and immunostained for ezrin, F-actin and DAPI.

(D) Quantifications of PDX#3 spheres' phenotypes after AIIB2, Calyculin-A treatment or shITGB1.

Scale bar=50μm.

Figure 6: Polarity reversion induced by actomyosin relaxation and TGFβ are mediated by β1-integrins.

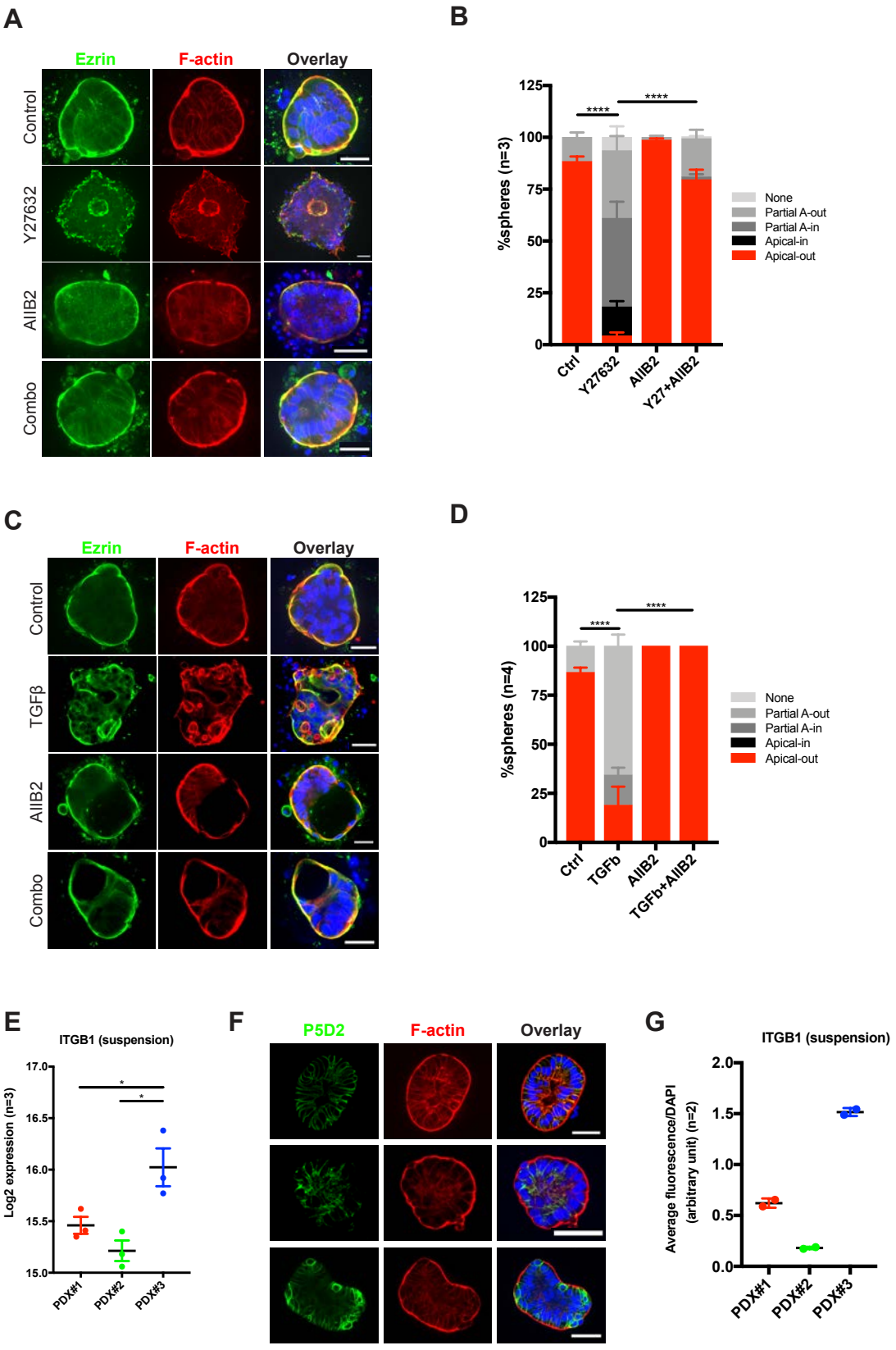

Figure 6: Polarity reversion induced by actomyosin relaxation and TGFβ are mediated by β1-integrins.

(A) PDX#1 spheres immunostained for ezrin, F-actin and DAPI after 6 days in collagen-I gels treated with Y27632 (25μM), AIIB2 (1μg/mL) or the two combined (combo).

(B) Quantifications of PDX#1 TSIPs polarity after Y27632, AIIB2 or combo treatments.

(C) PDX#1 spheres immunostained for ezrin, F-actin and DAPI after 6 days in collagen-I gels treated with TGFβ (20ng/mL), AIIB2 (1μg/mL) or the two combined (combo).

(D) Quantifications of PDX#1 TSIPs polarity after TGFβ, AIIB2 or combo treatments.

(F) ITGB1 Log2 expression of the three PDX models in suspension.

(G) Immunostainings for β1-integrins (P5D2), F-actin and DAPI of PDX#1, #2 and #3 in suspension.

Scale bar=50μm.

Figure 7: Histological assessment of apical-out clusters and polarity score stratifies MUC CRC patient survival.

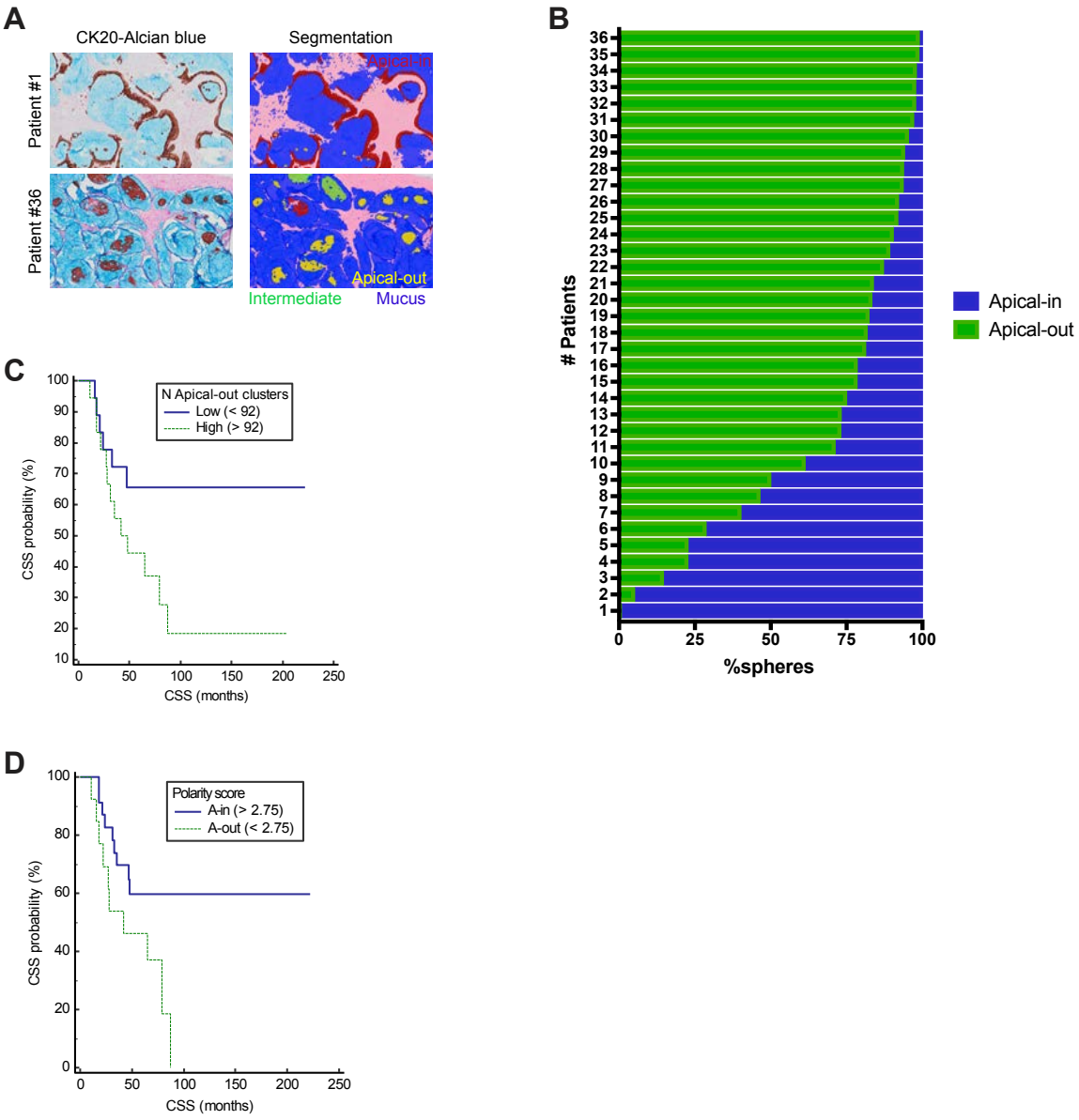

Figure 7: Histological assessment of apical-out clusters and polarity score stratifies MUC CRC patient survival.

(A) Staining for CK20 and Alcian blue of two MUC CRC patients and the corresponding segmentation from the morphometry analysis. The top panels show a region that is mostly represented by apical-in tumoral component while tumor in the bottom panels harbor an apical-out architecture.

(B) Quantitative representation of the apical-in (blue) and apical-out (green) component for each MUC CRC patient and the associated polarity score (apical-in/apical-out).

(C-D) Kaplan-Meier curves displaying cancer-specific survival depending on the number of apical-out clusters (C) and polarity score (D). The log-rank test indicates a significant difference between the survival curves.

Supplementary Figure 1

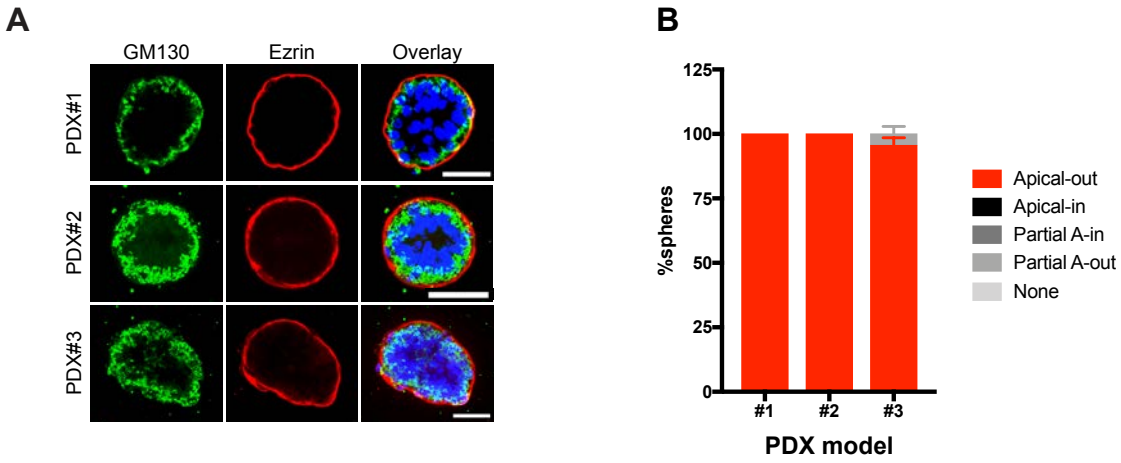

(A) PDXs spheres immunostained for GM130, ezrin and DAPI. Scale bar=50µm.

(B) Quantification of spheres A/B polarity orientation from one confocal-Z-section.

Supplementary Figure 2

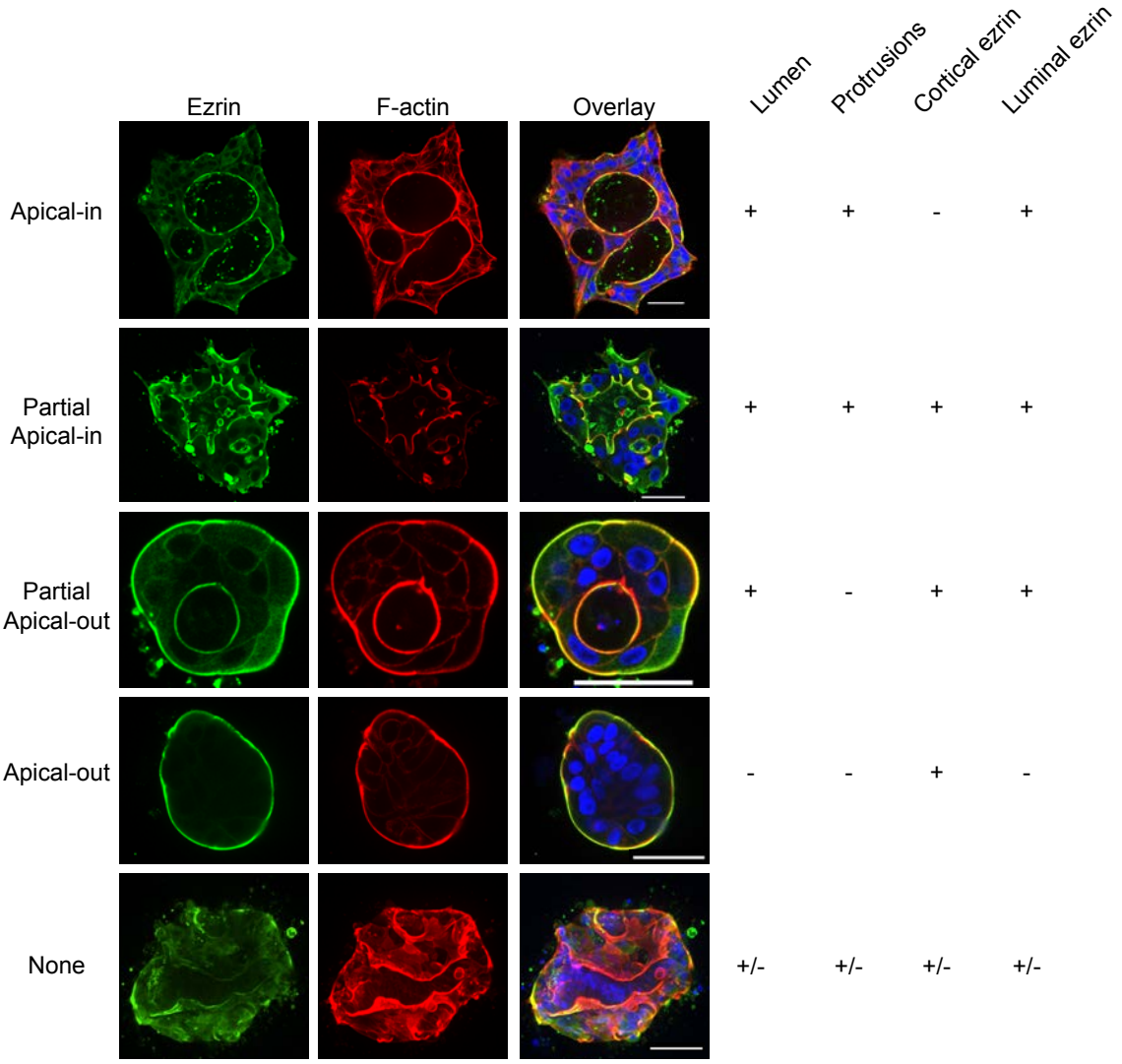

Representative images of TSIPs polarity in collagen-I immunostained for ezrin, F-actin and DAPI. Various topologies are observed and quantified based on morphological characteristics and localization of ezrin.

Supplementary Figure 3

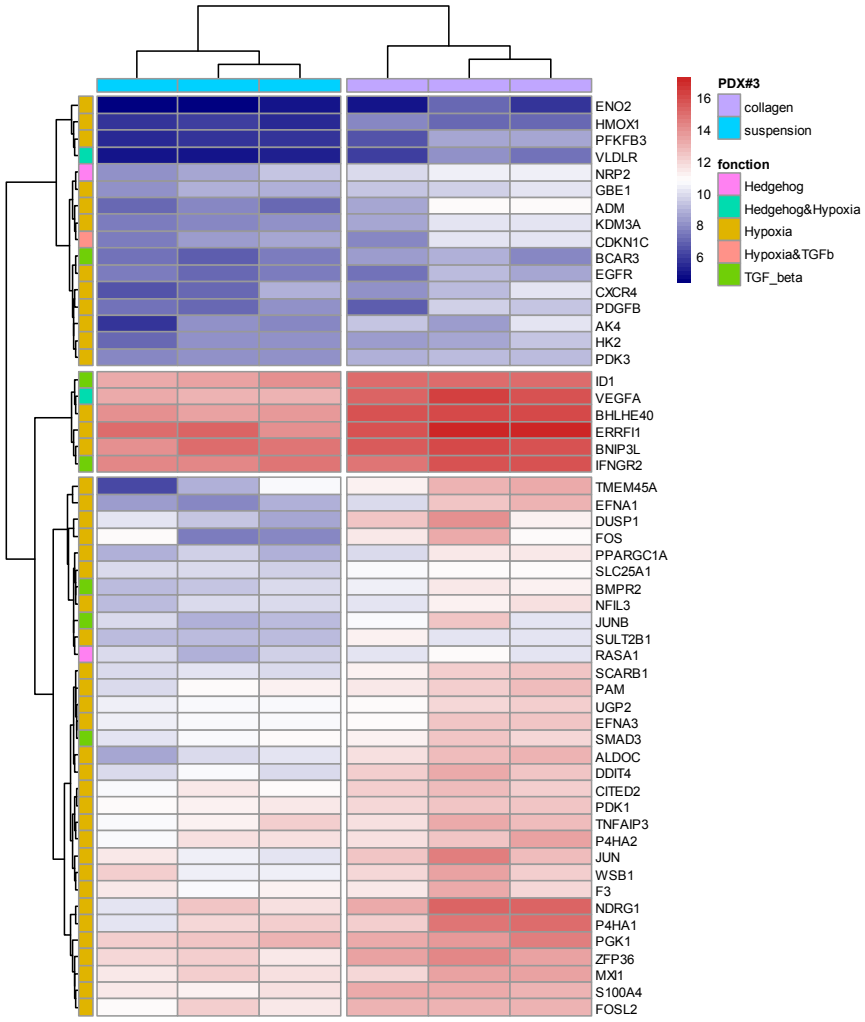

54 molecules with Fold Change over 2 in PDX#3 in collagen-I

In GSEA collagen-I PDX#3 specific signature, 54 genes were found up regulated with a fold change over 2 and reclassified experimental groups.

Supplementary Figure 4

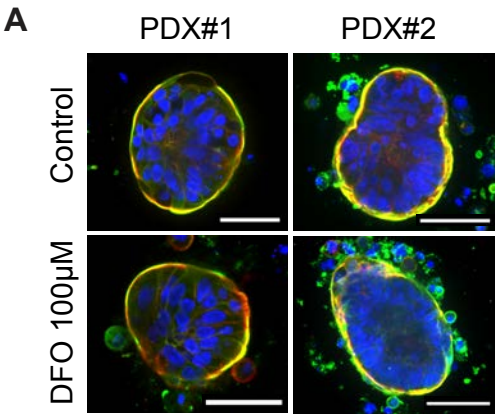

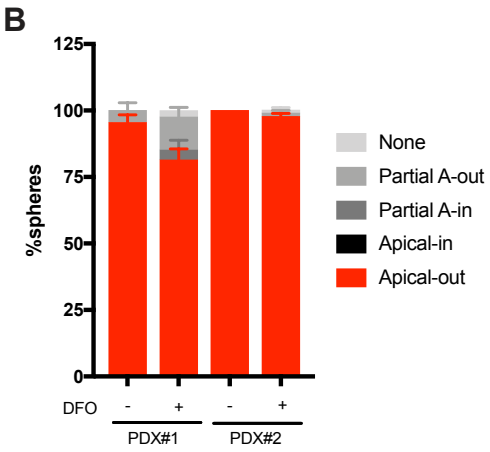

C

	Mut Code	GeneName	Chromosome	Position	ID	RefNucleo	AltNucleo	functionalClass	HGVS.c	HGVS.p	TranscriptID	Exon
PDX#1	TGR1	TGFBR2	chr3	30691871	rs79375991;COMS1744957,COSM1180952	GA	G	frameshift variant	c.458delA	p.Lys153fs	NM_001024847.2	4/8
	SMA2	SMAD4	chr18	48591918	rs80338963;COSM14140	C	T	missense variant	c.1081C>T	p.Arg361Cys	NM_005359.5	9/12
PDX#2	TGR1	TGFBR2	chr3	30691871	rs79375991;COMS1744957,COSM1180952	GA	G	frameshift variant	c.458delA	p.Lys153fs	NM_001024847.2	4/8
	SMA1	SMAD4	chr18	48584726		G	A	stop gained	c.804G>A	p.Trp268*	NM_005359.5	7/12
PDX#3	TGR1	TGFBR2	chr3	30691871	rs79375991;COMS1744957,COSM1180952	GA	G	frameshift variant	c.458delA	p.Lys153fs	NM_001024847.2	4/8

D

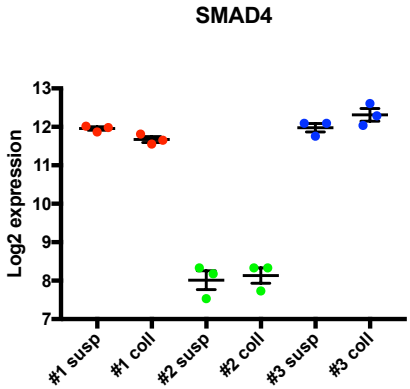

Supplementary Figure 4:

(A) TGFβ signaling pathway mutations in PDXs obtained after whole exome sequencing.

(B) SMAD4 Log2 expression for each PDX in suspension and after 3 days in collagen-I.

(C) TSIPs from PDX#1 and #2 treated with DFO (100μM, 3 days) and immunostained for ezrin, F-actin and DAPI.

(D) Quantifications of PDX#1 and PDX#2 spheres' phenotypes after DFO treatment.

Scale bar=50μm.

Supplementary Table 1

gene	PDX#3 ratio Coll/Susp
C3	45,88656794
KCTD11	14,89407546
CLIC3	12,90626815
GPER1	11,84878042
LRP1	10,43481656
ALOX15B	9,51365692
CA9	8,359017223
SORL1	8,092955522
SCD	7,799238846
CEMIP	7,34451216
VEGFA	6,78963177
AHNAK	6,742732358
HSD3B1	6,133313379
FLNB	5,938094283
DDIT4	5,869889452
SERPINA1	5,78907695
GAL3ST1	5,735820992
SLC22A18	5,578974665
MYO7B	5,438969491
SYNPO	5,327037118
NPY4R	4,890561111
PRKAA2	4,868014055
C6orf223	4,823231311
BHLHE40	4,75682846
PRAP1	4,691339797
CA2	4,469148552
PRKCDBP	4,267328972
NOXO1	4,208579393
ATP2B4	4,160239736
CDC42BPB	3,89061979
AGRN	3,881640926
ACSS2	3,84593221
FAM213A	3,434261746
DYNC1H1	3,426336076
QSER1	3,426336076
S100A4	3,348078452
TRIB3	3,234030609
PTPRF	3,21912069
TRIB2	3,066656689
MSL1	3,059579387
HMOX1	3,059579387
DUSP6	3,010493495
PRSS12	2,989698497
TFF3	2,975915028
AMOT	2,948538435
PIK3C2B	2,948538435
PLA2R1	2,948538435
ITGB4	2,928171392
NBEAL1	2,928171392
TMEM135	2,867910496
ID1	2,815387168
IGF2R	2,815387168
GTF2IRD2B	2,732080514
LAMA5	2,732080514
ZFAND3	2,713208655
BAZ2A	2,700699892
HIST1H2AC	2,694467154
PARP14	2,67585511
CIDEB	2,663518559
FOXN3	2,645120292
DOCK4	2,602683711
MTRNR2L9	2,560927954
KAT2B	2,560927954
EYA4	2,549121255
UGT2A3	2,5198421
MTRNR2L6	2,514026749
TLK1	2,496661098
ELMSAN1	2,496661098
TANC1	2,4794154
ANO6	2,462288827
PER2	2,445280555
SLC41A2	2,445280555
SPG11	2,428389769
PITX2	2,394957409
VPS13C	2,37841423
PRPF8	2,345669898
ARL4A	2,30271096

gene	PDX#3 ratio Coll/Susp
PTK6	2,286804974
NBAS	2,265767771
PTGR1	2,219138944
CCL14	2,208908001
MAN2A1	2,198724227
SEC24A	2,193649959
CST3	2,188587403
SLC25A1	2,128740365
FZD5	2,128740365
NAT8	2,123827608
PAK2	2,118926189
KDM5B	2,114036081
SECISBP2L	2,109157259
PSD4	2,075319318
ACSL3	2,070529848
PDK3	2,06575143
MIA3	2,03731162
PGAM1	2,02791896
EPAS1	2,018569602
RPL29	2,004626324
PSMD1	-2,0139111
C20orf196	-2,032609864
COL3A1	-2,046747784
RRP7A	-2,051482243
MED24	-2,080119868
SETD7	-2,084931522
TTC13	-2,099433367
GLE1	-2,104289696
MBTPS2	-2,118926189
DHDDS	-2,123827608
TSFM	-2,128740365
SLC20A2	-2,163449332
CASP2	-2,173469725
RGS2	-2,183536529
NT5DC2	-2,239743208
OGFOD1	-2,260538779
FAM109B	-2,313376368
SLC37A3	-2,324091174
C16orf62	-2,324091174
KLHL18	-2,367448977
MRRF	-2,37292527
IPO9	-2,383915887
ZAK	-2,394957409
MFSD1	-2,422785474
ITGAE	-2,422785474
L3MBTL2	-2,456606299
HSPA14	-2,490899245
NUBPL	-2,508224819
SUPT16H	-2,578740617
SLC39A8	-2,614738494
CHID1	-2,639015822
REEP4	-2,682044796
PADI2	-2,744734621
HACD3	-2,783049688
CMSS1	-2,821899614
SLC25A32	-2,907945035
NMU	-2,948538435
STEAP4	-3,052518418
CLPB	-3,080860445
RTKN2	-3,095129987
MTHFD1	-3,271608234
DDIAS	-3,466148183
CACNB4	-3,490257151
TRMT1	-3,588381635
ELOVL7	-3,663781161
RCC1	-3,810551992
APOBEC3B	-3,837056477
FANCI	-4,093495568
REP15	-4,469148552
CORO1A	-4,823231311
TACC1	-4,845570948
CDCA7L	-5,004872558
COCH	-5,401399785
CGB1	-6,276672783
TMEM173	-6,453134074
CGB	-6,758329389
CGB8	-7,908112163
SLC43A1	-9,084035433
REG1B	-11,65868633
HEPACAM2	-20,39297004
REG1A	-29,71940512

Ratio of the Log2 expression of PDX#3 in collagen/suspension.

Supplementary Table 2

gene	PDX#1 and PDX#2 ratio Coll/Susp
CCL20	34,73536455
UBD	23,45244882
CXCL8	12,68454619
MMP7	8,845845227
PI3	7,251770827
TNFAIP3	5,683054957
GLIPR1	5,650322969
TNFRSF9	5,241573615
BIRC3	4,884914575
PLAU	4,839976357
NDUFA4L2	4,407620464
CXCL1	4,301977562
SPRR2A	4,121968081
CXCL11	3,995381687
IL1B	3,913157921
IL32	3,462146244
IL1A	3,410539567
ARRDC3	3,07730335
KRT6A	3,034937206
S100A3	2,783049688
SERPINB9	2,728926113
DCBLD2	2,703821666
MAOB	2,685145006
VNN1	2,596677176
IFI6	2,560927954
CLIC3	2,332159834
LAMC2	2,221704075
SDC4	2,198724227
GUCA2A	2,198724227
B3GALT5	2,153475136
TGM2	2,131201003
BHLHE40	2,089754306
ADGRF1	2,082524305
SULT1B1	2,077718207
CD83	1,961104844
IFNGR2	1,95657896

Ratio of the Log2 expression of PDX#1 and PDX#2 in collagen/suspension.

Figure not submitted (control): TSIPs apico-basolateral polarity is neither an advantage nor a disadvantage in term of metastatic abilities.

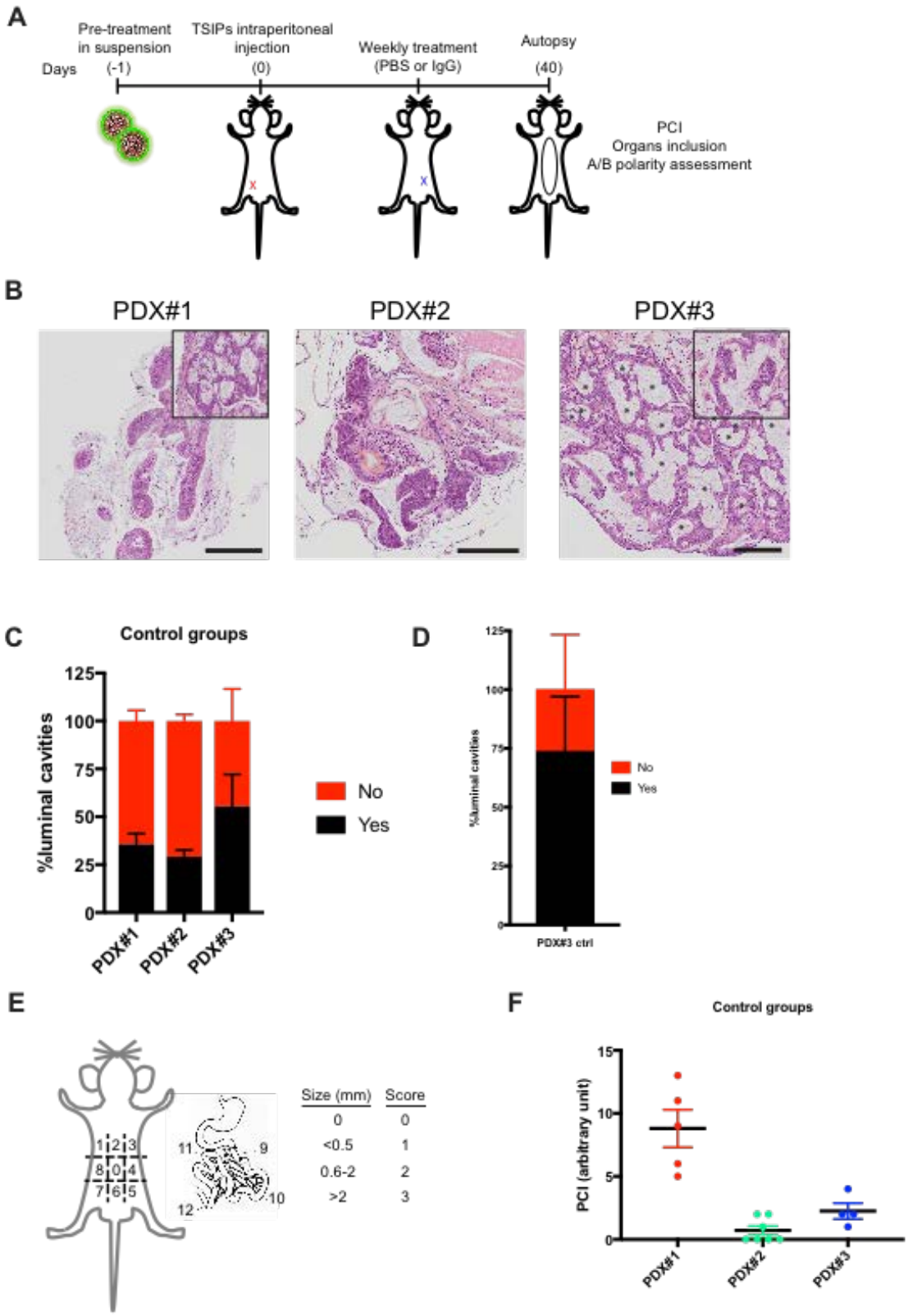

Figure not submitted (control): TSIPs apico-basolateral polarity is neither an advantage nor a disadvantage in terms of metastatic abilities (control groups).

(A) Schematic representation of the peritoneal carcinomatosis model obtained with PDX#1, PDX#2 and PDX#3 TSIPs in immunocompromised mice for the control groups.

(B) HES staining for the control groups. PDX#1 and PDX#3 display mixt phenotypes (see top right of HES staining). Scale bar=200μm.

(C) Quantification of the percentage of clusters displaying a luminal cavity for control groups of each PDX model.

(D) Quantification of the percentage of PDX#1 clusters in contact with stromal components and displaying a luminal cavity.

(E) Schematic representation of Peritoneal carcinomatosis index (PCI) evaluation.

(F) PCI for control groups of each PDX models.

Figure not submitted (treated): TSIPs apico-basolateral polarity is neither an advantage nor a disadvantage in terms of metastatic abilities (treated groups).

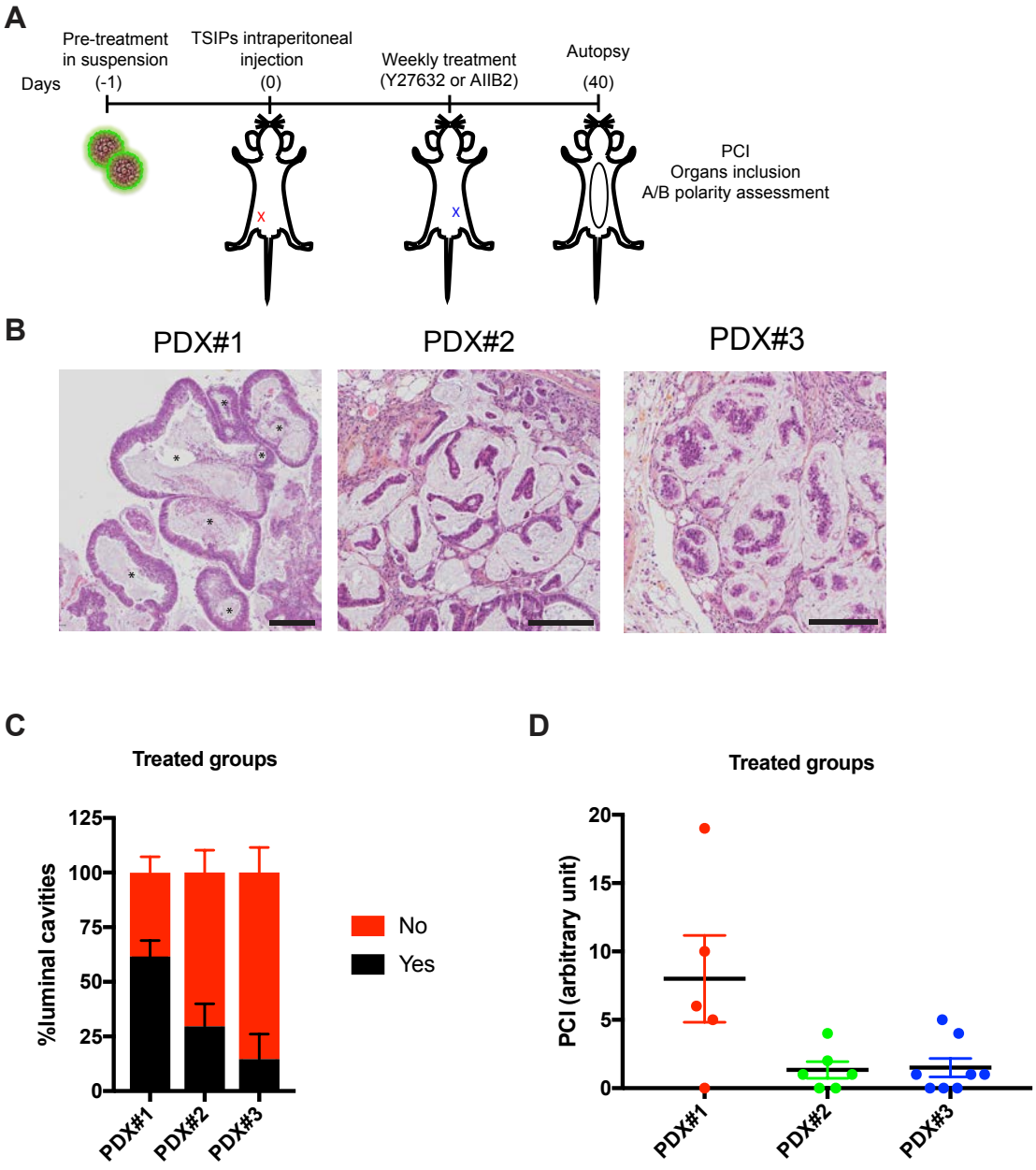

Figure not submitted (treated): TSIPs apico-basolateral polarity in neither an advantage nor a disadvantage in terms of metastatic abilities (treated groups).

(A) Schematic representation of the peritoneal carcinomatosis model obtained with PDX#1, PDX#2 and PDX#3 TSIPs in immunocompromised mice for the treated groups (Y27632 10mg/kg/twice a week for PDX#1 and PDX#2, AIIB2 2.5mg/kg/week for PDX#3).

(B) HES staining for the treated groups. Scale bar=200μm.

(C) Quantification of the percentage of clusters displaying a luminal cavity for treated groups of each PDX model.

(F) PCI for treated groups of each PDX models.

DISCUSSION

By studying MUC CRC patients' specimens, our team identified a new tumoral intermediate composed of about a hundred of tumor cells forming spheres and displaying a strong epithelial signature. In suspension, like in the peritoneal effusions where we found them in the first place, they display their apical pole at the cluster periphery. In those samples, only a few single cells were found, which did not survive in culture conditions (liquid or matrix), while the tumor clusters did. Their collective-dependent survival was further confirmed by the fact that the destabilization of their cell-cell junctions or their dissociation into single cells led to apoptosis after a few days. Furthermore, by injecting spheres or the equivalent number of single cells into the peritoneal cavity of mice, the clusters were much more efficient at forming metastases. Thus, the collective feature seems to be a requirement for cell survival and therefore for dissemination and colonization of distant organs. The fact that clusters are more efficient than single cells at forming metastases has already been described in breast[337,343], ovarian cancers[344] and melanoma[345] for example.

The absence of EMT activation (at cellular and molecular levels) and the strong epithelial characteristics of TSIPs correlate with the low TGFβ signaling associated with these cancers. Indeed, we have demonstrated that in patients, as well as in MUC CRC cell lines and PDXs, both the canonical and non-canonical TGFβ signaling were downregulated. Being a master inducer of EMT, this likely prevents the activation of this program[346] and participates to both TSIPs generation and A/B polarity preservation. Thus, MUC CRC dissemination seems to go against the predominant model based on EMT-like programs. This is in line with recent work demonstrating that metastasis can result from an EMT-independent mechanism in breast and pancreatic cancers[76,77]. A parallel study in the lab also identified that NOS CRC maintain their epithelial architecture and apico-basolateral polarity at early stage of their invasion into the mucosae[338].

By collecting patients live specimens, we were able to reveal a new mode of invasion and dissemination that could not be predicted by experimental model systems. TSIPs contradict the prevailing consensus that the loss of epithelial architecture is a requirement for cancer progression. This also allowed us to identify a second mode of collective migration that mechanistically resembles the ameboid locomotion of single cells. In Pagès et al.[210], we demonstrate that in confined environments, TSIPs indeed use a contraction-based mechanism for migration. While confinement in the peritoneal cavity has not yet been investigated, it likely takes place in lymphatic vessels where we identified both TSIPs and other tumor cell clusters.

Surprisingly, once embedded in matrix (at metastatic sites or in collagen gels) TSIPs display two different behaviors: for two-thirds of the patients TSIPs maintain their inverted topology (called “apical-out”), while one-third of TSIPs were able to relocalize their apical pole away from the ECM and formed a lumen (called “apical-in”).

My PhD work allowed me to solve the founding questions I raised 4 years ago that stand as follow: (i) what are the oncogenic alterations providing TSIPs with their inverted A/B polarity?

(ii) what are the mechanisms of A/B polarity orientation in MUC CRCs?

(iii) Does polarity orientation impact MUC CRC metastatic potential?

(iv) Is A/B polarity correlated to distinct patient outcome?

I will first discuss how the participation of TGFβ signaling to TSIPs biology and how this pathway could influence the balance between adhesion and contractility and TSIPs A/B polarity. Second, how spheres topology seems to not be sufficient to dictate their metastatic abilities and finally, see how the apical-out topology is linked to adverse forms of CRC which might rely on a decreased response to treatment.

(i) Apical-out TSIPs do not activate TGFβ and focal adhesion signaling when embedded into collagen-1 as compared to apical-in TSIPs.

We performed a Gene set enrichment analysis (GSEA) on microarray data comparing the expression profiles of TSIPs with apical-out versus apical-in topologies. This revealed that apical-in spheres react to collagen-1 by a strong change in gene expression, while apical-out TSIPs do not. This induces an upregulation of the cell cycle, Sonic-hedgehog, TGFβ signaling, hypoxia and the focal adhesion pathways. In this article, we chose not to address the cell cycle signaling pathways since they are not described in the literature as being involved in A/B polarity. Since we do not have the expression profile of the normal colon, we can only compare our models with each other.

In the Sonic-hedgehog pathway, only a few genes were shown to be modulated by collagen which were not the main actors of this pathway. Moreover, while extensively studied in morphogenesis[4], none of the gene in the SHH pathway has been described as regulator of A/B polarity establishment and/or orientation. Our preliminary data confirmed that the activation of this pathway in apical-out models (stimulation with SAG, a SHH agonist) or its downregulation in the apical-in (inhibition of SHH-targeted genes expression using GANT-61, a Gli-inhibitor) did not impact their topology (data not shown). A recent paper has correlated the activation of this pathway with increased tumor progression through apoptosis inhibition[347], which might correlate with our data on cell cycle progression for the apical-in model. For those reasons, we decided not to investigate it any further.

Concerning hypoxia signaling, genes involved seem downregulated in apical-out TSIPs compared to the apical-ins but treating spheres with an iron-chelator that stabilize HIF1α (by inhibiting PHD activity which induces HIF-1α degradation)[348] did not induce any A/B polarity reorientation. Thus, DFO-mediated hypoxia does not influence TSIPs topology. Nevertheless, blocking PHD activity only inhibit HIF-1α canonical pathway. Indeed, metabolic shifts (e.g. nutrient starvation, glucose deprivation) can increase the expression of HIF-1α through a non-canonical pathway, in a PHD-independent manner[349].

Also, it is possible that the upregulation of hypoxia signaling in PDX#3 is HIF-independent, meaning that there is an upregulation of genes involved in the hypoxia pathway (such as VEGF) that is not induced by HIF-dependent transcription[350]. Furthermore, as for SHH, none of the main genes were found to be modulated by collagen embedding.

In contrast to SHH and hypoxia, many key actors of the TGFβ pathway were found to be modulated by collagen in the apical-in PDX#3 (e.g. TGFBR1, SMAD3, SMAD6), but not in PDX#1 and PDX#2. This is in line with the fact that in Zajac et al., we showed that TSIP-producing tumors display a downregulation in the TGFβ pathway, reinforcing the relevance of this result. Moreover, PDX#1 and #2 display a mutation on SMAD4 which could be responsible for the downregulation of this pathway in those models. Indeed, PDX#1 displays a missense mutation which can be rescued by TGFβ stimulation, whereas PDX#2 harbor a stop gain mutation, completely impairing TGFβ signaling (Figure 4).

Lastly, PDX#3 collagen-embedding upregulates genes involved on the focal adhesion pathway. This was expected from the morphology of apical-in TSIPs which create numerous and strong interactions with the surrounding matrix. Indeed, genes involve in this pathway control the balance between contractility and adhesion, which is essential for A/B polarity orientation.

The origins of those signaling pathways alterations more likely relies on mutations in their key actors. It would be interesting to complete this data set with a whole exome sequencing to identify the molecular actors involved. Indeed, we only sequenced PDXs for the canonical TGFβ pathway, hence the data on SMAD4 mutation status.

(ii) The balance between adhesion and contractility controls TSIPs A/B polarity orientation.

I was able to demonstrate that the pathway described by the Mostov[297,298,305,308] lab to regulate A/B polarity orientation in normal renal cells is also at play in the control of MUC CRC polarity orientation. Indeed, manipulating ITGB1 and ROCK could revert the natural topology of both apical-in and apical-out TSIPs.

In PDX#3, the use of an ITGB1 blocking antibody prevents polarization in collagen. We think that the antibody was binding the “ready-to-go” integrins observed in suspension at the spheres’ surface (data not shown), preventing them from binding collagen-I fibers. the fact that the function-blocking antibody was put when spheres were embedded in collagen and was not renewed during the three days of experiment, was surprising. Indeed, the entire pool of many integrins is usually renewed in thirty minutes[351], it seems that once they have been blocked, they may not recycle back to the membrane. We can hypothesize that the balance between adhesion and contractility presents a threshold which cannot be overcome meaning that once spheres are locked in the inverted topology (the actomyosin cortex is completely homogeneous, leaving no room for integrins to be in their “ready-to-go” state), ECM stimulation cannot induce lumenogenesis anymore. Indeed, we might think that the increased contractility induced by adhesion inhibition decreases integrins levels, engaging them in cell-cell junctions and preventing them from sensing the ECM.

Indeed, data generated by the microarray demonstrated that in suspension and in collagen, apical-out models display less integrins (Figure 6). I tried to confirm that by western blot but despite many attempts, I did not succeed in getting specific signal. Still, this in line with the observations I did in immunofluorescence, even if we can question the relevance of quantifying expression levels using this technique. Moreover, I was not able to detect any “ready-to-go” integrins at the spheres surface in suspension which displayed a homogeneous actin cortex (data not shown), they always were at the basolateral pole. Thus, there might be two pools of ITGB1: a mobile one, able to traffic towards the ECM to sense it and activate downstream signaling such as polarity orientation, and an immobile one, here to reinforce epithelial cohesiveness and thus survival. Unfortunately, the role of ITGB1 at cell-cell junctions has not been investigated yet in the literature.

Nevertheless, despite the lower levels of ITGB1 in the apical-out models, they are functional and required for Y27632-induced reversion of polarity towards the apical-in phenotype (Figure 6). They seem sequestered at the basolateral pole. It is possible that they could participate in the stabilization of cell-cell junctions. The balance between adhesion and contractility is involved in the apical-out topology and is functional downstream of ROCK.

Indeed, inhibiting myosin-II using Blebbistatin also induces polarity reversion[209] (data not shown) which has not been described has participating in the adhesion/contractility balance involved in A/B polarity orientation before.

Moreover, by increasing contractility via Calyculin-A, I was able to prevent PDX#3 spheres polarization. This inhibition of protein phosphatase 2A (PP2A) might act on both contractility, through stabilization of phosphorylated myosin-II, but also by preventing PCX translation to the AMIS. Indeed, it is possible that there is an increase activity of PP2A in the apical-out spheres, preventing dephosphorylation of PCX, impairing recognition by Rab8- and Rab-11 trafficking vesicles and thus, impairing lumen formation[297]. It would be interesting to investigate PCX/NHERF1/Ezrin trafficking events occurring in PDX#3 A/B polarization by downregulating Rab8 and/or Rab11 to first, confirm that they are involved in the apical-in topology orientation and second, see if they are defective in our apical-out models.

(ii) Both canonical and non-canonical TGFβ signaling seem involved in TSIPs polarity.

TGFβ impact on A/B polarity has been extensively studied in the context of EMT where it induces a loss of this feature, mainly by dissolution of cell-cell junctions[150]. Here, we characterized it as a regulator of A/B polarity orientation. As mentioned before, since we do not have any data on normal colon tissue, we can only compare our models with each other. Thus, since A/B polarity is maintained and that no proof of EMT has been observed, it is possible that even the apical-in model is downregulated for TGFβ signaling. Indeed, all our models display mutations on TGFBRII (Supplementary Figure 4) which has been frequently found in MUC CRC patients[209].

In Zajac et al., we demonstrated that TSIPs-producing tumors display a low TGFβ signaling and that it seems important for TSIPs biogenesis and responsible for their inverted polarity. In order to decipher the molecular alterations in the TGFβ pathway involved in TSIPs behavior in, we first tested the effect of TGFβ canonical and non-canonical signaling on TSIPs biogenesis by LS174T using siRNA. Those experiments revealed that silencing either SMAD2 or PARD6A increased LS174T TSIPs formation and level of RhoA and phosphorylation of myosin-II.

When I looked at the role of TGFβ on polarity orientation in Zajac et al.[209], I chose to investigate the contribution of these two proteins, SMAD2 and PARD6A. By downregulating their expression using shRNA while treating with TGFβ, we could overcome the effects of TGFβ on A/B polarity with shPARD6A but not SMAD2. This suggested that TGFβ non-canonical signaling is important for maintaining TSIPs apical-out topology. Combined with the previous data showing that actomyosin relaxation (using Y27632 or Blebbistatin) was enough to induce polarity reversion in this model, we hypothesized that TGFβ induces a cortical relaxation through PARD6A-mediated RhoA/ROCK inhibition. As shSMAD2 had no effect, we concluded that the canonical pathway had not contribution in A/B polarity orientation, but we did not test SMAD4 in these experiments.

During my PhD, I showed that stimulating PDX#1 and PDX#2 with TGFβ gives different results (Figure 4): it decreases PDX#1 apical-out topology, as demonstrated before, but has no effect on PDX#2. This might be explained by the different mutations they harbor as mentioned before. Based on this observation, we could wonder if using a shRNA against SMAD4 would have the same effects as it did with PARD6A on PDX#1 treated with TGFβ. Moreover, it could be interesting to see if downregulating PARD6A and/or SMAD4 could prevent PDX#3 lumenogenesis.

Even though canonical and non-canonical TGFβ signaling have been studied as independent pathways, they both seem involved in TSIPs polarity. It might be interesting to see if there is a crosstalk between PARD6A and SMAD4, with the hypothesis that there is a need for a residual canonical signaling for the non-canonical to be functional.

The implication of TGFβ signaling in TSIPs A/B polarity was confirmed by treating apical-in TSIPs with TGFβ inhibitors. By doing so, I was able to shift their topology towards the apical-out phenotype. Nevertheless, SB431542 alone is not really efficient but there seems to be an additional effect when spheres are treated in suspension before. Indeed, pretreatment of spheres consists in cultivating them in suspension right after tumor dissociation, when they are not organized as a sphere yet.

This means that downregulating TGFβ signaling before cells are collectively organized prevents their correct A/B polarity orientation. It is important to note that this TGFβ inhibitor only acts on TGFβRI, thus, it is possible that TGFβ still signals through other receptors. Furthermore, by looking at the bar plot, we could imagine that increasing SB431542 concentrations might be more effective.

On the other hand, A83-01 is way more efficient at maintaining PDX#3 spheres in the apical-out topology (see Fig. 12.3 times alone, 3.4 times with a pretreatment). This might be explained by the fact that A83-01 has a more potent activity and targets both TGFβRI and activin/nodal type I receptors, preventing TGFβ signaling on a larger scale. Moreover, we are using it at a higher concentration than SB431542, it is possible that we are using in at a suboptimal concentration.

How is the balance between ITGB1 and ROCK related to TGFβ signaling? There were several hypotheses:
First, as mentioned above, TGFβ downregulation could be responsible for an increased contractility in apical-out TSIPs through the PARD6-ROCK axis. The literature states that activated TGFBR2 phosphorylates PAR6 which recruits SMURF1, a ubiquitin ligase, targeting RHOA for its degradation[170]. Nevertheless, by blotting P-MLC in our PDX models, we did not observe any difference in contractility. but the differences in contractility could relies on subcellular localization of the protein rather than on the expression level. This could be assessed by immunofluorescence.

Second, this axis precisely targets RHOA at cell-cell junctions, causing their dissolution and thus, favoring migration in an EMT context. In our apical-out models, it might be possible that TGFβ downregulation stabilizes cell-cell junctions more than it increases contractility.

Third, it has been shown that TGFβ canonical signaling increases the expression of many α subunits and β1 integrins, their assembly into the right dimers and their exposure at the cell surface[352]. Thus, TGFβ signaling downregulation through SMAD4 mutation might be responsible for the lower ITGB1 levels in the apical-out models and TGFβ effects on PDX#1 A/B polarity might go through an increase expression of those receptors.

(iii) TSIPs A/B polarity does not seem to dictate their invasive and metastatic abilities in mice models of peritoneal carcinomatosis.

After injecting TSIPs intraperitoneally and inducing polarity reversion in vivo, there was no difference between control and treated groups for each model in terms of metastatic burden. After quantifying spheres' A/B polarity, it seems that the treatment did not work on PDX#2. Nevertheless, polarity inversion was achieved in PDX#1 and PDX#3 without modifying their metastatic abilities. Thus, the presence of an inverted polarity is neither an advantage nor a disadvantage for the metastatic seeding of immunocompromised mice.

It is important to note that by quantifying the A/B polarity in all the spheres present in the slide of PDX#3, the phenotype was mixed (44.57% did not display a luminal cavity). Many of them were not in contact with any stroma, but rather surrounded by mucin. This could explain that the signaling for A/B polarity could not be triggered. Indeed, counting only TSIPs in contact with the stroma, revealed that 90.59% present a luminal cavity which correlates with the ex vivo observations. We should also note that the proportion of lumen-bearing TSIPs in the control group of PDX#1 is important. To be thorough, I should have done the same quantification on the apical-out models. Indeed, many clusters are in contact with the stroma, mainly composed of fibroblasts. Thus, we can speculate that they secrete many growth factors, such as TGFβ, which locally induces a switch of A/B polarity orientation.

We can also observe that PDX#1 is more invasive than PDX#2, despite the fact that they both produce apical-out TSIPs in control conditions and in collagen gels. This could be explained by the fact that PDX#1 comes from a peritoneal carcinomatosis while PDX#2 comes from a primary tumor, in a patient who never displayed metastases (pT3N2M0R0) and is in remission since its cytoreductive surgery. Thus, one can wonder about the fact that polarity itself is not sufficient to promote invasion, no matter the phenotype, and that it requires other cellular features. This is confirmed by PDX#3, also coming from a primary tumor where no metastases were observed in the patient, which has a similar invasion rate as PDX#2 and despite the effective A/B polarity reversion induced by AIIB2 treatment, did not became more invasive. It might be interesting to see if we can find an apical-in metastatic model to truly investigate the impact of an A/B polarity switch towards the apical-out phenotype on peritoneal invasion.

Moreover, by modeling a PC, we bypassed all the anterior steps of carcinogenesis which might be determinant for dissemination. It is possible that apical-out tumors are more effective at producing TSIPs and thus, more of them are delivered into the peritoneal cavity, facilitating metastasis. To investigate that, we could create an orthotopic model by directly injecting spheres into the colon mucosa[140,143,144] .

(iv) TSIPs could be used as a prognostic biomarker in clinic.

In Zajac et al.[209], we were able to correlate the presence of apical-out TSIPs with peritoneal carcinomatosis and a poor prognosis. However, at this time we did not distinguish between apical-in and apical-out TSIPs that were both found in metastatic patients. Thus, we wondered if there was a correlation between TSIPs topology and patient survival from a fully annotated cohort of MUC CRC[353]. Thanks to Valeria Barresi from the university of Verona, we had access to an independent cohort of MUC CRC patients. Using automated morphometry, we could quantify the proportions of apical-out and apical-in TSIPs in each patient and observed their progression and survival rates. By doing so, we were able to demonstrate that the presence of apical-out TSIPs was correlated with a lower cancer-specific survival. This showed that apical-out bearing tumors are associated with poorer outcome. Since we did not detect a significant change in the mice models, the difference in patient survival could result from their response to chemotherapy.

In line with this, there is no significant difference between the two groups during the first 50 months. Biologically, apical-out TSIPs could be more resistant to therapies as receptors responsible for drugs intake are mainly located at the basal pole and those involved in drugs outtake on the apical pole, which prevent drug accumulation in these tumors. This was demonstrated by Ashley et al.[354] two years ago where they showed that the localization of ABCB1, an apical out-take receptor involved in chemotherapies intracellular transport, dictates spheroids' response to treatment. apical-out spheroids present this receptor at their cell surface, preventing drugs from entering and thus, are more resistant to cytotoxic agents. Since they used cell lines, it will be interesting to confirm this in our PDXs. To do so, we could invert spheres polarity using shRNA targeting ITGB1 or ROCK, for apical-in or apical-out models respectively and see the impact A/B polarity on response to treatment in 3D collagen-I gels.

In Roy et al.[355], we were able to demonstrate that chemotherapies incubation for 1 hours as done in the HIPEC were never able to kill all the cells from tridimensional clusters such as organoids. This is in line with a recent clinical trial proving that HIPEC does not increase patient survival compared to cytoreductive surgery alone[356] and that it can also have adverse post-operative effects[357]. It is possible that the cytotoxic agents did not penetrate the clusters' core, leaving some cells unharmed, maybe inducing resistance mechanisms. Moreover, we cannot exclude the presence of multiple cell types within the spheres, in particular, the inner layer could be composed of cells displaying stemness properties which have been described to confer resistance to treatment[172]. Instead, in this study we showed that repeated cycles of treatment could significantly impact cell survival from organoids, thus applying cures of chemotherapy into the peritoneal cavity of patients through a catheter could be less invasive and more efficient and is currently tested in the Gustave Roussy hospital.

Finally, since CRC is a disease that develops overtime and is based on the sequential accumulation of genetic alterations, we could wonder if the apical-in topology represents an earlier stage which could evolve towards the apical-out. If so, by studying the later stages of the disease in patients, we might have enriched our data set in apical-out samples. It would be interesting to study the topology of early tumors and see if we increase the number of patients displaying apical-in spheres.

Indeed, during spheres identification on HES staining, we could observe that what we characterized as apical-in structures were classified as well differentiated tumors because of their glandular organization, whereas apical-out ones were identified as moderately to poorly differentiated. This correlates with the In-to-Out hypothesis since dedifferentiation of a tissue is usually observed in invasive carcinomas. Moreover, it would be interesting to compare the mutational landscape of apical-in versus apical-out tumors by phylogenetic bioinformatic studies to see if we could identify additional genetic lesions appearing overtime in the apical-out patients. In order to do that, the most relevant samples would be the ones displaying both topologies.

MATERIAL AND METHODS

Animal studies:

Animal experiments were compliant with French legislation and EU Directive 2010/63. The project was validated by the Ethical Committe (CEEA) n°26 and was then granted French government authorizations under number 517-2015042114005883 and 2734-2015111711418501. Mice were obtained from Charles River, housed and bred at the Gustave Roussy animal core facility (accreditation number E-94-076-11). Animals were humanely euthanized according to endpoints that were validated by the Ethical Commitee and the French government (Ministère de l'Enseignement Supérieur, de la Recherche et de l'Innovation).

Organoids retrieval and preparation from Patient-Derived Xenograft (TSIP-PDX): Three human colorectal tumours (PDX#1 corresponding to LRB-0009C, PDX#2 corresponding to IGR-0012P nad PDX#3 corresponding to IGR-014P) from the CReMEC tumour collection were maintained in NSG mice (NOD-scid IL2Rgamma^{null}, from Charles River, France) as previously described by Julien et al. Briefly, small tumour fragments were subcutaneously engrafted on the flank of anesthetized mice (2.5% isoflurane). Tumour growth was measured at least once a week. When the volume reach 1500 mm^3, mice were sacrificed and tumours were used for ex vivo experiments and 50 mm^3 fragments engrafted on the flank of new mice. Organoids were prepared according to Sato et al. and adapted for muco-secreting tumours as follows: The PDX#1, PDX#2 or PDX#3 tumours between 1000-1500 mm^3 were retrieved from the mice, minced into small fragments using a sterile scalpel and were incubated for 1h at 37°C in a final volume of 5 to 10 ml of culture medium (DMEM) without FBS and with 2 mg/ml collagenase (Sigma, C2139). The samples were then mixed with 20 ml of DMEM and filtered on 100 µm mesh size cell strainers (EASYstrainer, 542000). Digested tumour clusters were pelleted in by 4 pulse-centrifugations at 1500 rpm. The tumour fragments, free of single cells, were maintained 3 days in ultra-low attachment plates (Corning, CLS3471) in culture medium. Then, organoids were pelleted at 1500 rpm and characterized (staining with apico-basolateral polarity markers demonstrated the organoids display the characteristics of Spheres as show in Zajac et al). Spheres-PDX were used for survival and invasion experiments as well as for mice intraperitoneal injection.

Mice intraperitoneal injections: Spheres obtained from PDX#1, PDX#2 and PDX#3 (above) were prepared as described above. The medium was changed after 2 days then 1.10^4 spheres were treated in suspension with 0,5μg/mL of ITGB1 function blocking antibody AIIB2 or 25μM of ROCK inhibitor Y27632 (Calbiochem, 688000) for PDX#3 and PDX#1/#2 respectively. After 24h, they were washed and resuspended into 100μl culture media and injected intraperitoneally using 25G needle. For PDX#1 and PDX#2, treated groups intraperitoneally received 10mg/kg/twice a week of Y27632 diluted in PBS, control groups received only PBS. PDX#3 treated group received 2,5mg/kg/week of AIIB2 while control group received 2,5mg/kg/week of IgG. After 40 days, animals were humanely euthanized according to endpoints that were validated by the Ethical Commitee and the French government (Ministère de l'Enseignement Supérieur, de la Recherche et de l'Innovation). The Peritoneal carcinomatosis index was measured and macroscopic nodules were harvested and fixed in PFA 4%.

Spheres' polarity assessment:

Collagen-I (Corning, 354236) was neutralized with 1.0 M NaOH and 10x MEM (Life Technologies, 21430-02) according to the ratio: 1.0:0.032:0.1 (vol/vol/vol). The concentration was then adjusted to 2 mg/ml with DMEM 1X and the collagen was incubated on ice for 1-1h15. The spheres embedded in neutralized Collagen-I were added on top of the pre-coated well at a concentration of 30-50 Spheres/5μL (ibidi 8-well chamber). The gel was allowed to polymerize for 45 min at 37°C. Spheres were then cultured in culture medium supplemented with FBS 10 % for up to 6 days (3 days for PDX#3). The drugs were diluted in the media as followed: AIIB2 (DSHB, AB_528306), A83-01 (Sigma Aldrich, 909910-43-6, 100μM), , Blebbistatin (Calbiochem, 203391, 10 μM), Calyculin-A (Clinisciences, sc-24000A, 1nM), SB431542 (Sellekchem, S1067, 10 μM), TGFβ (R&D System, P01137, 20 ng/ml), Y27632 (Calbiochem, 688000, 25 μM). After incubation for 3 to 6 days, the apico-basolateral polarity of spheres was quantified after immunostaining using anti-Ezrin or anti-PERM. Spheres are considered with an inverted polarity when at least 75% of the total peripheral cells displayed an outward apical pole in one confocal Z-section and displays protrusions (see Supplementary Fig.1 for phenotypes). For spheres stained in suspension, they were fixed 10minutes in PFA 4% then embedded in collagen-I gels for immunofluorescent staining.

Immunofluorescence, immunohistochemistry, antibodies and histology.

Immunofluorescence: Samples were washed twice in PBS supplemented with Ca^{2+} (0.1 mM) and Mg^{2+} (1 mM) and fixed in 4% PFA for 45 min (TSIPs and peritoneum. Permeabilization was performed in PBS supplemented with 0.5% Triton X-100 for 45 min. Primary antibodies were incubated overnight at 4 °C at the dilutions listed below in antibody diluent, PBS with 10% serum supplemented by 0.1% Triton X-100. Secondary antibodies at 1/500 (Jackson ImmunoResearch, AffiniPure goat anti-mouse AlexaFluor, 488 715-545-150, AffiniPure goat anti-rabbit Cy3, 711-165-152 or LifeTechnologies goat anti-mouse 647, A21241, donkey anti-rabbit 488, A21206), phalloidin 1/1000 (Life Technologies) and DAPI (1μg/mL) were incubated overnight at 4°C or 2h at room temperature.

Primary antibodies: CK20 1/200 (Abcam, ab76126), E-cadherin 1/200 (Abcam, ab1416), EpCam 1/200 (MA5-12436), Ezrin 1/100 (DSHB, AB_210031), GM130 1/200 (NovusBio, NBP1-89757), Vimentin 1/500 (ThermoFisher Scientific, PA1-16759).

Electron microscopy: Isolated TSIPs were fixed in 2 % glutaraldehyde in 0.1 M phosphate buffer pH 7.3 and deposited in drops of neutralized collagen (2 mg/ml) allowed to polymerize 10 min at room temperature laid on a glass coverslip. TSIPs were washed 30 min in phosphate buffer, post-fixed with 2% osmic acid at room temperature and rinsed in water. Samples were dehydrated in ethanol and embedded in Epon. Polymerization was complete after 48 hours at 60°C. Ultrathin sections were collected on 100-mesh grids coated with Formvar and carbon, stained with uranyl acetate and lead citrate and observed with a FEI Technai Spirit transmission electron microscope at 80 Kv. Digital images were taken with a SIS MegaviewIII CCD camera.

Histology: CRC and peritoneum specimens obtained after surgical resection were formalin fixed and paraffin embedded according to routine protocols. Peritoneal effusions were concentrated by centrifugation and fixed in formalin, then embedded for cytoblock. Sections (3 μm) of formalin-fixed and paraffin- embedded samples were deparaffinized, unmasked (pH 8) and rehydrated before haematoxylin–eosin–saffron or alcian blue staining, immunohistochemistry or immunofluorescence.

Immunohistochemistry: Sections were immunostained with ezrin (1:100; 610603, BD Biosciences) or anti-CK20 mouse monoclonal antibody (clone Ks20.8, Dako). Stainings were performed with Ventana BenchMark XT immunostainer (Ventana Medical Systems) using the UltraView DABv3 kit (Ventana). The chromogene was 3,3'-diaminobenzidine (DAB) in all the stainings. Histochemical staining with Alcian Blue (pH 2.5) was performed with Ventana BenchMark Special Stains (Ventana Medical Systems) utilizing the V1.00.0010 process. Peritoneal effusion smears were stained using May–Grünwald–Giemsa.

Microscopy, images treatment and analyses

Confocal imaging: Images were acquired using a SpinningDisk CSU-W1 (Yokogawa) with a ZylasCMOC camera piloted with an Olympus X83. Images were processed using ImageJ or Metamorph softwares.

Microarray

Samples preparation: RNA was extracted using the RNeasy minikit (Qiagen, Cat. No. 74104) from spheres either after three days in suspension (wash one time in PBS supplemented with calcium and magnesium as mentioned above) or after three days in collagen-I gels (2mg/mL, see Spheres polarity assessment).

Colorectal cancer samples polarity characterization: RNA sequencing raw count were collected (International Cancer Genome Consortium (ICGC)) for colorectal cancer samples which were characterized histologically as IN and OUT phenotype. A merged matrix could be built with 7 samples characterized as OUT phenotype: A66781, AA3684, AA3950, CM5863, CM6162, F46704, D56534 and with 10 samples characterized as IN phenotype: AA3692, AA3555, AA3516, AA3877, AA3994, AAA00N, CA5796, D55539, DMA1D6, D56930. Resulting raw count matrix was normalized by Variance-stabilizing transformation algorithm in DeSeq2 R-package (Hubert).

Survival analysis: Public dataset of RNA sequencing performed on tumor samples of colorectal cancer by Cancer Genome Atlas Network consortium was used in Z-score transformed format to performed overall survival analysis on IN-OUT signature. This dataset comprised 244 samples which were treated for mRNA quantification by next generation sequencing[358].

Overall survival data were analyzed by Kaplan Meier representation and assessed to be significant with log rank test.

Transcriptome experiment: Whole transcriptome experiment have been processed on each PDX lines: 009C (#1), 012P (#2) and 014P (#3) and two experimental conditions: culture in suspension and culture on collagen. Each biological condition was tested in triplicate inside the transcriptome experimental map which represent 18 transcriptome experiments. Starting from 100 ng of total RNA microarray probes were synthetized and labeled with WT Plus Affymetrix chemistry in order to hybridized Clarium S Human microarray chip in Affymetrix microarray station.

Transcriptome analysis: Transcriptome analysis was performed with RMA normalization algorithm from Transcriptome Analysis Console (TAC, Applied Biosystems) software version 4.0. Two Analysis Of Variance (ANOVA) was performed with MEV standalone software (version 4.9.0) with implementation of 500 permutations and decomposition on supervised factors: collagen effect, PBX phenotype IN & OUT. During this supervised analysis interaction factor was subtract from the results. Downstream bioinformatics analyses were performed with open source R software environment version 3.5.3 under Bioconductor[359]. Supervised differential expressed gene signature to see collagen effect on PDX was performed with Significance Analysis for Microarray (SAM) algorithm[360] with a fold change threshold of 2 and a false discovery rate (FDR) less than 5 percent. Expression heatmap were drawn with pheatmap R-package with transcriptome normalized data. Unsupervised principal component analysis representation used FactoMineR library; Cleveland plot were performed with ggpubr library and Kaplan Meier with survival and ggplot2 libraries. Geneset enrichment analysis was done with Java standalone software GSEA version 4.0.3[361]. Functional interaction network was drawn with Cytoscape software version 3.6.0[362].

Patients segmentation:

Image analysis was performed after manual selection of the regions of interest by the senior pathologist. As these regions were too large to be assessed in totality, they were divided into blocks of pixels that were processed individually and finally stitched.

Images show four different classes: background, DAB stained CK, Alcian Blue colored mucus areas and eosin (pink) colored, areas of stroma.
All these classes were first segmented. Background areas are pixels whose brightness is higher than 215. CK clusters are pixels whose value is lower than 165 on blue component image. Mucin areas are pixels whose red component on blue component ratio is lower than 1, whereas stroma areas are pixels whose red on blue ratio is higher than 1, but that are not CK. Connected components are then computed for each class and small areas are discarded.
To find the apical status of each CK cluster, the program looks if it is surrounded by mucus (apical-out) or if it touches or is enclosed by a stroma area (apical-in). CK clusters surrounded by mucus that enclose a mucus area are discarded.

Statistical Analyses:

Significance was tested with unpaired two-tailed Student's t-test, one-way analysis of variance (ANOVA), linear regression using GraphPad Prism or one-sided and two-sided Fisher's exact test (using R and http://www.socscistatistics.com/tests/fisher/Default2.aspx), with the level of significance set at $\alpha = 0.05$ (95% confidence interval). The method used, P values and n numbers are indicated in the figure legends. P values of significance are represented as ****P < 0.0001, ***P < 0.001, **P < 0.01 and *P < 0.05. The exact value is indicated when possible.
No statistical method was used to predetermine sample size. No animals were excluded from the study. No method of randomization was used. The investigators were not blinded to allocation during experiments or outcome assessment.
Peritoneal effusions were collected from independent patients. The exact number of effusions analyzed is indicated in each figure legend.
All experiments, including the experiment using patient specimens, were repeated at least three times independently under similar technical conditions. For each figure panel, the exact number of biological replicates is indicated on the graph.
Quantitative data are represented as mean ± s.e.m., unless otherwise specified in the legend.

ANNEX

Cell clusters adopt a collective amoeboid mode of migration in confined non-adhesive environments.

As mentioned in the introduction, cell migration is a fundamental aspect of embryonic development, adult homeostasis and cancer progression. To date, cells have been described to move either as single cells using a traction-based or a propulsive mode of migration, or as collective protrusive strands displaying a leader-follower organization. In this paper, Pagès et al. demonstrated that cells clusters are able to migrate without the formation of focal adhesion in confined environments. They rather rely on a supracellular contractile cortex enriched in myosin II at the back. We defined this second mode of collective migration "collective ameboid", by analogy to single cells.

The founding observation of this study is that TSIPs invade into 3D environment despite their apical-out topology, precluding the participation of conventional integrin/ECM interactions.
I participated in this paper by providing a picture of an pical-out TSIP stained for ß1-integrin and actin in a 3D collagen-I gel, showing that integrins are sequestered at the basolateral pole, inside the spheres and thus, never in contact with the surrounding ECM (Fig1.A.a).

They further show that many normal and tumoral cell clusters are able to collectively migrate in non-adhesive PEG-coated microchannels. Using live imaging of HT29-MTX expressing F-tractin-mRuby3 and mTurquoise-MLC, they were able to demonstrate that static clusters display a homogenous apical expression of those two proteins, while migrating clusters present a polarized cortex with F-tractin and MLC enriched at the back. Furthermore, activating RHOA at the back of the cluster using optogenetic tool is sufficient to induce migration. These data demonstrate that collective amoeboid movement is supported by a supracellular contractile actin cortex.

Cell clusters adopt a collective amoeboid mode of migration in confined non-adhesive environments.

Short title: Collective amoeboid migration of cell clusters

Authors: Diane-Laure Pagès[1,2#], Emmanuel Dornier[1#], Jean De Seze[3], Li Wang[4], Rui Luan[1], Jérôme Cartry[1], Charlotte Canet-Jourdan[1,2], Joel Raingeaud[1], Raphael Voituriez[5,6], Mathieu Coppey[3], Matthieu Piel[4] and Fanny Jaulin[1*].

Affiliations :

[1] INSERM U-1279, Gustave Roussy, Villejuif, F-94805, France.

[2] Université Paris Saclay, 114 rue Edouard Vaillant, Villejuif, F-94805, France

[3] Laboratoire Physico Chimie Curie, Institut Curie, PSL Research University, Sorbonne Université, CNRS, Paris 75005, France.

[4] Institut Curie and Institut Pierre Gilles de Gennes, PSL Research University, CNRS, UMR 144, Paris, France

[5] Laboratoire de Physique Théorique de la Matière Condensée, UMR 7600 CNRS/Sorbonne Université, 4 Place Jussieu, 75255 Paris Cedex, France.

[6]Laboratoire Jean Perrin, UMR 8237 CNRS/Sorbonne Université, 4 Place Jussieu, 75255 Paris Cedex, France.

[#]Equal contribution

*Correspondence to: Fanny Jaulin: fanny.jaulin@gustaveroussy.fr

One Sentence Summary:

Clusters organise as polarised and contractile super-cells to migrate without adhesion.

Abstract:

Cell migration is essential to most living organisms. Single cell migration involves two distinct mechanisms, either a focal adhesion- and traction-dependent mesenchymal motility or an adhesion-independent but contractility-driven propulsive amoeboid locomotion. Cohesive migration of a group of cells, also called collective cell migration, has been only described as an adhesion- and traction-dependent mode of locomotion where the driving forces are mostly exerted at the front by leader cells. Here, by studying primary cancer specimens and cell lines from colorectal cancer, we demonstrate the existence of a second mode of collective migration which does not require adhesion to the surroundings and relies on a polarised supracellular contractility. Cell clusters confined into non-adhesive microchannels migrate in a rounded morphology, independently of the formation of focal adhesions or protruding leader cells, and lacking internal flow of cells, ruling-out classical traction-driven collective migration. Like single cells migrating in an amoeboid fashion, the clusters display a supracellular actin cortex with myosin II enriched at the rear. Using pharmacological inhibitors and optogenetics, we show that this polarised actomyosin activity powers migration and propels the clusters. This new mode of migration, that we named collective amoeboid, could be enabled by intrinsic or extrinsic neoplasic features to enable the metastatic spread of cancers.

Main Text:

Migration is a fundamental property of cells. Emerging in early eukaryotes, migration supports individual cell displacement as well as metazoan development and homeostasis (*1*). It is also deregulated in pathological conditions, such as cancer, where it fuels their metastatic spread (*2*). Two distinct mechanisms are used by single cells to generate the migration forces (*3*). They result from the cells' ability to adhere, or not, to the surrounding extracellular matrix (ECM) and their level of contractility. In traction-based mesenchymal migration, integrin interaction with the ECM and focal adhesion formation convert branched-actin polymerisation into large protrusions and forward forces (*3*, *4*). In contrast, amoeboid single cells use a propulsive locomotion that does not require specific adhesion and is driven by acto-myosin contractility of the rear (*5*, *6*). Cells can also move in a cohesive manner as a group (*7–9*). At the front of the cluster, leader cells form prominent protrusions where the combined action of actin polymerization and integrin engagement triggers lamellipodia and focal adhesion formation. Using the substrate as an anchor, leaders pull on follower cells, instructing directionality and generating important traction forces (*10*, *11*). The contribution of follower cells is more elusive, but it has recently been shown that their increased contractility produces a treadmilling of lateral cells to support the migration of neural crest clusters (*12*). To date, our knowledge on collective cell movement suggests it only takes the form of an adhesion-dependent traction-based mode of locomotion and whether it could also occur through an alternative mechanism has not been investigated.

Through the analysis of primary tumour explants retrieved from patients with metastatic colorectal cancer (CRC), we identified TSIPs (Tumour Spheres with Inverted Polarity) as tumour cell clusters with an inverted apico-basolateral polarity (*13*). The atypical topology of the clusters exposes carcinoma cells' apical membranes to the microenvironment and precludes adhesion

receptors, such as integrins, to interact with the surrounding ECM in the peritumoral stroma (Fig. 1A). Yet, TSIPs efficiently invade tissues and are associated with high metastatic burden and poor patient prognosis (*13*). This suggests that the motility of TSIPs does not require integrin function and raises the possibility of an adhesion-independent mode of collective cell migration. To test this hypothesis, we engineered micro-devices (channels and chambers) deprived of any physiological substrates and chemotactic cues by coating them with the anti-adhesive polymer polyethylene glycol (PEG, Fig. 1B). Time-lapse imaging proved that TSIPs obtained from two independent patients migrated into the non-adhesive microchannels (Fig. 1C(a), fig. S1A and movie S1). To determine whether this type of migration is specific to TSIPs or could be used by other collectives, we assessed the migration of clusters assembled from colorectal carcinoma cell lines in PEG-coated microchannels. Indeed, clusters from HT29, HT29-MTX and three lines of circulating tumour cells (CTC31,44, 45, (*14*)) were able to collectively migrate under these conditions (Fig. 1, C(b) to E, and movie S2). To characterise this new mode of collective migration, considering the durations of consecutive migration and pauses (fig. S1, B and C), we monitored trajectories of individual clusters every hour over one day (Fig. 1D). Some clusters did not move in the course of the experiment while some reached-up to 2 mm/d. Average speeds ranged from 150±21µm/d to 77±4µm/d for TSIPs and HT29s which are the fastest. The migration of CTCs was slower, varying from 37±2µm/d to 27±2µm/d (Fig. 1E) (values are expressed as speed ± standard error of the mean). Clusters displayed a very persistent migration over time (from 0.65±0.03 to 0.75±0.03 in average) and could reach a maximum instantaneous speed of 28±3µm/h in average (Fig. 1D and F, and fig. S1D). Although quite slow when compared with single cell migration in experimental settings, this is in the order of magnitude of collective migration speeds reported in vivo (*15*, *16*).

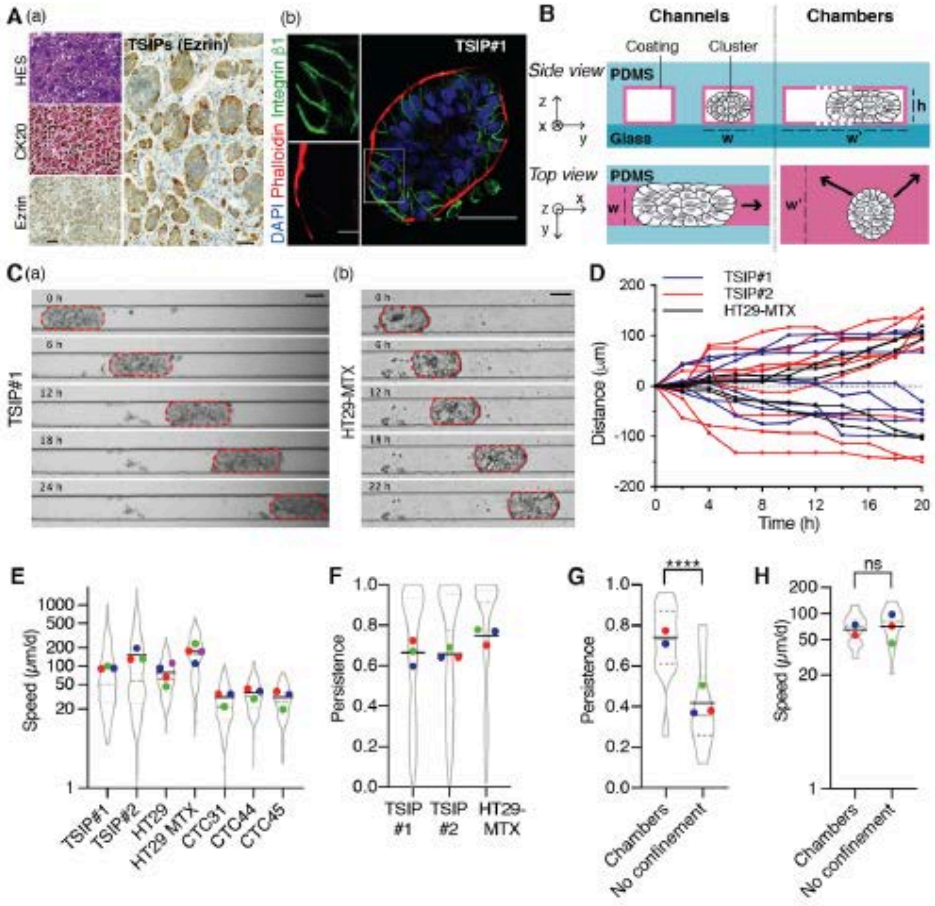

Fig. 1. Cell clusters migrate into non-adhesive microchannels. (**A**) Representative tumour specimen of CRC (micropapillary subtype) stained with Hematoxylin/Eosin/Saffron (HES), anti-Cytokeratin 20 (CK20) and anti-Ezrin at low (left) and high (right) magnification (a) and immunofluorescence of a transverse section of TSIP#1 embedded in collagen-1 for 24h (b). The boxed region is shown at high magnification. (**B**) Schematic representation, not to scale, of the channels (width: w=60μm; height: h=30μm) (left) and chambers (width: w'=500μm) (right). (**C**) Time-lapse sequences of migration of TSIP#1 (a) and HT29-MTX (b) in PEG-coated microchannels. (**D**) Representative tracks of clusters migrating in one direction (positive numbers) or the other (negative numbers) in PEG-coated microchannels. n=5 to 9 representative clusters of each cell type. (**E** and **F**) Clusters' migration speed (E, log2-scale, n=118 to 208 clusters per cell type) and persistence (F, n=107 to 124 clusters per cell type) in PEG-coated microchannels over one day. (**G** and **H**) Speed (G, log2-scale, unpaired Student's t-test) and persistence (H, Mann-Whitney test) for HT29-MTX migration over a day, depending on their confinement. Designs are coated with PEG+F127. n=30 clusters (chambers), n=18 clusters (no confinement). ns, not significant, ****P<0.0001 (Kruskal-Wallis test). Violin plots display the whole population of clusters, median (dashed grey line) and quartiles (dotted grey lines). The coloured dots represent the mean of each independent experiments and the black line the mean of all experiments for each condition. All data represented as violin plots are from N=3 independent experiments, except HT29 and HT29-MTX in (E, N=4) and chambers in (G) and (H) (N=2). Scale bars: 200μm (A,a, low magnification), 50μm [(A,a, high magnification), (A,b, low magnification), (C)] and 10μm (A,b, high magnification).

We next assessed the role of confinement by comparing migration of clusters confined in one dimension (microchambers, Fig. 1B and fig. S2A) or not confined (loading chambers, fig. S2B). Confinement did not increase clusters' speed but favoured persistence, as described for single cells (Fig. 1, G and H) (*6*, *17*, *18*). Once confined into microchannels, small clusters migrate as fast as the largest ones, showing no correlation between speed and size (fig. S2, C to E). In all instances, the collective migration is associated with a compact rounded morphology into non-adhesive microchannels that contrasts with the loose and spread shape clusters can adopt when the microchannels are coated with collagen-1 (Fig. 2A). Measuring the contact angles between the cluster boundary and the microchannel walls highlights the "dewetting" morphology of the clusters and the absence of protrusion for HT29, HT29-MTX and TSIPs migrating in PEG-coated microchannels (Fig. 2, A and B). Collagen-1 coating reduces HT29 and HT29-MTX migration speed while, as expected, TSIPs remain unaffected due to their inverted polarity (Fig. 2C and 1A). Together, these experiments suggest that confined cell clusters can display a persistent motility in non-adhesive environments.

To directly study the contribution of focal adhesion to cluster migration, we expressed turquoise-tagged paxillin in HT29-MTX. While fluorescent paxillin revealed numerous foci at collagen-1 interface, they were nearly absent in PEG-coated microchannels (Fig. 2, D and E, and movie S3). To functionally assess the participation of focal adhesions, we silenced talin-1, an essential component of integrin-mediated functions (*19*). This had no effect on HT29-MTX cluster migration (Fig. 2, F and G). Hence, interfering with intrinsic and extrinsic components of cell adhesion to their substrate demonstrates that clusters can migrate without the conventional molecular machinery powering traction-based collective migration (*20*–*22*).

We next tested whether a coordinated retrograde flow of cells, or cell treadmilling, could participate in this non-adhesive cluster migration, as was proposed before in a developmental context (*12*). To this end, we expressed cherry-tagged histone 2B (H2B) in HT29 clusters to monitor individual cell movements during migration in PEG-coated channels. Confocal fluorescence imaging showed that individual cell tracks follow the trajectory of the centre of mass of the cluster (Fig. 2H, fig. S3A and movie S4). To precisely test the hypothesis of flows of cells generating migration (Fig. S3, B to G), three areas were defined on a middle cross section of the cluster and cell trajectories were examined (Fig. 2I(a)). In each area, the measurement of the instantaneous speed of cells in the cluster's reference frame directly confirmed the absence of significant fluxes of cells (Fig. 2J and fig. S3, C and F). As a consequence, the relative velocity of cells in contact with the microchannel walls was positive, in the direction of the motion of the cluster (Fig. 2K). In the hypothesis of a propulsion mechanism based on flows of cells, this would indicate the presence of resistive friction forces only and the absence of propulsion forces, excluding a mechanism based on an internal treadmilling of cells (fig. S3 D and G). Thus, clusters translate, with all cells remaining at the same relative position in the group during migration (Fig. 2I(b) and fig.S3A).

The classical mechanisms of traction-driven collective migration being ruled-out, we reasoned that the acto-myosin cytoskeleton could power focal adhesion-independent cluster migration, as it does in amoeboid single cells (*5*, *6*, *23*, *24*). Expressing the fluorescent probes F-tractin and myosin light chain (MLC) in HT29-MTX revealed a robust peripheral supracellular acto-myosin cortex as reported at the boundaries of other migrating collectives (Fig. 3A) (*25*). This peripheral cortex is evenly distributed in static clusters, however, during migration, it exhibits

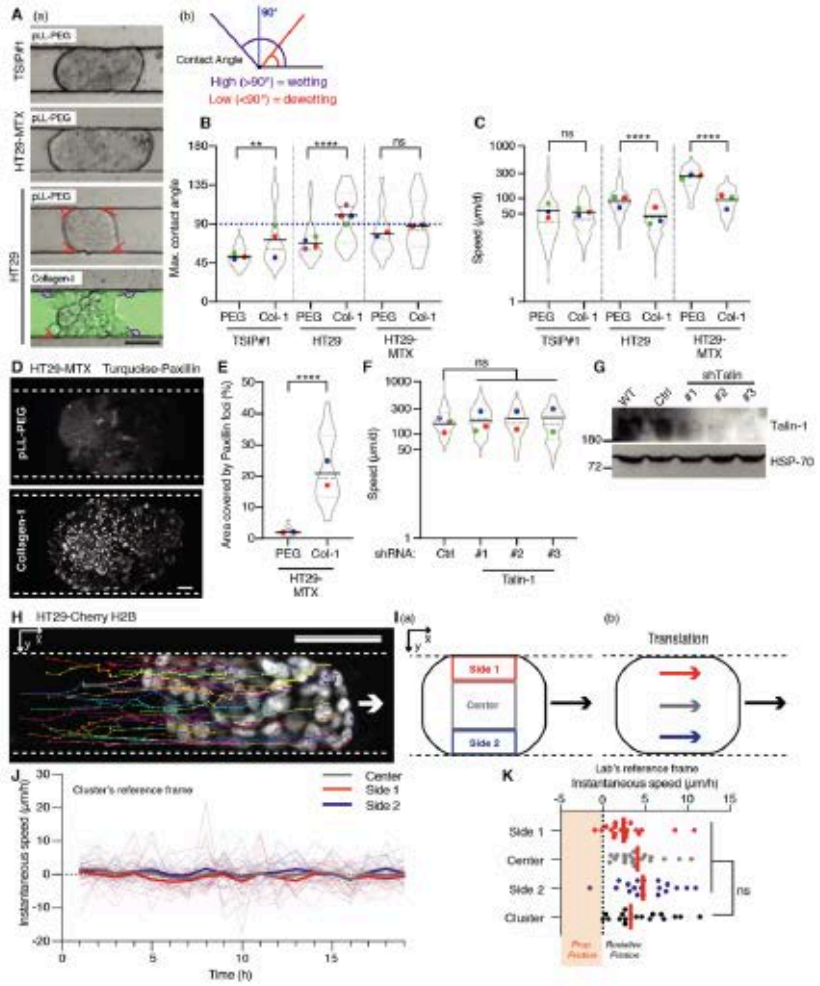

Fig. 2. Collective migration occurs without focal-adhesions nor cell flows. (**A** to **C**) Representative images (A), maximum contact angles (B) and speeds (C) of clusters migrating in PEG- or Cy5-collagen-1(Col-1)-coated microchannels. Wetting or dewetting contact angles are represented on the cluster (A,a) and as a schematic representation (A,b); n=39 to 59 clusters were used to quantify the maximum contact angle (B, Mann Whitney test). n=90 to 166 clusters were analysed to calculate migration speeds (C, two-tailed Student's t test). (**D** and **E**) Representative images of the bottom plan of the cluster (D) and area covered by paxillin foci (E) for HT29-MTX stably expressing mTurquoise-Paxillin in PEG- or Col-1-coated microchannels. n=19 to 28 clusters (E, Mann-Whitney test). (**F** and **G**) Speed of clusters in PEG-coated microchannels (F) and corresponding western blot (G) for HT29-MTX stably expressing 3 different shRNA targeting Talin-1 or a control shRNA. n=62 to 154 clusters (F, one-way ANOVA). (**H**) Representative nuclei tracks of the middle cross-section of an HT-29 cluster stably expressing mCherry-H2B, migrating one day in a PEG-coated microchannel. (**I**) Definition of areas in the cluster (a), to scale, and schematic representation of cluster's global translation (b). Side 1: cluster's side going most rearward/less forward in average. (**J**) Instantaneous speed of cells in each area, in the reference frame of the clusters. Bold lines: average of individuals tracks calculated from regions of n=16 clusters from 3 independent experiments. (**K**) For one representative cluster, instantaneous speed of cells in each area and cluster speed, lab's reference frame. Orange: cells could generate propulsive (Prop.) friction. n=19 timepoints (paired Friedman test). Experiments were performed independently for each cell lines. Violin plots are described in Fig. 1 legend and coloured dots refer to the same experiment. All data represented as violin plots are from N=3 independent experiments, except HT29-MTX in (B) and (E), and sRNA#2 and #3 in (F) that were performed twice. ns, not significant, **P<0.01, ****P<0.0001. Scale bars: 50µm [(A) and (H)], 10µm (D).

a front/rear polarisation, with a 1.5- and 1.8-fold enrichment toward the back of the cluster for F-tractin and MLC respectively (Fig. 3, A and B, and movie S5). To assess whether this supracellular acto-myosin cortex contributes to cluster migration, we first used pharmacological inhibitors. Interfering with Myosin-II or ROCK activities using blebbistatin and Y27632 reduced TSIP#1 migration speed from 80±7µm/d to 50±6 µm/d and 43±3 µm/d, respectively (Fig. 3, C and D, and fig. S4A). Similarly, using these inhibitors on HT29-MTX decreased their migration by 3- and 2.9-fold, respectively (Fig. 3, C and D, and fig. S4B). Then, we tested whether increasing contractility at the rear was sufficient to power cluster migration. To this end, we used optogenetics to manipulate acto-myosin contractility via its upstream regulator RhoA. We infected HT29-MTX cells with the optoRhoA system, which enables an acute spatiotemporal recruitment of RhoA activator ARHGEF11 to the membrane using the CRY2/CIBN light gated optogenetic dimerization system (fig. S5, A and B) (*26*). We illuminated one side of the clusters, either at the front of already moving clusters or randomly for static ones. We monitored their trajectories for up to 20 hours by using an automated stage and activation routine maintaining a constant illumination region despite the movement of the cluster (Fig. 3E). Control clusters expressing the optogenetic dimeriser without RhoA activator pursued their migration in their initial direction with their speed sometimes reduced by mild phototoxicity or large local protein recruitment at the membrane (*27*). In contrast, illuminating clusters expressing optoRhoA impacted their migratory behaviours. Light stimulation initiated the migration of static clusters and was even able to revert the direction of migrating ones (Fig. 3, F to H, and fig. S5C, and movie S6, 7). This demonstrates that increasing acto-myosin activity in a subset of cells is both sufficient to induce migration and dictate directionality taken by the entire cluster (Fig. 3, F to H, and fig. S5C). Altogether, these

experiments show that a supracellular polarised acto-myosin contractility contributes to the driving force that propels clusters of cells into non-adhesive environments.

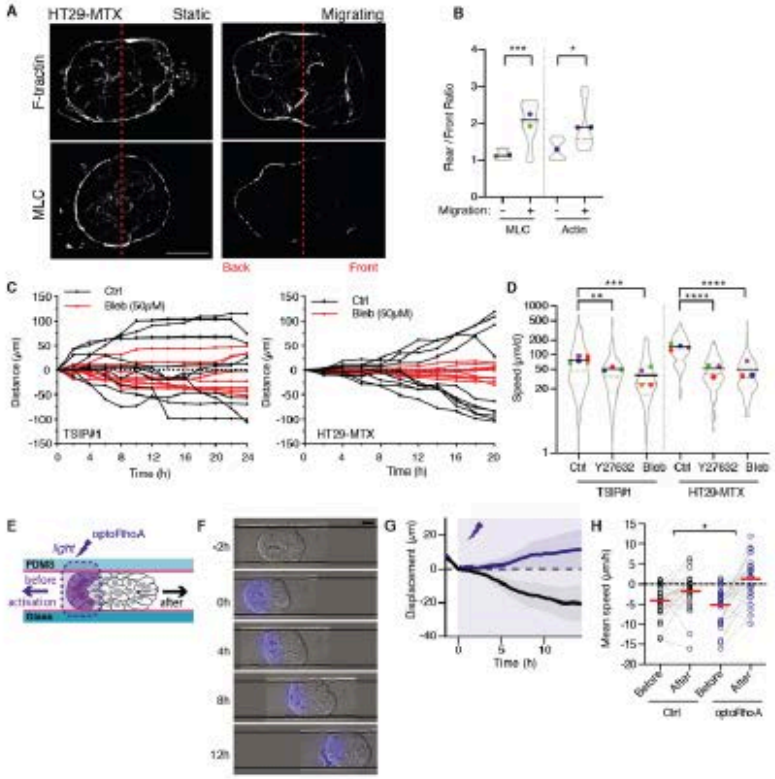

Fig. 3. A supracellular contractile actin cortex powers focal adhesion-independent collective migration. (**A**) Median section of HT29-MTX stably expressing F-tractin-mRuby3 (top) and mTurquoise-MLC (bottom), in PEG+F127-coated channels. (**B**) Quantification of the F-tractin (Actin) and MLC (Myosin Light Chain) ratios between rear and front of the clusters, as indicated in Methods. n=7 to 13 clusters (Mann-Whitney test). (**C**) Representative tracks of clusters treated with Blebbistatin. n=10 clusters each. (**D**) Speed of clusters treated with Y27632, Blebbistatin, or DMSO (Ctrl), log2-scale. n=106 to 205 clusters (Mann-Whitney test). (**E** to **H**) Optogenetic manipulations: Experimental setup (E), representative time-lapse sequences (F, dark grey lines are microchannel walls), migration profiles (G, means ± sem) and mean speeds before (-2h<t<0h) and after (4h<t<10h) optogenetic activation (H). In G and H, the control (CRY2PHR-mCherryN1/CIBN-eGFP-CaaX) is represented as black line or dots and optoRhoA as purple line or dots. The purple zones represent the optogenetic activation period. n=27 clusters from 3 independent experiments (two-tailed Student's t test on the after-before speed differences between control and optogenetic constructs). Experiments were performed independently for each cell types. Violin plots are described in Fig. 1 legend and coloured dots refer to the same experiment. All data represented as violin plots are from N=3 independent experiments, except in (B, N=2, and N=1 for Actin in non-migrating clusters), and TSIP#1 in Blebbistatin (E) (N=4). ns, not significant, *P<0.05, **P<0.01, ***P<0.001, **** P<0.0001. Scale bars, 30 µm.

Here, we report a second mode of collective migration that shares striking features with amoeboid single cell motility (Fig. 4). Cell clusters collectively migrate within non-adhesive

microchannels in the absence of protruding leader cells, focal adhesions or cell flows. Similar to amoeboid cells, clusters mobilise the contractility of a supracellular acto-myosin cortex at the rear and adopt a propulsive mode of migration. By analogy, we named this new mode of cell locomotion "collective amoeboid migration". Tumour cells have the capacity to hijack the 3 modes of cell migration described to date (*28*). Here, we show that colorectal cancer primary specimens and cell lines can also adopt collective amoeboid migration. This results from intrinsic oncogenic features, such as in TSIPs, where the inverted apico-basolateral polarity prevents cluster adhesion to ECM-rich tissues (*13*). This propulsion-based mode of collective migration could also be enabled as a non-cell autonomous process, when cancer cell clusters are exposed to environments deprived of conventional ECM. These encompass major dissemination routes such as the lumen of lymphatic vessels or the peritoneal and pleural cavities (*29–33*). Collective amoeboid migration could thus foster cancer metastatic spread.

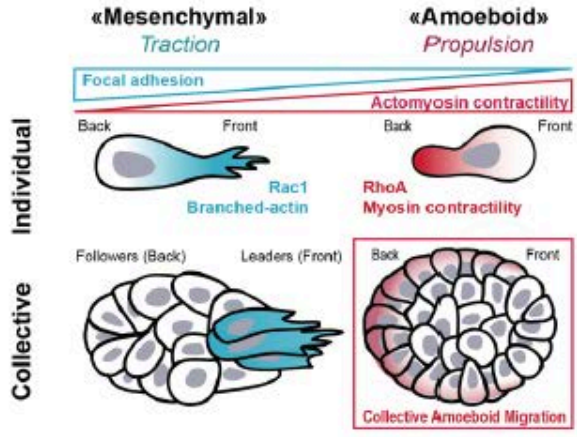

Fig. 4. Model of cell migration modes. Schematic representation of the different modes of cell migration based on the ability of the cells to adhere to each other (individual versus collective migration) and to their environment (mesenchymal versus amoeboid). This results in traction- or propulsion-based locomotion, where the force is respectively generated by Rac1-dependent actin polymerization or RhoA-dependent actomyosin contractility. The second mode of collective migration we report here occurs without the formation of focal adhesion and relies on acto-myosin contractility at the rear. By analogy with single cells, it has been named «collective amoeboid migration» and represents a fourth mode of cell migration.

References and Notes:

1. K. M. Yamada, M. Sixt, Mechanisms of 3D cell migration. *Nat Rev Mol Cell Biol.* **20**, 738–752 (2019).
2. A. W. Lambert, D. R. Pattabiraman, R. A. Weinberg, Emerging Biological Principles of Metastasis. *Cell.* **168**, 670–691 (2017).
3. D. L. Bodor, W. Pönisch, R. G. Endres, E. K. Paluch, Of Cell Shapes and Motion: The Physical Basis of Animal Cell Migration. *Dev. Cell.* **52**, 550–562 (2020).
4. M. Innocenti, New insights into the formation and the function of lamellipodia and ruffles in mesenchymal cell migration. *Cell Adh Migr.* **12**, 401–416 (2018).
5. E. K. Paluch, I. M. Aspalter, M. Sixt, Focal Adhesion-Independent Cell Migration. *Annu. Rev. Cell Dev. Biol.* **32**, 469–490 (2016).
6. Y.-J. Liu, M. Le Berre, F. Lautenschlaeger, P. Maiuri, A. Callan-Jones, M. Heuzé, T. Takaki, R. Voituriez, M. Piel, Confinement and low adhesion induce fast amoeboid migration of slow mesenchymal cells. *Cell.* **160**, 659–672 (2015).
7. P. Friedl, J. Locker, E. Sahai, J. E. Segall, Classifying collective cancer cell invasion. *Nat. Cell Biol.* **14**, 777–783 (2012).
8. P. Friedl, D. Gilmour, Collective cell migration in morphogenesis, regeneration and cancer. *Nat. Rev. Mol. Cell Biol.* **10**, 445–457 (2009).
9. K. J. Cheung, A. J. Ewald, A collective route to metastasis: Seeding by tumor cell clusters. *Science.* **352**, 167–169 (2016).
10. R. Mayor, S. Etienne-Manneville, The front and rear of collective cell migration. *Nat. Rev. Mol. Cell Biol.* **17**, 97–109 (2016).
11. E. Theveneau, C. Linker, Leaders in collective migration: are front cells really endowed with a particular set of skills? *F1000Res.* **6**, 1899 (2017).
12. A. Shellard, A. Szabó, X. Trepat, R. Mayor, Supracellular contraction at the rear of neural crest cell groups drives collective chemotaxis. *Science.* **362**, 339–343 (2018).
13. O. Zajac, J. Raingeaud, F. Libanje, C. Lefebvre, D. Sabino, I. Martins, P. Roy, C. Benatar, C. Canet-Jourdan, P. Azorin, M. Polrot, P. Gonin, S. Benbarche, S. Souquere, G. Pierron, D. Nowak, L. Bigot, M. Ducreux, D. Malka, C. Lobry, J.-Y. Scoazec, C. Eveno, M. Pocard, J.-L. Perfettini, D. Elias, P. Dartigues, D. Goéré, F. Jaulin, Tumour spheres with inverted polarity drive the formation of peritoneal metastases in patients with hypermethylated colorectal carcinomas. *Nature Cell Biology*, 1 (2018).
14. F. Grillet, E. Bayet, O. Villeronce, L. Zappia, E. L. Lagerqvist, S. Lunke, E. Charafe-Jauffret, K. Pham, C. Molck, N. Rolland, J. F. Bourgaux, M. Prudhomme, C. Philippe, S. Bravo, J. C. Boyer, L. Canterel-Thouennon, G. R. Taylor, A. Hsu, J. M. Pascussi, F. Hollande, J. Pannequin, Circulating tumour cells from patients with colorectal cancer have cancer stem cell hallmarks in ex vivo culture. *Gut.* **66**, 1802–1810 (2017).
15. D. Krndija, F. El Marjou, B. Guirao, S. Richon, O. Leroy, Y. Bellaiche, E. Hannezo, D. Matic Vignjevic, Active cell migration is critical for steady-state epithelial turnover in the gut. *Science.* **365**, 705–710 (2019).
16. B. Weigelin, G.-J. Bakker, P. Friedl, Intravital third harmonic generation microscopy of collective melanoma cell invasion: Principles of interface guidance and microvesicle dynamics. *Intravital.* **1**, 32–43 (2012).
17. B. Winkler, I. S. Aranson, F. Ziebert, Confinement and substrate topography control cell migration in a 3D computational model. *Commun Phys.* **2**, 1–11 (2019).
18. J. A. Mosier, A. Rahman-Zaman, M. R. Zanotelli, J. A. VanderBurgh, F. Bordeleau, B. D. Hoffman, C. A. Reinhart-King, Extent of Cell Confinement in Microtracks Affects Speed and Results in Differential Matrix Strains. *Biophys. J.* **117**, 1692–1701 (2019).
19. Z. Sun, M. Costell, R. Fässler, Integrin activation by talin, kindlin and mechanical forces. *Nat. Cell Biol.* **21**, 25–31 (2019).
20. F. Gunawan, A. Gentile, R. Fukuda, A. T. Tsedeke, V. Jiménez-Amilburu, R. Ramadass, A. Iida, A. Sehara-Fujisawa, D. Y. R. Stainier, Focal adhesions are essential to drive zebrafish heart valve morphogenesis. *J Cell Biol.* **218**, 1039–1054 (2019).
21. E. H. Barriga, K. Franze, G. Charras, R. Mayor, Tissue stiffening coordinates morphogenesis by triggering collective cell migration in vivo. *Nature.* **554**, 523–527 (2018).
22. Y. Hegerfeldt, M. Tusch, E.-B. Bröcker, P. Friedl, Collective cell movement in primary melanoma explants: plasticity of cell-cell interaction, beta1-integrin function, and migration strategies. *Cancer Res.* **62**, 2125–2130 (2002).
23. T. Lämmermann, B. L. Bader, S. J. Monkley, T. Worbs, R. Wedlich-Söldner, K. Hirsch, M. Keller, R. Förster, D. R. Critchley, R. Fässler, M. Sixt, Rapid leukocyte migration by integrin-independent flowing and squeezing. *Nature.* **453**, 51–55 (2008).
24. M. Bergert, A. Erzberger, R. A. Desai, I. M. Aspalter, A. C. Oates, G. Charras, G. Salbreux, E. K. Paluch, Force transmission during adhesion-independent migration. *Nat. Cell Biol.* **17**, 524–529 (2015).
25. A. Shellard, R. Mayor, Supracellular migration - beyond collective cell migration. *J. Cell. Sci.* **132** (2019), doi:10.1242/jcs.226142.
26. L. Valon, A. Marín-Llauradó, T. Wyatt, G. Charras, X. Trepat, Optogenetic control of cellular forces and mechanotransduction. *Nat Commun.* **8**, 14396 (2017).
27. X. Meshik, P. R. O'Neill, N. Gautam, Physical Plasma Membrane Perturbation Using Subcellular Optogenetics Drives Integrin-Activated Cell Migration. *ACS Synth Biol.* **8**, 498–510 (2019).
28. P. Friedl, S. Alexander, Cancer invasion and the microenvironment: plasticity and reciprocity. *Cell.* **147**, 992–1009 (2011).
29. D. J. Ruiter, J. H. van Krieken, G. N. van Muijen, R. M. de Waal, Tumour metastasis: is tissue an issue? *Lancet Oncol.* **2**, 109–112 (2001).
30. S.-B. Lim, C. S. Yu, S. J. Jang, T. W. Kim, J. H. Kim, J. C. Kim, Prognostic significance of lymphovascular invasion in sporadic colorectal cancer. *Dis. Colon Rectum.* **53**, 377–384 (2010).
31. V. Barresi, L. Reggiani Bonetti, E. Vitarelli, C. Di Gregorio, M. Ponz de Leon, G. Barresi, Immunohistochemical assessment of lymphovascular invasion in stage I colorectal carcinoma: prognostic relevance and correlation with nodal micrometastases. *Am. J. Surg. Pathol.* **36**, 66–72 (2012).
32. M. Brown, F. P. Assen, A. Leithner, J. Abe, H. Schachner, G. Asfour, Z. Bago-Horvath, J. V. Stein, P. Uhrin, M. Sixt, D. Kerjaschki, Lymph node blood vessels provide exit routes for metastatic tumor cell dissemination in mice. *Science.* **359**, 1408–1411 (2018).
33. J. Law, E. Martin, *"Transcoelomic Spread"*, in *Concise Medical Dictionary* (Oxford University Press, ed. 10, 2020).
34. S. Julien, A. Merino-Trigo, L. Lacroix, M. Pocard, D. Goéré, P. Mariani, S. Landron, L. Bigot, F. Nemati, P. Dartigues, L. B. Weiswald, D. Lantuas, L. Morgand, E. Pham, P. Gonin, V. Dangles-Marie, B. Job, P. Dessen, A. Bruno, A. Pierré, H. De Thé, H. Soliman, M. Nunes, G. Lardier, L. Calvet, B. Demers, G. Prévost, P. Vrignaud, S. Roman-Roman, O. Duchamp, C.

Berthet, Characterization of a large panel of patient-derived tumor xenografts representing the clinical heterogeneity of human colorectal cancer. *Clin. Cancer Res.* **18**, 5314-5328 (2012).

35. M. J. Kennedy, R. M. Hughes, L. A. Peteya, J. W. Schwartz, M. D. Ehlers, C. L. Tucker, Rapid blue-light-mediated induction of protein interactions in living cells. *Nat Methods*. **7**, 973-975 (2010).
36. K. E. Rothenberg, D. W. Scott, N. Christoforou, B. D. Hoffman. Vinculin force-sensitive dynamics at focal adhesions enable effective directed cell migration. *Biophys J*. **114**, 1680–1694 (2018).
37. A. Hayer, L. Shao, M. Chung, L.-M. Joubert, H. W. Yang, F. C. Tsai, A. Bisaria, E. Betzig, T. Meyer. Engulfed cadherin fingers are polarized junctional structures between collectively migrating endothelial cells. *Nat Cell Biol*. **18**, 1311–1323 (2016).
38. C. M. Kenific, S. J. Stehbens, J. Goldsmith, A. M. Leidal, N. Faure, J. Ye, T. Wittmann, J. Debnath. NBR1 enables autophagy-dependent focal adhesion turnover. *J. Cell Biol*. **212**, 577-590 (2012).
39. J. Schindelin, I. Arganda-Carreras, E. Frise, V. Kaynig, M. Longair, T. Pietzsch, S. Preibisch, C. Rueden, S. Saalfeld, B. Schmid, J.-Y. Tinevez, D. J. White, V. Hartenstein, K. Eliceiri, P. Tomancak, A. Cardona. Fiji: an open-source platform for biological-image analysis. *Nat. Methods* **9**, 676-682 (2012).
40. J.-Y. Tinevez, N. Perry, J. Schindelin, G. M. Hoopes, G. D. Reynolds, E. Laplantine, S. Y. Bednarek, S. L. Shorte, K. W. Eliceiri. TrackMate: An open and extensible platform for single-particle tracking. *Methods* **115**, 80-90 (2017).
41. S. J. Lord, K. B. Velle, R. D. Mullins, L. K. Fritz-Laylin. SuperPlots: Communicating reproducibility and variability in cell biology. *J. Cell Biol*. **219**, e202001064 (2020).

Acknowledgements: We thank the members of the Jaulin, Piel and Montagnac laboratories for helpful discussions. We thank T. Manoliu and C. Laplace from the PFIC facility for their technical help. We thank M. Polrot from the PFEP facility for assistance with the animal work. We thank the C. Robert lab for the plasma cleaner. We thank J. Pannequin for the CTC cell lines. We thank W. Beng and K. Vaidziulyte for the automated tracking algorithm used in optogenetics. Funding: This work was supported by grants from INCA-PLBIO (2018-1-PLBIO-04-IGR-1), ARC (PAJ20181208275) and LNCC-IDF (R19102LL) to F.J. as well as fund raising against colorectal cancer from the Gustave Roussy foundation. M.C. thanks the Labex CelTisPhyBio (ANR-10-LBX-0038) and the Institut Convergences Q-life ANR-17-CONV-0005. We thank the Philantropia fellowship to D.-L.P., the FRM fellowship to E.D., the AMX fellowship to J.D.S. and the Taxe d'Apprentissage 2019 (to D.-L.P., Univ. Paris-Saclay, France). **Author contributions:**

All authors provided intellectual input. D.-L.P., E.D., and R.L. designed the research, performed the experiments and analysed the data. J.D.S. and M.C. conceived, performed and analysed the optogenetics experiments. L.W. and M.P. designed and validated the microfabricated devices. J.C. prepared the organoids and helped for the animal work. C.C.-J. performed immunostainings on TSIPs. J.R. analysed the contractility of cell clusters. C.M.C, R.V. and M.P. provided scientific input. F.J. conceptualised the project, designed the research and wrote the manuscript. **Competing interests:** Authors declare no competing interests. **Data and materials availability:** All data is available in the main text or the supplementary materials.

REFERENCES

1. Levine, D. S. & Haggitt, R. C. Normal histology of the colon. *American Journal of Surgical Pathology* vol. 13 966–984 (1989).
2. Mao, J., Kim, B. M., Rajurkar, M., Shivdasani, R. A. & McMahon, A. P. Hedgehog signaling controls mesenchymal growth in the developing mammalian digestive tract. *Development* (2010) doi:10.1242/dev.044586.
3. Williams, M. L. & Bhatia, S. K. Engineering the extracellular matrix for clinical applications: Endoderm, mesoderm, and ectoderm. *Biotechnology Journal* (2014) doi:10.1002/biot.201300120.
4. Madison, B. B. *et al.* Epithelial hedgehog signals pattern the intestinal crypt-villus axis. *Development* (2005) doi:10.1242/dev.01576.
5. Haramis, A. P. G. *et al.* De Novo Crypt Formation and Juvenile Polyposis on BMP Inhibition in Mouse Intestine. *Science (80-.).* (2004) doi:10.1126/science.1093587.
6. Crosnier, C., Stamataki, D. & Lewis, J. Organizing cell renewal in the intestine: Stem cells, signals and combinatorial control. *Nature Reviews Genetics* (2006) doi:10.1038/nrg1840.
7. Korinek, V. *et al.* Depletion of epithelial stem-cell compartments in the small intestine of mice lacking Tcf-4. *Nat. Genet.* (1998) doi:10.1038/1270.
8. Karlsson, L., Lindahl, P., Heath, J. K. & Betsholtz, C. Abnormal gastrointestinal development in PDGF-A and PDGFR-α deficient mice implicates a novel mesenchymal structure with putative instructive properties in villus morphogenesis. *Development* (2000).
9. Vermeulen, L. & Snippert, H. J. Stem cell dynamics in homeostasis and cancer of the intestine. *Nat. Rev. Cancer* **14**, 468–480 (2014).
10. van der Flier, L. G. & Clevers, H. Stem Cells, Self-Renewal, and Differentiation in the Intestinal Epithelium. *Annu. Rev. Physiol.* **71**, 241–260 (2009).
11. Barker, N. Adult intestinal stem cells: Critical drivers of epithelial homeostasis and regeneration. *Nat. Rev. Mol. Cell Biol.* **15**, 19–33 (2014).
12. Cheng, H. & Leblond, C. P. Origin, differentiation and renewal of the four main epithelial cell types in the mouse small intestine V. Unitarian theory of the origin of the four epithelial cell types. *Am. J. Anat.* (1974) doi:10.1002/aja.1001410407.
13. Blanpain, C. & Simons, B. D. Unravelling stem cell dynamics by lineage tracing. *Nature Reviews Molecular Cell Biology* (2013) doi:10.1038/nrm3625.
14. POTTEN, C. S., BOOTH, C. & PRITCHARD, D. M. The intestinal epithelial stem cell: the mucosal governor. *Int. J. Exp. Pathol.* (1997) doi:10.1046/j.1365-2613.1997.280362.x.
15. Barker, N. *et al.* Identification of stem cells in small intestine and colon by marker gene Lgr5.

Nature (2007) doi:10.1038/nature06196.

16. Sato, T. *et al.* Single Lgr5 stem cells build crypt-villus structures in vitro without a mesenchymal niche. *Nature* (2009) doi:10.1038/nature07935.
17. Van der Flier, L. G. *et al.* The Intestinal Wnt/TCF Signature. *Gastroenterology* (2007) doi:10.1053/j.gastro.2006.08.039.
18. De Lau, W. *et al.* Lgr5 homologues associate with Wnt receptors and mediate R-spondin signalling. *Nature* (2011) doi:10.1038/nature10337.
19. Cavallo, R. A. *et al.* Drosophila Tcf and Groucho interact to repress wingless signalling activity. *Nature* (1998) doi:10.1038/26982.
20. Roose, J. *et al.* The Xenopus Wnt effector XTcf-3 interacts with Groucho-related transcriptional repressors. *Nature* (1998) doi:10.1038/26989.
21. Yang, Q., Bermingham, N. A., Finegold, M. J. & Zoghbi, H. Y. Requirement of Math1 for secretory cell lineage commitment in the mouse intestine. *Science (80-.).* (2001) doi:10.1126/science.1065718.
22. Sancho, E., Batlle, E. & Clevers, H. Signaling Pathways in Intestinal Development and Cancer. *Annu. Rev. Cell Dev. Biol.* **20**, 695–723 (2004).
23. Jensen, J. *et al.* Control of endodermal endocrine development by Hes-1. *Nat. Genet.* (2000) doi:10.1038/71657.
24. Shroyer, N. F., Wallis, D., Venken, K. J. T., Bellen, H. J. & Zoghbi, H. Y. Gfi1 functions downstream of Math1 to control intestinal secretory cell subtype allocation and differentiation. *Genes Dev.* (2005) doi:10.1101/gad.1353905.
25. VanDussen, K. L. & Samuelson, L. C. Mouse atonal homolog 1 directs intestinal progenitors to secretory cell rather than absorptive cell fate. *Dev. Biol.* (2010) doi:10.1016/j.ydbio.2010.07.026.
26. Karam, S. M. Lineage commitment and maturation of epithelial cells in the gut. *Frontiers in bioscience : a journal and virtual library* (1999) doi:10.2741/karam.
27. Birchenough, G. M. H., Johansson, M. E. V., Gustafsson, J. K., Bergström, J. H. & Hansson, G. C. New developments in goblet cell mucus secretion and function. *Mucosal Immunol.* **8**, 712–719 (2015).
28. Marillier, R. G. *et al.* IL-4/IL-13 independent goblet cell hyperplasia in experimental helminth infections. *BMC Immunol.* (2008) doi:10.1186/1471-2172-9-11.
29. Latorre, R., Sternini, C., De Giorgio, R. & Greenwood-Van Meerveld, B. Enteroendocrine cells: A review of their role in brain-gut communication. *Neurogastroenterology and Motility* (2016) doi:10.1111/nmo.12754.
30. Gribble, F. M. & Reimann, F. Enteroendocrine Cells: Chemosensors in the Intestinal

Epithelium. *Annu. Rev. Physiol.* (2016) doi:10.1146/annurev-physiol-021115-105439.

31. Crawley, S. W., Mooseker, M. S. & Tyska, M. J. Shaping the intestinal brush border. *J. Cell Biol.* **207**, 441–451 (2014).
32. Maury, J., Nicoletti, C., Guzzo-Chambraud, L. & Maroux, S. The Filamentous Brush Border Glycocalyx, a Mucin-like Marker of Enterocyte Hyper-Polarization. *Eur. J. Biochem.* (1995) doi:10.1111/j.1432-1033.1995.tb20267.x.
33. Conner, S. D. & Schmid, S. L. Regulated portals of entry into the cell. *Nature* (2003) doi:10.1038/nature01451.
34. Pappenheimer, J. R. Intestinal absorption of hexoses and amino acids: From apical cytosol to villus capillaries. *Journal of Membrane Biology* (2001) doi:10.1007/s00232-001-0094-1.
35. Sato, A. Tuft cells. *Anatomical Science International* (2007) doi:10.1111/j.1447-073X.2007.00188.x.
36. Luciano, L. & Reale, E. Brush cells of the mouse gallbladder - A correlative light- and electron-microscopical study. *Cell Tissue Res.* (1990) doi:10.1007/BF00309889.
37. Höfer, D., Püschel, B. & Drenckhahn, D. Taste receptor-like cells in the rat gut identified by expression of α-gustducin. *Proc. Natl. Acad. Sci. U. S. A.* (1996) doi:10.1073/pnas.93.13.6631.
38. Bezençon, C. *et al.* Murine intestinal cells expressing Trpm5 are mostly brush cells and express markers of neuronal and inflammatory cells. *J. Comp. Neurol.* (2008) doi:10.1002/cne.21768.
39. Akimori, T. *et al.* Quantitative distribution of brush cells in the rat gastrointestinal tract: Brush cell population coincides with NaHCO 3 secretion. *Med. Mol. Morphol.* (2011) doi:10.1007/s00795-009-0488-1.
40. WHO, Asia, S. S., Asia, S. S. & Hdi, H. Source: Globocan 2020. *Globocan 2020* **419**, 1–2 (2020).
41. *AJCC Cancer Staging Manual*. *AJCC Cancer Staging Manual* (2017). doi:10.1007/978-3-319-40618-3.
42. Galon, J. *et al.* Type, density, and location of immune cells within human colorectal tumors predict clinical outcome. *Science (80-.).* (2006) doi:10.1126/science.1129139.
43. Galon, J., Fridman, W. H. & Pages, F. The adaptive immunologic microenvironment in colorectal cancer: A novel perspective. *Cancer Research* (2007) doi:10.1158/0008-5472.CAN-06-4806.
44. Galon, J., Angell, H. K., Bedognetti, D. & Marincola, F. M. The Continuum of Cancer Immunosurveillance: Prognostic, Predictive, and Mechanistic Signatures. *Immunity* (2013) doi:10.1016/j.immuni.2013.07.008.
45. Angell, H. & Galon, J. From the immune contexture to the Immunoscore: The role of prognostic and predictive immune markers in cancer. *Current Opinion in Immunology* (2013) doi:10.1016/j.coi.2013.03.004.

46. Fridman, W. H., Pagès, F., Saut̀s-Fridman, C. & Galon, J. The immune contexture in human tumours: Impact on clinical outcome. *Nature Reviews Cancer* (2012) doi:10.1038/nrc3245.
47. Fleming, M., Ravula, S., Tatishchev, S. F. & Wang, H. L. Colorectal carcinoma: Pathologic aspects. *Journal of Gastrointestinal Oncology* (2012) doi:10.3978/j.issn.2078-6891.2012.030.
48. Nagtegaal, I. D. *et al.* The 2019 WHO classification of tumours of the digestive system. *Histopathology* (2020) doi:10.1111/his.13975.
49. Hyngstrom, J. R. *et al.* Clinicopathology and outcomes for mucinous and signet ring colorectal adenocarcinoma: Analysis from the National Cancer Data Base. *Ann. Surg. Oncol.* (2012) doi:10.1245/s10434-012-2321-7.
50. Hugen, N. *et al.* Prognosis and value of adjuvant chemotherapy in stage III mucinous colorectal carcinoma. *Ann. Oncol.* (2013) doi:10.1093/annonc/mdt378.
51. Hugen, N., Brown, G., Glynne-Jones, R., De Wilt, J. H. W. & Nagtegaal, I. D. Advances in the care of patients with mucinous colorectal cancer. *Nature Reviews Clinical Oncology* vol. 13 361–369 (2016).
52. Mekenkamp, L. J. M. *et al.* Mucinous adenocarcinomas: Poor prognosis in metastatic colorectal cancer. *Eur. J. Cancer* (2012) doi:10.1016/j.ejca.2011.12.004.
53. Barresi, V., Branca, G., Vitarelli, E. & Tuccari, G. Micropapillary Pattern and Poorly Differentiated Clusters Represent the Same Biological Phenomenon in Colorectal Cancer: A Proposal for a Change in Terminology. *Am. J. Clin. Pathol.* (2014) doi:10.1309/AJCPFEA7KA0SBBNA.
54. Laiho, P. *et al.* Serrated carcinomas form a subclass of colorectal cancer with distinct molecular basis. *Oncogene* (2007) doi:10.1038/sj.onc.1209778.
55. Wick, M. R., Vitsky, J. L., Ritter, J. H., Swanson, P. E. & Mills, S. E. Sporadic medullary carcinoma of the colon: A clinicopathologic comparison with nonhereditary poorly differentiated enteric-type adenocarcinoma and neuroendocrine colorectal carcinoma. *Am. J. Clin. Pathol.* (2005) doi:10.1309/1VFJ-1C3L-P52A-4FP8.
56. Hugen, N. *et al.* Colorectal signet-ring cell carcinoma: Benefit from adjuvant chemotherapy but a poor prognostic factor. *Int. J. Cancer* (2015) doi:10.1002/ijc.28981.
57. Karkouche, R. *et al.* Colorectal neuroendocrine carcinomas and adenocarcinomas share oncogenic pathways. A clinico-pathologic study of 12 cases. *Eur. J. Gastroenterol. Hepatol.* (2012) doi:10.1097/MEG.0b013e3283583c87.
58. Nagtegaal, I. D. & Hugen, N. The Increasing Relevance of Tumour Histology in Determining Oncological Outcomes in Colorectal Cancer. *Current Colorectal Cancer Reports* (2015) doi:10.1007/s11888-015-0280-7.
59. Budinska, E. *et al.* Gene expression patterns unveil a new level of molecular heterogeneity in

colorectal cancer. *J. Pathol.* (2013) doi:10.1002/path.4212.

60. Marisa, L. *et al.* Gene Expression Classification of Colon Cancer into Molecular Subtypes: Characterization, Validation, and Prognostic Value. *PLoS Med.* (2013) doi:10.1371/journal.pmed.1001453.
61. Roepman, P. *et al.* Colorectal cancer intrinsic subtypes predict chemotherapy benefit, deficient mismatch repair and epithelial-to-mesenchymal transition. *Int. J. Cancer* (2014) doi:10.1002/ijc.28387.
62. De Sousa E Melo, F. *et al.* Poor-prognosis colon cancer is defined by a molecularly distinct subtype and develops from serrated precursor lesions. *Nat. Med.* (2013) doi:10.1038/nm.3174.
63. Sadanandam, A. *et al.* A colorectal cancer classification system that associates cellular phenotype and responses to therapy. *Nat. Med.* (2013) doi:10.1038/nm.3175.
64. Schlicker, A. *et al.* Subtypes of primary colorectal tumors correlate with response to targeted treatment in colorectal cell lines. *BMC Med. Genomics* (2012) doi:10.1186/1755-8794-5-66.
65. Guinney, J. *et al.* Consensus molecular subtypes and the evolution of precision medicine in colorectal cancer. *Nature Reviews Cancer* (2017) doi:10.1038/nrc.2016.126.
66. Perucho, M. Microsatellite instability: The mutator that mutates the other mutator. *Nature Medicine* (1996) doi:10.1038/nm0696-630.
67. Thibodeau, S. N., Bren, G. & Schaid, D. Microsatellite instability in cancer of the proximal colon. *Science (80-.).* (1993) doi:10.1126/science.8484122.
68. Hughes, L. A. E. *et al.* The CpG island methylator phenotype: What's in a name? *Cancer Research* (2013) doi:10.1158/0008-5472.CAN-12-4306.
69. Llosa, N. J. *et al.* The vigorous immune microenvironment of microsatellite instable colon cancer is balanced by multiple counter-inhibitory checkpoints. *Cancer Discov.* (2015) doi:10.1158/2159-8290.CD-14-0863.
70. Son, J. *et al.* Glutamine supports pancreatic cancer growth through a KRAS-regulated metabolic pathway. *Nature* (2013) doi:10.1038/nature12040.
71. Ying, H. *et al.* Oncogenic kras maintains pancreatic tumors through regulation of anabolic glucose metabolism. *Cell* (2012) doi:10.1016/j.cell.2012.01.058.
72. Kalluri, R. & Zeisberg, M. Fibroblasts in cancer. *Nature Reviews Cancer* (2006) doi:10.1038/nrc1877.
73. Dunne, P. D. *et al.* Challenging the cancer molecular stratification dogma: Intratumoral heterogeneity undermines consensus molecular subtypes and potential diagnostic value in colorectal cancer. *Clin. Cancer Res.* (2016) doi:10.1158/1078-0432.CCR-16-0032.
74. Isella, C. *et al.* Stromal contribution to the colorectal cancer transcriptome. *Nat. Genet.* (2015)

doi:10.1038/ng.3224.

75. Spaderna, S. *et al.* A Transient, EMT-Linked Loss of Basement Membranes Indicates Metastasis and Poor Survival in Colorectal Cancer. *Gastroenterology* (2006) doi:10.1053/j.gastro.2006.06.016.
76. Fischer, K. R. *et al.* Epithelial-to-mesenchymal transition is not required for lung metastasis but contributes to chemoresistance. *Nature* (2015) doi:10.1038/nature15748.
77. Zheng, X. *et al.* Epithelial-to-mesenchymal transition is dispensable for metastasis but induces chemoresistance in pancreatic cancer. *Nature* (2015) doi:10.1038/nature16064.
78. Fessler, E. & Medema, J. P. Colorectal Cancer Subtypes: Developmental Origin and Microenvironmental Regulation. *Trends in Cancer* vol. 2 505–518 (2016).
79. Barker, N. *et al.* Crypt stem cells as the cells-of-origin of intestinal cancer. *Nature* (2009) doi:10.1038/nature07602.
80. Schwitalla, S. *et al.* Intestinal tumorigenesis initiated by dedifferentiation and acquisition of stem-cell-like properties. *Cell* (2013) doi:10.1016/j.cell.2012.12.012.
81. Lee, G. H. *et al.* Is right-sided colon cancer different to left-sided colorectal cancer? - A systematic review. *European Journal of Surgical Oncology* (2015) doi:10.1016/j.ejso.2014.11.001.
82. Nguyen, H. T. & Duong, H. Q. The molecular characteristics of colorectal cancer: Implications for diagnosis and therapy (review). *Oncology Letters* (2018) doi:10.3892/ol.2018.8679.
83. Vogelstein, B. *et al.* Genetic Alterations during Colorectal-Tumor Development. *N. Engl. J. Med.* (1988) doi:10.1056/NEJM198809013190901.
84. Galiatsatos, P. & Foulkes, W. D. Familial adenomatous polyposis. *American Journal of Gastroenterology* (2006) doi:10.1111/j.1572-0241.2006.00375.x.
85. Segditsas, S. & Tomlinson, I. Colorectal cancer and genetic alterations in the Wnt pathway. *Oncogene* (2006) doi:10.1038/sj.onc.1210059.
86. Polakis, P. The many ways of Wnt in cancer. *Current Opinion in Genetics and Development* (2007) doi:10.1016/j.gde.2006.12.007.
87. Aoki, K. & Taketo, M. M. Adenomatous polyposis coli (APC): A multi-functional tumor suppressor gene. *Journal of Cell Science* (2007) doi:10.1242/jcs.03485.
88. Malumbres, M. & Barbacid, M. RAS oncogenes: The first 30 years. *Nature Reviews Cancer* (2003) doi:10.1038/nrc1097.
89. Bogaert, J. & Prenen, H. Molecular genetics of colorectal cancer. *Ann. Gastroenterol.* **27**, 9–14 (2014).
90. Tasdemir, E. *et al.* Regulation of autophagy by cytoplasmic p53. *Nat. Cell Biol.* (2008) doi:10.1038/ncb1730.

91. Jass, J. R. Classification of colorectal cancer based on correlation of clinical, morphological and molecular features. *Histopathology* (2007) doi:10.1111/j.1365-2559.2006.02549.x.
92. Bettington, M. *et al.* The serrated pathway to colorectal carcinoma: Current concepts and challenges. *Histopathology* (2013) doi:10.1111/his.12055.
93. Kahi, C. J. Screening relevance of sessile serrated polyps. *Clin. Endosc.* (2019) doi:10.5946/ce.2018.112.
94. East, J. E. *et al.* British Society of Gastroenterology position statement on serrated polyps in the colon and rectum. *Gut* (2017) doi:10.1136/gutjnl-2017-314005.
95. O'Brien, M. J., Zhao, Q. & Yang, S. Colorectal serrated pathway cancers and precursors. *Histopathology* **66**, 49–65 (2015).
96. Wajapeyee, N., Serra, R. W., Zhu, X., Mahalingam, M. & Green, M. R. Role for IGFBP7 in senescence induction by BRAF. *Cell* (2010) doi:10.1016/j.cell.2010.05.014.
97. Kriegl, L. *et al.* Up and downregulation of p16 Ink4a expression in BRAF-mutated polyps/adenomas indicates a senescence barrier in the serrated route to colon cancer. *Mod. Pathol.* (2011) doi:10.1038/modpathol.2011.43.
98. Egeblad, M., Nakasone, E. S. & Werb, Z. Tumors as organs: Complex tissues that interface with the entire organism. *Developmental Cell* (2010) doi:10.1016/j.devcel.2010.05.012.
99. Jodele, S., Blavier, L., Yoon, J. M. & DeClerck, Y. A. Modifying the soil to affect the seed: Role of stromal-derived matrix metalloproteinases in cancer progression. *Cancer and Metastasis Reviews* (2006) doi:10.1007/s10555-006-7887-8.
100. Pankova, D. *et al.* Cancer-associated fibroblasts induce a collagen cross-link switch in tumor stroma. *Mol. Cancer Res.* (2016) doi:10.1158/1541-7786.MCR-15-0307.
101. Dunn, G. P., Bruce, A. T., Ikeda, H., Old, L. J. & Schreiber, R. D. Cancer immunoediting: From immunosurveillance to tumor escape. *Nature Immunology* (2002) doi:10.1038/ni1102-991.
102. O'Donnell, J. S., Teng, M. W. L. & Smyth, M. J. Cancer immunoediting and resistance to T cell-based immunotherapy. *Nature Reviews Clinical Oncology* (2019) doi:10.1038/s41571-018-0142-8.
103. Dolcetti, R. *et al.* High prevalence of activated intraepithelial cytotoxic T lymphocytes and increased neoplastic cell apoptosis in colorectal carcinomas with microsatellite instability. *Am. J. Pathol.* (1999) doi:10.1016/S0002-9440(10)65436-3.
104. Schwitalle, Y. *et al.* Immune Response Against Frameshift-Induced Neopeptides in HNPCC Patients and Healthy HNPCC Mutation Carriers. *Gastroenterology* (2008) doi:10.1053/j.gastro.2008.01.015.
105. Waldner, M. J. & Neurath, M. F. Colitis-associated cancer: The role of T cells in tumor development. *Seminars in Immunopathology* (2009) doi:10.1007/s00281-009-0161-8.

106. Jawad, N., Direkze, N. & Leedham, S. J. Inflammatory bowel disease and colon cancer. *Recent results in cancer research. Fortschritte der Krebsforschung. Progrès dans les recherches sur le cancer* (2011) doi:10.1007/978-3-642-03503-6_6.

107. Chaffer, C. L. & Weinberg, R. A. A perspective on cancer cell metastasis. *Science* (2011) doi:10.1126/science.1203543.

108. Bray, F. *et al.* Global cancer statistics 2018: GLOBOCAN estimates of incidence and mortality worldwide for 36 cancers in 185 countries. *CA. Cancer J. Clin.* (2018) doi:10.3322/caac.21492.

109. Leong, S. P. L. *et al.* Clinical patterns of metastasis. in *Cancer and Metastasis Reviews* (2006). doi:10.1007/s10555-006-8502-8.

110. Pretzsch, E. *et al.* Mechanisms of Metastasis in Colorectal Cancer and Metastatic Organotropism: Hematogenous versus Peritoneal Spread. *Journal of Oncology* (2019) doi:10.1155/2019/7407190.

111. Lambert, A. W., Pattabiraman, D. R. & Weinberg, R. A. Emerging Biological Principles of Metastasis. *Cell* (2017) doi:10.1016/j.cell.2016.11.037.

112. Lemoine, L., Sugarbaker, P. & Van Der Speeten, K. Pathophysiology of colorectal peritoneal carcinomatosis: Role of the peritoneum. *World Journal of Gastroenterology* (2016) doi:10.3748/wjg.v22.i34.7692.

113. van der Wal, J. B. C. & Jeekel, J. Biology of the peritoneum in normal homeostasis and after surgical trauma. *Color. Dis.* (2007) doi:10.1111/j.1463-1318.2007.01345.x.

114. Aoyagi, T., Terracina, K. P., Raza, A. & Takabe, K. Current treatment options for colon cancer peritoneal carcinomatosis. *World Journal of Gastroenterology* (2014) doi:10.3748/wjg.v20.i35.12493.

115. Lambert Lack, H. A CONTRIBUTION TO THE OPERATIVE TREATMENT OF MALIGNANT DISEASE OF THE LARYNX, WITH SPECIAL REFERENCE TO THE DANGER OF CANCEROUS WOUND INFECTION. *Lancet* (1896) doi:10.1016/S0140-6736(01)64038-8.

116. Gresham, E. & Don Parsa, F. Iatrogenic Implantation of Cancer Cells During Surgery. *Hawai'i J. Heal. Soc. Welf.* **79**, 4–6 (2020).

117. Backes, Y. *et al.* Tumor Seeding During Colonoscopy as a Possible Cause for Metachronous Colorectal Cancer. *Gastroenterology* **157**, 1222-1232.e4 (2019).

118. Amit, M., Na'Ara, S. & Gil, Z. Mechanisms of cancer dissemination along nerves. *Nature Reviews Cancer* (2016) doi:10.1038/nrc.2016.38.

119. Dodd, G. D., Dolan, P. A., Ballantyne, A. J., Ibanez, M. L. & Chau, P. The dissemination of tumors of the head and neck via the cranial nerves. *Radiologic Clinics of North America* (1970).

120. Liebig, C. *et al.* Perineural invasion is an independent predictor of outcome in colorectal cancer. *J. Clin. Oncol.* (2009) doi:10.1200/JCO.2009.22.4949.

121. Krasna, M. J., Flancbaum, L., Cody, R. P., Shneibaum, S. & Ari, G. Ben. Vascular and neural invasion in colorectal carcinoma. Incidence and prognostic significance. *Cancer* (1988) doi:10.1002/1097-0142(19880301)61:5<1018::AID-CNCR2820610527>3.0.CO;2-H.

122. Corrò, C., Novellasdemunt, L. & Li, V. S. W. A brief history of organoids. *Am. J. Physiol. - Cell Physiol.* (2020) doi:10.1152/ajpcell.00120.2020.

123. Drost, J. *et al.* Sequential cancer mutations in cultured human intestinal stem cells. *Nature* (2015) doi:10.1038/nature14415.

124. Tuveson, D. & Clevers, H. Cancer modeling meets human organoid technology. *Science* (2019) doi:10.1126/science.aaw6985.

125. Burkitt, M. D., Duckworth, C. A., Williams, J. M. & Pritchard, D. M. Helicobacter pylori-induced gastric pathology: Insights from in vivo and ex vivo models. *DMM Disease Models and Mechanisms* (2017) doi:10.1242/dmm.027649.

126. Wen, Y. A. *et al.* Adipocytes activate mitochondrial fatty acid oxidation and autophagy to promote tumor growth in colon cancer. *Cell Death Dis.* (2017) doi:10.1038/cddis.2017.21.

127. Wong, S. H. & Yu, J. Gut microbiota in colorectal cancer: mechanisms of action and clinical applications. *Nature Reviews Gastroenterology and Hepatology* (2019) doi:10.1038/s41575-019-0209-8.

128. Hill, D. R. & Spence, J. R. Gastrointestinal Organoids: Understanding the Molecular Basis of the Host–Microbe Interface. *CMGH* (2017) doi:10.1016/j.jcmgh.2016.11.007.

129. Lau, H. C. H., Kranenburg, O., Xiao, H. & Yu, J. Organoid models of gastrointestinal cancers in basic and translational research. *Nature Reviews Gastroenterology and Hepatology* (2020) doi:10.1038/s41575-019-0255-2.

130. Van De Wetering, M. *et al.* Prospective derivation of a living organoid biobank of colorectal cancer patients. *Cell* **161**, 933–945 (2015).

131. LISCO, H., FINKEL, M. P. & BRUES, A. M. Carcinogenic properties of radioactive fission products and of plutonium. *Radiology* (1947) doi:10.1148/49.3.361.

132. Hoffmann, M. *et al.* A refined and translationally relevant model of chronic DSS colitis in BALB/c mice. *Lab. Anim.* (2018) doi:10.1177/0023677217742681.

133. Fearon, E. R. & Vogelstein, B. A genetic model for colorectal tumorigenesis. *Cell* (1990) doi:10.1016/0092-8674(90)90186-I.

134. Donehower, L. A. *et al.* Mice deficient for p53 are developmentally normal but susceptible to spontaneous tumours. *Nature* (1992) doi:10.1038/356215a0.

135. Dow, L. E. *et al.* Apc Restoration Promotes Cellular Differentiation and Reestablishes Crypt Homeostasis in Colorectal Cancer. *Cell* (2015) doi:10.1016/j.cell.2015.05.033.

136. Chanrion, M. *et al.* Concomitant Notch activation and p53 deletion trigger epithelial-to-

mesenchymal transition and metastasis in mouse gut. *Nat. Commun.* (2014) doi:10.1038/ncomms6005.

137. Takaku, K. *et al.* Intestinal tumorigenesis in compound mutant mice of both Dpc4 (Smad4) and Apc genes. *Cell* (1998) doi:10.1016/S0092-8674(00)81132-0.
138. Anderson, R. L. *et al.* A framework for the development of effective anti-metastatic agents. *Nature Reviews Clinical Oncology* (2019) doi:10.1038/s41571-018-0134-8.
139. Yang, G. *et al.* Dominant effects of an Msh6 missense mutation on DNA repair and cancer susceptibility. *Cancer Cell* (2004) doi:10.1016/j.ccr.2004.06.024.
140. Bürtin, F., Mullins, C. S. & Linnebacher, M. Mouse models of colorectal cancer: Past, present and future perspectives. *World Journal of Gastroenterology* (2020) doi:10.3748/WJG.V26.I13.1394.
141. Blomme, A. *et al.* Murine stroma adopts a human-like metabolic phenotype in the PDX model of colorectal cancer and liver metastases. *Oncogene* (2018) doi:10.1038/s41388-017-0018-x.
142. Choi, Y. *et al.* Studying cancer immunotherapy using patient-derived xenografts (PDXs) in humanized mice. *Experimental and Molecular Medicine* (2018) doi:10.1038/s12276-018-0115-0.
143. O'Rourke, K. P. *et al.* Transplantation of engineered organoids enables rapid generation of metastatic mouse models of colorectal cancer. *Nat. Biotechnol.* **35**, 577–582 (2017).
144. Roper, J. *et al.* In vivo genome editing and organoid transplantation models of colorectal cancer and metastasis. *Nat. Biotechnol.* **35**, 569–576 (2017).
145. Schepers, A. G. *et al.* Lineage tracing reveals Lgr5+ stem cell activity in mouse intestinal adenomas. *Science (80-.).* (2012) doi:10.1126/science.1224676.
146. Thiery, J. P., Acloque, H., Huang, R. Y. J. & Nieto, M. A. Epithelial-Mesenchymal Transitions in Development and Disease. *Cell* vol. 139 871–890 (2009).
147. Nelson, W. J. Adaptation of core mechanisms to generate cell polarity. *Nature* (2003) doi:10.1038/nature01602.
148. Aijaz, S., Balda, M. S. & Matter, K. Tight junctions: Molecular architecture and function. *International Review of Cytology* (2006) doi:10.1016/S0074-7696(06)48005-0.
149. Rafelski, S. M. & Marshall, W. F. Building the cell: Design principles of cellular architecture. *Nature Reviews Molecular Cell Biology* (2008) doi:10.1038/nrm2460.
150. Lamouille, S., Xu, J. & Derynck, R. Molecular mechanisms of epithelial-mesenchymal transition. *Nature Reviews Molecular Cell Biology* (2014) doi:10.1038/nrm3758.
151. Thiery, J. P. & Sleeman, J. P. Complex networks orchestrate epithelial-mesenchymal transitions. *Nature Reviews Molecular Cell Biology* (2006) doi:10.1038/nrm1835.
152. Huang, R. Y. J., Guilford, P. & Thiery, J. P. Early events in cell adhesion and polarity during

epithelialmesenchymal transition. *J. Cell Sci.* (2012) doi:10.1242/jcs.099697.

153. Nisticò, P., Bissell, M. J. & Radisky, D. C. Epithelial-mesenchymal transition: General principles and pathological relevance with special emphasis on the role of matrix metalloproteinases. *Cold Spring Harb. Perspect. Biol.* (2012) doi:10.1101/cshperspect.a011908.
154. Maschler, S. M. *et al.* Tumor cell invasiveness correlates with changes in integrin expression and localization. *Oncogene* (2005) doi:10.1038/sj.onc.1208423.
155. Ridley, A. J. Life at the leading edge. *Cell* (2011) doi:10.1016/j.cell.2011.06.010.
156. McNiven, M. A. Breaking away: Matrix remodeling from the leading edge. *Trends in Cell Biology* (2013) doi:10.1016/j.tcb.2012.08.009.
157. Anastasiadis, P. Z. & Reynolds, A. B. Regulation of Rho GTPases by p120-catenin. *Current Opinion in Cell Biology* (2001) doi:10.1016/S0955-0674(00)00258-1.
158. Nelson, W. J. Remodeling epithelial cell organization: transitions between front-rear and apical-basal polarity. *Cold Spring Harbor perspectives in biology* (2009) doi:10.1101/cshperspect.a000513.
159. Wrana, J. L., Attisano, L., Wieser, R., Ventura, F. & Massagué, J. Mechanism of activation of the TGF-β receptor. *Nature* (1994) doi:10.1038/370341a0.
160. Shi, Y. & Massagué, J. Mechanisms of TGF-β signaling from cell membrane to the nucleus. *Cell* (2003) doi:10.1016/S0092-8674(03)00432-X.
161. Fuentealba, L. C. *et al.* Integrating Patterning Signals: Wnt/GSK3 Regulates the Duration of the BMP/Smad1 Signal. *Cell* (2007) doi:10.1016/j.cell.2007.09.027.
162. Kavsak, P. *et al.* Smad7 binds to Smurf2 to form an E3 ubiquitin ligase that targets the TGFβ receptor for degradation. *Mol. Cell* (2000) doi:10.1016/S1097-2765(00)00134-9.
163. Ebisawa, T. *et al.* Smurf1 Interacts with Transforming Growth Factor-β Type I Receptor through Smad7 and Induces Receptor Degradation. *J. Biol. Chem.* (2001) doi:10.1074/jbc.C100008200.
164. Vincent, T. *et al.* A SNAIL1-SMAD3/4 transcriptional repressor complex promotes TGF-β mediated epithelial-mesenchymal transition. *Nat. Cell Biol.* (2009) doi:10.1038/ncb1905.
165. Ozdamar, B. *et al.* Regulation of the polarity protein Par6 by TGFβ receptors controls epithelial cell plasticity. *Science (80-.).* (2005) doi:10.1126/science.1105718.
166. Viloria-Petit, A. M. *et al.* A role for the TGFβ-Par6 polarity pathway in breast cancer progression. *Proc. Natl. Acad. Sci. U. S. A.* (2009) doi:10.1073/pnas.0906796106.
167. Foletta, V. C. *et al.* Direct signaling by the BMP type II receptor via the cytoskeletal regulator LIMK1. *J. Cell Biol.* (2003) doi:10.1083/jcb.200212060.
168. Kang, Y., Chen, C. R. & Massagué, J. A self-enabling TGFβ response coupled to stress signaling: Smad engages stress response factor ATF3 for Id1 repression in epithelial cells. *Mol. Cell*

(2003) doi:10.1016/S1097-2765(03)00109-6.

169. Padua, D. *et al.* TGFβ Primes Breast Tumors for Lung Metastasis Seeding through Angiopoietin-like 4. *Cell* (2008) doi:10.1016/j.cell.2008.01.046.
170. Massagué, J. TGFβ signalling in context. *Nature Reviews Molecular Cell Biology* (2012) doi:10.1038/nrm3434.
171. Brabletz, T., Kalluri, R., Nieto, M. A. A. & Weinberg, R. A. A. EMT in cancer. *Nature Reviews Cancer* (2018) doi:10.1038/nrc.2017.118.
172. Nieto, M. A., Huang, R. Y. Y. J., Jackson, R. A. A. & Thiery, J. P. P. EMT: 2016. *Cell* (2016) doi:10.1016/j.cell.2016.06.028.
173. Barrallo-Gimeno, A. & Nieto, M. A. The Snail genes as inducers of cell movement and survival: Implications in development and cancer. *Development* (2005) doi:10.1242/dev.01907.
174. Ansieau, S. *et al.* Induction of EMT by Twist Proteins as a Collateral Effect of Tumor-Promoting Inactivation of Premature Senescence. *Cancer Cell* (2008) doi:10.1016/j.ccr.2008.06.005.
175. Liu, Y., El-Naggar, S., Darling, D. S., Higashi, Y. & Dean, D. C. Zeb1 links epithelial-mesenchymal transition and cellular senescence. *Development* (2008) doi:10.1242/dev.007047.
176. Cochrane, D. R., Spoelstra, N. S., Howe, E. N., Nordeen, S. K. & Richer, J. K. MicroRNA-200c mitigates invasiveness and restores sensitivity to microtubule-targeting chemotherapeutic agents. *Mol. Cancer Ther.* (2009) doi:10.1158/1535-7163.MCT-08-1046.
177. Tan, T. Z. *et al.* Epithelial-mesenchymal transition spectrum quantification and its efficacy in deciphering survival and drug responses of cancer patients. *EMBO Mol. Med.* (2014) doi:10.15252/emmm.201404208.
178. Kudo-Saito, C., Shirako, H., Takeuchi, T. & Kawakami, Y. Cancer Metastasis Is Accelerated through Immunosuppression during Snail-Induced EMT of Cancer Cells. *Cancer Cell* (2009) doi:10.1016/j.ccr.2009.01.023.
179. Julien, S. *et al.* Activation of NF-κB by Akt upregulates Snail expression and induces epithelium mesenchyme transition. *Oncogene* (2007) doi:10.1038/sj.onc.1210546.
180. Mani, S. A. *et al.* The Epithelial-Mesenchymal Transition Generates Cells with Properties of Stem Cells. *Cell* (2008) doi:10.1016/j.cell.2008.03.027.
181. Bergert, M., Chandradoss, S. D., Desai, R. A. & Paluch, E. Cell mechanics control rapid transitions between blebs and lamellipodia during migration. *Proc. Natl. Acad. Sci. U. S. A.* (2012) doi:10.1073/pnas.1207968109.
182. Blanchoin, L., Boujemaa-Paterski, R., Sykes, C. & Plastino, J. Actin dynamics, architecture, and mechanics in cell motility. *Physiol. Rev.* (2014) doi:10.1152/physrev.00018.2013.
183. Schmidt, S. & Friedl, P. Interstitial cell migration: Integrin-dependent and alternative adhesion mechanisms. *Cell and Tissue Research* vol. 339 83–92 (2010).

184. Friedl, P., Wolf, K. & Lammerding, J. Nuclear mechanics during cell migration. *Current Opinion in Cell Biology* (2011) doi:10.1016/j.ceb.2010.10.015.
185. Bachir, A. I. *et al.* Integrin-associated complexes form hierarchically with variable stoichiometry in nascent adhesions. *Curr. Biol.* (2014) doi:10.1016/j.cub.2014.07.011.
186. Geiger, B., Spatz, J. P. & Bershadsky, A. D. Environmental sensing through focal adhesions. *Nature Reviews Molecular Cell Biology* (2009) doi:10.1038/nrm2593.
187. te Boekhorst, V., Preziosi, L. & Friedl, P. Plasticity of Cell Migration In Vivo and In Silico. *Annu. Rev. Cell Dev. Biol.* (2016) doi:10.1146/annurev-cellbio-111315-125201.
188. Paluch, E. K., Aspalter, I. M. & Sixt, M. Focal Adhesion–Independent Cell Migration. *Annu. Rev. Cell Dev. Biol.* (2016) doi:10.1146/annurev-cellbio-111315-125341.
189. Lehmann, S. *et al.* Hypoxia Induces a HIF-1-Dependent Transition from Collective-to-Amoeboid Dissemination in Epithelial Cancer Cells. *Curr. Biol.* (2017) doi:10.1016/j.cub.2016.11.057.
190. Case, L. B. *et al.* Molecular mechanism of vinculin activation and nanoscale spatial organization in focal adhesions. *Nat. Cell Biol.* (2015) doi:10.1038/ncb3180.
191. Paluch, E. K. & Raz, E. The role and regulation of blebs in cell migration. *Current Opinion in Cell Biology* (2013) doi:10.1016/j.ceb.2013.05.005.
192. Lämmermann, T. & Sixt, M. Mechanical modes of 'amoeboid' cell migration. *Current Opinion in Cell Biology* (2009) doi:10.1016/j.ceb.2009.05.003.
193. Petrie, R. J. & Yamada, K. M. At the leading edge of three-dimensional cell migration. *Journal of Cell Science* (2012) doi:10.1242/jcs.093732.
194. Friedl, P. & Bröcker, E. B. The biology of cell locomotion within three-dimensional extracellular matrix. *Cellular and Molecular Life Sciences* (2000) doi:10.1007/s000180050498.
195. Pan, Y. R. *et al.* STAT3-coordinated migration facilitates the dissemination of diffuse large B-cell lymphomas. *Nat. Commun.* (2018) doi:10.1038/s41467-018-06134-z.
196. Mayor, R. & Etienne-Manneville, S. The front and rear of collective cell migration. *Nature Reviews Molecular Cell Biology* (2016) doi:10.1038/nrm.2015.14.
197. Etienne-Manneville, S. Adherens junctions during cell migration. *Subcell. Biochem.* (2012) doi:10.1007/978-94-007-4186-7_10.
198. Bazellières, E. *et al.* Control of cell-cell forces and collective cell dynamics by the intercellular adhesome. *Nat. Cell Biol.* (2015) doi:10.1038/ncb3135.
199. Borghi, N., Lowndes, M., Maruthamuthu, V., Gardel, M. L. & Nelson, W. J. Regulation of cell motile behavior by crosstalk between cadherin- and integrin-mediated adhesions. *Proc. Natl. Acad. Sci. U. S. A.* (2010) doi:10.1073/pnas.1002662107.
200. Burute, M. & Thery, M. Spatial segregation between cell-cell and cell-matrix adhesions.

Current Opinion in Cell Biology (2012) doi:10.1016/j.ceb.2012.07.003.

201. Padmanaban, V. *et al.* E-cadherin is required for metastasis in multiple models of breast cancer. *Nature* **573**, 439–444 (2019).
202. Cheung, K. J., Gabrielson, E., Werb, Z. & Ewald, A. J. Collective invasion in breast cancer requires a conserved basal epithelial program. *Cell* **155**, 1639–1651 (2013).
203. Shellard, A., Szabó, A., Trepat, X. & Mayor, R. Supracellular contraction at the rear of neural crest cell groups drives collective chemotaxis. *Science (80-.).* (2018) doi:10.1126/science.aau3301.
204. Peng, H., Ong, Y. M., Shah, W. A., Holland, P. C. & Carbonetto, S. Integrins regulate centrosome integrity and astrocyte polarization following a wound. *Dev. Neurobiol.* (2013) doi:10.1002/dneu.22055.
205. Nguyen, B. P., Ryan, M. C., Gil, S. G. & Carter, W. G. Deposition of laminin 5 in epidermal wounds regulates integrin signaling and adhesion. *Current Opinion in Cell Biology* (2000) doi:10.1016/S0955-0674(00)00131-9.
206. Das, T. *et al.* A molecular mechanotransduction pathway regulates collective migration of epithelial cells. *Nat. Cell Biol.* (2015) doi:10.1038/ncb3115.
207. Leckband, D. E. & de Rooij, J. Cadherin Adhesion and Mechanotransduction. *Annu. Rev. Cell Dev. Biol.* (2014) doi:10.1146/annurev-cellbio-100913-013212.
208. Friedl, P., Locker, J., Sahai, E. & Segall, J. E. Classifying collective cancer cell invasion. *Nature Cell Biology* vol. 14 777–783 (2012).
209. Zajac, O. *et al.* Tumour spheres with inverted polarity drive the formation of peritoneal metastases in patients with hypermethylated colorectal carcinomas. *Nat. Cell Biol.* (2018) doi:10.1038/s41556-017-0027-6.
210. Pagès, D.-L. *et al.* Cell clusters adopt a collective amoeboid mode of migration in confined non-adhesive environments. 1–17 (2020) doi:10.1101/2020.05.28.106203.
211. Taddei, M. L. *et al.* EphA2 induces metastatic growth regulating amoeboid motility and clonogenic potential in prostate carcinoma cells. *Mol. Cancer Res.* (2011) doi:10.1158/1541-7786.MCR-10-0298.
212. Taddei, M. L. *et al.* Mesenchymal to amoeboid transition is associated with stem-like features of melanoma cells. *Cell Commun. Signal.* (2014) doi:10.1186/1478-811X-12-24.
213. Wolf, K. *et al.* Compensation mechanism in tumor cell migration: Mesenchymal-amoeboid transition after blocking of pericellular proteolysis. *J. Cell Biol.* **160**, 267–277 (2003).
214. Sanz-Moreno, V. *et al.* Rac Activation and Inactivation Control Plasticity of Tumor Cell Movement. *Cell* (2008) doi:10.1016/j.cell.2008.09.043.
215. Hale, R. & Strutt, D. Conservation of Planar Polarity Pathway Function Across the Animal

Kingdom. *Annu. Rev. Genet.* (2015) doi:10.1146/annurev-genet-112414-055224.

216. Lawrence, P. A. & Shelton, P. M. J. The determination of polarity in the developing insect retina. *J. Embryol. Exp. Morphol.* (1975).
217. Lawrence, P. A., Struhl, G. & Casal, J. Planar cell polarity: One or two pathways? *Nature Reviews Genetics* (2007) doi:10.1038/nrg2125.
218. Martin-Belmonte, F. & Mostov, K. Regulation of cell polarity during epithelial morphogenesis. *Current Opinion in Cell Biology* vol. 20 227–234 (2008).
219. Di Paolo, G. & De Camilli, P. Phosphoinositides in cell regulation and membrane dynamics. *Nature* (2006) doi:10.1038/nature05185.
220. Yin, H. L. & Janmey, P. A. Phosphoinositide Regulation of the Actin Cytoskeleton. *Annu. Rev. Physiol.* (2003) doi:10.1146/annurev.physiol.65.092101.142517.
221. Lemmon, M. A. Phosphoinositide recognition domains. *Traffic* (2003) doi:10.1034/j.1600-0854.2004.00071.x.
222. Kutateladze, T. G. Translation of the phosphoinositide code by PI effectors. *Nature Chemical Biology* (2010) doi:10.1038/nchembio.390.
223. Shewan, A., Eastburn, D. J. & Mostov, K. Phosphoinositides in cell architecture. *Cold Spring Harbor Perspectives in Biology* (2011) doi:10.1101/cshperspect.a004796.
224. Guerriero, C. J., Weixel, K. M., Bruns, J. R. & Weisz, O. A. Phosphatidylinositol 5-kinase stimulates apical biosynthetic delivery via an Arp2/3-dependent mechanism. *J. Biol. Chem.* (2006) doi:10.1074/jbc.M601239200.
225. Gassama-Diagne, A. *et al.* Phosphatidylinositol-3,4,5-trisphosphate regulates the formation of the basolateral plasma membrane in epithelial cells. *Nat. Cell Biol.* **8**, 963–970 (2006).
226. Román-Fernández, Á. *et al.* The phospholipid PI(3,4)P 2 is an apical identity determinant. *Nat. Commun.* **9**, (2018).
227. Martin-Belmonte, F. & Mostov, K. Phosphoinositides Control Epithelial Development. *Cell Cycle* (2007) doi:10.4161/cc.6.16.4583.
228. Di Paolo, G. *et al.* Recruitment and regulation of phosphatidylinositol phosphate kinase type 1γ by the FERM domain of talin. *Nature* (2002) doi:10.1038/nature01147.
229. Iden, S. & Collard, J. G. Crosstalk between small GTPases and polarity proteins in cell polarization. *Nature Reviews Molecular Cell Biology* (2008) doi:10.1038/nrm2521.
230. Etienne-Manneville, S. & Hall, A. Rho GTPases in cell biology. *Nature* (2002) doi:10.1038/nature01148.
231. Ridley, A. J. & Hall, A. The small GTP-binding protein rho regulates the assembly of focal adhesions and actin stress fibers in response to growth factors. *Cell* (1992) doi:10.1016/0092-8674(92)90163-7.

232. Ridley, A. J., Paterson, H. F., Johnston, C. L., Diekmann, D. & Hall, A. The small GTP-binding protein rac regulates growth factor-induced membrane ruffling. *Cell* (1992) doi:10.1016/0092-8674(92)90164-8.

233. Nobes, C. D. & Hall, A. Rho, Rac, and Cdc42 GTPases regulate the assembly of multimolecular focal complexes associated with actin stress fibers, lamellipodia, and filopodia. *Cell* (1995) doi:10.1016/0092-8674(95)90370-4.

234. Hodge, R. G. & Ridley, A. J. Regulating Rho GTPases and their regulators. *Nature Reviews Molecular Cell Biology* vol. 17 496–510 (2016).

235. Yamazaki, D., Oikawa, T. & Takenawa, T. Rac-WAVE-mediated actin reorganization is required for organization and maintenance of cell-cell adhesion. *J. Cell Sci.* (2007) doi:10.1242/jcs.03311.

236. Kobielak, A., Pasolli, H. A. & Fuchs, E. Mammalian formin-1 participates in adherens junctions and polymerization of linear actin cables. *Nat. Cell Biol.* (2004) doi:10.1038/ncb1075.

237. Kovacs, E. M., Goodwin, M., Ali, R. G., Paterson, A. D. & Yap, A. S. Cadherin-directed actin assembly: E-cadherin physically associates with the Arp2/3 complex to direct actin assembly in nascent adhesive contacts. *Curr. Biol.* (2002) doi:10.1016/S0960-9822(02)00661-9.

238. Georgiou, M. & Baum, B. Polarity proteins and Rho GTPases cooperate to spatially organise epithelial actin-based protrusions. *J. Cell Sci.* (2010) doi:10.1242/jcs.060772.

239. Vicente-Manzanares, M., Ma, X., Adelstein, R. S. & Horwitz, A. R. Non-muscle myosin II takes centre stage in cell adhesion and migration. *Nature Reviews Molecular Cell Biology* (2009) doi:10.1038/nrm2786.

240. Yoneda, A., Multhaupt, H. A. B. & Couchman, J. R. The Rho kinases I and II regulate different aspects of myosin II activity. *J. Cell Biol.* (2005) doi:10.1083/jcb.200412043.

241. Thumkeo, D. *et al.* Targeted Disruption of the Mouse Rho-Associated Kinase 2 Gene Results in Intrauterine Growth Retardation and Fetal Death. *Mol. Cell. Biol.* (2003) doi:10.1128/mcb.23.14.5043-5055.2003.

242. Li, Z. *et al.* Regulation of PTEN by Rho small GTPases. *Nat. Cell Biol.* (2005) doi:10.1038/ncb1236.

243. Martin-Belmonte, F. *et al.* PTEN-Mediated Apical Segregation of Phosphoinositides Controls Epithelial Morphogenesis through Cdc42. *Cell* (2007) doi:10.1016/j.cell.2006.11.051.

244. Schlüter, M. A. *et al.* Trafficking of Crumbs3 during cytokinesis is crucial for lumen formation. *Mol. Biol. Cell* (2009) doi:10.1091/mbc.E09-02-0137.

245. Ngok, S. P., Lin, W. H. & Anastasiadis, P. Z. Establishment of epithelial polarity - GEF who's minding the GAP? *Journal of Cell Science* (2014) doi:10.1242/jcs.153197.

246. Georgiou, M., Marinari, E., Burden, J. & Baum, B. Cdc42, Par6, and aPKC Regulate Arp2/3-

Mediated Endocytosis to Control Local Adherens Junction Stability. *Curr. Biol.* (2008) doi:10.1016/j.cub.2008.09.029.

247. Elbediwy, A. *et al.* Epithelial junction formation requires confinement of Cdc42 activity by a novel SH3BP1 complex. *J. Cell Biol.* (2012) doi:10.1083/jcb.201202094.
248. Ann Mack, N. & Georgiou, M. The interdependence of the Rho GTPases and apicobasal cell polarity. *Small GTPases* **5**, (2014).
249. Vasioukhin, V., Bauer, C., Yin, M. & Fuchs, E. Directed actin polymerization is the driving force for epithelial cell- cell adhesion. *Cell* (2000) doi:10.1016/S0092-8674(00)81559-7.
250. Takaishi, K., Sasaki, T., Kotani, H., Nishioka, H. & Takai, Y. Regulation of cell-cell adhesion by Rac and Rho small G proteins in MDCK cells. *J. Cell Biol.* (1997) doi:10.1083/jcb.139.4.1047.
251. Ehrlich, J. S., Hansen, M. D. H. & Nelson, W. J. Spatio-temporal regulation of Rac1 localization and lamellipodia dynamics during epithelial cell-cell adhesion. *Dev. Cell* (2002) doi:10.1016/S1534-5807(02)00216-2.
252. Fukuyama, T., Ogita, H., Kawakatsu, T., Inagaki, M. & Takai, Y. Activation of Rac by cadherin through the c-Src-Rap1-phosphatidylinositol 3-kinase-Vav2 pathway. *Oncogene* (2006) doi:10.1038/sj.onc.1209010.
253. Hordijk, P. L. *et al.* Inhibition of invasion of epithelial cells by Tiam1-Rac signaling. *Science (80-.).* (1997) doi:10.1126/science.278.5342.1464.
254. Malliri, A., Van Es, S., Huveneers, S. & Collard, J. G. The Rac exchange factor Tiam1 is required for the establishment and maintenance of cadherin-based adhesions. *J. Biol. Chem.* (2004) doi:10.1074/jbc.M401192200.
255. Ratheesh, A., Priya, R. & Yap, A. S. Coordinating Rho and Rac: The regulation of Rho GTPase signaling and cadherin junctions. in *Progress in Molecular Biology and Translational Science* (2013). doi:10.1016/B978-0-12-394311-8.00003-0.
256. Ivanov, A. I., Hunt, D., Utech, M., Nusrat, A. & Parkos, C. A. Differential roles for actin polymerization and a myosin II motor in assembly of the epithelial apical junctional complex. *Mol. Biol. Cell* (2005) doi:10.1091/mbc.E05-01-0043.
257. Vaezi, A., Bauer, C., Vasioukhin, V. & Fuchs, E. Actin cable dynamics and Rho/Rock orchestrate a polarized cytoskeletal architercture in the early steps of assembling a stratified epithelium. *Dev. Cell* (2002) doi:10.1016/S1534-5807(02)00259-9.
258. Ohta, Y., Hartwig, J. H. & Stossel, T. P. FilGAP, a Rho- and ROCK-regulated GAP for Rac binds filamin A to control actin remodelling. *Nat. Cell Biol.* (2006) doi:10.1038/ncb1437.
259. Ratheesh, A. *et al.* Centralspindlin and α-catenin regulate Rho signalling at the epithelial zonula adherens. *Nat. Cell Biol.* (2012) doi:10.1038/ncb2532.
260. Izumi, G. *et al.* Endocytosis of E-cadherin regulated by Rac and Cdc42 small G proteins through

IQGAP1 and actin filaments. *J. Cell Biol.* (2004) doi:10.1083/jcb.200401078.

261. White, C. D., Erdemir, H. H. & Sacks, D. B. IQGAP1 and its binding proteins control diverse biological functions. *Cellular Signalling* (2012) doi:10.1016/j.cellsig.2011.12.005.
262. Gomez, G. A., McLachlan, R. W. & Yap, A. S. Productive tension: Force-sensing and homeostasis of cell-cell junctions. *Trends in Cell Biology* (2011) doi:10.1016/j.tcb.2011.05.006.
263. Rossman, K. L., Der, C. J. & Sondek, J. GEF means go: Turning on Rho GTPases with guanine nucleotide-exchange factors. *Nature Reviews Molecular Cell Biology* (2005) doi:10.1038/nrm1587.
264. Schmidt, A. & Hall, A. Guanine nucleotide exchange factors for Rho GTPases: Turning on the switch. *Genes and Development* (2002) doi:10.1101/gad.1003302.
265. Peck, J., Douglas IV, G., Wu, C. H. & Burbelo, P. D. Human RhoGAP domain-containing proteins: Structure, function and evolutionary relationships. *FEBS Letters* (2002) doi:10.1016/S0014-5793(02)03331-8.
266. Kemphues, K. J., Priess, J. R., Morton, D. G. & Cheng, N. Identification of genes required for cytoplasmic localization in early C. elegans embryos. *Cell* (1988) doi:10.1016/S0092-8674(88)80024-2.
267. Joberty, G., Petersen, C., Gao, L. & Macara, I. G. The cell-polarity protein Par6 links Par3 and atypical protein kinase C to Cdc42. *Nat. Cell Biol.* (2000) doi:10.1038/35019573.
268. Hurd, T. W., Gao, L., Roh, M. H., Macara, I. G. & Margolis, B. Direct interaction of two polarity complexes implicated in epthelial tight junction assembly. *Nat. Cell Biol.* (2003) doi:10.1038/ncb923.
269. Gao, L. & Macara, I. G. Isoforms of the polarity protein Par6 have distinct functions. *J. Biol. Chem.* (2004) doi:10.1074/jbc.M403723200.
270. Lin, D. *et al.* A mammalian PAR-3-PAR-6 complex implicated in Cdc42/Rac1 and aPKC signalling and cell polarity. *Nat. Cell Biol.* (2000) doi:10.1038/35019582.
271. Mizuno, K. *et al.* Self-association of PAR-3-mediated by the conserved N-terminal domain contributes to the development of epithelial tight junctions. *J. Biol. Chem.* (2003) doi:10.1074/jbc.M303593200.
272. Itoh, M. *et al.* Junctional adhesion molecule (JAM) binds to PAR-3: A possible mechanism for the recruitment of PAR-3 to tight junctions. *J. Cell Biol.* (2001) doi:10.1083/jcb.200103047.
273. Chen, X. & Macara, I. G. RNA interference techniques to study epithelial cell adhesion and polarity. *Methods in Enzymology* (2006) doi:10.1016/S0076-6879(06)06003-4.
274. Suzuki, A. *et al.* Atypical protein kinase C is involved in the evolutionarily conserved PAR protein complex and plays a critical role in establishing epithelia-specific junctional structures. *J. Cell Biol.* (2001) doi:10.1083/jcb.152.6.1183.

275. Tepass, U., Theres, C. & Knust, E. crumbs encodes an EGF-like protein expressed on apical membranes of Drosophila epithelial cells and required for organization of epithelia. *Cell* (1990) doi:10.1016/0092-8674(90)90189-L.

276. Lemmers, C. *et al.* CRB3 Binds Directly to Par6 and Regulates the Morphogenesis of the Tight Junctions in Mammalian Epithelial Cells. *Mol. Biol. Cell* (2004) doi:10.1091/mbc.E03-04-0235.

277. Roh, M. H. & Margolis, B. Composition and function of PDZ protein complexes during cell polarization. *American Journal of Physiology - Renal Physiology* (2003) doi:10.1152/ajprenal.00086.2003.

278. Straight, S. W. *et al.* Loss of PALS1 Expression Leads to Tight Junction and Polarity Defects. *Mol. Biol. Cell* (2004) doi:10.1091/mbc.E03-08-0620.

279. Wang, Q., Chen, X. W. & Margolis, B. PALS1 regulates E-cadherin trafficking in mammalian epithelial cells. *Mol. Biol. Cell* (2007) doi:10.1091/mbc.E06-07-0651.

280. Lemmers, C. *et al.* hINAd1/PATJ, a homolog of discs lost, interacts with crumbs and localizes to tight junctions in human epithelial cells. *J. Biol. Chem.* (2002) doi:10.1074/jbc.M202196200.

281. Michel, D. *et al.* PATJ connects and stabilizes apical and lateral components of tight junctions in human intestinal cells. *J. Cell Sci.* (2005) doi:10.1242/jcs.02528.

282. Shin, K., Straight, S. & Margolis, B. PATJ regulates tight junction formation and polarity in mammalian epithelial cells. *J. Cell Biol.* (2005) doi:10.1083/jcb.200408064.

283. Bilder, D. & Perrimon, N. Localization of apical epithelial determinants by the basolateral PDZ protein Scribble. *Nature* (2000) doi:10.1038/35001108.

284. Bilder, D., Li, M. & Perrimon, N. Cooperative regulation of cell polarity and growth by Drosophila tumor suppressors. *Science (80-.).* (2000) doi:10.1126/science.289.5476.113.

285. Laprise, P., Viel, A. & Rivard, N. Human Homolog of Disc-large Is Required for Adherens Junction Assembly and Differentiation of Human Intestinal Epithelial Cells. *J. Biol. Chem.* (2004) doi:10.1074/jbc.M309843200.

286. Matsumine, A. *et al.* Binding of APC to the human homolog of the Drosophila discs large tumor suppressor protein. *Science (80-.).* (1996) doi:10.1126/science.272.5264.1020.

287. Yamanaka, T. *et al.* Mammalian Lgl forms a protein complex with PAR-6 and aPKC independently of PAR-3 to regulate epithelial cell polarity. *Curr. Biol.* (2003) doi:10.1016/S0960-9822(03)00244-6.

288. Müsch, A. *et al.* Mammalian homolog of Drosophila tumor suppressor lethal (2) giant larvae interacts with basolateral exocytic machinery in Madin-Darby canine kidney cells. *Mol. Biol. Cell* (2002) doi:10.1091/mbc.01-10-0496.

289. Plant, P. J. *et al.* A polarity complex of mPar-6 and atypical PKC binds, phosphorylates and regulates mammalian Lgl. *Nat. Cell Biol.* (2003) doi:10.1038/ncb948.

290. Nagai-Tamai, Y., Mizuno, K., Hirose, T., Suzuki, A. & Ohno, S. Regulated protein-protein interaction between aPKC and PAR-3 plays an essential role in the polarization of epithelial cells. *Genes to Cells* (2002) doi:10.1046/j.1365-2443.2002.00590.x.

291. Martin-Belmonte, F. & Perez-Moreno, M. Epithelial cell polarity, stem cells and cancer. *Nature Reviews Cancer* (2012) doi:10.1038/nrc3169.

292. Ebnet, K. *et al.* The cell polarity protein ASIP/PAR-3 directly associates with junctional adhesion molecule (JAM). *EMBO J.* (2001) doi:10.1093/emboj/20.14.3738.

293. O'Brien, L. E., Zegers, M. M. P. & Mostov, K. E. Building epithelial architecture: Insights from three-dimensional culture models. *Nature Reviews Molecular Cell Biology* (2002) doi:10.1038/nrm859.

294. Debnath, J. & Brugge, J. S. Modelling glandular epithelial cancers in three-dimensional cultures. *Nature Reviews Cancer* (2005) doi:10.1038/nrc1695.

295. Lubarsky, B. & Krasnow, M. A. Tube morphogenesis: Making and shaping biological tubes. *Cell* (2003) doi:10.1016/S0092-8674(02)01283-7.

296. Montesano, R., Schaller, G. & Orci, L. Induction of epithelial tubular morphogenesis in vitro by fibroblast-derived soluble factors. *Cell* (1991) doi:10.1016/0092-8674(91)90115-F.

297. Bryant, D. M. *et al.* A molecular network for de novo generation of the apical surface and lumen. *Nat. Cell Biol.* **12**, 1035–1045 (2010).

298. Bryant, D. M. *et al.* A molecular switch for the orientation of epithelial cell polarization. *Dev. Cell* **31**, 171–187 (2014).

299. Van der Flier, A. & Sonnenberg, A. Function and interactions of integrins. *Cell and Tissue Research* (2001) doi:10.1007/s004410100417.

300. Wehrle-Haller, B. Assembly and disassembly of cell matrix adhesions. *Current Opinion in Cell Biology* (2012) doi:10.1016/j.ceb.2012.06.010.

301. Springer, T. A. & Dustin, M. L. Integrin inside-out signaling and the immunological synapse. *Current Opinion in Cell Biology* (2012) doi:10.1016/j.ceb.2011.10.004.

302. Kechagia, J. Z., Ivaska, J. & Roca-Cusachs, P. Integrins as biomechanical sensors of the microenvironment. *Nature Reviews Molecular Cell Biology* (2019) doi:10.1038/s41580-019-0134-2.

303. Zhu, L. *et al.* Structure of Rap1b bound to talin reveals a pathway for triggering integrin activation. *Nat. Commun.* (2017) doi:10.1038/s41467-017-01822-8.

304. Moreno-Layseca, P., Icha, J., Hamidi, H. & Ivaska, J. Integrin trafficking in cells and tissues. *Nature Cell Biology* (2019) doi:10.1038/s41556-018-0223-z.

305. O'brien, L. E. *et al.* Rac1 orientates epithelial apical polarity through effects on basolateral laminin assembly. *Nat. Cell Biol.* (2001) doi:10.1038/ncb0901-831.

306. Cohen, D., Fernandez, D., Lázaro-Diéguez, F. & Müsch, A. The serine/threonine kinase Par1b regulates epithelial lumen polarity via IRSp53-mediated cell-ECM signaling. *J. Cell Biol.* (2011) doi:10.1083/jcb.201007002.

307. Yu, W. *et al.* β1-integrin orients epithelial polarity via Rac1 and laminin. *Mol. Biol. Cell* (2005) doi:10.1091/mbc.E04-05-0435.

308. Yu, W. *et al.* Involvement of RhoA, ROCK I and myosin II in inverted orientation of epithelial polarity. *EMBO Rep.* **9**, 923–929 (2008).

309. Adams, S. A., Smith, M. E. F., Cowley, G. P. & Carr, L. A. Reversal of glandular polarity in the lymphovascular compartment of breast cancer. *J. Clin. Pathol.* (2004) doi:10.1136/jcp.2004.016980.

310. Apodaca, G., Gallo, L. I. & Bryant, D. M. Role of membrane traffic in the generation of epithelial cell asymmetry. *Nature Cell Biology* (2012) doi:10.1038/ncb2635.

311. Traub, L. M. Regarding the amazing choreography of clathrin coats. *PLoS Biol.* (2011) doi:10.1371/journal.pbio.1001037.

312. Gan, Y., McGraw, T. E. & Rodriguez-Boulan, E. The epithelial-specific adaptor AP1B mediates post-endocytic recycling to the basolateral membrane. *Nat. Cell Biol.* (2002) doi:10.1038/ncb827.

313. Schuck, S. & Simons, K. Polarized sorting in epithelial cells: Raft clustering and the biogenesis of the apical membrane. *J. Cell Sci.* (2004) doi:10.1242/jcs.01596.

314. Rodriguez-Boulan, E. & Gonzalez, A. Glycans in post-Golgi apical targeting: Sorting signals or structural props? *Trends in Cell Biology* (1999) doi:10.1016/S0962-8924(99)01595-0.

315. Weisz, O. A. & Rodriguez-Boulan, E. Apical trafficking in epithelial cells: Signals, clusters and motors. *Journal of Cell Science* (2009) doi:10.1242/jcs.032615.

316. Boscher, C., Dennis, J. W. & Nabi, I. R. Glycosylation, galectins and cellular signaling. *Current Opinion in Cell Biology* (2011) doi:10.1016/j.ceb.2011.05.001.

317. Delacour, D. *et al.* Loss of galectin-3 impairs membrane polarisation of mouse enterocytes in vivo. *J. Cell Sci.* (2008) doi:10.1242/jcs.020800.

318. Simons, K. & Gerl, M. J. Revitalizing membrane rafts: New tools and insights. *Nature Reviews Molecular Cell Biology* (2010) doi:10.1038/nrm2977.

319. Jaulin, F., Xue, X., Rodriguez-Boulan, E. & Kreitzer, G. Polarization-Dependent Selective Transport to the Apical Membrane by KIF5B in MDCK Cells. *Dev. Cell* (2007) doi:10.1016/j.devcel.2007.08.001.

320. Jaulin, F. & Kreitzer, G. KIF17 stabilizes microtubules and contributes to epithelial morphogenesis by acting at MT plus ends with EB1 and APC. *J. Cell Biol.* (2010) doi:10.1083/jcb.201006044.

321. Gerke, V., Creutz, C. E. & Moss, S. E. Annexins: Linking Ca2+ signalling to membrane dynamics. *Nature Reviews Molecular Cell Biology* (2005) doi:10.1038/nrm1661.

322. Pocard, T., Le Bivic, A., Galli, T. & Zurzolo, C. Distinct v-SNAREs regulate direct and indirect apical delivery in polarized epithelial cells. *J. Cell Sci.* (2007) doi:10.1242/jcs.007948.

323. Lambert, M., Choquet, D. & Mège, R. M. Dynamics of ligand-induced, Rac1-dependent anchoring of cadherins to the actin cytoskeleton. *J. Cell Biol.* (2002) doi:10.1083/jcb.200107104.

324. Fehon, R. G., McClatchey, A. I. & Bretscher, A. Organizing the cell cortex: The role of ERM proteins. *Nature Reviews Molecular Cell Biology* vol. 11 276–287 (2010).

325. Saotome, I., Curto, M. & McClatchey, A. I. Ezrin is essential for epithelial organization and villus morphogenesis in the developing intestine. *Dev. Cell* (2004) doi:10.1016/j.devcel.2004.05.007.

326. Muzny, D. M. *et al.* Comprehensive molecular characterization of human colon and rectal cancer. *Nature* (2012) doi:10.1038/nature11252.

327. Pino, M. S. & Chung, D. C. The Chromosomal Instability Pathway in Colon Cancer. *Gastroenterology* (2010) doi:10.1053/j.gastro.2009.12.065.

328. Domenica, F. *et al.* The Molecular Hallmarks of the Serrated Pathway in Colorectal Cancer. *Cancers (Basel).* **11**, 3–5 (2019).

329. Yamane, L., Scapulatempo-Neto, C., Reis, R. M. & Guimarães, D. P. Serrated pathway in colorectal carcinogenesis. *World Journal of Gastroenterology* (2014) doi:10.3748/wjg.v20.i10.2634.

330. Brabletz, T. *et al.* Invasion and metastasis in colorectal cancer: Epithelial-mesenchymal transition, mesenchymal-epithelial transition, stem cells and β-catenin. *Cells Tissues Organs* (2005) doi:10.1159/000084509.

331. Wellner, U. *et al.* The EMT-activator ZEB1 promotes tumorigenicity by repressing stemness-inhibiting microRNAs. *Nat. Cell Biol.* (2009) doi:10.1038/ncb1998.

332. Spaderna, S. *et al.* The transcriptional repressor ZEB1 promotes metastasis and loss of cell polarity in cancer. *Cancer Res.* (2008) doi:10.1158/0008-5472.CAN-07-5682.

333. Reggiani Bonetti, L., Barresi, V., Bettelli, S., Domati, F. & Palmiere, C. Poorly differentiated clusters (PDC) in colorectal cancer: What is and ought to be known. *Diagnostic Pathology* (2016) doi:10.1186/s13000-016-0481-7.

334. Commander, R. *et al.* Subpopulation targeting of pyruvate dehydrogenase and GLUT1 decouples metabolic heterogeneity during collective cancer cell invasion. *Nat. Commun.* (2020) doi:10.1038/s41467-020-15219-7.

335. Ilina, O. *et al.* Cell–cell adhesion and 3D matrix confinement determine jamming transitions in

breast cancer invasion. *Nat. Cell Biol.* (2020) doi:10.1038/s41556-020-0552-6.

336. Friedl, P. & Gilmour, D. Collective cell migration in morphogenesis, regeneration and cancer. *Nature Reviews Molecular Cell Biology* (2009) doi:10.1038/nrm2720.
337. Aceto, N. *et al.* Circulating tumor cell clusters are oligoclonal precursors of breast cancer metastasis. *Cell* **158**, 1110–1122 (2014).
338. Libanje, F. *et al.* ROCK 2 inhibition triggers the collective invasion of colorectal adenocarcinomas . *EMBO J.* (2019) doi:10.15252/embj.201899299.
339. Julien, S. *et al.* Characterization of a large panel of patient-derived tumor xenografts representing the clinical heterogeneity of human colorectal cancer. *Clinical Cancer Research* vol. 18 5314–5328 (2012).
340. Samowitz, W. S. & Slattery, M. L. Transforming growth factor-β receptor type 2 mutations and microsatellite instability in sporadic colorectal adenomas and carcinomas. *Am. J. Pathol.* (1997).
341. Yu, W. *et al.* -Integrin Orients Epithelial Polarity via Rac1 and Laminin □ D. *Mol. Biol. Cell* **16**, 433–445 (2005).
342. Schwartz, M. Rho signalling at a glance. *Journal of Cell Science* (2004) doi:10.1242/jcs.01582.
343. Hanley, C. J., Henriet, E., Sirka, O. K., Thomas, G. J. & Ewald, A. J. Tumor-Resident Stromal Cells Promote Breast Cancer Invasion through Regulation of the Basal Phenotype. *Mol. Cancer Res.* (2020) doi:10.1158/1541-7786.mcr-20-0334.
344. Al Habyan, S., Kalos, C., Szymborski, J. & McCaffrey, L. Multicellular detachment generates metastatic spheroids during intra-abdominal dissemination in epithelial ovarian cancer. *Oncogene* **37**, 5127–5135 (2018).
345. Hegerfeldt, Y., Tusch, M., Bröcker, E.-B. & Friedl, P. Collective Cell Movement in Primary Melanoma Explants. *Cancer Res.* (2002).
346. Chaffer, C. L., San Juan, B. P., Lim, E. & Weinberg, R. A. EMT, cell plasticity and metastasis. *Cancer Metastasis Rev.* (2016) doi:10.1007/s10555-016-9648-7.
347. Bissey, P. A. *et al.* Blocking SHH/Patched interaction triggers tumor growth inhibition through patched-induced apoptosis. *Cancer Res.* (2020) doi:10.1158/0008-5472.CAN-19-1340.
348. Triantafyllou, A. *et al.* Cobalt induces hypoxia-inducible factor-1α (HIF-1α) in HeLa cells by an iron-independent, but ROS-, PI-3K- and MAPK-dependent mechanism. *Free Radic. Res.* (2006) doi:10.1080/10715760600730810.
349. Rohwer, N. *et al.* Non-canonical HIF-1 stabilization contributes to intestinal tumorigenesis. *Oncogene* (2019) doi:10.1038/s41388-019-0816-4.
350. Arany, Z. *et al.* HIF-independent regulation of VEGF and angiogenesis by the transcriptional coactivator PGC-1α. *Nature* (2008) doi:10.1038/nature06613.

351. Paul, N. R., Jacquemet, G. & Caswell, P. T. Endocytic Trafficking of Integrins in Cell Migration. *Current Biology* (2015) doi:10.1016/j.cub.2015.09.049.

352. Munger, J. S. & Sheppard, D. Cross talk among TGF-β signaling pathways, integrins, and the extracellular matrix. *Cold Spring Harb. Perspect. Biol.* **3**, (2011).

353. Barresi, V., Reggiani Bonetti, L., Ieni, A., Domati, F. & Tuccari, G. Prognostic significance of grading based on the counting of poorly differentiated clusters in colorectal mucinous adenocarcinoma. *Hum. Pathol.* **46**, 1722–1729 (2015).

354. Ashley, N., Ouaret, D. & Bodmer, W. F. Cellular polarity modulates drug resistance in primary colorectal cancers via orientation of the multidrug resistance protein ABCB1. *J. Pathol.* **247**, 293–304 (2019).

355. Roy, P. *et al.* Organoids as preclinical models to improve intraperitoneal chemotherapy effectiveness for colorectal cancer patients with peritoneal metastases: Preclinical models to improve HIPEC. *Int. J. Pharm.* **531**, 143–152 (2017).

356. Quénet, F. *et al.* Cytoreductive surgery plus hyperthermic intraperitoneal chemotherapy versus cytoreductive surgery alone for colorectal peritoneal metastases (PRODIGE 7): a multicentre, randomised, open-label, phase 3 trial. *Lancet Oncol.* (2021) doi:10.1016/S1470-2045(20)30599-4.

357. Charrier, T. *et al.* Cytoreductive Surgery Combined with Hyperthermic Intraperitoneal Chemotherapy with Oxaliplatin Increases the Risk of Postoperative Hemorrhagic Complications: Analysis of Predictive Factors. *Ann. Surg. Oncol.* (2016) doi:10.1245/s10434-016-5143-1.

358. Koboldt, D. C. *et al.* Comprehensive molecular portraits of human breast tumours. *Nature* (2012) doi:10.1038/nature11412.

359. Huber, W. *et al.* Orchestrating high-throughput genomic analysis with Bioconductor. *Nat. Methods* (2015) doi:10.1038/nmeth.3252.

360. Tusher, V. G., Tibshirani, R. & Chu, G. Significance analysis of microarrays applied to the ionizing radiation response. *Proc. Natl. Acad. Sci. U. S. A.* (2001) doi:10.1073/pnas.091062498.

361. Subramanian, A. *et al.* Gene set enrichment analysis: A knowledge-based approach for interpreting genome-wide expression profiles. *Proc. Natl. Acad. Sci. U. S. A.* (2005) doi:10.1073/pnas.0506580102.

362. Cline, M. S. *et al.* Integration of biological networks and gene expression data using cytoscape. *Nat. Protoc.* (2007) doi:10.1038/nprot.2007.324.